ULTRAFAST SWITCHING OF CO_2 LASER PULSES BY OPTICALLY-INDUCED PLASMA REFLECTION IN SEMICONDUCTORS

By

ABDULHAKEM Y. ELEZZABI

B. Sc.(Hon.), (Physics), Brock University, 1987

M. Sc., (Physics), University of British Columbia, 1989

A THESIS SUBMITTED IN PARTIAL FULFILLMENT OF

THE REQUIREMENTS FOR THE DEGREE OF

DOCTOR OF PHILOSOPHY

in

THE FACULTY OF GRADUATE STUDIES

DEPARTMENT OF PHYSICS

We accept this thesis as conforming

to the required standard

THE UNIVERSITY OF BRITISH COLUMBIA

July 1995

In presenting this thesis in partial fulfilment of the requirements for an advanced degree at the University of British Columbia, I agree that the Library shall make it freely available for reference and study. I further agree that permission for extensive copying of this thesis for scholarly purposes may be granted by the head of my department or by his or her representatives. It is understood that copying or publication of this thesis for financial gain shall not be allowed without my written permission.

(Signature)

Department of PHYSICS

The University of British Columbia
Vancouver, Canada

Date Aug 3 1995

DE-6 (2/88)

Abstract

Ultrafast mid-infrared laser pulse generation using optical semiconductor switching is investigated experimentally for application to subpicosecond CO_2 laser pulse generation at 10.6 μm. Time-resolved infrared measurements, which are based on cross-correlation and reflection-reflection correlation techniques, are used to determine the duration of the reflected infrared pulses from a GaAs infrared reflection switch. These time-resolved measurements together with time-integrated measurements are used to derive a model describing the behaviour of the GaAs infrared reflection switch. It is found that diffusion and two-body recombination whose rate is taken to be density-dependent, can accurately describe the ultrafast infrared reflectivity switching process in GaAs. We have also investigated some novel semiconductor materials with ultrafast recombination lifetimes for ultrafast semiconductor switching application. A molecular beam epitaxy low temperature grown GaAs (LT-GaAs) and radiation damaged GaAs (RD-GaAs) are successfully used to switch out ultrashort CO_2 laser pulses. Application of the time-resolved cross-correlation technique to nonequilibrium carrier lifetime measurements in highly excited LT-GaAs, RD-GaAs, and $In_{0.85}Ga_{0.15}As/GaAs$ relaxed superlattice structure are found to be in good agreement with other reported techniques. As an application to semiconductor probing, ultrafast infrared transmission experiments are conducted to determine the absorption of infrared pulses in Si of various dopings after free carriers have been generated by absorption of a subpicosecond laser pulse of above band gap photon energy. By fitting the experimental data to a theoretical model, the free-carrier absorption cross-sections and the momentum relaxation times are calculated.

Table of Contents

List of Figures

Acknowledgments

I wish to especially thank my supervisor, Prof. Jochen Meyer, for providing me with the opportunity to work with him and for creating an intellectually stimulating research environment. His constant guidance and encouragement are most appreciated.

I deeply thank and appreciate my parents, Youssef Elezzabi and Amna Quaia, and the rest of my family, for allowing me the opportunity to pursue my post-secondary studies in Canada, and for their continuous moral support.

Special thanks goes to Lara Cleven whose encouragement and help made the experimental setbacks insignificant.

It is also a pleasure to acknowledge Hubert Houtman for a great deal of assistance, guidance, and endless hours of stimulating discussion, which have had a strong positive impact on my research.

Thanks to my colleague Michael Hughes for his help in operating the experiments, his assistance in setting up the laser systems, and his valuable discussions. His help accelerated my progress.

Thanks to Shane Johnson for growing the semiconductor structures.

Prof. Irving Ozier deserves thanks for his thorough reading of the thesis and suggestions for the manuscript corrections.

Also, I wish to express appreciation to Prof. Thomas Tiedje for the use of the MBE machine and his useful experimental assistance.

Thanks to my fellow colleagues: Ross McKenna, Steven Leffler, Dr. Peter Zhu, Dr. Samir Aouadi, Dr. Michel Laberge, and Dr. James Booth. Their presence made the work more satisfying and pleasant.

My special thanks are extended to the following persons for the unequalled technical support:

Philip Akers, Jacobus Bosma, Ole Christiansen, Domenic Di Tomaso, Tom Felton, James Gislason, Stan Knotek, Heinrich Manfred, Beat Meyer, Joseph O'Connor, Mary Ann Potts, Brian Smith, Douglas Wong, and especially to Alan Cheuck for providing great service and ensuring that the equipment worked and that supplies were available.

Thanks are also due to the staff of the U.B.C. Physics Department: Bridget Hamilton, Lore Hoffmann, and Kim Spears for superb administrative help.

The financial assistance of the Libyan Ministry of Higher Education, and the Natural Sciences and Engineering Research Council is appreciated.

Chapter 1

Introduction

Since the first demonstration of optical semiconductor switching by Alcock et al. in 1976 [43], the technique has gained wide interest to its potential application in generating femtosecond laser pulses at 10.6 μm. Despite the rapid advances in ultrafast laser technology in the last decade, the focus of femtosecond laser research is directed towards visible, near infrared, and ultraviolet wavelengths. In comparison to other laser wavelengths, minimal research has been devoted to ultrashort pulse generation schemes at 10.6 μm. Ultrashort coherent mid-infrared laser pulses are of interest for the investigation of fundamental processes occurring on short-time scales which cannot be studied with the current ultrafast lasers. Ultrafast CO_2 laser pulses operating in the mid-infrared range are of valuable interest to many research fields. Femtosecond/picosecond 10.6 μm laser pulses have a wide range of application to semiconductor physics, plasma physics, and chemistry.

In semiconductor and solid state physics, ultrashort 10.6 μm lasers provide an important tool for exploring several fundamental processes involving carrier dynamics, such as intraband transitions, interband transitions in low band gap materials, intervalence band absorption of free holes, free-carrier absorption, intersubband transitions in quantum wells, momentum relaxation times, carrier lifetimes, carrier energy relaxation rates, and diffusion coefficients. Many of the experimental conclusions can be gained by time resolved measurements of transmission and reflectivity changes induced by nonequilibrium carrier distributions. The knowledge of these processes aids in the development of new and faster semiconductor and optoelectronic devices. Moreover, ultrashort mid-infrared

pulses are essential for testing high-speed mid-infrared devices such as detectors and modulators. In the field of photochemistry, femtosecond 10.6 μm infrared laser pulses are of great interest for application to infrared spectroscopy of molecules. The advances in ultrashort pulses have permitted the investigation of the vibrational-rotational modes in polyatomic molecules, study of fast chemical reaction rates and dynamics, chemical kinetics and energy transfer in liquids, multiphoton excitation, multiphoton ionization, infrared absorption, and local charge distribution of organic molecules. A 10.6 μm femtosecond laser pulse provides an important tool for application to ultrafast nonlinear processes in laser-plasma interactions.

1.1 Present Investigation

The primary objective of this thesis work is to perform a complete experimental study of femtosecond CO_2 laser pulse generation operating at 10.6 μm as a part of the development of a subpicosecond terawatt table top laser system. To achieve this goal we would like to employ optical semiconductor switching techniques to generate these pulses. Clearly, before developing such a laser system, there are several studies that must be performed. Specifically, the main issues addressed in this work are:

1. The feasibility of generating femtosecond laser pulses at 10.6 μm using a single optical semiconductor switch, including the switching dynamics of the optical semiconductor switching mechanism to determine the limits on the shortest pulse that can be generated.

2. The study of the temporal behaviour of the reflected infrared pulses as a function of injected carrier density.

3. Investigation of the role of carrier diffusion and recombination on the speed of the optical infrared switch.

4. To explore some novel semiconductor materials for their use in mid-infrared femtosecond pulse generation.

5. To investigate the use of infrared probing for the measurement of carrier lifetimes.

6. To measure the free-carrier absorption cross-sections and momentum relaxation times in semiconductors.

7. To develop accurate methods for measuring mid-infrared laser pulse temporal shapes, and to explore their limitations and sensitivities.

8. To develop simple models that describe the infrared reflection/transmission semiconductor switching process.

1.2 Thesis Organization

This thesis is divided into seven chapters discussing the details of the experimental and theoretical work. Four appendices are devoted to the aspects of some technical designs of the experimental equipment. The thesis is organized as follows: the standard methods used in the generating of laser pulses in the mid-infrared range, and especially at 10.6 μm, are briefly discussed in Chapter 2. A qualitative overview is presented for each experimental technique evaluating its general features, advantages, and limitations. An introduction of the physical process of optical infrared semiconductor switching and the principles behind the generation scheme are also presented in this chapter. The general formalism describing the dielectric function of a semiconductor along with some important absorption processes at 10.6 μm are also introduced in Chapter 2.

In Chapter 3 a model describing the infrared optical semiconductor switching process is presented. The model is based on the reflection of the infrared radiation from a thin plasma layer with the carrier dynamics determined by ambipolar diffusion. The wave propagation equation is solved numerically for some experimental semiconductor plasma conditions, and the time evolution of the plasma is governed by ambipolar diffusion. From the numerical simulations, femtosecond/picosecond pulse generation conditions and characteristics are obtained. The calculations presented in this chapter provide the necessary background on the subject of infrared semiconductor switching.

A brief description of the experimental equipment that are used during the investigation, the optical setups, and the experimental conditions are presented in Chapter 4. Part of this experimental work is dedicated to the installation, maintenance, and characterizations of the commercial laser system. Thus, a brief review of the major laser system components is outlined. The details of the construction and the design of the high-power CO_2 laser are also reviewed in this chapter. The electronic and optical instrumentations that are constructed and developed for specific experimental purposes are also briefly discussed in this chapter. Moreover, the specific techniques and the optical setups for time-resolved and frequency-resolved measurements used to perform the experiments are outlined in detail.

The time-resolved and time-integrated experimental results on optical semiconductor switching using GaAs are presented in Chapter 5. Interpretations of the experimental data and some estimates of the importance of the physical mechanisms governing the time evolution of the switch reflectivity are discussed. Based on the experimental observations, a simple model describing the switching process in GaAs is developed to predict the switching behaviour. The results for free-carrier absorption cross-section and momentum relaxation times in both doped and intrinsic Si transmission cut-off switches are presented in the same chapter. A complete model describing the infrared transmission through Si

is developed and compared with the experimental results.

The growth procedures, sample preparations, and the experimental results of novel ultrafast recombination semiconductors are discussed in detail in Chapter 6. Here, the results of infrared probing of the temporal carrier lifetimes of several semiconductors are presented. Ultrashort 10.6 μm pulses generated using ultrafast recombination semiconductors are also discussed.

Finally, in Chapter 7, we briefly summarize the results of the thesis, with special emphasis on the major original thesis contributions. A concluding remark on the nature of the free-carriers' recombination mechanism in GaAs is made. Moreover, suggestions for an interesting ultrashort pulse generation scheme and a novel optical arrangement for semiconductors probing are presented. Also, a numerical estimate on the limit of generated pulse duration is discussed in this chapter.

Chapter 2

Semiconductor Switching and Ultrashort Laser Pulses at 10.6 μm

2.1 Introduction

This chapter is intended as an overview of the basic physics and technology dealing with the generation of ultrashort laser pulses in the mid-infrared region. Since our objective is to produce subpicosecond pulses at the CO_2 laser wavelength, the review is directed towards mid-infrared pulses generated at a wavelength of 10.6 μm.

The first section of this chapter introduces the essential issues and constraints associated with the generation of ultrashort laser pulses at 10.6 μm. The second section presents brief overviews of some standard techniques employed for ultrashort 10.6 μm pulse generation such as: mode locking, optical free induction decay, nonlinear frequency mixing, and free electron lasers. In the third section, we introduce optical semiconductor switching, and discuss the basic physical principles behind the generation scheme. Finally, in section four, we present some relevant processes which occur during ultrafast optical excitation of the semiconductor switch and introduce the semiconductor switch dielectric function.

2.2 Ultrashort Pulse Generation Using a CO_2 Laser

Before proceeding with the techniques of ultrashort pulse generation, one should highlight the basic physical principles that govern the generation of ultrashort laser pulses at 10.6 μm.

The gain spectrum of the CO_2 laser consists of several discrete vibrational-rotational lines. In order to produce subpicosecond laser pulses directly from the laser medium, the gain spectrum must be wide enough to amplify these pulses. The gain spectrum of the CO_2 laser can be enhanced to support the generation of ultrashort laser pulses simply by increasing the operating laser gas pressure [1]. The overlap of the adjacent rotational lines of the CO_2 molecules modulates and widens the gain spectrum and helps to minimize pulse distortion. However, high pressure operation decreases the gain risetime and lifetime due to the increased collisional excitations/de-excitations of the laser levels [2]–[4]. In other words, due to high gas pressure, the excited CO_2 molecules relax faster (inversely proportional to the pressure). In addition, the limited gain lifetime restricts the duration of the generated pulse by limiting the effective number of pulse round trips in the laser cavity. That is, if the generated pulse is to be made short enough, a higher number of cavity round trips is required to take advantage of the wide gain spectrum. It was pointed out by Houtman and Meyer [5] that the gain duration for a 10 atmosphere CO_2 laser is only $\sim$ 750 ns at FWHM (full width at half maximum) and hence, active mode lockers cannot produce pulses shorter than $\sim$ 800 ps. These two facts reduce the effectiveness of ultrashort pulse generation by mode locking [5, 6].

2.2.1 Mode Locking of a CO_2 Laser

Due to the limited gain bandwidth of a TEA (transverse electric atmospheric) CO_2 laser, the long $\sim$ 100-200 ns pulses from a so-called hybrid CO_2 laser (a combination of a CW laser and a TEA laser sharing the same laser resonator) can be shortened by mode locking of multiatmosphere transversely excited lasers. Passive and active mode locking techniques are commonly used to shorten the duration of a laser pulse.

Passive mode locking relies on absorption saturation to generate amplitude modulation by providing an intensity-dependent loss in the laser cavity. That is, the transmission

of a saturable absorber follows the shape of the radiation laser pulse; the peak of the laser pulse experiences a lower loss than the wings, consequently, the peak of the pulse is amplified, thus resulting in the pulse compression. The technique is especially successful in generating ultrashort pulses of less than 1 ns [7]–[13] at 10.6 μm. The minimum pulse duration that is achievable with a fast saturable absorber is limited by the absorber's recovery time and the CO_2 laser gain line width. Laser pulses of a duration between 1 to 5 ns have been generated using SF_6 as a fast saturable absorber [7, 8]. Shorter pulses of duration between 80 to 500 ps were obtained by using P-type Ge as a bleachable absorber [9]–[13]. The CO_2 laser pulses generated with passive mode locking techniques are limited in their pulse duration to $\sim$ 80 ps.

Active mode locking utilizes the beating of the laser oscillation with an external oscillator frequency [14]. The gain or loss of the laser cavity is periodically modulated at the oscillator's frequency (amplitude modulation or frequency modulation) [14]. A complete review of the subject of active mode locking is presented in reference [15]. Actively mode locked multiatmosphere CO_2 lasers [5, 11] [16]–[19], result in longer pulse durations ($\sim$ 1 ns) than the passive mode locking technique. Pulses as short as $\sim$ 500 ps (detector limited) have been generated by Houtman et al. [16] with a novel square-wave mode locking and cavity dumping of a 10 atmosphere CO_2 laser system. This pulse generation system produced the shortest pulse ever generated using an active mode locking scheme. In general, the technique can be used to produce pulses as short as 200 ps [15, 16]; however, the amount of extracted power is limited to low damage threshold of the pockels cell crystal.

The short gain lifetime and the lack of a wide gain bandwidth necessary to support the generation of picosecond or femtosecond pulses makes the generation of pulses shorter than 500 ps very challenging by the standard mode locking techniques similar to the ones applied to solid state lasers [14]. For these reasons, alternative nonconventional

ways to produce ultrashort mid-infrared laser pulses have been developed: including optical free induction decay, free electron lasers, nonlinear frequency mixing and optical semiconductor switching.

2.2.2 Optical Free Induction Decay (OFID)

OFID is originally proposed and demonstrated by Yablonovitch and Goldhar [20] as a method for generating high power picosecond pulses at 10.6 μm. The central components of the system are: a single mode high-power CO_2 laser, a plasma shutter, and a hot CO_2 absorption cell. The principle behind OFID is simple: first the frequency spectrum of the CO_2 laser pulse has to be widened and then the original central frequency is filtered out. In such pulse generating systems, an optical transmission switch turns off a long single mode CO_2 laser pulse in a time of approximately a few picoseconds. As a result of this ultrafast pulse truncation, frequency sidebands are generated around the central frequency of the CO_2 laser line. The central component frequency can be rejected by using a narrow resonance absorption filter such as hot CO_2 gas. A hot CO_2 gas only allows the sidebands of the frequency spectrum to be transmitted, hence, producing an ultrashort pulse. An alternative time-domain explanation of the OFID process is to consider a CO_2 cell which is heated to $\sim$ 450 °C to increase the absorption of the 10.6 μm radiation. If the hot cell is long enough, then a complete attenuation of the CO_2 laser beam is possible. Under a steady state one can view the absorption process as a destructive interference between the CO_2 laser radiation electric field and the induced electric-dipole radiation from the hot CO_2 gas. The polarization induced electric field is always coherent with the input electric field but with the opposite phase. Now, when the CO_2 electric field is suddenly turned off by the plasma shutter in a time duration which is much faster than the relaxation time of the CO_2 molecules, then the fields are no longer canceled by destructive interference and the excited CO_2 hot molecules continue

to radiate in phase with each other (but still out of phase with the applied electric field). That is, turning off the input signal quickly results in the generation of an ultrashort pulse whose width is limited by the relaxation time (due to dephasing and energy decay) of the dipole radiation. Figure 2.1 illustrates the OFID principle both in time and frequency domains.

The CO_2 laser pulse duration can by approximated by the following empirical formula [21]:

$$\tau_p(ps) \simeq 0.67(\frac{T_d}{\gamma_a \ell}) + 10 \tag{2.1}$$

where T_d, γ_a, and ℓ are the dephasing time of the resonant absorber, absorption coefficient of the resonant absorber, and its length, respectively.

Several OFID experiments employing various shutters [20]–[30] demonstrated the feasibility of this technique in the generation of ultrashort picosecond pulses of a duration adjustable between 33 and 200 ps. The pulse duration is found to be strongly dependent on the CO_2 gas pressure which is related to the relaxation time, T_d, through the relation [24]:

$$T_d(ns) = \frac{42}{P\sqrt{\Theta/300}} \tag{2.2}$$

where P and Θ are the CO_2 gas pressure in torr and its temperature in degrees Kelvin, respectively. The relaxation time of the CO_2 molecules limits the width of the generated pulses to $\sim$ 30 ps. Other techniques must be employed to reduce to pulse duration below 30 ps.

Scherrer and Kneubühl [25] proposed a new picosecond 10 μm CO_2 laser based system with far-infrared laser gases (CH_3F, D_2O, and NH_3) as spectral line filters. This OFID system has advantages over the hot CO_2 based OFID setup: it can be operated at considerably lower gas pressure and at room temperature; in addition, the frequency of the pulse can be selected very precisely by proper choice of the gas. However, to date,

the authors did not present any measurements on their pulse durations using these gases.

The OFID pulse is short when the dip in the frequency spectrum is wide [21]; therefore, a major concern, which is usually ignored in the literature and by groups performing OFID experiments, is the background level of the generated pulses. Since the generated pulses lack the central frequency component in their frequency spectrum, the generated pulses are in fact not as short as they are claimed to be. With simple mathematical analysis it can easily be shown that if one takes a Fourier transform of the OFID pulse frequency spectrum, the results when mapped into time domain show a short spike of the order of 30 ps riding on a significantly longer pedestal. The amount of energy contained in the background can be as high as that contained in the ultrafast peak. The pulse durations are usually determined from autocorrelation measurements which, in all of the reported experiments [20]–[30], are performed above a certain background level.

Moreover, in OFID experiments, there are always pulse transients following the initial fast spike lasting for $\sim$ 100 ps. These pulses contain $\sim$ 25% of the energy of the central peak [22]. Clearly, it is undesirable to have this type of background or post pulses for conducting time-resolved picosecond experiments.

We should emphasize that OFID pulse generation cannot be performed with CW (continuous wave) CO_2 lasers. The generation scheme requires a high-power CO_2 laser which limits the repetition rate of the pulse train to that of the high-power laser.

2.2.3 Ultrashort Mid-Infrared Pulse Generation with Free Electron Lasers

A free electron laser is a device which consists of a linear accelerator (an electron gun, a pulse compression section, and traveling-wave acceleration stage), an electron transport system, an undulator magnet array and an optical resonator cavity [31]. Injected electrons exhibit periodic oscillations in the undulator magnetic field (made from a series of magnets of alternating polarities) and lose energy through synchrotron radiation.

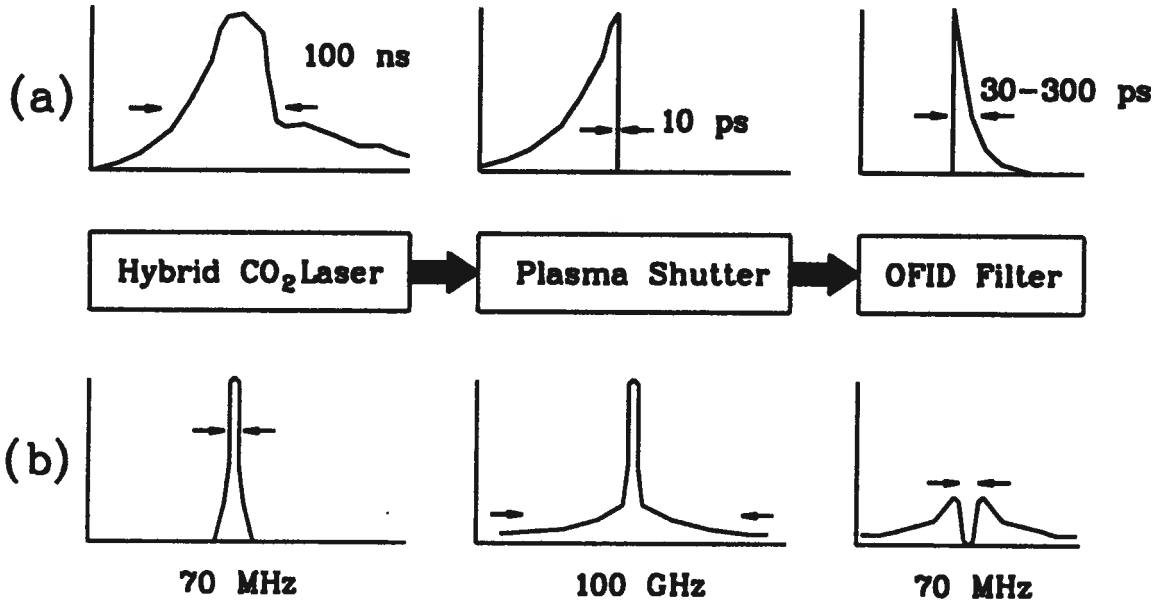

Figure 2.1: Principle of OFID short pulse generation. (a) In the time domain, (b) in the frequency domain.

A resonance condition can be achieved through the interaction of the electrons with the electromagnetic field and the undulator magnetic field which causes the electrons to form bunches in a scale comparable to the optical wavelength. This resonance condition provides photon emission coherence and optical gain.

Free electron lasers generate a wide band laser spectrum. Recently, free electron lasers have been used to generate ultrashort infrared pulses covering wide ranges of wavelengths and durations [32]–[36]. The micropulse widths are measured to be between 3 - 12 ps with peak powers up to 10 MW at a peak wavelength of 8 μm. These pulses are emitted in macropulses of a duration of $\sim$ 10 μs at a repetition rate of $\sim$ 6-50 Hz [35]. Glotin et al. [32] pointed out that the limiting factor in reducing the pulse width is the amount of detuning of the cavity length. In their experiment, they managed to produced subpicosecond pulses as short as 200 fs at 8.5 μm by simply dephasing the RF field by $\sim$ 30° relative to the electron bunches in the accelerator stage. However, the second order autocorrelation traces presented in the publication [32] show a short 200 fs spike on top of a long $\sim$ 1 ps pulse. We believe that because of the nature of the autocorrelation measurements, a small noise signal in the pulse trace can show the same effect. Clearly, a time-resolved cross correlation experiment (see section 4.10.2) should definitely provide the exact pulse duration.

Since the electron bunches must be accelerated up to $\sim$ 50 MeV, short pulse generation with free electron lasers is a very complicated, expensive, cumbersome process, and cannot used as a table top ultrashort infrared system.

2.2.4 Ultrashort Mid-Infrared Pulse Generation with Nonlinear Frequency Mixing

Recently, remarkable progress has been made in the generation and the tunability of ultrafast mid-infrared pulses by using nonlinear difference frequency mixing [37]–[42].

There are several techniques of frequency mixing: to produce a pulse at a wavelength λ_{ir}= 10.6 μm, two ultrashort near infrared pulses are needed. For example, if a 1.064 μm pulse from an Nd:YAG laser and a 1.183 μm pulse from a dye laser are directed simultaneously into a nonlinear mixing crystal (GaSe) one can produce coherent photons at 10.6 μm. A variation on this method consists of amplifying pulses from a femtosecond laser oscillator and using these pulses to generate a broadband continuum, a selected frequency range from the continuum spectrum is in turn mixed with the laser oscillator frequency to produce ultrashort mid-infrared pulses [42].

Dahinten et al. [40] generated 1 ps mid-infrared pulses via difference frequency mixing of a mode locked Nd:glass laser 2 ps pulses at $\lambda = 1.053$ μm and tunable traveling-wave dye laser pulses (dye heptamethine pyrylium: 5: 1.16 μm -1.4 μm and dye A 9860: 1.10 μm-1.6 μm) in $AgGaS_2$ and GaSe crystals. The resulting output covers a broadband mid-infrared spectrum between 4 μm and 18 μm with photon conversion efficiency as high as 2%. For wavelengths above 10 μm, GaSe is used as a mixing crystal. The peak energy of the 1 ps 10.6 μm pulses is measured to be of the order of a 0.2 μJ.

Becker et al. [39] generated mid-infrared pulses by frequency mixing two colour femtosecond mode locked Ti:sapphire laser pulse in a $AgGaS_2$ crystal. The Ti:sapphire pulses can be tuned from (760 nm to 790 nm) and (820 nm to 865 nm) and the generated infrared pulses can be tuned between 7 μm to 12 μm with a constant pulse duration of 310 fs over the whole tuning range.

The generated pulse duration is only limited by the duration of the shortest of the seed pulses, and by group velocity dispersion in the nonlinear mixing crystals. On time scales less than or equal to 1 picosecond, the pulse broadening effect is found to be directly proportional to thickness of the nonlinear mixing crystal [38]. Seifert et al. [38] pointed out that frequency conversion in a $AgGaS_2$ crystal with laser pulse wavelengths below 1 μm restricts the duration of the mid-infrared pulse to the lower limit of approximately

300 fs. They attributed this lower limit to the group velocity dispersion of the laser pulses in the nonlinear mixing crystal. They demonstrated that by mixing regeneratively amplified Ti:Sapphire (740 nm to 850 nm) pulses with 1 μm to 2.5 μm pulses generated from an optical parametric generator/amplifier system, pulse durations of ~ 160 fs (50 nJ, 1 kHz) are produced with wide tunability range between 3.3 μm to 10 μm [38].

In view of the above progress on difference frequency mixing, this method is very promising for the generation of femtosecond pulses at 10.6 μm. However, in terms of conversion efficiency, semiconductor switching may have an advantage over nonlinear frequency mixing. It should be noted that since the frequency mixing process is highly nonlinear, one requires high-power infrared pulses for the mixing process.

2.3 Optical Semiconductor Switching

Application of optical semiconductor switching technique for the purpose of generating subpicosecond 10.6 μm laser pulses from a CO_2 laser is discussed below.

2.3.1 The Semiconductor Switch

Optical semiconductor switching of 10.6 μm CO_2 laser radiation [43]–[60] offers an alternative and a much simpler method for the generation of ultrashort laser pulses than the previously discussed methods. It is based on the principle of modulating and enhancing the reflection and transmission characteristics of a semiconductor by optically controlling the free-carrier density. This technique is often used outside the infrared laser cavity to temporally gate an ultrashort pulse from a long 10.6 μm pulse or a continuous beam by simply reflecting the infrared radiation from an optically injected semiconductor carriers. The process requires three simple components: an ultrafast visible laser pulse, a CO_2 laser (pulsed or CW), and an optically-flat undoped semiconductor wafer that is

transparent to the 10.6 μm radiation or the infrared radiation to be switched out. Pioneering experiments by Jamison and Nurmikko [45] and by Alcock et al. [47] have shown that photoinjection of a high carrier density ($\geq 10^{19}$) in semiconductors modifies the reflectivity of the material to 10.6 μm. These experiments serve as the basis for optical semiconductor switching. The method has been demonstrated to provide a very powerful and currently the only sub-100 fs pulse generation method in the mid- and far-infrared part of the spectrum [55]. Its low power operation makes it very attractive compared to the previous methods.

The basic principle of optical semiconductor switching technique is illustrated in figure 2.2 and is described as follows: a semi-insulating semiconductor is transparent to mid-(far)-infrared laser radiation in the absence of free carriers. Semiconductor reflectivity to infrared radiation is determined by the number density of free carriers (semiconductor plasma). The minimum electron-hole density needed to achieve a full reflection is known as the critical carrier density, n_c, and it can be determined from the following expression in c.g.s. units,

$$n_c = \frac{m^* \omega^2 \epsilon_b}{4\pi e^2}, \tag{2.3}$$

where m^*, ω, ϵ_b, and e are the effective carrier mass, the infrared radiation frequency in vacuum, the static dielectric constant and the electron charge, respectively. For moderate photoinjection carrier density $\leq 10^{20}$ such critical density corresponds to a plasma frequency, ω_p, in the mid- or far-infrared regions. It should be noted that in deriving the above expression for, n_c, the plasma absorption effects are ignored.

The critical density at the CO_2 laser wavelength is calculated to be $\sim 10^{19}$ cm^{-3}. For a specific operating infrared wavelength, λ_{ir}, one selects an appropriate direct band gap semiconductor which is transparent to the infrared radiation. This requires that the band gap energy of the semiconductor switch, E_g, be higher than the energy of the

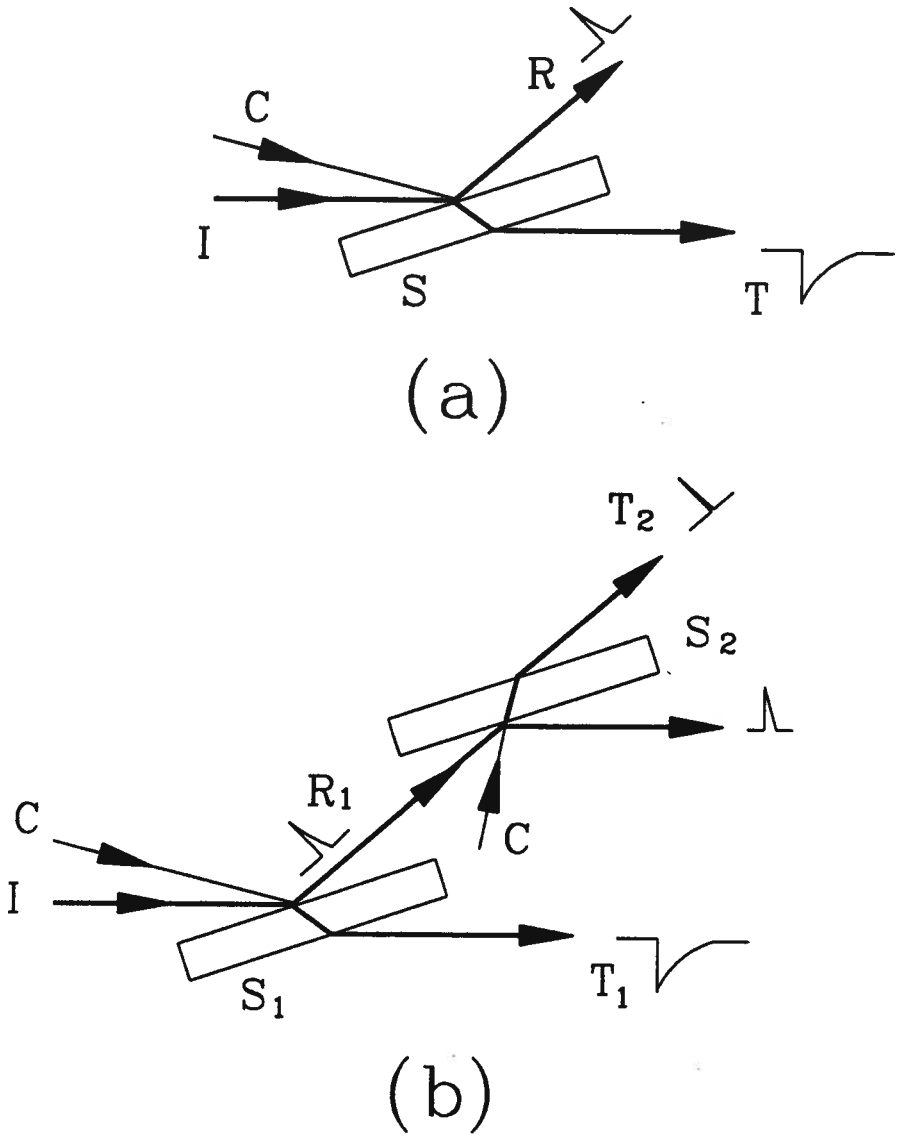

Figure 2.2: Typical schematic configurations of optical semiconductor switching operating in a (a) reflection mode, (b) reflection-transmission mode. I = infrared beam (pulse), C = control pulse, S_1 = reflection switch, S_2 = transmission switch, R_1 and R_2 are the infrared reflected pulses, T_1 is the transmitted infrared beam (pulse) and T_2 is the transmitted pulse.

infrared photon (117 meV for a CO_2 laser photons). In order to obtain a high signal to background ratio, the CO_2 laser radiation is polarized in the plane of incidence (P-polarized) and the semiconductor wafer is set at Brewster's angle with respect to the infrared radiation beam. With this optical arrangement, the 10.6 μm laser radiation is transmitted through the switch and none of the radiation is reflected, thus reducing the background reflected signal to the zero level. This state is known as the off-state of the semiconductor switch. In order for the infrared transparent switch to become reflective to the infrared radiation, one must increase the free-carrier density in the switch. This can be accomplished by illuminating the semiconductor switch with an intense optical laser pulse (control pulse) with photon energy exceeding the forbidden band gap energy of the semiconductor. The control pulse is used to photoexcite the electrons from the valence band to the conduction band of the semiconductor switch by means of interband absorption. These carriers are confined in a thin layer of a thickness approximately equal to the absorption skin depth of the control pulse radiation. If a large enough carrier density, $\geq n_c$, is generated, then the semiconductor's surface appears metallic to the infrared radiation and effectively a very fast transient infrared reflecting "mirror" is made at the semiconductor's surface. That is, the photoexcited carriers cause a change in both the refractive index and the extinction coefficient, resulting in infrared beam (pulse) being reflected at Brewster's angle with the same divergence as the source infrared beam (pulse). The reflection efficiency of the infrared semiconductor switch at 10.6 μm ranges between 40% to 80% depending on the density of the photoexcited carriers.

For subpicosecond infrared pulse generation, the turn-on speed of the infrared reflectivity is determined by the photoinjection carrier generation rate, which in turn is determined by the pulse width of the excitation control laser pulse. Ultrafast switching can be easily accomplished by photoinjecting the carriers with a subpicosecond visible

laser pulse. The infrared semiconductor switch remains reflective as long as the photoexcited carrier density is above the critical density; hence, an ultrafast risetime infrared pulse is generated. The temporal termination (decay) of the reflected infrared pulse is determined by various carrier dynamics such as recombination and diffusion. It is shown later in this work that by proper choice of the semiconductor material and the carrier density, the decay time of the reflectivity pulse can by dramatically reduced to a subpicosecond time scale. The ultrafast temporal variation of the optical reflectivity and transmission due to the semiconductor plasma can be used as a powerful diagnostic tool to probe the transient plasma dynamics on the picosecond or femtosecond time scale.

Optical semiconductor switching has been widely used as an active switching element, placed outside the laser cavity, to temporally gate the already generated long pulses or CW far-infrared laser beams. Conventional mode locking, Q-switching of far-infrared lasers with electrooptic crystals is an extremely inefficient process; therefore, for fast optical modulation at these wavelengths, optical semiconductor switching provides an alternative. Ultrashort pulses at 119 μm using H_2O [58] and CH_3OH [52] lasers, and at 100-1000 μm from a free electron laser [56] have been produced with this scheme; however, no attempt has been made to produce pulses in the far-infared region with picosecond duration. Semiconductor switching has been applied to some novel cavity dumping techniques, where the semiconductor switch is placed at Brewster's angle inside the laser cavity, of optically pumped molecular gas far-infrared lasers such as: CH_3OH at 119 μm [59], NH_3 at 90.8, 148, 292 μm and CH_3F at 231 μm and 496 μm [57]. The advantage of using semiconductor switching is that output power is increased since the circulating pulse can be coupled out of the laser cavity very efficiently.

An interesting and effective method of producing ultrashort pulses is using a combination of two infrared semiconductor switches in series [55] (as shown in figure 2.2(b)). The first one is usually a GaAs or a CdTe wafer operating in the reflection mode to

generate ultrafast risetime pulses, and the second switch is also set at Brewster's angle; however, it is operating in a transmission mode. Silicon is usually used as a transmission switch due to its large free-carrier absorption cross-section and high reflectivity at 10.6 μm [55].

The operation of the reflection-transmission combination switching method is as follows: the infrared reflected pulse, after being generated by the reflection switch, is directed onto the silicon transmission switch. Silicon transmits the infrared radiation; however, when it is irradiated with a delayed laser pulse (relative to the reflection switch) above band gap radiation, it results in the production of free carriers in a layer $\sim$ 3 μm thick. Due to the induced infrared reflection and free-carrier/intervalence band absorption, the transmission property of silicon to the 10.6 μm pulse is altered from full transmission to zero in a short time that is required to reach the critical carrier density and remains unrecovered for a long time (a few nanoseconds). The duration of the infrared pulses is determined by the time interval between the turn-on and turn-off times of the reflection and transmission switches, respectively. By proper adjustment of the relative delay of the excitation control pulses between the two switches, one can only allow the fast rising edge of the infrared reflected pulse to pass through the transmission switch, thus, the transmitted infrared pulse width consists of the ultrafast rising edge from the reflection switch pulse and the ultrafast falling edge from the transmission switch. Figure 2.2(b) illustrates a typical schematics of the reflection-transmission switching operation. Rolland and Corkum [55] used amplified 70 fs (620 nm) pulses from a colliding-pulse mode locked dye laser to control the switching operation. They demonstrated this technique for the generation of CO_2 laser pulses at 9.5 μm with duration as short as 130 fs. These pulses correspond to only $\sim$ 4 optical cycles and are the shortest pulses ever generated at the CO_2 laser wavelength. With this method, it is possible to produce infrared pulses of

durations shorter than the excitation control pulse duration by simply reducing the duration of the excitation control pulse. Recently, table-top high-power, sub-30 fs pulses have been routinely produced in research laboratories; with the application of these pulses to semiconductor switching, it is possible to reduce the infrared pulse duration even further to less than one infrared oscillation cycle of the CO_2 laser. It seems that the limit of the generated pulse duration is mainly restricted by the risetime of the control pulse duration required to produce the critical plasma density in the transmission switch. Clearly, the drawback in using two semiconductor switching elements compared to one switching element lies in the fact that a high degree to synchronization between the two switches must be maintained very accurately by the optical setup. It is extremely advantageous in terms of practicality and simplicity to use a single optical infrared semiconductor switch to generate subpicosecond 10.6 μm laser pulses. This alternative possibility is part of this thesis investigation; therefore, in order to design such a device more effectively, an understanding of the physical properties of the photoexcited carriers is essential.

To sum up, the advantages of using optical semiconductor switching compared to other ultrashort pulse generation schemes are:

1. To perform the infrared switching, the technique requires only one ultrashort pulse with a photon energy greater than the band gap energy of the semiconductor. This makes it simple and inexpensive to implement;

2. A high reflection efficiency of $\sim$ 40% for a 1 ps pulse duration at 10.6 μm can be obtained;

3. An ultrahigh pulse contrast ratio (signal/background) of the order of 10^4:1 (for one reflective switch) can be achieved, and it can be increased to $\sim$ 10^6:1 by using two reflective switches in series;

4. The duration of the generated infrared pulses are only limited by the source control pulse duration and the type of the semiconductor switching material;

5. The power of the switched infrared pulses is only limited by the input power of the source infrared laser;

6. It offers the possibility of the generation of sub-30 fs infrared laser pulses at 10.6 μm, and at other infrared wavelengths;

7. No critical phase/wavelength matching conditions, nonlinear crystal temperature control, and group velocity dispersion are required for the switching process;

8. It provides inherent synchronization between the optical control pulse and the reflected infrared pulse which is very useful for pump-probe type experiments;

9. It can be applied to infrared laser beams or pulses of low power;

10. The switched pulse duration can by varied over a wide range;

11. The repetition rate of the reflected pulses is limited by the repetition rate of the control laser;

12. A high optical-damage power density of ~ 1 GW/cm^2;

13. The reflected and transmitted pulses basically map the temporal evolution of the semiconductor plasma; therefore, the shapes of these pulses provide information on the carrier dynamics in the semiconductor switch.

A complete understanding of the processes involved in optical semiconductor switching requires the knowledge of the semiconductor plasma properties, the behaviour of the optically generated carriers under ultrafast optical excitation, the dielectric function of the semiconductor, the propagation of the infrared radiation in a semiconductor plasma,

and finally the absorption processes such as free-carrier and intervalence band absorption that may limit (enhance) the speed of the reflection (transmission) switch.

2.4 Ultrafast Optical Excitation

The dynamics of ultrashort laser pulse interaction with a semiconductor are very complex. In the following paragraphs we present the basic carrier dynamics and a sequence of the time events in order to help in the understanding of infrared switching operation. A comprehensive review on the subject is presented in references [61]–[74].

When a semiconductor is excited by an ultrafast laser pulse whose photon energy is above the band gap energy of the semiconductor, then electrons (e) and holes (h) are placed into energy states that are defined by the band structure of the semiconductor material and the power spectrum of the absorbed light pulse. The free carriers can gain excess kinetic energy from the difference between the excitation photon energy and the band gap energy of the semiconductor. In ultrafast optical excitation of GaAs with a 616 nm laser pulse, a narrow band of states can be excited creating nonthermal free-carrier distribution for a very short time which is comparable to the excitation pulse width. The electrons are initially injected to the Γ valley with excess energies. The electrons are excited with three distinct energy values of: 0.5 eV (from the heavy hole band), 0.43 eV (from the light hole band), and 0.15 eV (from the split-off band). Approximately 84% of the electrons are injected from the heavy/light hole valence bands with equal strength and the rest are injected from the split-off valence band. Optical excitation results in an instanteous production of extremely hot nonequilibrium electron and hole distributions. Carrier-carrier (e-e, and h-h) elastic collisions, due to Coulomb forces, is the initial internal relaxation process which the electrons and holes immediately undertake after excitation. These scattering events take place in a time scale of the order of $\sim$ 10 fs,

Clearly, since the effective mass of the electrons is smaller than that of the holes, the initial temperature of the electrons is higher than the hole's temperature. Energy can be transferred from the hot electrons to the relatively cold holes through e-h scattering. The e-h collisions eventually drive the plasma towards a thermalized distribution (characterized by a common carrier temperature) within $\sim$ 200 fs after excitation. The free carriers are in thermal equilibrium among each other but not at equilibrium with the lattice which is still at room temperature. Cooling of the hot carriers occurs primarily through inelastic collisions between the hot carriers and phonons on a time scale of $\sim$ 2 ps. The overall effect of relaxation is to reduce the carrier temperature and increase the lattice temperature. Carrier recombination takes place $\sim$ 100 ps later after excitation.

2.4.1 The Dielectric Function

The electrical and optical characteristics of a semiconductor are closely related to the dielectric properties of the material; therefore, it is essential to have an understanding of the dielectric function of the semiconductor switch so that one can predict its switching behaviour. Infrared reflection properties of the semiconductor switch can be charactretized by a complex index of refraction or in general by the complex dielectric function, $\epsilon(\omega)=\epsilon_1(\omega) + i\epsilon_2(\omega)$, where ϵ_1 and ϵ_2 are the real and imaginary parts of the frequency-dependent dielectric function. In general, ϵ_1 and ϵ_2 can be obtained from quantum mechanical calculations [75]–[79], which require a detailed knowledge of the band structure, and free-carrier distribution.

A widely accepted model for the derivation of the dielectric function is based on Drude treatment of a free electron-hole gas [80]. The free carriers are described in terms of collective harmonic oscillations with a single frequency similar to ionized carriers in a gaseous plasma. In a semiconductor, when the optical frequency of the radiation is much less than the interband transition frequency between the valence and conduction

band, the Drude model provides an excellent description of the dielectric function of the optically excited carriers.

A simple way of obtaining the dielectric function is to consider an isotropic one-dimensional, non-interacting classical free electron gas of density, n. The long wavelength dielectric response function, $\epsilon(\omega)$, of free electron gas can be modeled microscopically in terms of the equation of motion of a free electron in a perturbing external electric field:

$$m^* \left(\frac{d^2}{dt^2} + \nu_c \frac{d}{dt} \right) \delta \mathbf{r} = -e\mathbf{E}. \tag{2.4}$$

Here ν_c is the collision frequency, which describes the damping of the electron motion due to phonons, impurities, and carrier-carrier scattering, etc., and it is inversely related to the momentum relaxation time of the carriers; $\delta \mathbf{r}$ is the spatial displacement; and m^* is the effective mass of the free carrier. By taking into account the polarization due to free charges, $\mathbf{P} = -ne\delta \mathbf{r}$, the displacement vector $\mathbf{D}$, and $\delta \mathbf{r}$ from the solution to equation 2.4, one obtains the Drude dielectric function of the form:

$$\epsilon(\omega) = \epsilon_b \left(1 - \frac{\omega_p^2}{\omega^2} \left(1 + i\frac{\nu_c}{\omega} \right)^{-1} \right). \tag{2.5}$$

Here, ω_p is the plasma frequency $\omega_p = (4\pi n e^2/\epsilon_b m^*)^{1/2}$, and ϵ_b is the background dielectric constant of the material. In arriving at the above expression, a rapid thermalization of the excess electron and hole energies is assumed; therefore, the effective mass can be considered to be a time-independent quantity. Moreover, other mechanisms such as band gap renormalization by hot carriers, semiconductor lattice heating, and intervalence band absorption are ignored.

The temporal and spatial dependence of the dielectric function can be explicitly included through a time and spatially varying electron-hole plasma density, $n(z,t)$; hence, equation 2.5 can be generalized to have the following form:

$$\epsilon(\omega) = \epsilon_b \left(1 - \frac{n(z,t)}{n_c} \left(1 + i\frac{\nu_c}{\omega} \right)^{-1} \right) \tag{2.6}$$

Here, n_c is defined by equation 2.3. Since the photoexcitation process of the e-h plasma occurs through the absorption of the above band gap radiation by the semiconductor surface, the amount of radiation penetrating the surface decays exponentially with increasing depth through the bulk semiconductor. Consequently, the e-h plasma density spatial profile follows the spatial profile of the absorbed radiation. One can write such profile as:

$$n(z,0) = n_o e^{-\gamma z} \tag{2.7}$$

where n_o is the density of the e-h plasma at the surface immediately after excitation, and γ is the absorption length of the above band gap radiation.

In writing equation 2.6 we have assumed a local response of the dielectric function; that is, the dielectric function at any point z depends on the values of the fields at that point. This is equivalent to assuming that the dielectric function fluctuations are large compared to the electron mean free path.

At high excitation levels, the plasma frequency, ω_p, will exceed the infrared probe frequency, ω. In such a situation, the refractive index becomes imaginary, leading to strong reflection in the infrared range. Experimentally, Siegal et al. [81, 82] have shown that under ultrafast high intensity laser excitations, the dielectric function of GaAs can be described be equation 2.5 up to an excitation energy fluence of 1 kJ/m^2. This energy fluence is the damage threshold energy fluence of GaAs. Our experiments are performed at much lower energy fluences and hence Drude's dielectric function is an adequate description of the optical properties of the optical semiconductor switch.

2.4.2 Free-Carrier and Intervalence Band Absorptions

Optical excitation of a semiconductor switch induces a change in the imaginary part of the dielectric function through optical intraband transitions. It is experimentally shown

in section 5.2 that absorption processes at 10.6 μm influence the operating speed of the semiconductor switch.

Directly after electrons (holes) have been injected with an ultrashort laser pulse in the conduction (valence) band and once the thermalization has occurred, the carriers occupy energy states in the conduction/valence bands up to an energy level determined by the excess laser photon energy. Consequently, two intraband infrared absorption processes occur: free-carrier absorption and intervalence band absorption. Both absorption coefficients are proportional to the photoexcited carrier density and, therefore, may effect the switching speed and efficiency at higher excitation levels.

Free-carrier absorption is a three-particle interaction process. When the 10.6 μm radiation passes through the semiconductor plasma, an infrared photon can excite a free carrier to a virtual state in k-space, and since the absorption mechanism of the 10.6 μm photons requires the conservation of wavevectors, the electrons (holes) interact with the lattice through the emission or absorption of phonons in order to settle in a final state in the conduction (valence) band (similar to indirect absorption in semiconductors).

On the other hand, intervalence band absorption occurs between light and heavy hole valence bands. Holes are excited from the heavy hole band to the light hole band by the absorption of 10.6 μm photons. Intervalence band absorption has been shown to be less effective in comparison to free-carrier absorption [83].

Chapter 3

Theory: Infrared Reflection from a Semiconductor Plasma

3.1 Introduction

The basic theoretical background for optical semiconductor switching and some numerical simulations are presented in this chapter. The basis of the numerical modelling has been presented in our previous publications [84, 85]. The general approach to ultrafast infrared optical semiconductor switching can be divided into two problems. One is dealing with a reflection of infrared radiation from a plasma, and the other is dealing with the temporal behaviour of the reflecting plasma after optical excitation. Combining these two effects, one should be able to obtain a complete description of the physical situation. In this chapter, the general features of electromagnetic wave propagation in a semiconductor plasma are reviewed. In order to estimate the fastest process controlling the infrared switching speed, the physical processes governing the temporal decay of the optically generated semiconductor plasma are discussed. The rest of the chapter is devoted to the analyses of the numerical simulations.

3.2 Propagation of an Obliquely Incident Electromagnetic Wave in an Inhomogeneous Dielectric Medium

In this section of the thesis the specific problem of electromagnetic wave propagation at an oblique angle in an inhomogeneous plasma is discussed. A theoretical discussion is given of the specific problem of the reflection of a probing 10.6 μm electromagnetic

wave from a semiconductor plasma. In our situation, we are interested in the reflection of 10.6 μm radiation from a thin plasma layer where the layer thickness is basically the absorption length of the excitation visible radiation ($\sim$ 220 nm). The plasma thickness is much thinner than the infrared wavelength. Moreover, presence of plasma spatial inhomogeneity requires a generalization of the standard theory dealing with plasma reflection [86, 87, 88]. Therefore, our problem reduces to a reflection of an electromagnetic wave from an inhomogeneous medium whose dielectric function depends on position.

The analysis is presented for both electric field polarizations, S (where the electric field is normal to the plane of incidence) and P (where the electric field is parallel to the plane of incidence). Our method involves deriving an expression for the electric and magnetic field components. We will also discuss the difficulties associated with obtaining an analytical solution for the P-polarized case at the point where the dielectric function vanishes.

Here, we use the free electron gas model to describe the optical response of the semiconductor plasma to the incident radiation. This implies that we neglect the contribution of free-carrier absorption, intervalence band transitions, and intraband transitions. Even though this model is simple and very crude, it can be used successfully to give a fairly good description of the reflectivity at 10.6 μm.

We start by considering Maxwell's equations for electromagnetic waves in a dielectric medium in Gaussian units:

$$\nabla \times \mathbf{H} = \frac{4\pi}{c}\mathbf{J} + \frac{1}{c}\frac{\partial \mathbf{D}}{\partial t} \tag{3.1}$$

$$\nabla \times \mathbf{E} = -\frac{1}{c}\frac{\partial \mathbf{B}}{\partial t} \tag{3.2}$$

$$\nabla.\mathbf{B} = 0 \tag{3.3}$$

where $\mathbf{H}$ and $\mathbf{E}$ are the magnetic and the electric field vectors, respectively, and $\mathbf{D}$, $\mathbf{J}$ are

the electric displacement and the current density. For an isotropic plasma, we can define $\mathbf{J} = \sigma\mathbf{E}$, $\mathbf{D} = \epsilon_b\mathbf{E}$, and $\mathbf{B} = \mu\mathbf{H}$. Here, for a semiconductor plasma we have assumed the magnetic permeability, μ, to be equal to unity; ϵ_b is the background dielectric constant. By taking the curl of equation 3.2 and substituting equation 3.1, we obtain the following expression:

$$\nabla \times \nabla \times \mathbf{E} = -\frac{1}{c}\frac{\partial}{\partial t}(\frac{4\pi}{c}\mathbf{J} + \frac{1}{c}\frac{\partial \mathbf{D}}{\partial t}) \tag{3.4}$$

It should be pointed out that in the following derivations we make use of the fact that the time variation of the dielectric function is negligible during the oscillation of the wave and hence may be regarded as being constant. Moreover, we also assume that there is no absorption of the radiation, such that the amplitudes of the electric and magnetic fields do not change during the oscillation of the wave. In general, we can assume that the form of $\mathbf{D}$ and $\mathbf{J}$ are harmonic functions of time and are written as:

$$\mathbf{D}(\mathbf{r}, t) = \epsilon_b\mathbf{E}(\mathbf{r})e^{i\omega t} \tag{3.5}$$

$$\mathbf{J}(\mathbf{r}, t) = \sigma(r)\mathbf{E}(\mathbf{r})e^{i\omega t}. \tag{3.6}$$

Therefore equation 3.4 can be expressed as:

$$\nabla \times \nabla \times \mathbf{E} = (\frac{\omega}{c})^2(\mathbf{D} - i\frac{4\pi}{\omega}\mathbf{J}). \tag{3.7}$$

By introducing the following identity

$$\nabla \times \nabla \times \mathbf{E} = -\nabla^2\mathbf{E} + \nabla(\nabla.\mathbf{E}) \tag{3.8}$$

and the following expressions for $\mathbf{D}$ and $\mathbf{J}$

$$\mathbf{D} = \epsilon_b\mathbf{E}, \qquad \mathbf{J} = \sigma\mathbf{E}, \tag{3.9}$$

the above equation (3.7) can be written as:

$$\nabla^2\mathbf{E} - \nabla(\nabla.\mathbf{E}) + (\frac{\omega}{c})^2\epsilon(r)\mathbf{E} = 0 \tag{3.10}$$

where we have defined the dielectric function as $\epsilon(r) = \epsilon_b - (i4\pi\sigma(r)/\omega)$. Equation 3.10 describes the electromagnetic wave electric field components in a semiconductor plasma which has an effective dielectric function defined by $\epsilon(r)$ [86, 89]. It should be noted that in deriving equation 3.7 we assume that the local temporal variation of $\sigma(r)$ is slow compared to the period of oscillation of the electric field.

As it will be pointed out later in sections 3.1.1 and 3.1.2, this differential equation will be solved exactly for the S-polarized electric field components for a specific dielectric function profile. However, for the P-polarized electromagnetic wave case, this equation reduces to two coupled differential equations [86]. An alternative approach to the P-polarization case is to consider the differential equation for the magnetic field.

Next, we need to derive the differential equation that describes the components of the magnetic field propagating in the plasma. From equations 3.1, 3.5, and 3.6, and by taking the curl of the expression, we can write

$$\nabla \times \nabla \times \mathbf{B} = \frac{i\omega}{c}(\nabla\epsilon(r) \times \mathbf{E} + \epsilon(\mathbf{r})(\nabla \times \mathbf{E})) \tag{3.11}$$

Using the following identity

$$\nabla \times \nabla \times \mathbf{B} = -\nabla^2\mathbf{B} + \nabla(\nabla.\mathbf{B}) \tag{3.12}$$

and equation 3.11, we can write the equation for the magnetic field as:

$$\nabla^2\mathbf{B} + \frac{1}{\epsilon(r)}\nabla\epsilon(r) \times (\nabla \times \mathbf{B}) + (\frac{\omega}{c})^2\epsilon(r)\mathbf{B} = 0 \tag{3.13}$$

The above equation describes the magnetic field components strength of the probing electromagnetic wave [86, 89].

3.2.1 The S-Polarized Electric Field Case

We proceed in this section with the physics of propagation of S-polarized radiation (when the electric field of the wave is perpendicular to the plane of incidence) in a semiconductor

plasma. The typical geometry of the problem is shown in figure 3.1, where the subscripts i, r, and t denote incident, reflected, and transmitted electric or magnetic fields, respectively. A uniform electromagnetic plane wave is propagating in free space along the positive z direction. This wave has a frequency ω and is incident on a semiconductor plasma from the vacuum side at an arbitrary angle θ_i with respect to the surface normal of the semiconductor. As mentioned before, the solution to the reflected electric field in the S-polarized case can be obtained by solving the differential equation for the electric field. In this case we treat the situation as a one dimensional problem and hence we can treat the dielectric function $\epsilon(r)$ as having only a z component dependence. As shown in figure 3.1, let the plane of incidence be defined by the xz plane, where the z axis is perpendicular to the face of the semiconductor (and hence the plasma layer). The wave vector, $\mathbf{k}_i$, then lies in the plane of incidence (xz) such that $\mathbf{k_i} = k_i(\sin\theta_i, 0, \cos\theta_i)$. We are interested in the y-component of the electric field. Hence we can write this component as [86]:

$$E_y = \tilde{E}(z)e^{\pm ik_i x \sin\theta_i}. \tag{3.14}$$

With this choice of the plane of incidence, the y-component of equation 3.10 can be written as [86]:

$$\frac{\partial^2 E_y}{\partial x^2} + \frac{\partial^2 E_y}{\partial z^2} + (\frac{\omega}{c})^2 \epsilon(z) E_y = 0. \tag{3.15}$$

By using equations 3.14 and 3.15 we can derive the following equation:

$$\frac{\partial^2 \tilde{E}(z)}{\partial z^2} + k_i^2 \left(\epsilon(z) - \sin^2\theta_i\right) \tilde{E}(z) = 0 \tag{3.16}$$

which describes the electric field component strength of interest. It should be pointed out that there is no general solution to the above equation and each functional dependence of $\epsilon(z)$ requires a special approach to the specific problem [86], [89]–[94]. In order to solve the differential equation (3.16), one has to assume a form for the dielectric function. Here, we

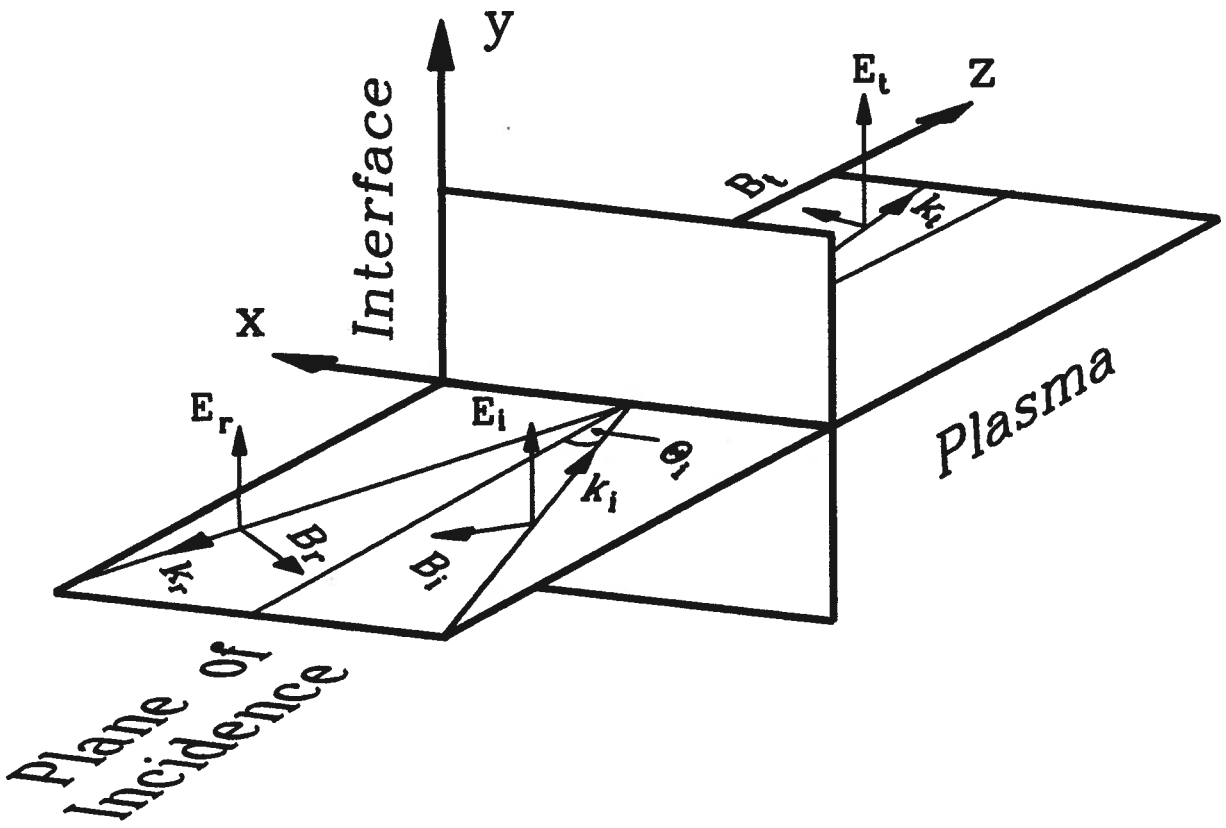

Figure 3.1: An incoming wave whose electric field, $\mathbf{E_i}$, is normal to the plane of incidence (S-polarization).

consider the exponentially decaying dielectric function presented in section 2.4.1, which is expressed by the formula:

$$\epsilon(z) = \epsilon_b \left(1 - \frac{ne^{-\gamma z}}{n_c(1 + \frac{i\nu_c}{\omega})}\right) \tag{3.17}$$

and equation 3.16 can be written in the form:

$$\frac{\partial^2 \tilde{E}(z)}{\partial z^2} + (\alpha - k_i^2 \left(\frac{n\epsilon_b}{n_c(1 + \frac{i\nu_c}{\omega})}\right) e^{-\gamma z})\tilde{E}(z) = 0 \tag{3.18}$$

where $\alpha = k_i^2(\epsilon_b - \sin^2\theta_i)$. The simple transformation of [91, 94]

$$X = i\frac{2\omega}{c\gamma}\sqrt{\epsilon_b \frac{n}{n_c(1 + \frac{i\nu_c}{\omega})}}e^{-\gamma z/2} \tag{3.19}$$

can be applied to equation 3.18. This reduces equation 3.18 to a familiar form:

$$X^2\frac{\partial^2 \tilde{E}(X)}{\partial X^2} + X\frac{\partial \tilde{E}(X)}{\partial X} + (X^2 - \tilde{\nu}^2)\tilde{E}(X) = 0 \tag{3.20}$$

where we have defined $\tilde{\nu} = -i2\sqrt{\alpha}/\gamma$. The above equation is the familiar Bessel equation. $J_{\tilde{\nu}}(X)$ is the Bessel function of imaginary order $\tilde{\nu}$ and complex argument X. The general solution to this equation has the form

$$\tilde{E}(X) = C_1 J_{-\tilde{\nu}}(X) + C_2 J_{\tilde{\nu}}(X). \tag{3.21}$$

By using the boundary condition (i.e. as $z \to \infty$), only the transmitted wave exists inside the plasma, and we can conclude that C_2=0 [91, 94].

3.2.2 The P-Polarized Electric Field Case

Let us consider the problem of the solution to equation 3.13 with the same form of the dielectric function (equation 3.17). As shown in figure 3.2, in the case of a P-polarized electric field, we take the wave vector $\mathbf{k_i}$ to lie in the xz plane of incidence and the electric field components $\mathbf{E_i} = (E_x, 0, E_z)$; hence the magnetic field has only one component in

the y-direction. The magnetic field can be written as $\mathbf{B_i} = (0, B_y, 0)$. With this choice of the magnetic field, the differential equation can be reduced to the form:

$$\frac{\partial^2 B_y}{\partial x^2} + \frac{\partial^2 B_y}{\partial z^2} - \frac{1}{\epsilon(z)}\frac{\partial \epsilon(z)}{\partial z}\frac{\partial B_y}{\partial z} + (\frac{\omega}{c})^2 B_y = 0. \tag{3.22}$$

In order to further simplify the above equation, let us represent the incident wave to be a plane wave with its propagation vector lying in the xz plane:

$$B_y = b(z)e^{\pm ik_i x \sin\theta_i}. \tag{3.23}$$

By substituting equation 3.23 into 3.22, we get

$$\frac{\partial^2 b(z)}{\partial z^2} - \frac{1}{\epsilon(z)}\frac{\partial \epsilon(z)}{\partial z}\frac{\partial b(z)}{\partial z} + k_i\left(\epsilon(z) - \sin^2\theta_i\right) b(z) = 0. \tag{3.24}$$

Equation 3.24 is known as the Maxwell-Helmholtz wave equation [86, 89, 90, 95]. The corresponding electric field components can be determined from Maxwell's relationships:

$$E_x = \frac{ic}{\omega\epsilon(z)}\frac{\partial B_y}{\partial z} \tag{3.25}$$

and

$$E_z = \frac{-ic}{\omega\epsilon(z)}\frac{\partial B_y}{\partial x}. \tag{3.26}$$

This situation is different from the S-polarization case. In this problem, we need to consider the dielectric function given by equation 3.17. Upon examining the differential equation for the magnetic field, it is clear that the second term in equation 3.24 approaches infinity as the dielectric function approaches zero.

That is, the dielectric function changes sign as the plasma density exceeds the critical density. The dielectric function of the plasma approaches zero where equation 3.24 approaches a singularity. As a result, all of the field components B_y, E_x and E_z approach infinity as the point of singularity is approached. Several authors have discussed in great detail the exact nature of this type of singularity [86, 95, 96]; they have shown

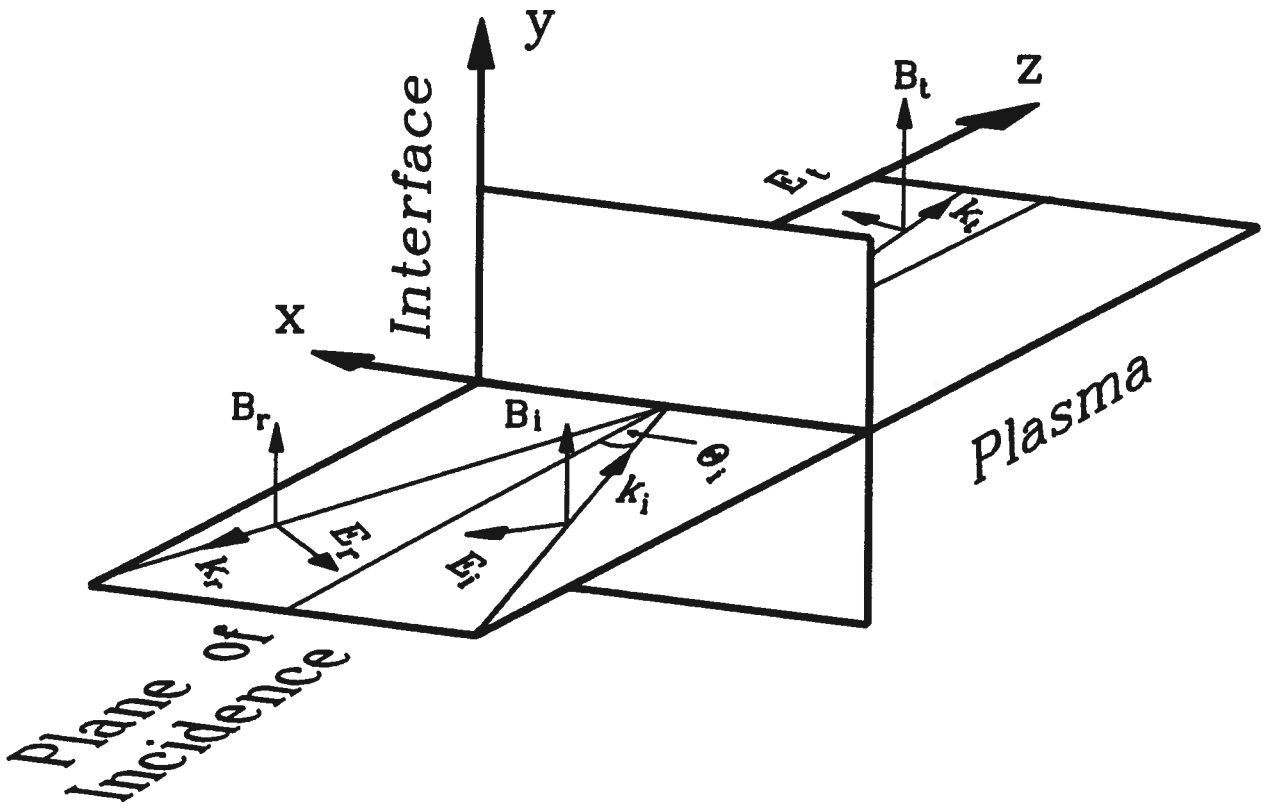

Figure 3.2: An incoming wave whose electric field, $\mathbf{E_i}$, is parallel to the plane of incidence (P-polarization).

that in the neighbourhood of the near zero point of the dielectric function, the electric field component E_z approaches infinity as $\epsilon(z)^{-1}$ and the other component E_x approaches infinity logarithmically. For P-polarized electromagnetic waves, there exists a longitudinal component of the electric field along the density gradient. Under these conditions, this component of the electric field resonantly excites high amplitude oscillations at the critical density of the CO_2 probe radiation with an oscillating frequency of $\omega=\omega_p$, where ω_p is the plasma frequency. These large amplitude oscillations can influence the motion of the electrons and may result in anharmonic oscillations of the electron plasma. The transfer of electromagnetic to electrostatic energy and its subsequent dissipation is known as resonance absorption [89, 90, 97]. The process is also responsible for higher harmonic generation from the probe frequency [98, 99].

It should be pointed out that if the angle of incidence θ_i is set equal to zero, the magnetic field structures can be described in the same manner as in the case for the electric fields in the S-polarization situation where no plasma oscillations are excited at the critical density. We made several attempts to solve equation 3.24 analytically; however, we were not successful in deriving an analytical solution. To our knowledge, when all the features are simultaneously present (such as spatially and time varying dielectric function and the introduction of free-carrier absorption), the general problem has no analytical solution. At best, one may be able to obtain a numerical solution to the problem. An extensive body of literature has been devoted to the study of this problem [84]–[86],[95, 96].

3.3 Numerical Approach to the Solution: P-Polarization Case

As we mentioned previously, an analytical solution of equation 3.24 proved to be impossible. The next step is to adopt a numerical method for the solution of the differential

equation. There are several problems associated with any numerical technique when dealing with singularities of the differential equation. Obviously, numerical integration near the point where the dielectric function approaches zero leads to an abrupt growth of the electric field E_x. An infinitesimally small change around the singular point can result numerically in an unphysical value for the electric field.

Another difficulty is associated with the lack of proper boundary conditions at the surface of the semiconductor (at z=0). These boundary conditions for $b(z = 0)$ and $(\partial b(z)/\partial z)_{z=0}$ are required in order to initiate the numerical integration procedure for the second order differential equation for $b(z)$. In fact, we are primarily solving the differential equation in order to obtain the boundary condition values at the vacuum-semiconductor interface. These problems make our numerical approach much more involved than standard numerical solutions.

In order to remove the singularity from the differential equation for the magnetic field, one has to evaluate the magnitude of the imaginary part of the dielectric function. Effectively, the magnitude of the ν_c/ω term determines the rate at which the critical density is approached. It is clear that if this ratio is $\gg 1$, the large amplitude oscillations driven by the longitudinal component of the electric field will be strongly damped due to absorption, and the numerical solution to the differential equation does not result in unphysical electric fields. However, in a plasma the damping is often very small since the imaginary part of $\epsilon(z)$ is small. One must bear in mind that given the reported experimental results on the collision frequency ν_c, one has to consider a more realistic ratio in order to obtain physical solutions. In our numerical calculations we take ν_c/ω=10^{-2} [85].

A simple technique for obtaining a boundary condition value is to examine the differential equation far away from the plasma and far into the bulk of the semiconductor. This is similar to the method used in reference [100]. Here, one expects the solution for

the magnetic field to take the form of a simple plane wave. Therefore, one is required to obtain a solution for $b(z)$ at a distance where $z \gg \gamma^{-1}$. At a large distance, z, the differential equation reduces to the following equation:

$$\frac{\partial^2 b(z)}{\partial z^2} + k_i^2(\epsilon_b - \sin^2\theta_i)b(z) = 0, \tag{3.27}$$

which we can easily show to have a solution of the form of a simple plane wave [84]:

$$b(z) = Ae^{-i(k_i z\sqrt{\epsilon_b - \sin^2\theta_i} + \varphi)} \tag{3.28}$$

where A and φ, are the amplitude and the phase of the magnetic field plane wave, respectively. Ideally, this solution is valid as $z \to \infty$. In doing numerical calculations this limiting condition ($z \to \infty$) cannot be satisfied; therefore, before performing the numerical calculation one must examine the range of z that can satisfy the condition above. We found that by using a value of γz=10, the difference between our calculations and the ideal condition is only $\sim 10^{-4}$ which is adequate for our application.

The simulations are performed with the following parameters:

1. The calculations do not take into account the time evolution of the semiconductor plasma density. This will be treated later on in section 3.6.

2. The excitation laser pulse wavelength is 616 nm which corresponds to absorption coefficients, γ, of 4.5×10^4 cm^{-1} [101, 102] for GaAs and 2.56×10^4 cm^{-1} for CdTe [102].

3. The wavelength of the probe radiation is taken to be that of the CO_2 laser operating at 10.6 μm.

4. The background dielectric constant, ϵ_b, is taken to be 10.89 for GaAs and 7.29 for CdTe [103].

5. The angle of incidence of the infrared radiation is set at Brewster's angle for the bulk materials at 10.6 μm (θ_B=72° and 70° for GaAs and CdTe, respectively).

In general, the magnetic field is a complex function. We transformed equation 3.24 into two coupled second-order differential equations for the real and the imaginary part of $b(z)$. Both equations are solved in parallel using a modified fourth order Runge-Kutta method. The details of the technique are outlined in detail in references [84, 85, 104, 105]. The numerical integration is performed in a reverse fashion where we have defined a final interval z_f and performed the integration backward to the initial value at z_i=0 with an integration step of $-\delta z$. In trying to manoeuver the integration near the points around the critical density, the integration step size is reduced by a factor of 10 in order to obtain higher accuracy [106]; moreover, the value of the calculated magnetic field is monitored to check for signs of an abrupt growth. If this occurs, the integration step is further reduced by a factor of 10 and the calculations are repeated again around the region near the critical density. It should be pointed out that the exact value of the electric field component E_x cannot be obtained at the critical density, but only in the neighbourhood near the position of critical density.

The calculations for the fields are performed at several initial plasma densities ranging from $10n_c$ to zero [84]. The values of $b(z)$, E_x and $\epsilon(z)E_z$ amplitudes are calculated as functions of normalized distance, $\xi = \gamma z$, and the results for GaAs are presented in figure 3.3 for an initial plasma density equal to $5n_c$ for both of the real and imaginary components. From figure 3.3(a) and 3.3(c) as the critical density is approached, the magnitudes of $b(z)$ and ϵE_z vary smoothly. For n/n_c=5, this critical density is reached when ξ=1.61. In the $\epsilon(z)E_z$ case, both $\epsilon(z)$ and $\partial b(z)/\partial x$ approach the ξ=1.61 point at the same rate, and thus their product has a finite value.

It is interesting to note that at $n(\xi)$=n_c, both of the E_x and E_z curves resemble

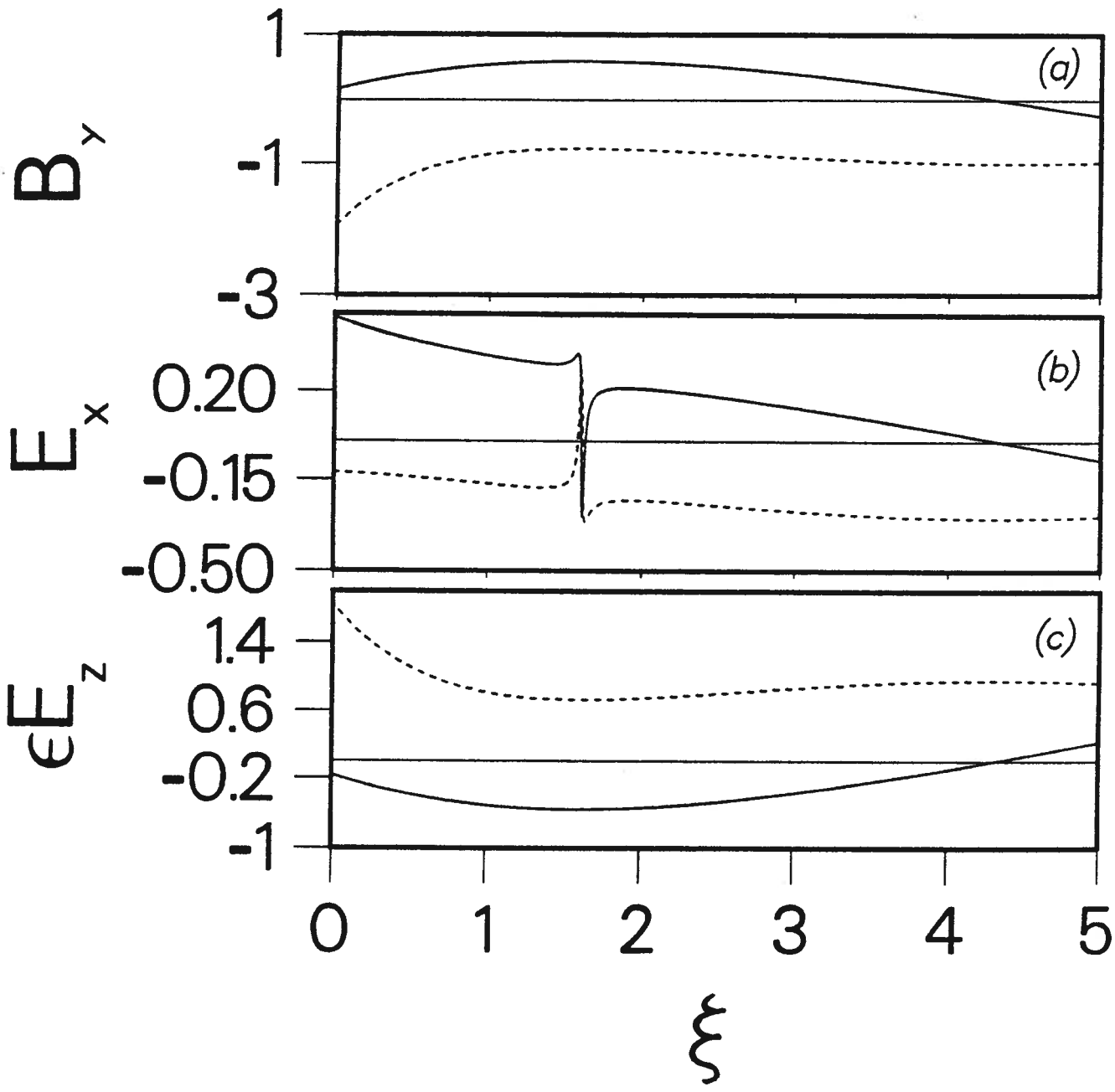

Figure 3.3: 10.6 μm laser radiation magnetic and electric field amplitude components $\mathbf{B_y}$ (curve a), $\mathbf{E_x}$ (curve b), and $\epsilon\mathbf{E_z}$ (curve c) as a function of $\xi = \gamma z$ in GaAs. The initial carrier density is $n = 5n_c$. Solid curves represent the real parts and dashed curves represent the imaginary parts.

step discontinuities reminiscent of a phase transition as the GaAs changes from being a semiconductor to a "metal" for the 10.6 μm radiation.

Once the values of the electromagnetic field amplitudes are obtained as functions of the initial plasma densities, one needs to calculate the reflectivity of 10.6 μm radiation from the plasma layer. The tangential component of the electric field and the perpendicular component of the displacement field have to be continuous across the vacuum-semiconductor plasma interface. The reflectivity can be obtained by matching the tangential electric field component, E_x, and the displacement field, ϵE_z, at ξ=0. Hence we obtain the following relation for the amplitude reflectivity [107]:

$$r = \frac{E_x \sin\theta_o + \epsilon_s E_z \cos\theta_o}{E_x \sin\theta_o - \epsilon_s E_z \cos\theta_o} \tag{3.29}$$

where ϵ_s is the dielectric function at the surface of the semiconductor evaluated at ξ=0. The intensity reflectivity, R, and its corresponding phase, Φ, are calculated from the following relations

$$R = \mid r \mid^2 \qquad \Phi = \tan^{-1}\left(\frac{Im(r)}{Re(r)}\right) \tag{3.30}$$

where $Re(r)$ and $Im(r)$ are the real and the imaginary parts of the amplitude reflectivity, r, respectively.

Figure 3.4 shows the results of such calculations of the intensity reflectivity for GaAs and CdTe as a function of initial normalized plasma density (n/n_c). Both curves show overall similar behaviour. In the density range $0 \leq n/n_c \leq 0.9$ the intensity reflectivity is calculated to be 0.7%; however, in the density range at near the critical density, the intensity reflectivity can be as high as 100%. It should be noted that figure 3.4 shows the intensity reflectivity maximum value to be only $\sim$ 40%. More elaborate calculations near the critical density show that in fact this value is $\sim$ 100%. Of importance to the ultrafast reflection switch scheme is the sharp resonance-like peak occurring at n/n_c=1.

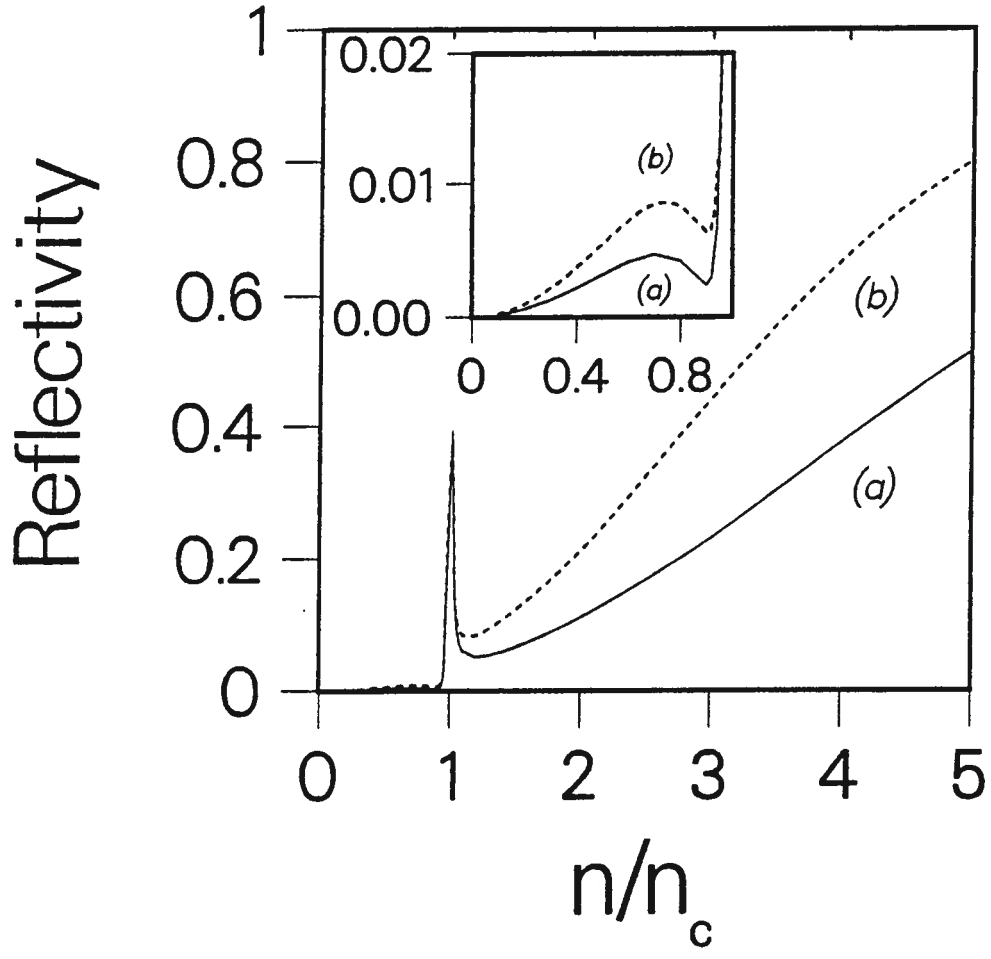

Figure 3.4: Brewster angle reflectivity for 10.6 μm laser radiation as function of an exponentially decaying plasma density profile of (a) GaAs and (b) CdTe. The inset figure shows an enlarged plot of the reflectivity for $0 \leq n/n_c \leq 1.0$.

For a small change in the plasma density from (n/n_c) to 0.9 (n/n_c), the reflectivity drops to approximately zero. The magnitude of the reflectivity peak is determined by the magnitude of the complex part of the dielectric function. When the plasma density, $n/n_c \geq 1.2$, the intensity reflectivity increases monotonically with increasing density to a maximum value of 100%. The higher reflectivity from CdTe semiconductor plasma compared to the one from GaAs is due to the reflection from a thicker plasma layer. This is to be expected since the wavelength of the infrared radiation (10.6 μm) is much longer than the plasma layer thickness and one expects the infrared radiation to penetrate through the plasma layer.

Figure 3.5 shows the phase angle change of the reflectivity as a function of the normalized plasma density. The curve shows that at the critical density the reflectivity suffers a phase change of π. This curve has proven to be very useful in interpreting the temporal shape of the reflectivity pulses.

With our complicated numerical simulations, it not clear how to explain the structures observed in figures 3.3 and 3.4, and one has to resort to a much simpler analytical model in order to confirm that the peak in the reflectivity is not just an artifact of the numerical procedure.

3.4 Reflection of 10.6 μm Radiation from a Thin Film Plasma

In this section we discuss a much simpler model which describes the reflection of 10.6 μm radiation from a thin plasma layer. The analyses are based on the Fresnel equation for P-polarized electromagnetic radiation [108]. The plasma layer is assumed to be isotropic, homogeneous, and lossless.

We consider the reflections from two semi-infinite plane-parallel regions: one contains the semiconductor plasma and the second involves the bulk semiconductor material.

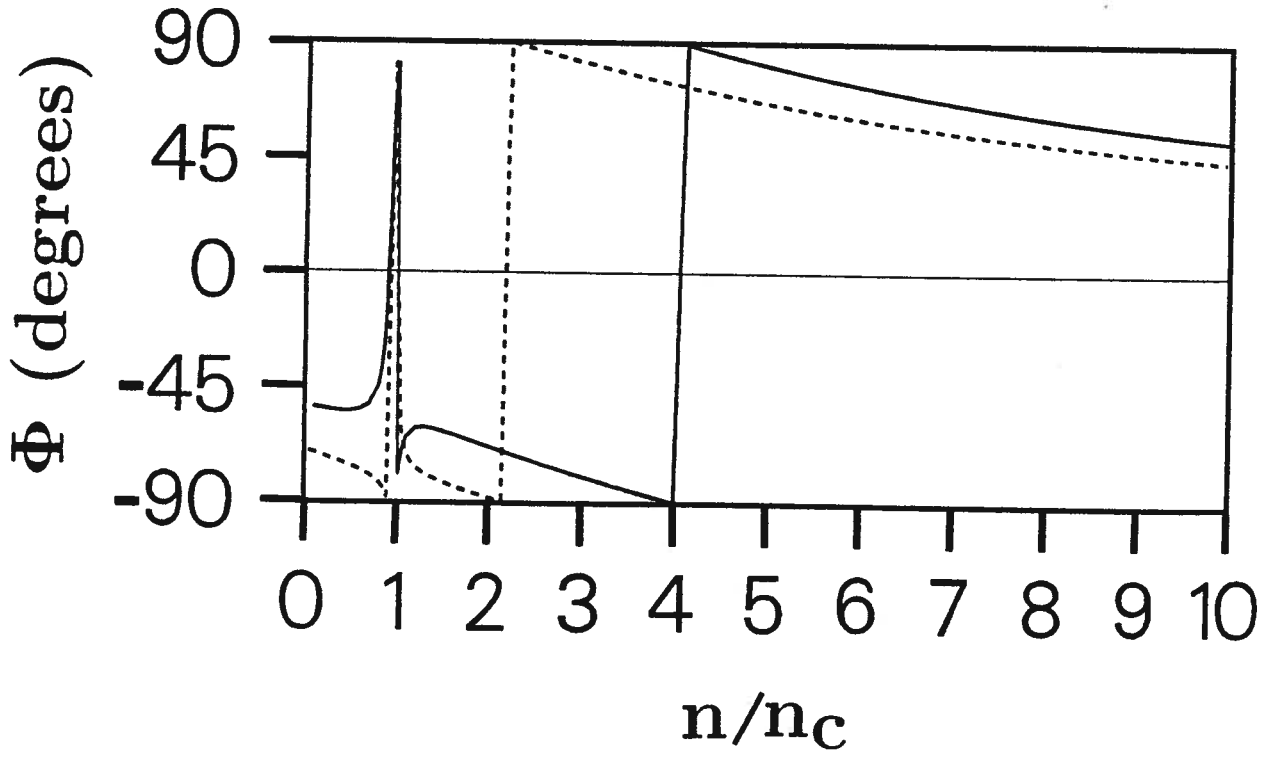

Figure 3.5: Phase angle change as a function of plasma density. The solid lines are calculated from the differential equation model. Dashed lines are calculated from the thin film plasma model.

Since we know that the plasma initial spatial distribution is most likely to have an exponential profile, we can consider the plasma film thickness, δ, to be equal to the absorption length of the visible radiation, γ^{-1}. In this thin film layer, the plasma density is assumed to be constant throughout the entire film thickness. The second film layer contains the bulk semiconductor material and extends to infinity. We also assume that the boundary between the two films is sharp. The geometry of the problem is shown in figure 3.6. With the above assumptions in mind, the dielectric function of the switch can be written as [85]:

$$\epsilon(z) = \begin{cases} \epsilon_b(1 - \frac{n}{n_c}) & \text{if } z \leq \delta \\ \epsilon_b, & \text{if } z > \delta. \end{cases}$$

In order to obtain an expression for the reflectivity at each interface, we have to utilize the usual boundary conditions derived from Maxwell's equations, that the tangential, E_x, and the normal, $\epsilon(z)E_z$, components are continuous through the vacuum-plasma thin film and through the plasma thin film-bulk semiconductor interfaces [107]–[109]. As illustrated in figure 3.6, the 10.6 μm radiation is incident on the vacuum-plasma thin film interface at an angle θ_o, and is transmitted through the interface at an angle θ_1 relative to the normal to the surface. By matching the boundary conditions, we obtain the following expressions for the amplitude reflectivity at the first interface

$$r_{12} = \frac{\cos\theta_1 - \sqrt{\epsilon_b(1 - n/n_c)}\cos\theta_o}{\cos\theta_1 + \sqrt{\epsilon_b(1 - n/n_c)}\cos\theta_o}. \tag{3.31}$$

For the second interface, the radiation is transmitted at an angle θ_2 into the semiconductor bulk. By matching the boundary conditions at the second interface, we obtain the following expression for the amplitude reflectivity [84]:

$$r_{23} = \frac{\sqrt{\epsilon_b(1 - n/n_c)}\cos\theta_2 - \sqrt{\epsilon_b}\cos\theta_1}{\sqrt{\epsilon_b(1 - n/n_c)}\cos\theta_2 + \sqrt{\epsilon_b}\cos\theta_1}, \tag{3.32}$$

where we have used the fact that the refractive index of vacuum is equal to unity. Under an incident angle equal to Brewster's angle, we have the conditions that $\sin\theta_o = \sqrt{\epsilon_b/(1+\epsilon_b)}$, and $\cos\theta_o = 1/\sqrt{1+\epsilon_b}$ at the surface. Also, by using Snell's law,

$$\sin\theta_o = \sqrt{\epsilon_b(1-n/n_c)}\sin\theta_1 = \sqrt{\epsilon_b}\sin\theta_2, \tag{3.33}$$

we obtain the following relation for $\cos\theta_1$:

$$\cos\theta_1 = \sqrt{1 - \frac{1}{(\epsilon_b+1)(1-n/n_c)}} \tag{3.34}$$

and for $\cos\theta_2$:

$$\cos\theta_2 = \sqrt{\frac{\epsilon_b}{1+\epsilon_b}}. \tag{3.35}$$

Hence, the amplitude reflectivity, r_{12}, can be expressed as:

$$r_{12} = \frac{\sqrt{\epsilon_b(1-n/n_c)-(n/n_c)} - \sqrt{\epsilon_b}(1-n/n_c)}{\sqrt{\epsilon_b(1-n/n_c)-(n/n_c)} + \sqrt{\epsilon_b}(1-n/n_c)} \tag{3.36}$$

and we can show that the amplitude reflectivity,

$$r_{23} = -r_{12}. \tag{3.37}$$

Multiple reflections and interferences between the two interfaces have to be taken into account in the calculations for an effective amplitude reflectivity, r. Let us denote the incident electric field on the vacuum-plasma interface and the reflected electric field by E_i and E_r, respectively. Let the reflection amplitudes be defined in terms of the direction of propagation of the incident electric field as defined in figure 3.7. That is, we use the subscript notation of + (refers to the left of the interface) and – (refers to the right of the interface). The other subscript notation, 1 and 2, denote the first and second interfaces, respectively. We can define [110]

$$r_{1+} = -r_{1-} = r_{12}, \tag{3.38}$$

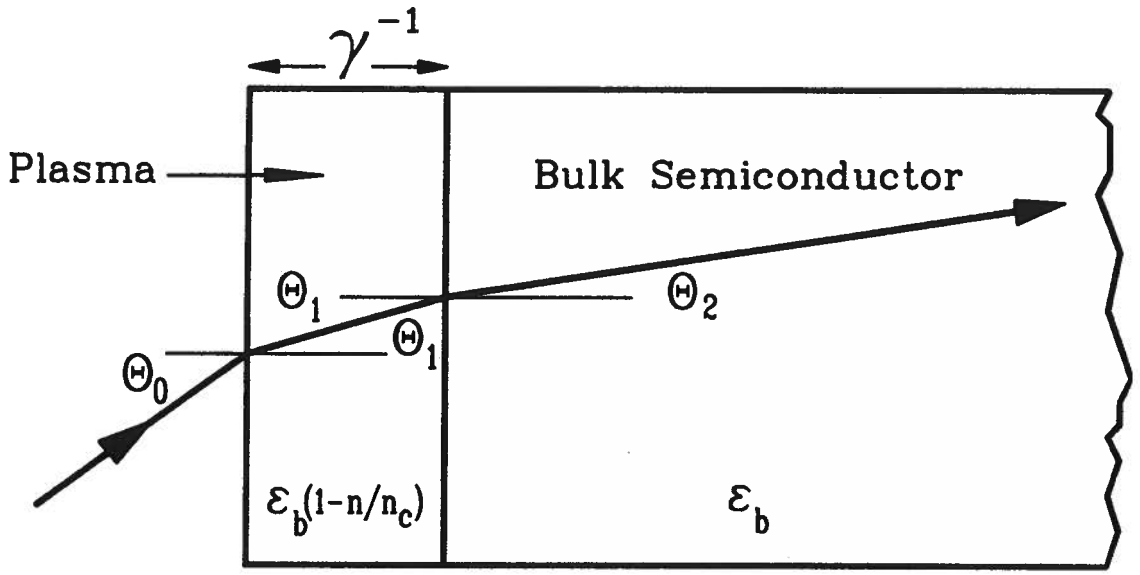

Figure 3.6: Geometry of the vacuum-plasma-semiconductor interfaces for the thin film plasma model.

$$r_{2+} = -r_{2-} = r_{23}, \tag{3.39}$$

$$t_{1+}t_{1-} - r_{1+}r_{1-} = t_{1+}t_{1-} + r_{1+}^2 = 1. \tag{3.40}$$

Here, the first subscript denoted the interface. Then the amplitude reflectivity due to multiple reflections from both surface can be written as:

$$\begin{aligned} r &= \frac{E_r}{E_i} \\ &= r_{1+} + r_{2+}t_{1+}t_{1-}e^{-2i\beta} + r_{2+}^2 r_{1-}t_{1+}t_{1-}e^{-4i\beta} + r_{2+}^3 r_{1-}^2 t_{1+}t_{1-}e^{-6i\beta} + \ldots \end{aligned} \tag{3.41}$$

where the phase shift, due to propagation through the plasma film, is given by: $\beta = k_i\sqrt{\epsilon}\gamma^{-1}\cos\theta_1$. At Brewster's angle propagation, we obtain the following equation:

$$\beta = k_i\gamma^{-1}\sqrt{\epsilon_b/(1+\epsilon_b)}\sqrt{\epsilon_b(1-n/n_c) - (n/n_c)} \tag{3.42}$$

which describes the phase change due to the propagation through the plasma layer. Here, k_i is the wave vector in vacuum. Summing up the infinite series for r and using equations 3.37-3.40, we arrive with the following relation for the effective amplitude reflectivity [108, 110, 111]

$$r = \frac{r_{12} + r_{23}e^{-2i\beta}}{1 + r_{12}r_{23}e^{-2i\beta}}. \tag{3.43}$$

We have calculated the above equation for various initial plasma densities in the range $0 \leq n/n_c \leq 10$ for the GaAs switch. The result of the intensity reflectivity from the plasma thin film model is presented in figure 3.8(a) for the density range $0 \leq n/n_c \leq 2.5$ and is compared to the previous reflectivity calculations from solving the Maxwell-Helmholtz equation (figure 3.8(b)). It is clear that there is very good agreement between the two curves and the reflectivity peak at n/n_c=1 is not an artifact of our numerical integration. The result for the calculated reflectivity phase shift is shown in figure 3.5; they also show a fair agreement with more elaborate calculations.

Since both systems show the same relative reflectivity variations, indicating (a) if we have a better understanding of the functional dependence of $R(n)$ for the plasma thin film,

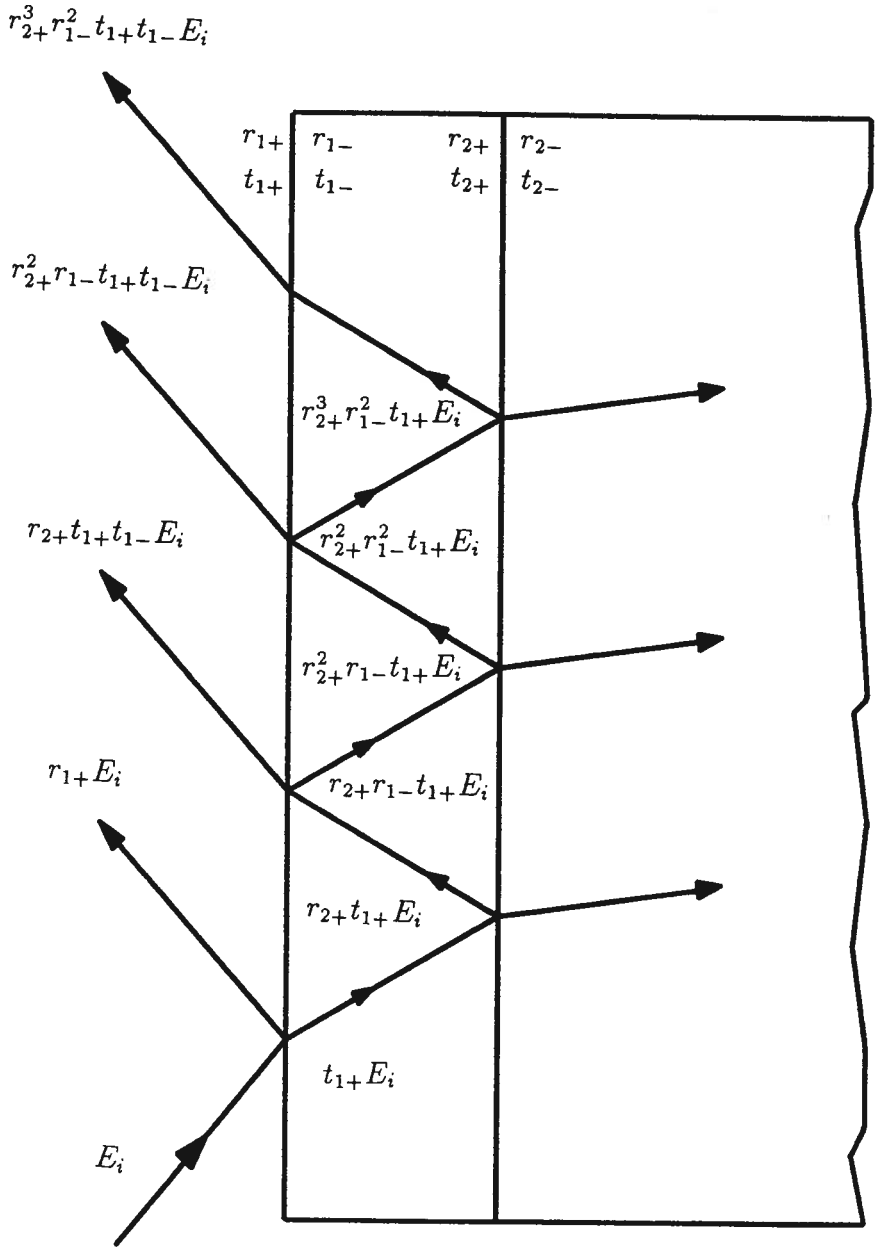

Figure 3.7: Geometry of multiple reflections from vacuum-plasma and plasma - semiconductor interfaces.

we should be able to explain the results from our complicated numerical simulations, and (b) that the reflectivity variation depends predominately on the surface plasma density rather than the function $n(z)$ in the bulk of the semiconductor [84, 85].

The calculation also indicates that a better modelling of the thin film plasma, for example, dividing the plasma layer into smaller multilayers and calculating the reflectivity of each one, adding them with the proper phase shift, should provide a better approximation of the physical situation [111].

It is simple to explain the features in figure 3.8 for the plasma thin film model [84]. The electron density increases from zero, the reflectivity R, reaches a small maximum value of $\sim 0.5\%$ at a plasma density near $(n/n_c) = (\epsilon_b - 1)/(\epsilon_b + 1)$ (labelled (I) in in figure 3.8(a)). At this value of the density, the intensity reflectivity from the first interface $\mid r_{12} \mid^2$ is minimum. At $(n/n_c) = (\epsilon_b - 1)/\epsilon_b$ the refractive index, $\sqrt{\epsilon(z=0)}$ is unity and the vacuum-plasma interface disappears. Hence, the plasma layer is illuminated directly at the Brewster angle, and as a result the reflectivity here is zero. This explains the first minimum in the reflectivity curve (labelled (II) in figure 3.8(a)) After passing through the point of frustrated internal reflection at $(n/n_c) = \epsilon_b/(\epsilon_b + 1)$ complete reflectivity is reached once $(n/n_c) \sim 1$ (labelled (III) in figure 3.8(a)). This is the region where the reflectivity shows a resonance-like peak. As the plasma density increases, $(n/n_c) \geq 1$, the amplitude reflectivities, r_{12} and r_{23}, are both complex in this region and for simplicity, we can write

$$r_{12} = e^{i\zeta} \tag{3.44}$$

where

$$\tan\zeta = \frac{2\sqrt{\epsilon_b}[(n/n_c) - 1]\sqrt{\epsilon_b[(n/n_c) - 1] + (n/n_c)}}{\epsilon_b[(n/n_c) - 1]^2 - \epsilon_b[(n/n_c) - 1] - (n/n_c)}. \tag{3.45}$$

Then the intensity reflectivity can be expressed as:

$$R = \frac{(1-a)^2}{1 - 2a\cos 2\zeta + a^2}. \tag{3.46}$$

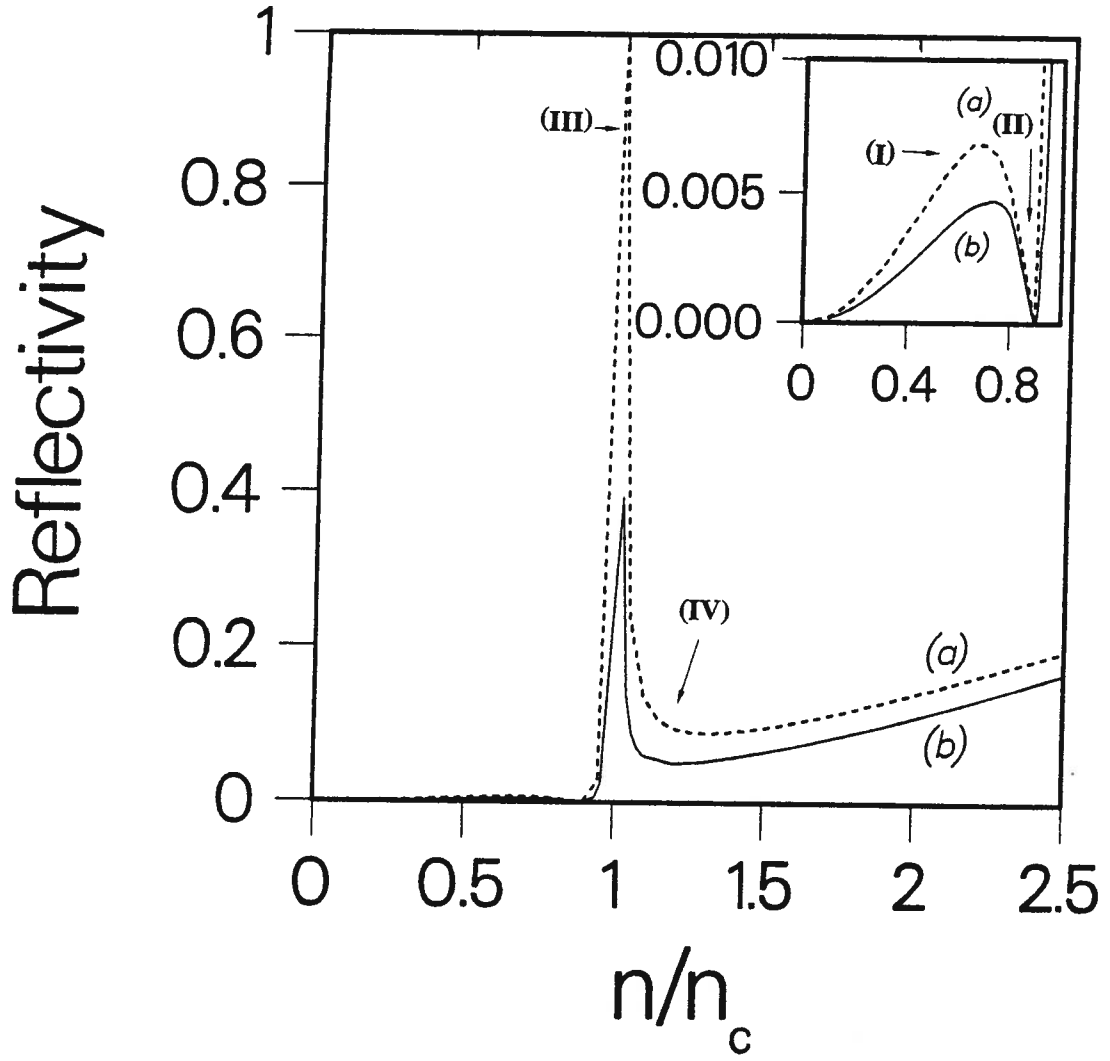

Figure 3.8: Brewster angle reflectivity for CO_2-laser radiation as a function of free carrier surface density of GaAs for (a) a uniform film thickness γ^{-1} and (b) for an exponentially decaying density profile. The inset figure shows an enlarged plot of the reflectivity for $0 \leq n/n_c \leq 1$.

Here, $a = exp(2i\beta)$ is a real function which rapidly decreases with increasing (n/n_c). Now, as ζ increases its value from zero at (n/n_c)=1 towards $\zeta = (\pi/2)$, R decreases towards a second minimum (labelled (IV) in figure 3.8(a)). Thereafter, the reflectivity increases monotonically with (n/n_c) and asymptotically approaches 1.

Clearly, with our simple model we have managed to understand the structures involved in the reflectivity curve. It also shows that the intensity reflectivity is a function of the phase shift, Φ, suffered by the incident radiation and the thickness of the plasma layer.

3.5 Temporal Variations of the Plasma Density

The temporal variation of the plasma density can manifest itself in the temporal behaviour of infrared reflectivity through the time evolution of the dielectric function.

In this section we briefly review of the processes that are responsible for the decay of the plasma density. Investigation of the recombination and diffusion processes allows us to selectively assess the relative importance of the mechanisms determining the e-h plasma decay. Ultimately, we are interested in an ultrafast plasma decay process occurring on the subpicosecond time scale.

3.5.1 Electron-Hole Plasma Recombination

When a semiconductor equilibrium state is perturbed by an optical excitation pulse, the balance of the equilibrium carriers is disturbed. If the excitation pulse is removed, the excess photogenerated carriers will return to the equilibrium state through recombinations.

Excess electrons and holes can recombine with each other through several recombination mechanisms: radiative, Auger, multiphonon recombination, capture at impurity sites (which can be either radiative or nonradiative process), and surface recombination

[112]. These processes determine the lifetime of optically generated excess carriers. In general, the selection of the recombination process depends on several factors, such as the e-h plasma density, carrier temperature, band structure of the semiconductor material, lattice temperature, impurity concentration, and the semiconductor surface condition. The fundamental theoretical and experimental aspects of recombination processes are discussed in great detail in references [112]–[117].

Two-body recombination is a radiative recombination process. In direct gap semiconductors, an electron in the conduction band can recombine with a hole in the valence band, resulting in an emission of a photon [118]. The decay rate of the plasma depends on the densities of electrons and holes according to the following relation [119]

$$\frac{\partial n(t)}{\partial t} = -B_o n^2 \tag{3.47}$$

where B_o is the two-body recombination coefficient. For GaAs the two-body recombination coefficient for optically injected carriers is measured to be $(3.40\pm1.17)\times10^{-11}$ $cm^3\ s^{-1}$ [101]. Clearly, two-body recombination remains insignificant even at the highest carrier density obtained in our experiments.

The Auger recombination process is usually the most dominant recombination process in intrinsic bulk semiconductors at high carrier concentrations and high carrier temperatures. It is a three-carrier process where a conduction band electron and a hole in the valence band recombine, and the associated excess recombination energy is transferred to a third carrier as kinetic energy. This energy is then thermalized with the rest of the carriers. The presence of a third carrier is necessary in order to conserve energy and momentum. It should be pointed out that the Auger recombination process does not change the total energy of the plasma e-h distribution; however, since the number of carriers has decreased, the total energy of the carriers is divided among fewer carriers. This results in a significant increase in the individual carrier's temperature and a decrease in the carrier

density.

Since Auger recombination is a three-body interaction, its recombination rate is strongly dependent on the plasma density. The recombination rate increases with the third power of the injected carrier density. The decay rate of the plasma density due to Auger recombination can be written as:

$$\frac{\partial n(t)}{\partial t} = -\Gamma_a n^3 \tag{3.48}$$

where Γ_a is the Auger coefficient.

Theoretical calculations and experimental measurements of Auger coefficient have been made for a GaAs [101, 120, 121]. Mclean et al. [101] have investigated the Auger recombination rate in optically excited carriers, and they measured an Auger coefficient of $(7\pm4)\times\ 10^{-31}$ cm^6/s. Evidently, the Auger recombination decay rate is a slow process compared to the time scale of interest.

In the case of a semiconductor sample of finite size, surface recombination can influence the temporal behaviour of the plasma density through the introduction of surface states. These states basically are discrete energy levels in the forbidden energy gap introduced by the discontinuity in the lattice. Since the photoinjected plasma is generated near the surface, where these levels exist, the surface states can act as recombination centres. The surface recombination velocity is determined by the surface conditions [122]. The rate of surface recombination is different from that of the bulk and is defined by a surface recombination velocity, S, as

$$S = \sigma_{ec} v_{th} N_{str} \tag{3.49}$$

where, σ_{ec} is the carrier capture cross section ($\sim$ 10$-$15 cm^2), v_{th} is the free carrier thermal velocity ($\sim\ 10^7$ cm/s), and N_{str} is the surface trap density ($\sim\ 10^{14}$ cm^{-2}). The recombination time due to surface states is of the order of $\sim$ 20 ns.

Multiphonon recombination is a recombination process by which an electron and a hole recombine with a cascade emission of several phonons in place of a photon. This mechanism is very inefficient considering the large number of phonons required to make up the energy of a single photon [123].

By examining the above recombination rates, it is evident that their contribution to the reflectivity occurs in time scales longer than $\sim$ 500 ps (for $n = 6n_c$). Therefore, one has to search for an alternative ultrafast carrier density decay mechanism.

3.5.2 Diffusion and Time-Dependent Density Profile of the Free Carriers

Diffusion of free carriers can result in a dramatic decrease in the plasma density. Here, we will examine the time evolution of the carrier density on a subpicosecond time scale.

Directly after optical excitation, high density nonequilibrium electrons and holes are photogenerated in the semiconductor switch. The behaviour of the plasma depends primarily upon the processes of diffusion and surface recombination. The spatial distribution of the optically generated plasma through the semiconductor will be inhomogeneous, thus the temporal dependence of the carrier diffusion should be considered as a factor in reducing the e-h plasma density.

Diffusion is characterized in terms of a diffusion coefficient, D, which describes the number of free carriers passing through a unit area per unit time in the density gradient. In the case of a laser produced e-h plasma, the diffusion of both carriers is described by an ambipolar diffusion coefficient. Because any separation of charge would create an electric field between the electrons and holes, the two carriers must diffuse at the same rate. It is often difficult to experimentally isolate the effects of diffusion on the plasma density. To our knowledge, there is no experiment designed to directly measure the diffusion coefficient of nonequilibrium semiconductor plasma for time scale less than 500 fs. Hence, one has to rely on model calculations for D. We will assume that the

electrons and holes are in thermal equilibrium with the lattice. The plasma, although inhomogeneous in its spatial distribution, is assumed to have a uniform temperature. A crude approximation to our problem is to consider a nondegenerate plasma distribution where the diffusion coefficient is defined by

$$D = \frac{2D_e D_h}{(D_e + D_h)} \tag{3.50}$$

where D_e and D_h are the diffusion coefficients for electrons and holes, respectively. A more general scenario would be to include the density and temperature dependence of the diffusion coefficient. The carrier's diffusion coefficient is known to increase with the carrier temperature and decrease with lattice temperature; moreover, the diffusion coefficient is also shown to have a strong dependence on the carrier density above $\sim 10^{19}$ cm^{-3} where carrier degeneracy is reached. Several authors have considered this dependence to explain the observed experimental results [124]–[130]. The dependence of D on density can be calculated using the Boltzmann transport theory in the relaxation time approximation [126]. A rigorous analysis of the diffusion coefficient has been performed by Young and van Driel [124] where they have included many-body effects in the plasma. Here, we used the ambipolar diffusion coefficient value of 20 cm^2/s [131, 132].

The temporal and spatial distributions of the plasma density in a semiconductor switch are described by the diffusion equation in one dimensional form:

$$\frac{\partial n(z,t)}{\partial t} = D\frac{\partial^2 n(z,t)}{\partial z^2} + G(z,t). \tag{3.51}$$

Here, z is the spatial coordinate perpendicular to the semiconductor switch surface, $n(z,t)$ is the number of photogenerated electron-hole pairs, and term $G(z,t)$ is the generation rate of the plasma. No provision was made for the radial plasma concentration dependence introduced by the gaussian beam profile. This is justified by the value of the effective diffusion length, L_D, relative to the beam size, given the time scale of interest.

Equation 3.50 is an approximation of the situation where the diffusion coefficient depends on the density, temperature of the plasma, and the position. In our experiment, we are interested in a plasma density around $\sim 1\times10^{19}$ cm^{-3} before the onset of the plasma degeneracy [130], thus, we are justified in our assumption. In our calculations, the semiconductor is illuminated with an ultrashort (< 100 fs) laser pulse having a photon energy greater than the band gap of the semiconductor. Hence, the rate of generation of the plasma is considered to be a delta function excitation in time; therefore, we can ignore the generation term. This is justified because the duration of the actual excitation pulse is much shorter than the characteristic times of the physical processes which occur after the plasma is generated. We can write the initial condition for the above equation as

$$n(z,0) = n_o e^{-\gamma z}. \tag{3.52}$$

Equation 3.51 will be solved subject to a boundary condition at the surface of the semiconductor, which can mathematically be represented by setting the carrier flux at the surface equal to the rate of surface recombination:

$$\left(\frac{\partial n(z,t)}{\partial z}\right)_{z=0} = \frac{S}{D} n(0,t), \tag{3.53}$$

where S is the density independent surface recombination velocity. With the above conditions, this linear partial differential diffusion equation can be solved analytically, and we obtain the following solution

$$\begin{aligned} n(z,t) &= \frac{n_o}{2}\left\{ e^{\gamma(\gamma Dt - z)} erfc\left(\frac{2\gamma Dt - z}{2\sqrt{Dt}}\right)\right. \\ &+ \frac{\gamma Dt + z}{\gamma Dt - z} e^{\gamma(\gamma Dt + z)} erfc\left(\frac{2\gamma Dt + z}{2\sqrt{Dt}}\right) \\ &- \left.\frac{2S}{\gamma D - S} e^{S(St+z)/D} erfc\left(\frac{2St + z}{2\sqrt{Dt}}\right)\right\}. \end{aligned} \tag{3.54}$$

Similar solutions are reported before [122, 132, 133] The above equation reduces to the initial condition (equation.3.52) at t =0.

Using typical values for GaAs for γ=4.5×10^4 cm^{-1}, an ambipolar diffusion coefficient D=20 cm^2/s and a surface recombination velocity S=1×10^3 cm/s [131, 132], we calculated the temporal evolution of the plasma density $n(z,t)$. The calculations are performed in 500 fs time steps. The result in figure 3.9 displays the normalized density of the plasma with respect to the normalized penetration depth ξ=γz at various times after delta function excitation pulse. Figure 3.9 indicates that (n/n_o) has decreased from 1 to 0.85 within the first 500 fs. This ultrafast initial decay will be the subject of further study later in this chapter. As time evolves, the density decay rate is much slower and the density profile is no longer an exponentially decreasing function with respect to depth, but more likely to resemble a gaussian profile. At longer times ($\geq$ 80 ps), the plasma continues to diffuse until it is nearly uniform across the depth of the semiconductor.

By then one has to include the effects of the recombination processes. We have found that the result in figure 3.9 is fairly insensitive to the actual value of S indicating that the initial variation of n_o is limited by ambipolar diffusion from the surface and into the bulk.

3.6 Simulation of the Reflectivity Pulses from GaAs

In the previous sections we have performed time-independent calculations for the reflectivity as a function of the initial excitation plasma density. In general, if we combine those calculations with a process which describes the time evolution of the plasma density, we should have a better understanding of the temporal response of the semiconductor switch. From the data displayed in figures 3.4, 3.8 and 3.9, it is easy to see how the infrared reflectivity changes as a function of time after a flash (100 fs) illumination with

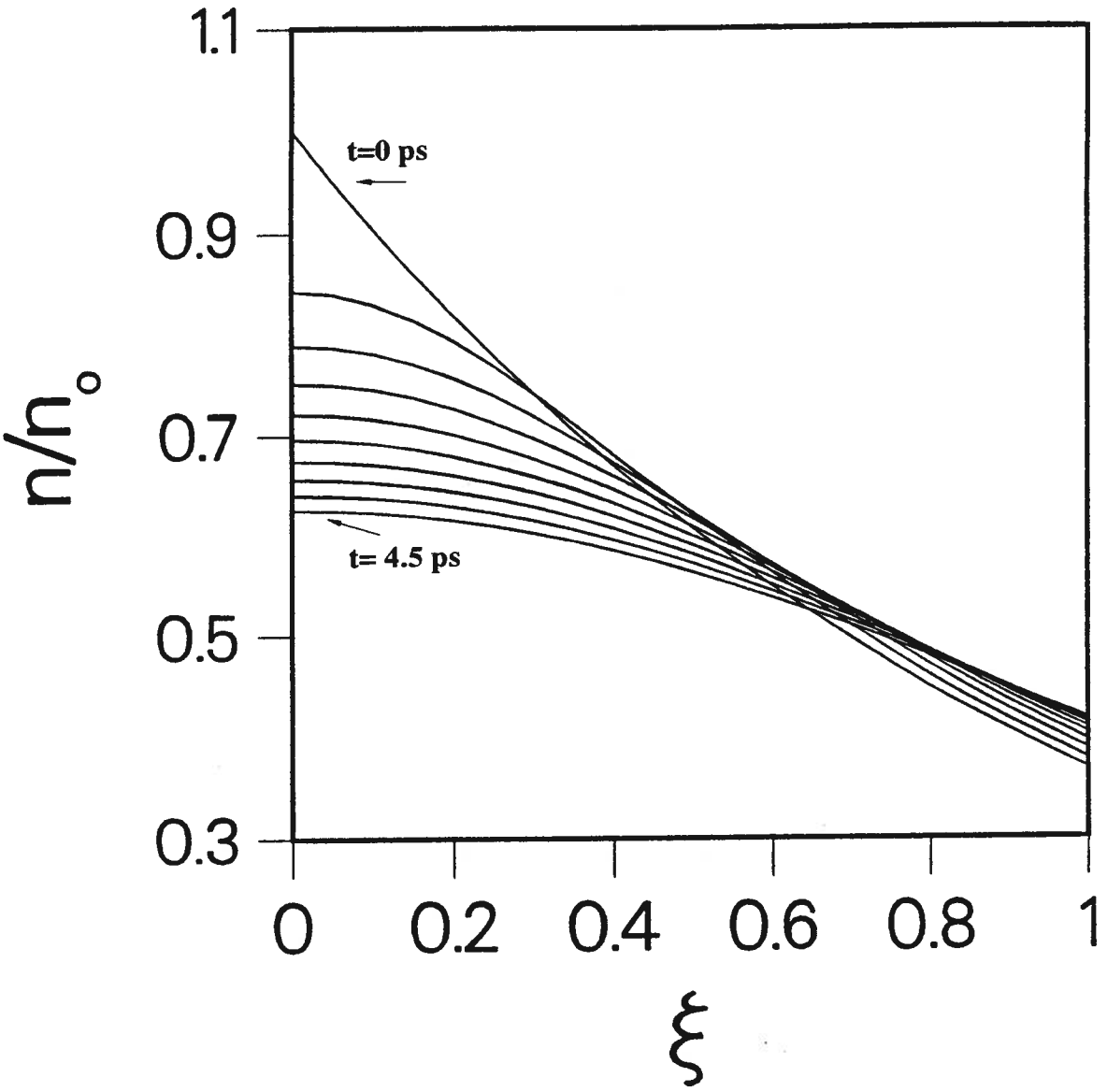

Figure 3.9: The variation due to diffusion of carrier density, $n(z,t)/n_\circ$ as a function of longitudinal position and time. The curves are plotted in increasing time steps of 500 fs. The top curve is calculated at t= 0 ps, and the botttom curve is calculated at t= 4.5 ps.

above band gap radiation. For the proposed reflection switch scheme it is necessary to tailor the exciting laser pulse intensity so that the critical density is produced. This may involve intensity discrimination techniques depending on the laser system used. The surface density then has only to decrease to reach $(n/n_c) = (\epsilon_b - 1)/\epsilon_b \sim 0.9$ in order for the reflectivity to decrease to zero.

In order to gain an insight into the pulse shapes and durations, we compare our calculations to the calculations performed with the simpler plasma thin film model. We can treat the time dependent dielectric function as [85]

$$\epsilon(z,t) = \begin{cases} \epsilon_b(1 - \frac{n(t)}{n_c}) & \text{if } z \leq \delta(t) \\ \epsilon_b, & \text{if } z > \delta(t) \end{cases}$$

where $\delta(t)$ is the thickness of the plasma film at time t, and $\delta(t = 0)=\gamma^{-1}$. Since this model avoids the problems resulting from the singularity of $\epsilon(z,t)$ we are able to calculate the reflectivity at the critical density. The change in the infrared reflectivity is related to the changes in the excess-carrier density, and the generation of ultrashort pulses makes use of the initial rapid decay of the electron density. We can account for the rapid drop in the reflectivity by using a simple physical argument [85]. The reflectivity of the switch is $\sim$ 100% whenever (n/n_c)=1, and the plasma generated by the femtosecond visible excitation pulse is contained in a thin layer of thickness of the order of the absorption length of the radiation, γ^{-1}=2.22$\times 10^{-5}$ cm. Assume that the photogenerated plasma is uniform in the transverse direction, and suppose that the transverse cross sectional area of the plasma is A, and that the total number of electrons generated at t=0 is N. Then the plasma density is given by the simple relation:

$$n_{(t=0)} = \frac{N}{A\gamma^{-1}}. \tag{3.55}$$

Next, the plasma diffuses into the bulk with a diffusion coefficient D= 20 cm^2/s, such

that in 500 fs the effective diffusion length L_D=3.162 $\times 10^{-6}$ cm. Effectively, all the electrons move into the bulk of the semiconductor by L_D. The electrons at the edge of the plasma thin film will diffuse by L_D and the effective plasma thickness becomes $(\gamma^{-1}+L_D)$. Note that there is no generation of new electrons after the optical excitation is over, and we still have the N electrons in the same effective cross sectional area A (here we have ignored the transverse diffusion of the carriers since the excitation laser spot size on the semiconductor surface is much larger than L_D). The new plasma density at 500 fs is then given by

$$n_{(t=500fs)} = \frac{N}{A(\gamma^{-1} + L_D)} \tag{3.56}$$

and the ratio of the two densities

$$\frac{n_{(t=0)}}{n_{(t=500fs)}} = \frac{1}{1 + \gamma L_D}. \tag{3.57}$$

This ratio is $\sim$ 0.875. That is, the density $n_{t=0}$ has decreased by $\sim$ 12% in only 500 fs. As previously mentioned, the reflectivity (see figure 3.8) around the peak drops from 100% to almost zero when the plasma density in reduced from $n = n_c$ by only 10% and this could happen in about 500 fs; therefore, it should be possible to generate ultrashort pulses if the semiconductor is excited to generate plasma density near the critical density.

The temporal behaviour of the semiconductor plasma is very complicated. With the density profiles of equation 3.54, the differential equation 3.24 becomes even more cumbersome to solve numerically. We have performed the calculation using the Maxwell-Helmholtz differential equation with a time dependent dielectric function $\epsilon(z,t)$.

With the plasma density profiles given by equation 3.54, the calculations are repeated for $b(x,z,t)$, $E_x(x,z,t)$, $E_z(x,z,t)$ and $R(n,t)$ using a fourth-order Runge-Kutta method. The $b(x,z,t)$ field amplitude is assumed not to change rapidly during one oscillation period of the electromagnetic wave. The computer code was modified to include

the temporal dependence of the plasma density; hence, we were able to calculate the reflectivity $R(t)$ as a function of time for each plasma density profile. That is, for each time interval the plasma density profile takes a different gaussian shape and the differential equation is solved for that specific form.

Here, we performed the calculations using GaAs as the semiconductor with some typical values D= 20 cm^2/s, S= 10^3 cm/s and the rest of the parameters are the same as the ones used for the time independent calculations [85]. The reflected infrared pulses are shown in figures 3.10 to 3.11 for some representative values of the initial plasma density profile. These values are chosen to cover a wide span of the reflectivity curve in figures 3.10 and 3.11. The regions between the solid lines in the figures indicate the times where the electron density in the differential equation approaches the critical density. The reflectivity is calculated in a small region around the singular point.

For (n/n_c)= 1.2, the FWHM is 200 fs and the reflected pulse increases slowly to reach a maximum value of 0.96 and then decreases slowly to zero in about 1 ps. As the singular point is approached, the reflectivity approaches unity, and because the change in the plasma density with time is slow, the dielectric function remains approximately zero for that period of time. Later, the reflectivity decays back to zero. The fast rise and fall times of the reflected signals indicate that the semiconductor switch can remain reflective with $R = 1$ in the region where $\epsilon(z,t)$ approaches zero, thus , resulting in reflected pulses of near rectangular pulse shapes. The initial part ($\leq$ 100 fs) of the reflected pulse is approximately zero; as a result, during the pumping by the visible wavelength control pulse, none of the 10.6 μm radiation is reflected. At (n/n_c)= 1.3, the calculated FWHM is 350 fs. By adjusting the excitation laser fluence so that the initial plasma density is $\leq 0.9n_c$, longer pulses in the picosecond range can be obtained. For example, when the initial densities are $0.74n_c$ and $0.9n_c$, the reflected pulse widths are 60 and 65 ps, respectively. These pulse intensities are two orders of magnitude lower than the ones

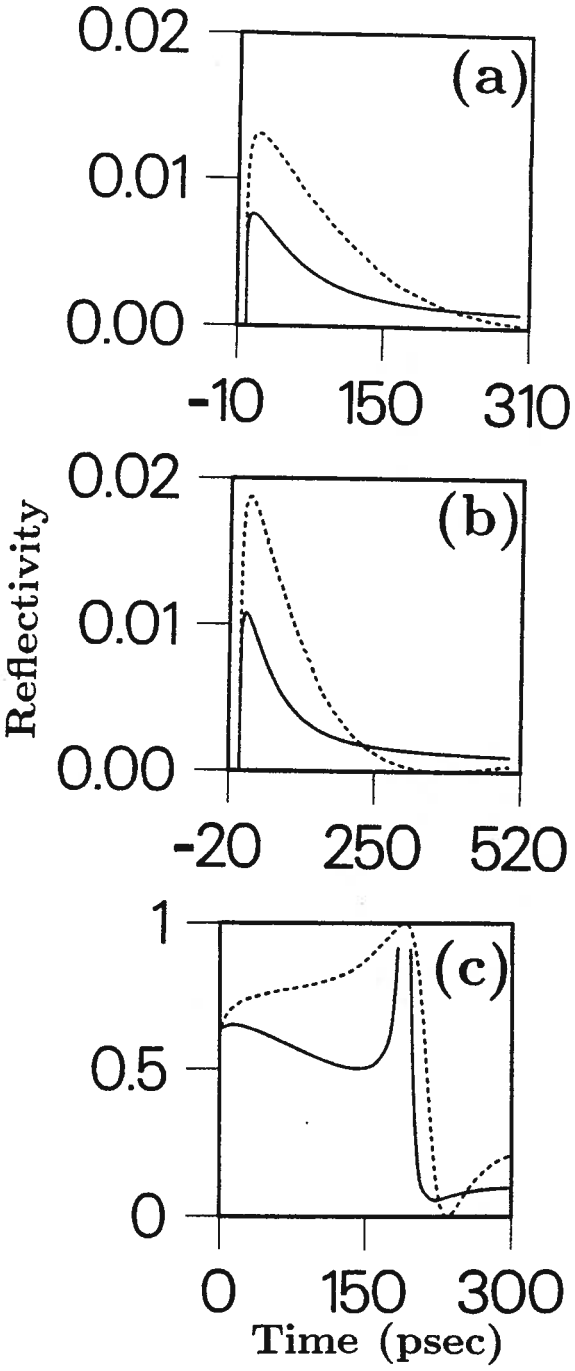

Figure 3.10: Reflected 10.6 μm pulses as a function of time for initial plasma density of (a) $n = 0.7n_c$, (b) $n = 0.9n_c$, and (c) $n = 6n_c$. The solid lines are calculated from the differential equation model and the dashed lines are calculated from the thin film plasma model.

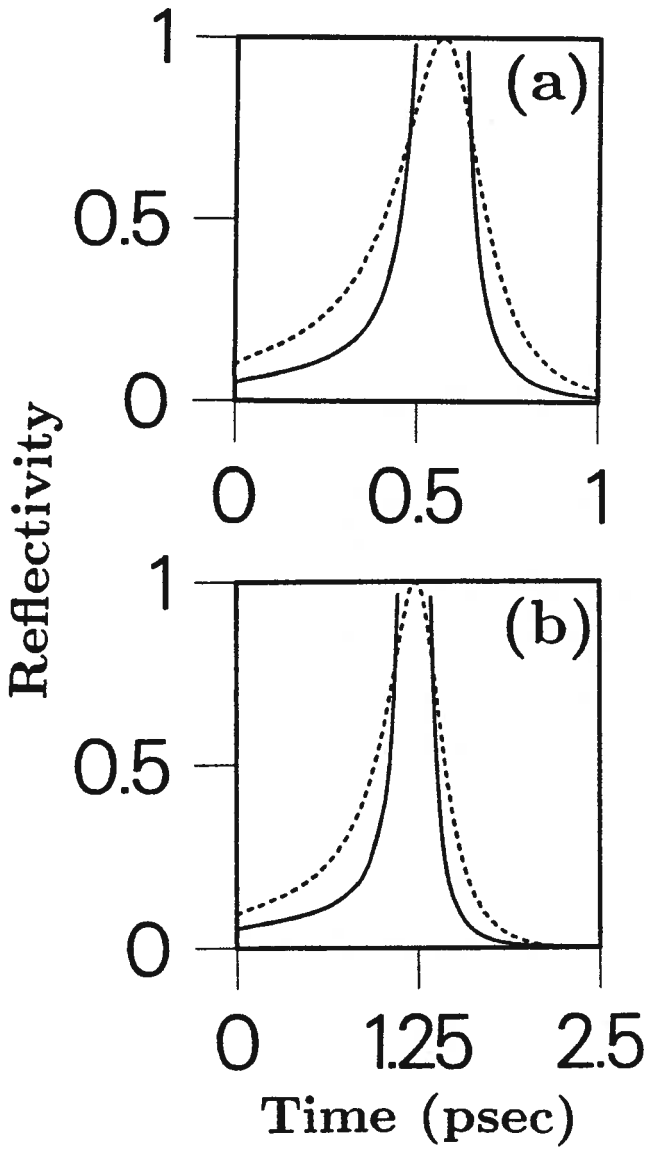

Figure 3.11: Reflected 10.6 μm pulses as a function of time for initial plasma density of (a) $n = 1.2n_c$ and (b) $n = 1.3n_c$. The solid lines are calculated from the differential equation model and the dashed lines are calculated from the thin film plasma model.

calculated near the critical density.

We have also calculated the phase shift experienced by the reflected infrared pulses for (n/n_c)= 0.74, 0.9, 1.2, 1.3, and 6. The results are presented in figures 3.12 to 3.14. The dashed lines in in figure 3.13 curves illustrate the points where the plasma density has reached the critical density, and one has to extrapolate around them. By examining figure 3.13, we realize that the reflected pulses suffer a phase change of $\sim\pi$ at the time of the peak of the reflection.

For comparison, we have also performed the calculations for the thin film plasma model using rectangular variations of the plasma density with depth. As time progresses, the thin film plasma is expanding into the bulk; and to incorporate the time dependence in this film model, we calculate the $1/e$ point of the density profile at the surface given by equation 3.54 and we note the corresponding time. These are used to simulate the expanding step-like film illustrated in figure 3.15. The results are displayed in figure 3.16(a). The figure shows that after the first $\sim$ 20 ps the plasma film thickness remains almost constant. From that, we calculated the corresponding effective thickness of the film, $\delta(t)$, as a function of time during the first 300 ps.

The results are shown in figure 3.16(b); here the plasma is treated as a step-like film whose thickness increases with time. Multiple simulations are performed for the initial normalized electron densities of 0.74, 0.9, 1.2 1.3, and 6. The results are displayed in figures 3.10 to 3.11 and are found to be in good agreement with the above numerical calculations. The rise and the fall times of the reflected pulses are much slower than the ones calculated previously. This is to be expected from such a model, since the change in the plasma density with time is much smoother. At the point where $\epsilon(z,t)$ =0, the reflectivity reaches unity which is in agreement with what is expected from the solution of the differential equation.

We can write the reflectivity as a function of three variables: the phase shift, film

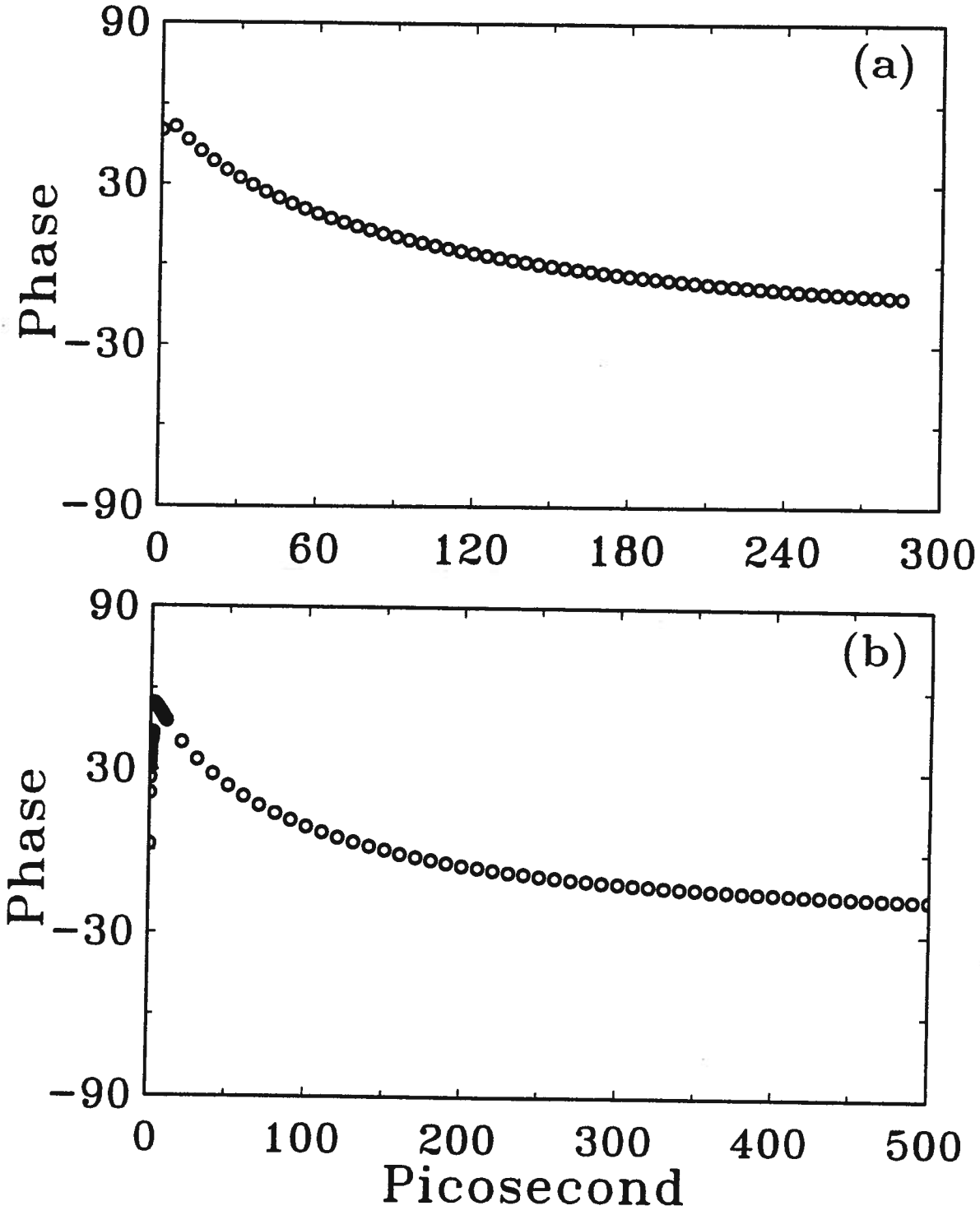

Figure 3.12: Phase change in degrees of the reflected 10.6 μm pulses as a function of time for initial plasma density of (a) $n = 0.7n_c$ and (b) $n = 0.9n_c$. The plots are calculated from the differential equation model.

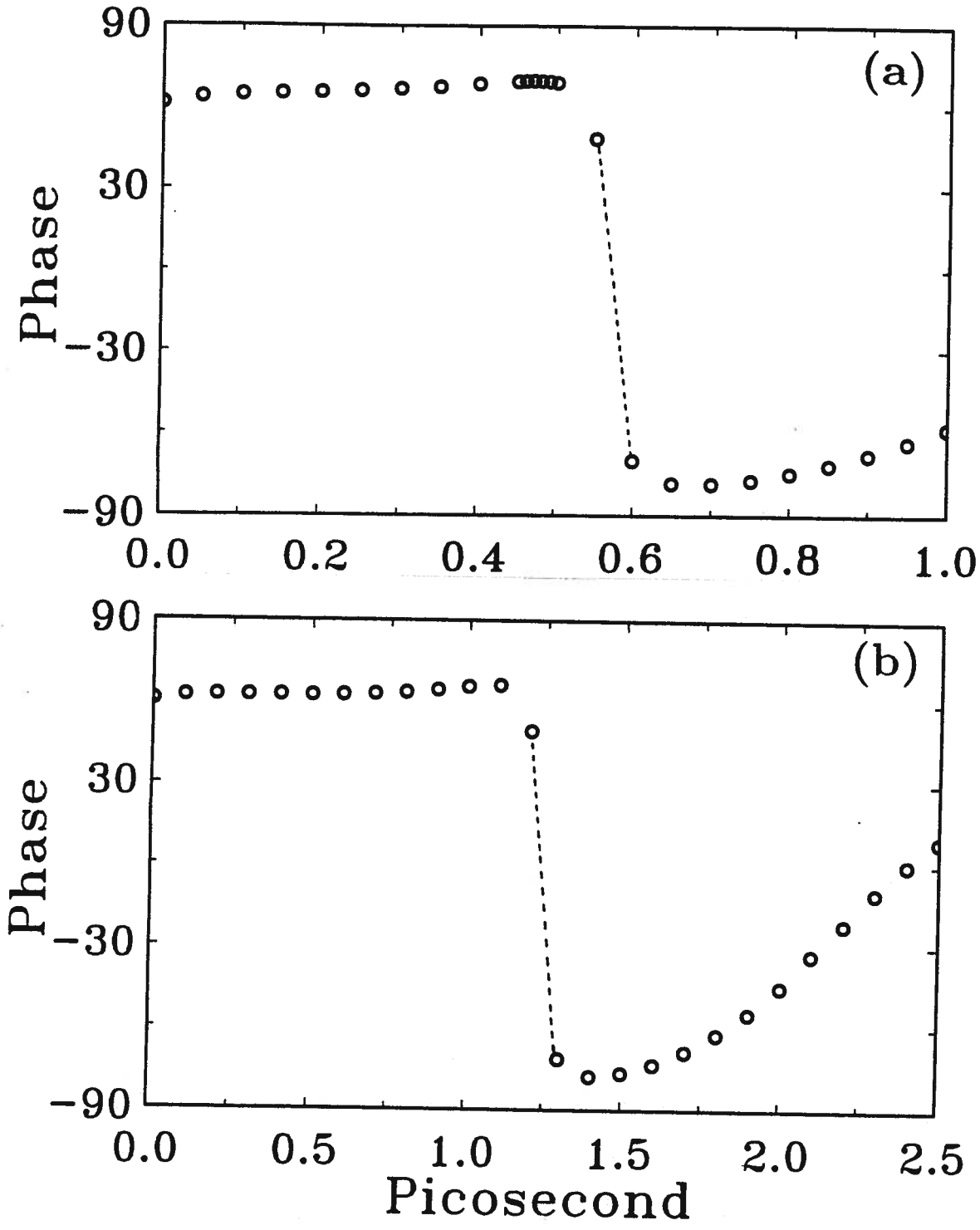

Figure 3.13: Phase change in degrees of the reflected 10.6 μm pulses as a function of time for initial plasma density of (a) $n = 1.2n_c$ and (b) $n = 1.3n_c$. The plots are calculated from the differential equation model.

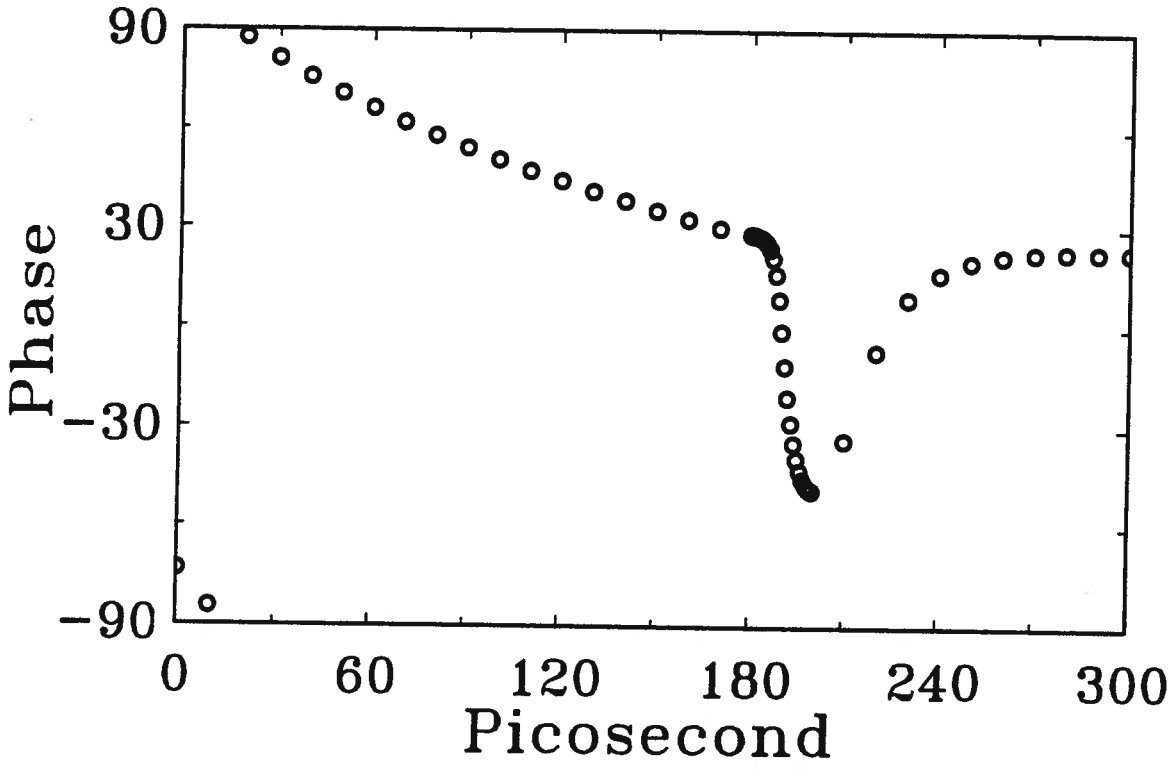

Figure 3.14: Phase change in degrees of the reflected 10.6 μm pulses as a function of time for initial plasma density of $n = 6n_c$. The plot is calculated from the differential equation model.

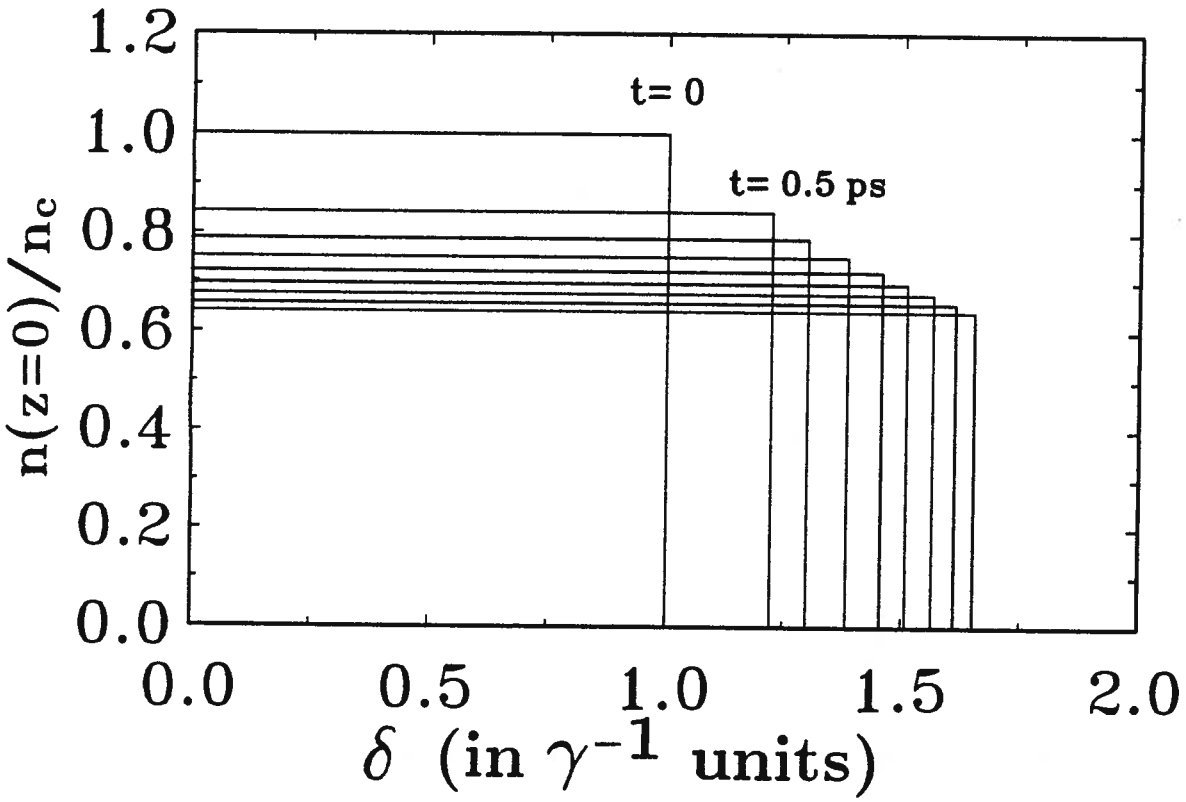

Figure 3.15: Illustration of the plasma profile used to estimate a constant plasma depth and density from a plasma density profile at a given time after the onset of laser illumination.

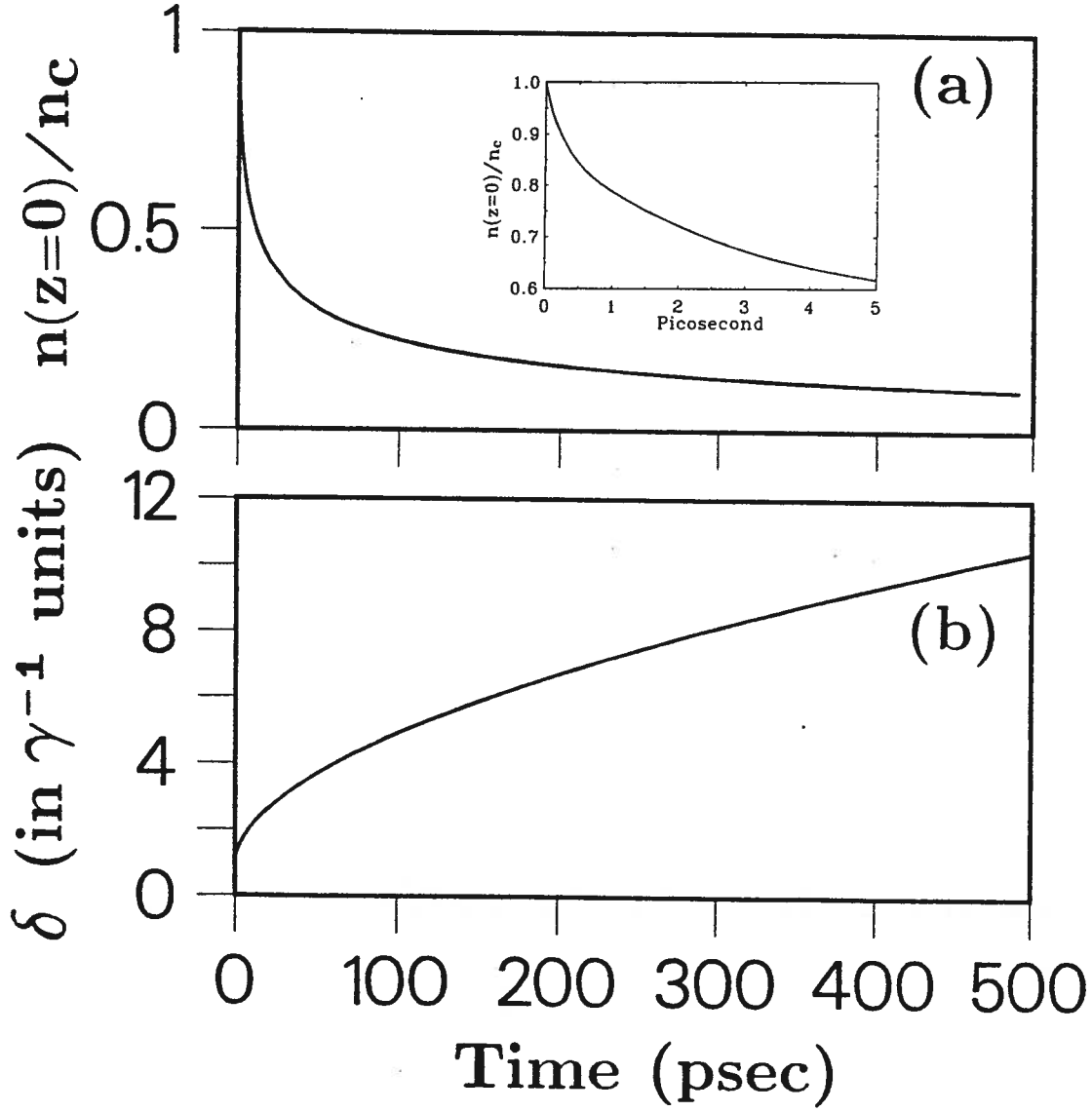

Figure 3.16: (a) Normalized surface plasma density at z=0 as a function of time. (b) Effective thickness of the plasma film as a function of time.

thickness and electron density. Therefore, the dynamical behaviour of the switch can be written as the total derivative of the reflectivity with respect to time.

$$\frac{dR}{dt} = \frac{dR}{dn}\frac{dn}{dt} + \frac{dR}{d\Phi}\frac{d\Phi}{dt} + \frac{dR}{d\delta}\frac{d\delta}{dt}. \tag{3.58}$$

Note that at all times we have $(dn/dt) < 0$. This means that if the semiconductor is illuminated by a laser fluence sufficient to produce a large enough initial plasma density, i.e. $(n/n_c) = 6$, then a competition between the derivatives of the phase, the density, and the thickness of the plasma film, with respect to time determines the temporal evolution of the reflected infrared pulses. By examining figure 3.4 and figure 3.5, the first two terms $(dR/dn)(dn/dt)$ and $(dR/d\Phi)(d\Phi/dt)$ are both negative, whereas the last term $(dR/d\delta)(d\delta/dt)$ is positive. The rate of change of the reflectivity depends on whether the sum of the three terms is positive or negative. Initially, the reflectivity changes at a slow rate because the rate of change of the first two terms is slow in the first 10 ps, and the rate of change of the reflectivity is dominated by the change in the thickness of the plasma film, thus making (dR/dt) positive. When the reflectivity approaches ~ 0.65, it begins to decrease slowly since the last term no longer dominates the sign of (dR/dt). For the next 140 ps the reflectivity decreases until the plasma density decays to $1.26n_c$. At the point where (n/n_c)=1.26, the contributions of all three terms are positive, and the reflectivity increases slowly from 0.5 to 0.91 in about 33 ps. When R approaches unity, the electron density approaches the point near the critical density. As soon as $(n/n_c) \leq 1$, we have a different region of reflectivity, where the contribution of the phase to the reflectivity is zero in this region. For the plasma density in the range $0.9 \leq (n/n_c) \leq 1$, the term $(dR/d\delta)(d\delta/dt) > 0$ and $(dR/dn)(dn/dt) < 0$. Because of the fast decay of the electron density compared to the increase in R due to increasing plasma thickness, the reflectivity decays very quickly from unity to zero level (at (n/n_c) =0.9). For the plasma density range $0 \leq (n/n_c) < 0.9$, the term $(dR/dn)(dn/dt)$ reverses sign and becomes positive but

the term $(dR/d\delta)(d\delta/dt) > 0$ and the reflectivity increases until it reaches a minimum value at the point where $(dR/dn) = 0$ (at $(n/n_c) \sim 0.74$). The reflected signal then decreases slowly because $(dR/dn)(dn/dt)$ switches sign and becomes negative, whereas $(dR/d\delta)(d\delta/dt) > 0$ and the reflectivity becomes zero at (n/n_c) =0.

From the above analysis, we can draw the following conclusions. Femtosecond and picosecond pulses of variable durations can be generated depending on the initial value of (n/n_c). For a control pulse of the order of 100 fs, one needs to adjust the energy fluence of the laser pulse such that the number density of the photoinjected electrons is in the range $1.2n_c$–$1.3n_c$ in order to obtain ultrafast infrared reflection. It seems that the temporal response of the switch is limited only by the control pulse duration and the ambipolar diffusion coefficient of the semiconductor.

The next task is to perform the experiment at different excitation energy fluences on GaAs. Whether our conclusions from the calculation are correct depend on the assumptions we have made in deriving the model.

Chapter 4

Laser Systems, Optical Setups, and Experimental Procedures

4.1 Introduction

In this chapter, the laser systems, the experimental apparatus, and the techniques used during the course of this work are discussed. A brief overview of the femtosecond laser pulse generating/amplifying system is presented with special emphasis on the system performance and characteristics. All the CO_2 lasers used in this work have been designed and built in this laboratory and considerable time and effort is spent in characterizing their performance as well as their operating conditions. Moreover, the construction details of these high-power CO_2 lasers are discussed. Further details of the fast electrical discharge excitation circuits and on the lasers' designs and construction are published in our review paper on the subject [134]. In this chapter, we also discuss the design of a home-made autocorrelator constructed to measure the duration of the pump laser system. A brief overview on the detection units, some custom electronic modules that are used for data collection and laser synchronization are discussed in this chapter. Detailed schematics of the electronic circuits are presented in Appendices A to C. Finally, the experimental setups for time-integrated reflectivity, reflection-reflection correlation, cross-correlation techniques, and frequency spectrum measurements are presented and discussed in detail.

4.2 The Femtosecond Laser System

The high power laser pulse excitation system used to operate the optical semiconductor switch is described in this section. Much of the time during the course of the experimental work was spent installing, maintaining, fixing, and optimizing the performance of the laser system. The layout of the laser system is illustrated in figure 4.1. A brief description of the characteristics of each component is presented below.

4.2.1 The Femtosecond Laser Pulse Generation System

The ultrafast laser pulse generating system is a commercial laser system consisting of an Nd:YAG (Nd^{3+} doped Yttrium Aluminum Garnet), a pulse compression stage, and a dye laser.

The Nd:YAG Laser

The Nd:YAG laser is a Spectra Physics Model 3800 mode locked laser. The laser is driven by an acousto-optic mode locker, placed inside the laser cavity near the output mirror, operating at a resonance frequency of 41.0245 MHz and producing a single longitudinal and transverse mode, quasi-continuous pulse train at a wavelength of 1.064 μm. The output pulse train repetition rate is 82.049 MHz with a single pulse duration of 70 ps. The average output power from the laser is between 13 to 14 W.

The Pulse Compressor

The Spectra Physics Model 3695 Optical Pulse Compressor utilizes a fibre-grating optical arrangement to shorten the 70 ps (1.064 μm) pulse duration from the mode locked Nd:YAG laser to $\sim$ 4–5 ps. The 1.064 μm pulse is frequency doubled to 0.532 μm using a second harmonic generation crystal. With frequency doubling, the duration of the 0.532

μm pulse is reduced even further to $\sim$ 3 ps. The maximum output that can be obtained from the pulse compressor is $\sim$ 1.1 W at 0.532 μm.

The Dye Laser

A Spectra Physics Model 3500 Ultrashort Pulse Dye laser is utilized in the final stage of the femtosecond pulse generation system. The dye laser uses Rhodamine 6G dye as a gain medium which is synchronously pumped by $\sim$ 850–900 mW, 0.532 μm (3 ps) output from the pulse compressor. The laser produces 83–250 mW average power with a tuning range between 575 to 635 nm. The output pulse train (82 MHz) consists of individual $\leq$ 500 fs pulses with 1–3 nJ/pulse.

4.2.2 The Femtosecond Laser Pulse Amplifying System

The nanojoule femtosecond laser pulses are amplified to a higher energy with a subpicosecond laser pulse amplifying system consisting of a three stage dye amplifier pumped by a Nd:YAG regenerative amplifier.

The Nd:YAG Regenerative Amplifier

A Continuum Nd:YAG Regenerative Amplifier Model RGA60 is used to pump a subpicosecond laser dye amplifier. A dielectric beam splitter is used to split off $\sim$ 5% from the Nd:YAG laser mode locked train and is injected into the regenerative amplifier. Single pulses are selected from the train and are amplified to produce 200 mJ, 70 ps, 1.064 μm laser pulses at a maximum repetition rate of 10 Hz. The output is frequency doubled in a second harmonic generation crystal to produce $\sim$ 100 mJ at 0.532 μm in a single transverse mode.

4.2.3 The Subpicosecond Dye Laser Pulse Amplifier

The femtosecond dye laser pulse is amplified in a Continuum Picosecond Amplifier Model PTA60 consisting of three Rhodamine 640 dye cells. The dye laser pulse amplifier is pumped synchronously with 25 mJ from the frequency doubled output from the Nd:YAG regenerative amplifier. The injected nanojoule 616 nm dye laser pulses are amplified to a maximum energy of $\sim$ 1 mJ at 10 Hz with a minimum of pulse broadening.

4.3 The CO_2 Laser Oscillators

In this section we give a brief introduction to the continuous wave (CW) CO_2 and pulsed lasers used in our experiments. The CO_2 lasers have been designed, built, and upgraded in our laboratory, and hence, a considerable amount of time and effort is devoted to determine their optimum operating conditions and design configuration. Our goal is to construct high-power single longitudinal and transverse mode CO_2 lasers to carry out the optical semiconductor switching experiments. The simplicity of the devices' designs and constructions make them attractive and inexpensive laboratory instruments.

4.3.1 The CW CO_2 Laser Oscillator

During the course of our experimental work with the CW CO_2 laser, the laser design was frequently modified and upgraded to suit our purpose. The original CO_2 laser delivered only 1.5 W at 10.6 μm. Clearly, this laser power was not enough to be useful in our experiments. Another larger laser has been designed to produce $\sim$ 10 W, and several experiments were performed using this laser; however, the detected signals are weak and it was decided to further upgrade it to a higher power ($\geq$ 30 W).

The CW CO_2 laser consists of two independent sections. The simple schematic of the laser is illustrated in figure 4.2. Both sections use a DC glow discharge to achieve

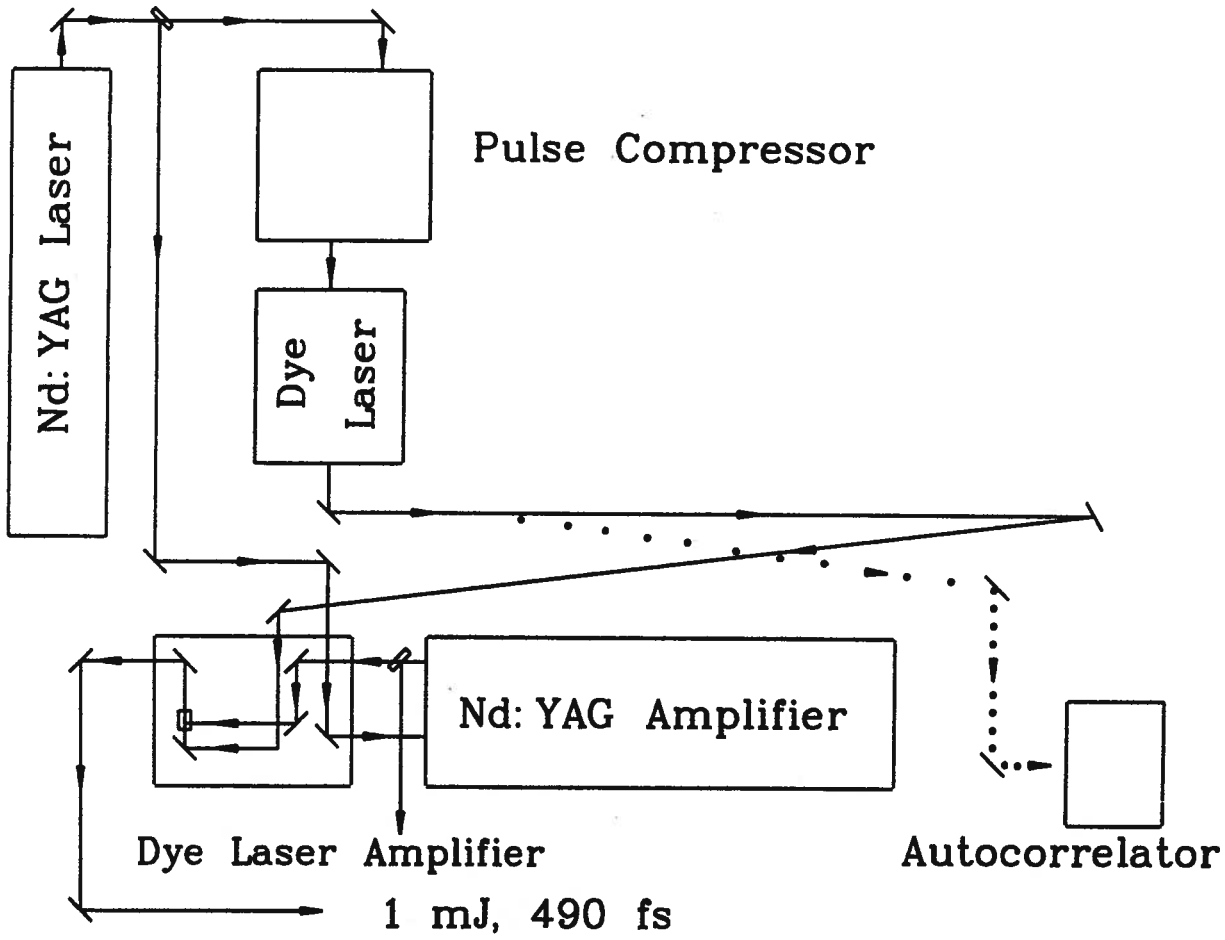

Figure 4.1: The layout of the femtosecond laser pulse generating system.

laser inversion in the CO_2 molecules. The two ends of the laser sections are maintained at a high voltage of 25 kV and are separated by a ground cathode at the centre of the discharge. Each section consists of a pyrex tube 103 cm in length and 12 mm in diameter, and can be operated independently. The effective laser cavity length is 3 m (end-to-end) with one end being terminated by a 0.64 cm thick, 5.08 cm diameter KCl Brewster's angle window to ensure a single polarization beam output, and the other end of the laser tube is terminated by the resonator cavity mirror. Two cold-water ($\sim$ 14 °C) lucite-jacket tubes (6.4 cm in diameter) are used to cool the discharge plasma.

In order to have a stable glow discharge between the laser brass electrodes, the negative dynamic resistance (after the CO_2 gas breaks down) must be suppressed. This is done by connecting a series of ballast resistors in series with the high voltage DC power supply. Both anodes are connected to the power supply via four 0.1 MΩ resistors with a total resistance in each arm of 0.4 MΩ. The cathode is connected directly to ground. This arrangement ensures that both sections can break down evenly and more reliably.

The laser cavity design consists of a concave, 8 m radius of curvature, gold-coated mirror which is mounted inside the discharge volume and an output coupler consisting of an uncoated plane-parallel Ge window of 5 mm thickness and 2.54 cm diameter. As in any etalon, both the front and the back contribute to the reflection. The refractive index of Ge at 10.6 μm is 4.2; hence at normal incidence, the contribution of the surface reflection is only $\sim$ 36%; however, interference between the two faces can result in reflectivity between 0–80% depending on the free spectral range of the Ge etalon.

The CO_2 can lase on several vibrational-rotational lines simultaneously between 8.7 μm to 11.8 μm. These laser transitions are highly competitive, and as a result the beating of the longitudinal mode causes fluctuations in the laser power output. The Ge flat can be used as a tunable Fabry-Perot etalon to suppress the oscillation on all lines but the one which matches the free spectral range of the Ge etalon. The free spectral range can be

tuned by adjusting the temperature of the Ge flat. A feed-back temperature electronic control system is used to actively stabilize the resonator cavity. The temperature of the output coupler is fixed at 30.15°C at which the laser lases at 10.6 μm and exhibits excellent stability. Due to the large length to diameter ratio of the discharge, the laser is forced to operate on a single transverse mode, TEM_{00}, with a beam spot size of 1.5 mm.

The discharge current determines the rate of pumping of the CO_2 molecules and thus determines the output power. In this laser, the maximum pumping current is 40 mA (20 mA for each section). The laser is operated with a gas mixture of He:CO_2:N_2 with a mixture ratio of 84:8:8 and a total gas pressure of 15 torr. During the electrical discharge the CO_2 molecules dissociate and; therefore, the replacement of the gain medium is required. The laser gas mixture is flowed through the discharge region, where it is injected from both anodes and exited through the cathode.

With the above operating conditions, the output laser power is measured to be $\sim$ 40 W. It seems that the limiting factor in determining the output power of the laser is the flow rate of the CO_2 gas. Improvements on the gas flow system should increase the output power. It is clear that the CW CO_2 laser does not require synchronization with the femtosecond laser/amplifier system; therefore, it is used to perform all the time-resolved experiments.

4.3.2 The High Pressure TEA CO_2 Laser Oscillator

TEA CO_2 Laser Body and Circuit

Here we present a design for a TEA discharge CO_2 laser which is used to perform some optical semiconductor switching experiments, especially for measuring the frequency spectrum of the reflected infrared pulses. An illustration of a cross section of the laser body and its electrical circuit components is shown in figure 4.3. The laser is designed to

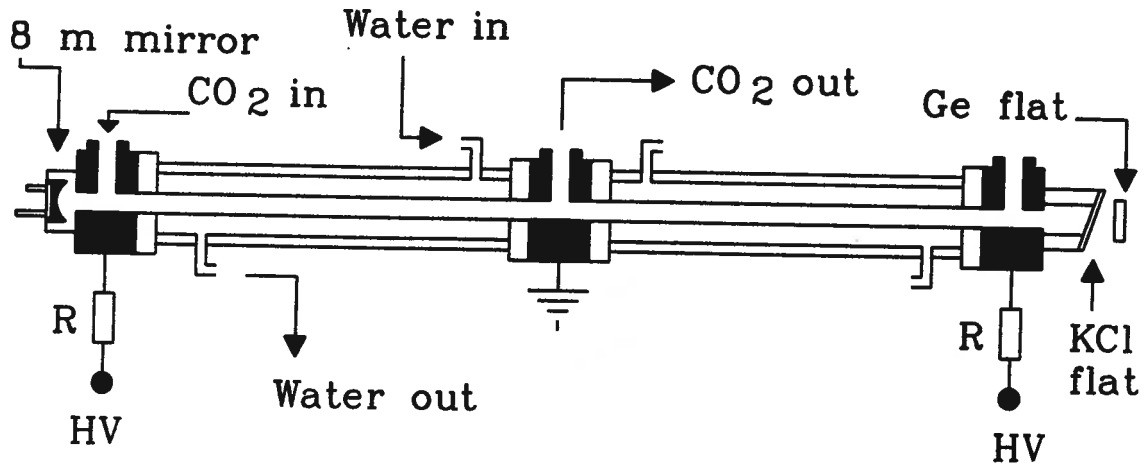

Figure 4.2: An illustration of the 40 W CW CO_2 laser. R = 0.4 MΩ and HV = 25 kV.

operate at high gas pressures in the range between 1 to 7 atmospheres and to be used as part of a more elaborate CO_2 laser system known as a "hybrid laser" arrangement. Most of the electrical, laser energy, and pulse duration measurements discussed in this section are performed with the discharge laser operating at 1 atmosphere with a lasing gas composition of (CO_2:N_2:He) and a mixture ratio of (15:15:70). The laser electrodes are made from aluminum plates with an electrode separation of 9.5 mm. The electrodes are designed to be flat over a 9.5×350 mm^2 area, with rounded corners similar to the design in reference [135]. The radius of curvature of these rounded corners is 6.3 mm. The gas glow discharge is observed to be uniform over the (9.5×9.5×350) mm^3 volume as indicated by photographing the discharge region.

The high pressure electrical discharge is automatically preionized using a double sided LC inversion circuit which is first described in reference [136]. This circuit is one of the most efficient ways to excite high pressure CO_2 gas discharge lasers [134]. Efficient operation of a high pressure gas discharge laser depends strongly on both the low inductance

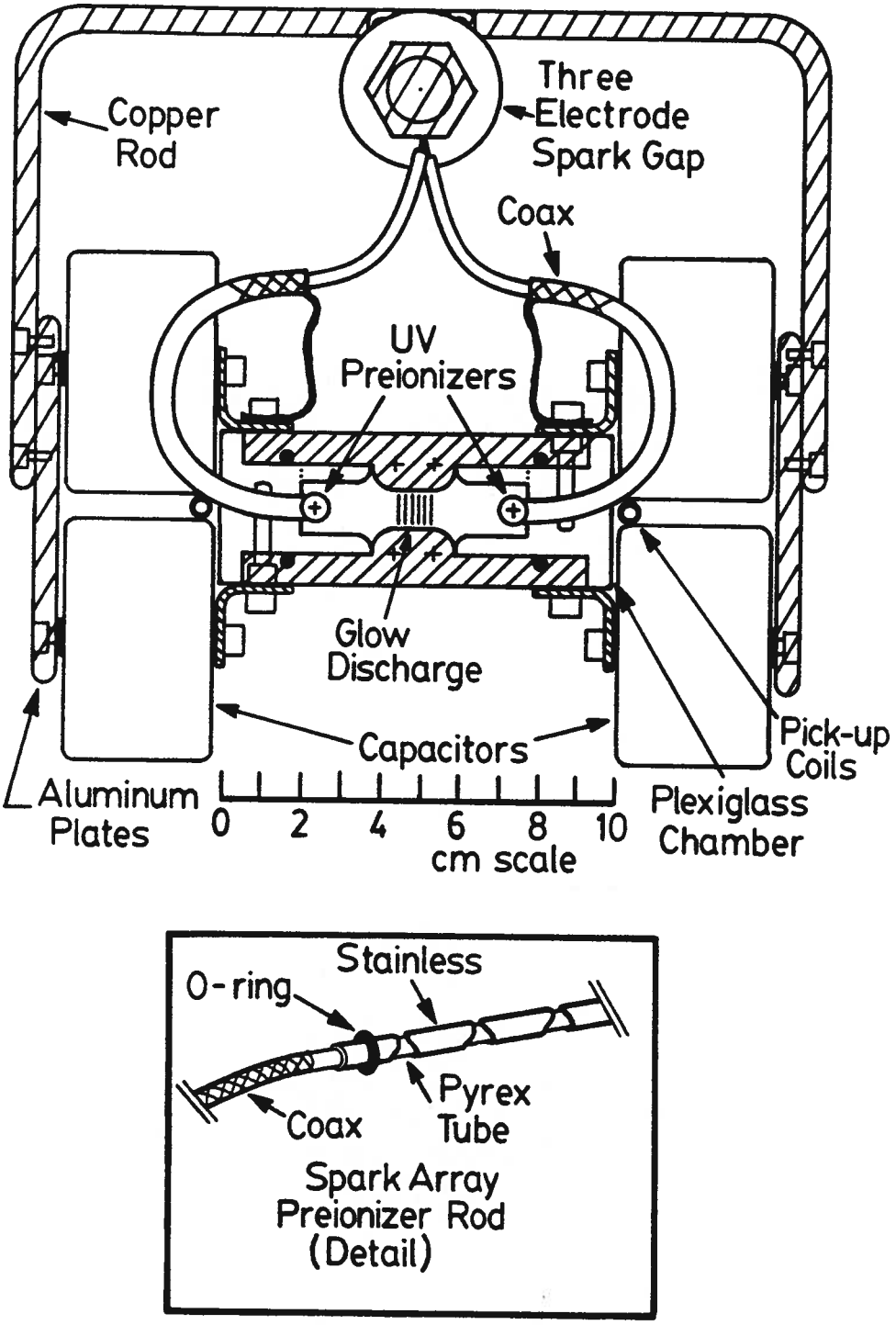

Figure 4.3: The TEA CO_2 laser using an automatically preionized, doublesided, LC inversion circuit. Electrical conductors (aluminum and copper) are shown shaded. The preionizer rod design is also shown below.

of the driving circuit and the density distribution of the initial electrons produced by the preionization process. The schematics of the circuit design is presented in figure 4.4. The principle operation of the LC inversion is as follows: the capacitors are charged in parallel and no voltage appears across the laser electrodes; then, when the spark gap switch is triggered and hence closed, the voltage across the top capacitor banks discharges through the preionizer rods [135],[137]–[140].

Due to the high inductance of the resistors and the preionizer rods, the current continues to flow and the top capacitor bank polarity reverses direction. The voltage across the laser electrode, at this time, becomes double the charging voltage of the capacitors. The laser gas breaks down as soon as the electrode voltage reaches the pressure-dependent breakdown voltage of the gas mixture.

The switching of the discharge is made possible by a low inductance spark gap which is pressurized with dry air to $\sim$ 50 Psi to withstand a charging voltage of $\sim$ 22 kV. The spark gap is triggered by a triggering pin connected through a krytron (EG&G) high voltage (10 kV) triggering unit through a 6:1 step-up transformer. Twenty-four discrete $BaTiO_3$ doorknob capacitors (Murata Corp. no. DHS60Z5V272Z-40, 2.7 nF, 40 kV ceramic capacitors) are mounted symmetrically, six in each quadrant, between both sides of the discharge chamber as shown in figure 4.3. This arrangement gives an ultralow inductance configuration. As shown in figure 4.3, the body of the laser is machined out of a single lucite block, with one additional plate of lucite (surrounding the upper electrode) glued into it using cyanoacrylate, "Krazy glue".

Preionization of the main discharge is provided by two arrays of U.V. sparks. Each preionizer rod is constructed as described in references [138, 139], with the centre conductor (a length of Belden no. 8868 high voltage wire) passing through the outer conductor of the 20 cm length of a home-made $\sim$ 50 Ω coaxial cable, and then all the way through the glass tubing to the last stainless steel preionizer electrode. The edges of the stainless

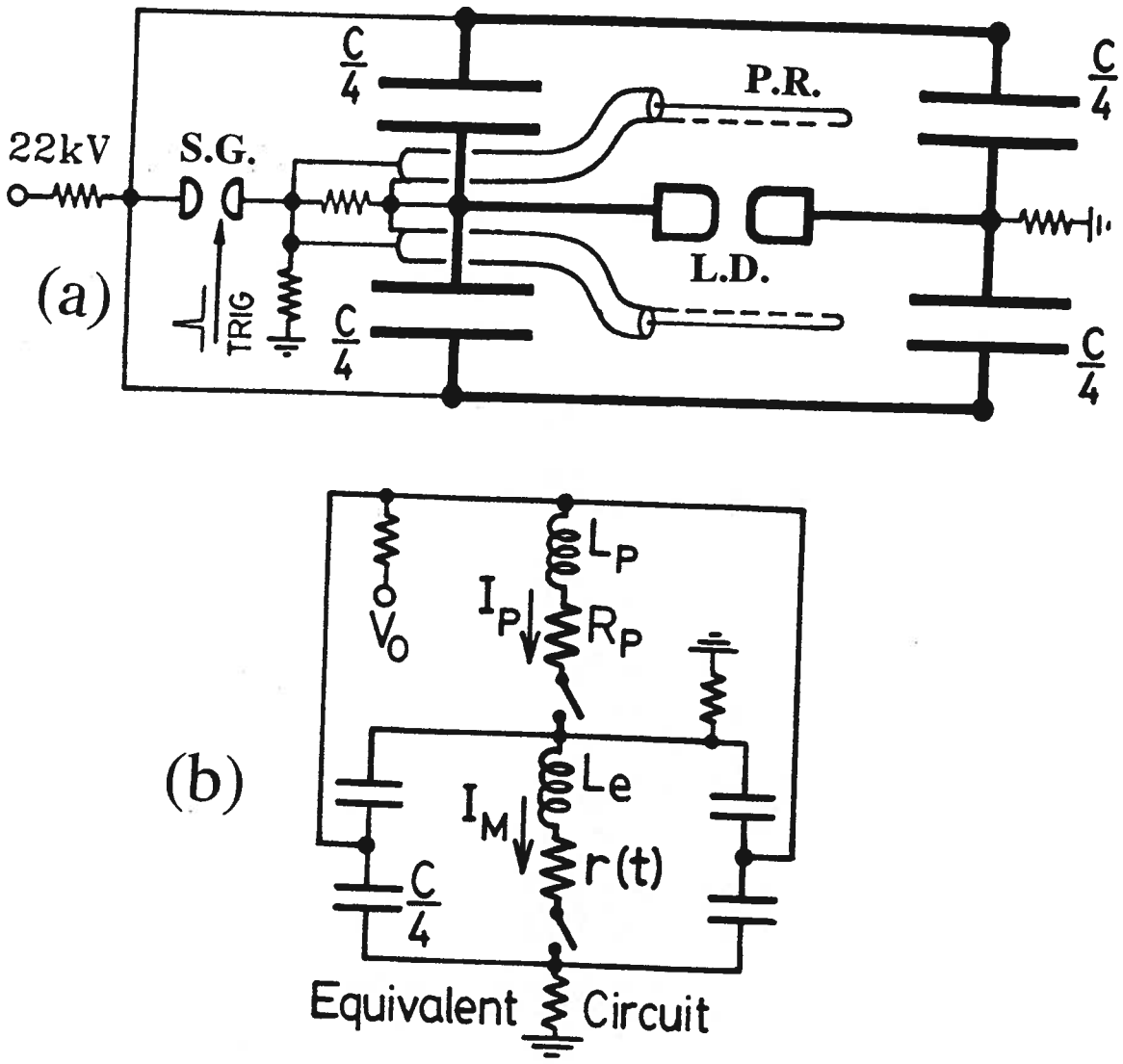

Figure 4.4: (a) The CO_2 laser LC inversion circuit and the preionizers connections. P.R.= preionization rod, S.G.= spark gap, and L.D.= laser discharge. (b) The equivalent circuit with $C = 64.8$ nF, $L_P = 420$ nH, $R_P = 1.05\ \Omega$, $C = 64.8$ nF, and $L_e = 6.8$ nH.

steel tubes are cut at 30° to the axis of the tube. A drop of cyanoacrylate glue is used at each end of the Belden wire to seal the wire against its insulation, and this glue is also used to seal the insulation against the first stainless steel preionizer electrode, as shown in figure 4.3. The end of the preionizer is sealed against the lucite laser chamber with an O-ring fitting. The other preionizer electrodes are attached to a 5 mm (outside diameter) pyrex tube using the same glue. We used 15 preionizer spark gaps of 400 μm each, at 2.5 cm interval along each preionizer rod. We found that the breakdown of the two preionizer rods is very reliable if the total length of U.V. sparks, 15×(400 μm), is less than the main electrode spacing of 9.5 mm. In order to minimize the electrical jitter to less than ±3 ns, we made use of the "capacitive coupling" to the return lead, so these sparks actually form sequentially [141]–[143], rather than all at once; the process requires about 20 ns [142, 143] to form a so-called "running spark" or "sliding spark", and it is only after all the sparks have formed that the inversion and preionizer current, I_p, starts to climb significantly [141]. The preionizer rods are mounted along the sides of the main discharge and parallel to the laser electrodes at distance of $\sim$ 14 mm, so that unwanted sparks between them are avoided and uniform preionization of the main discharge is obtained.

Electrical Current and Voltage Measurements of the Laser Discharge

The discharge current risetime is directly related to the rate of energy deposition. In this laser discharge, the electric current changes very quickly which induces a time-varying magnetic field. By taking advantage of this, very accurate transient current measurements can be performed. The current pulse is measured using twin, subnanosecond-risetime, 10-turn pick-up coils [144] installed between the capacitors, within the fast discharge main loop, on opposite sides of the chamber, as indicated in figure 4.3. The two coils therefore give equal and opposite signals which, when subtracted by a 1 GHz

oscilloscope (Tektronix 7104 with two 7A29 plug-in units), give the low-noise voltage signal V_C, proportional to the rate change of the main current,

$$V_C = A_M \frac{dI_M}{dt}, \tag{4.1}$$

where A_M is a constant. The current noise is substantially eliminated by "common-mode rejection." The two signal lines are first carefully adjusted to have identical delay times, to within ±50 ps. The delay is measured using an oscilloscope and a coaxial spark gap [137]–[139] cable discharge circuit [137]–[139], [145, 146]. The discharge circuit provides 1000 V electrical pulses having a risetime of 300 ps.

Measuring the discharge breakdown voltage gives an insight into the amount of electrical excitation energy that is being delivered during the laser operation. In measuring the transient discharge high voltage, it is convenient to use a high voltage divider. The voltage, V_M, on the main electrodes is measured using twin, resistor divider, high-voltage probes of $10^4\times$ attenuation (each consisting of 15 two-watt carbon resistors soldered together in series with a terminated 50 Ω cable), one for each electrode. The risetime of each probe is measured to be 10 ns. Again, the signals are subtracted by the 1 GHz oscilloscope, giving a low-noise signal representing the voltage, V_M, across the discharge; the noise, again, is thereby substantially eliminated by "common-mode rejection." The voltage, V_M, across the main electrodes is measured in this way, for an initial charging voltage of V_o = 22 kV, and is shown in figure 4.5(a). The main current, I_M, starts at t = 300 ns, with a jitter of < ±2 ns, relative to the primary/preionizer current, I_P. The current, I_P, starts with a jitter < ±3 ns, relative to the time of firing the spark gap.

As observed previously for CO_2 lasers [138, 139, 141],[147]–[149], the main current, I_M, essentially stops with a finite voltage of V_M = 13 kV remaining on the main electrodes. This occurs, presumably, since there is no longer enough voltage to maintain a discharge. However, since the spark gap (and preionizer) current, I_P, are still supplying a charge

to the main loop, we observe small current oscillations immediately following the large initial pulse, as shown in figure 4.5(b). This initial current pulse contains at least 90% of the energy of the entire current pulse, I_M. The current pulse FWHM is measured to be 40 ns, which is fairly close to the critically damped value of 25.6 ns, given by equations (5) and (16) in reference [134].

During these current oscillations following the large initial pulse, the voltage, V_L, induced in the measurement loop of area, A_L, is by Faraday's law,

$$V_L = \int_{A_L} \left(\frac{d\mathbf{B}}{dt}\right) .d\mathbf{s} \approx \left(\frac{\mu_o A}{2l}\right) \frac{dI_M}{dt}, \tag{4.2}$$

where A and l are the cross sectional area of the and the length of the current sheet, respectively. V_L has a ≤ 2 kV amplitude. Since dI_M/dt is 0 at certain times t_i (maxima and minima of I_M in figure 4.5(b)), one can compute the discharge resistance at these times from the following equation:

$$r(t_i) = \frac{V_M(t_i)}{I_M(t_i)} \tag{4.3}$$

which has strong oscillations also, and this function $r(t)$ is sketched in figure 4.5(a). The voltage which would have been on the electrodes during this time had the main discharge not occurred is shown by the dotted line, V_M', in figure 4.5(a). We measured this voltage signal by firing the laser with higher pressure in the chamber so that only the primary circuit fired without a main discharge. Since $V_M' = 36$ kV at the end of the strong current pulse, the charge which flowed in the main discharge up to that time is approximately

$$\triangle Q_c = C_e(36.0 - 13.0)kV = 370 \quad \mu\text{Coulomb}, \tag{4.4}$$

while the electrical energy delivered is approximately

$$\triangle E = \frac{1}{2} C_e(36.0^2 - 13.0^2)kV^2 = 9.1J, \tag{4.5}$$

corresponding to a deposition of 280 $Jl^{-1}atm^{-1}$.

The derivative signal of the equation for dI_M/dt, and also one for the preionizer (primary) loop, dI_P/dt, are each integrated to give the current pulse shapes. In order to calculate the inductance of the discharge, the main discharge loop area is measured to have an area of A = 38.4 $\pm$0.1 cm^2. A second integration is required for I_M to give the charge which flowed through the discharge and, when equated with the change in the capacitor charge given by equation 4.4, we are able to find the absolute current pulse, I_M, as shown in figure 4.5 (b). The preionizer/inversion current I_P, is also shown in figure 4.5(b) and is scaled by solving the differential equation for an underdamped oscillator [134], using the same algorithm as mentioned in reference [134], now with parameters C_P = 32.4 nF, L_P = 420 nH and R_P = 1.05 Ω which are the primary loop parameters found in the same way as described in reference [135] This algorithm also gave the energy E_P deposited into the preionizers in the first 300 ns preceding the main discharge, as E_P = 4.4 J.

Energy and Pulse Output of the TEA CO_2 Laser

The laser optical cavity consists of two KCl windows mounted on O-rings at Brewster's angle, a 5 m radius of curvature gold-coated full reflector, and a Ge flat, 80% reflector as an output coupler. The CO_2 laser pulse is measured using a Labimex P005 HgCdTe room-temperature detector and is shown in figure 4.6.

The shape of the infrared pulse from the free running electrically pumped CO_2 laser depends on several laser parameters, such as: the duration of the pumping electrical pulse, the energy delivered by the excitation circuit, the operating gas pressure, and the ratio of the composition gases. The output pulse duration of the above TEA CO_2 discharge laser is usually of the order of 400 ns. The overall temporal pulse shape consists of an initial spike (50 ns long) and a long decay tail ($\sim$ 0.5 μs long). The initial peak

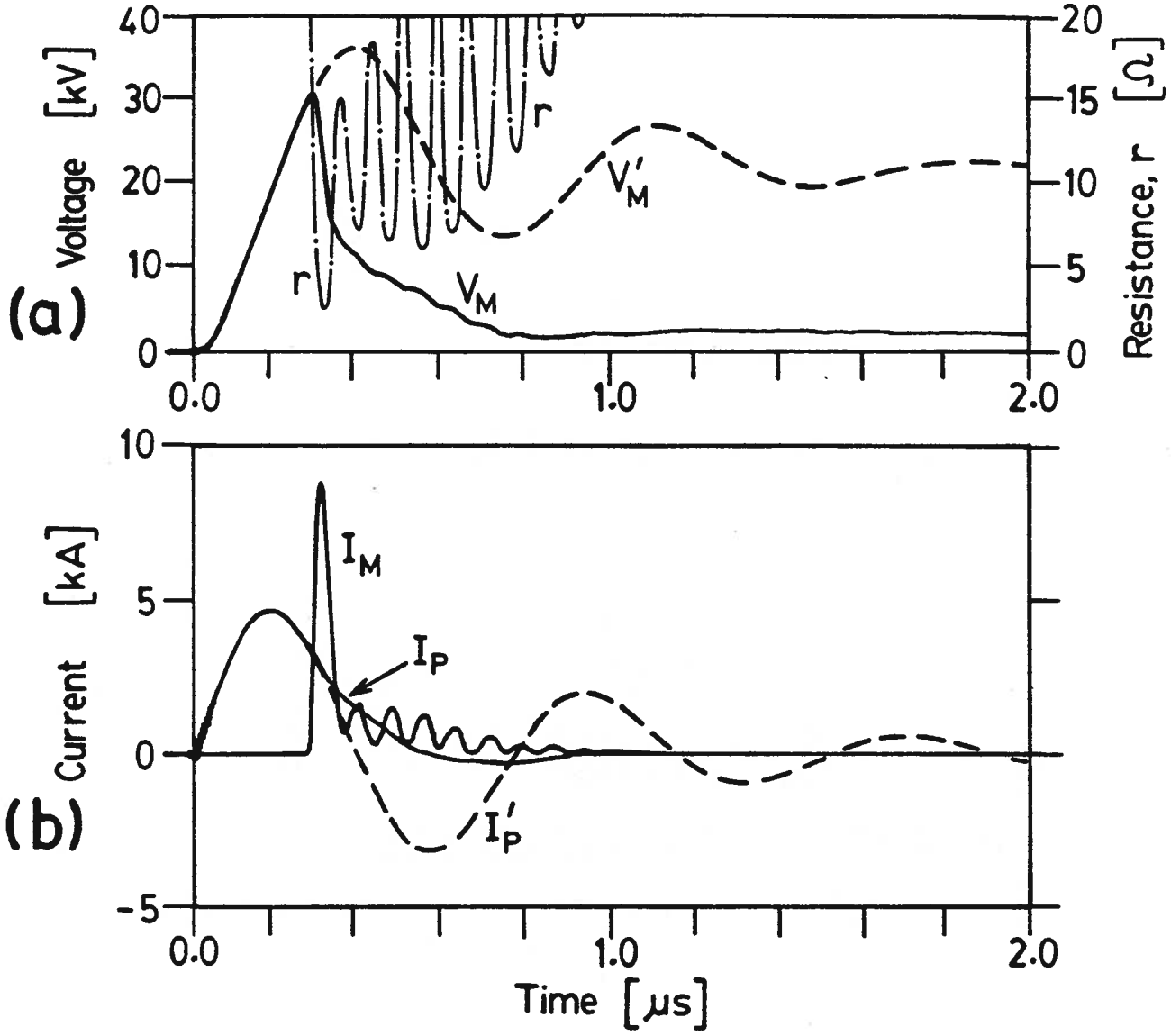

Figure 4.5: (a) Main electrode voltage without the glow discharge, V_M', and with the glow discharge, V_M. (b) Preionizer/inversion current without the glow discharge, I_P', and with the glow discharge, I_P; the main electrode current, I_M.

is known as the gain switched peak which is due to the short time required to build up enough gain compared to cavity round trip time. That is, the gain in the CO_2 laser can be turned on quickly by the pumping circuit so that population inversion above the threshold value is established before the onset of any noise build up of laser oscillations. The origin of the long tail is due to the gain recovery by collisional energy transfer from the vibrationally excited N_2 buffer molecules to the vibrational states of the CO_2 molecules. This long pulse is usually known as "the nitrogen tail." The output usually consists of a superposition of several competing longitudinal modes, as shown in figure 4.6(b).

The laser pulse energy is measured to be 800 mJ (multimode) using a GenTec energy meter (ED 200). The laser energy output is found to be stable to $\pm 2\%$. The specific output energy is 25 Jl^{-1}, which is among the highest values reported for TEA CO_2 lasers. The overall efficiency is 5.1%, and the pulse to pulse energy reliability is 100%. The output beam is uniform over the 9.5 mm $\times$ 9.5 mm area as indicated by Polaroid film burn spots. However, after about ten shots, one of the new intercavity salt windows exhibited severe damage due to the high-power laser pulse, which has not, to our knowledge, been reported previously for TEA CO_2 lasers of only 35 cm discharge length. Because of this damage problem, we are not able to make a detailed study of the laser output at higher pressures using the configuration described above. With weaker mixtures, in a hybrid laser configuration, operation should be possible up to about 7 atmospheres.

4.3.3 The Hybrid CO_2 Laser

For ultrashort pulse generation the switching task is made much easier if the CO_2 laser pulse incident on the optical semiconductor switch is made as long as possible with a maximum amount of energy. When the CO_2 laser pulse is > 50 ns, one may consider the temporal change of the pulse intensity to be insignificant during the switching time of

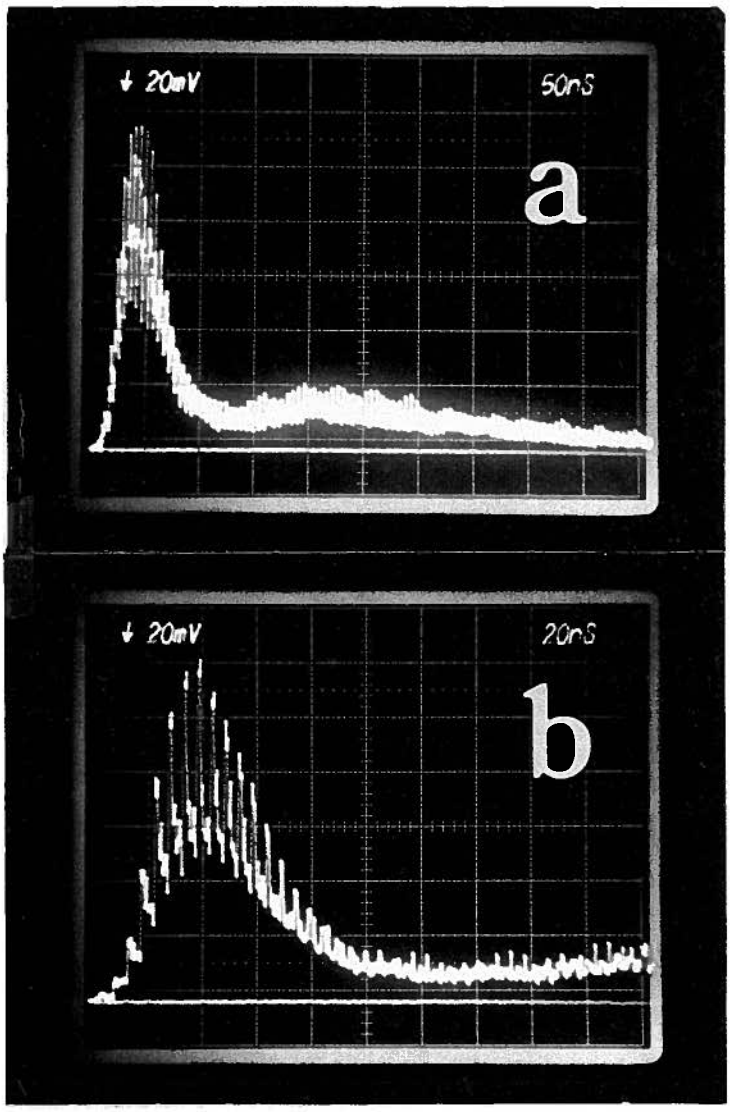

Figure 4.6: (a) The CO_2 laser pulse shape at 10.6 μm, with an energy of 800 mJ. (b) Longitudinal mode beating during the laser oscillation.

a few picoseconds or less. In addition, a long CO_2 laser pulse reduces the constraint on the accuracy of the timing and jitter between the control visible pulse and the CO_2 laser pulse. Clearly, with long CO_2 laser pulses, the experimental situation resembles that of CW CO_2 laser switching.

For our application, the temporal power modulation due to longitudinal mode beating of the above TEA CO_2 laser is highly undesirable and single mode operation is required. A combined arrangement of a single longitudinal mode CW CO_2 (narrow gain) laser, with a TEA CO_2 laser sharing the same resonator cavity, provides a single longitudinal and transverse mode with high power output of the order of 50 kW. This CO_2 laser arrangement is known as a "hybrid laser". A typical hybrid configuration is illustrated in figure 4.7. In this laser arrangement, only one section of the CW CO_2 laser delivering $\sim$ 6 W is used to lock the longitudinal mode of the TEA CO_2 laser. The cavity resonator is the same as the one used in the CW CO_2 laser with a total effective resonator cavity length of 2.9 m. The high pressure section is operated at 1 atmosphere with a lasing gas mixture of CO_2:N_2:He of 6:6:88 at a repetition rate between 1 to 2 Hz. The laser maximum output energy is measured to be $\sim$ 25 mJ.

The low-pressure CW laser section with a frequency bandwidth narrower than the longitudinal mode spacing of the optical resonator provides the initial 10.6 μm laser photons and laser gain at only one particular laser mode. Figure 4.8(a) shows the single mode pulse output from the CO_2 hybrid laser with the CW CO_2 laser turned on. The pulse shape differs from that of figure 4.6, which can be explained as follows: the CW laser gain is above the lasing threshold of the TEA CO_2 laser, thus the laser pulse does not evolve from noise as in the case of a free running TEA laser; this results in the optical pulse occurring at an earlier time than in the free running TEA laser. Moreover, the time required to build up enough gain needed for the gain switched pulse is dramatically reduced. Consequently, the output pulse shows a single mode pulse with a risetime of $\sim$

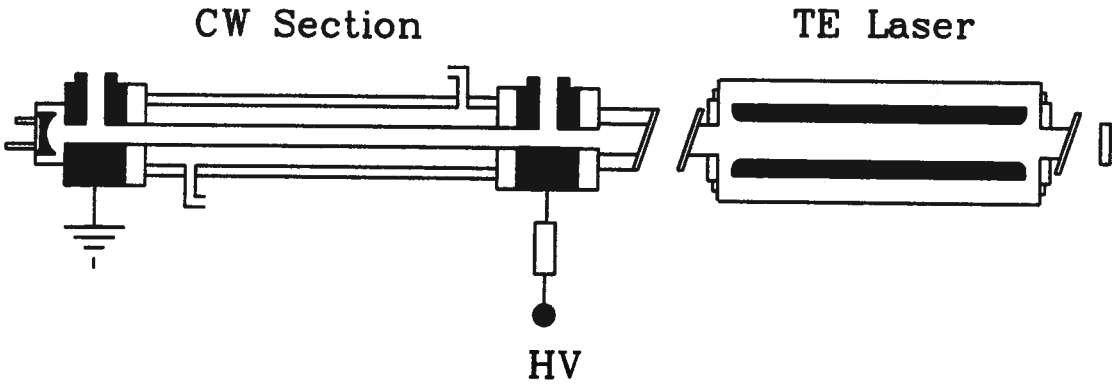

Figure 4.7: The hybrid CO_2 laser system arrangement.

220 ns and a long decay tail of $\sim$ 1.5 μs long. This temporal width of this pulse is ideal for performing optical semiconductor switching experiments.

4.4 Synchronization of the Hybrid CO_2 Laser and the Femtosecond Laser System

It is crucial that accurate synchronization be maintained between the hybrid CO_2 laser and the femtosecond pulses from the dye amplifier. This has proved to be an extremely difficult problem for the following reasons: the whole femtosecond laser system is internally synchronized with respect to the Nd:YAG mode locker's frequency of 41.0245 MHz. Moreover, the combined delay in the krytron circuit, spark gap, the LC inversion circuit, and the CO_2 laser gain build-up time amounts to $\sim$ 1.5 μs which is long compared to the mode locker's clock of 24 ns. That is, the CO_2 laser must be triggered about 1.5 μs before the laser amplifier output to allow for perfect pulse synchronization at the optical semiconductor switch. An electronic timing system that does not disturb the performance of

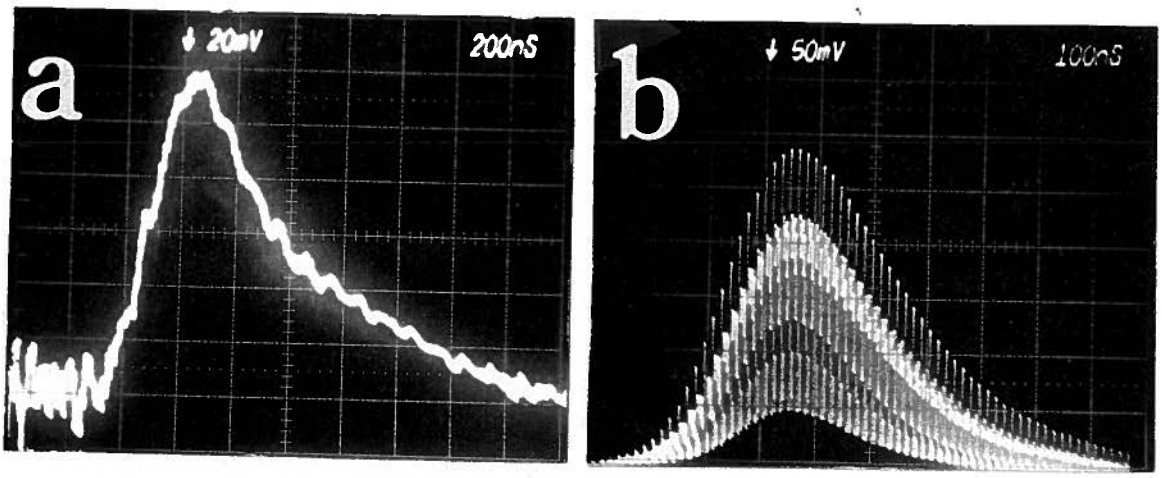

Figure 4.8: (a) Single longitudinal and transverse mode from the hybrid CO_2 laser. (b) Same hybrid laser with the CW laser turned off.

the femtosecond laser system is the most important priority in our design.

An adjustable electronic synchronization unit was designed and built through the UBC Physics Department Electronics Shop to perform the task. The details of the circuit design are presented in Appendix A. The unit has dual channel TTL output units which can be adjusted independently over the delay range between 0 to 3 μs relative to the Nd:YAG RGA60 output pulse. For proper operation of the timing unit, the commercial laser system triggering input was modified with no observable change in the system performance. The RF from the mode locker was diverted from its input to the Nd:YAG RGA60 amplifier unit, and was directed into the synchronization unit. The synchronization unit circuit locks on the 41.0245 MHz clock from the mode locker and triggers a TTL output signal. The 5 V-TTL signal is amplified to 30 V and is used to trigger the CO_2 laser krytron unit that triggers the laser discharge spark gap. After the onset of the channel delay ($\sim$ 1.1 μs) the timing unit triggers the RGA60 timing circuit to begin optical pulse injection. Figure 4.9 shows a layout of the lasers' timing

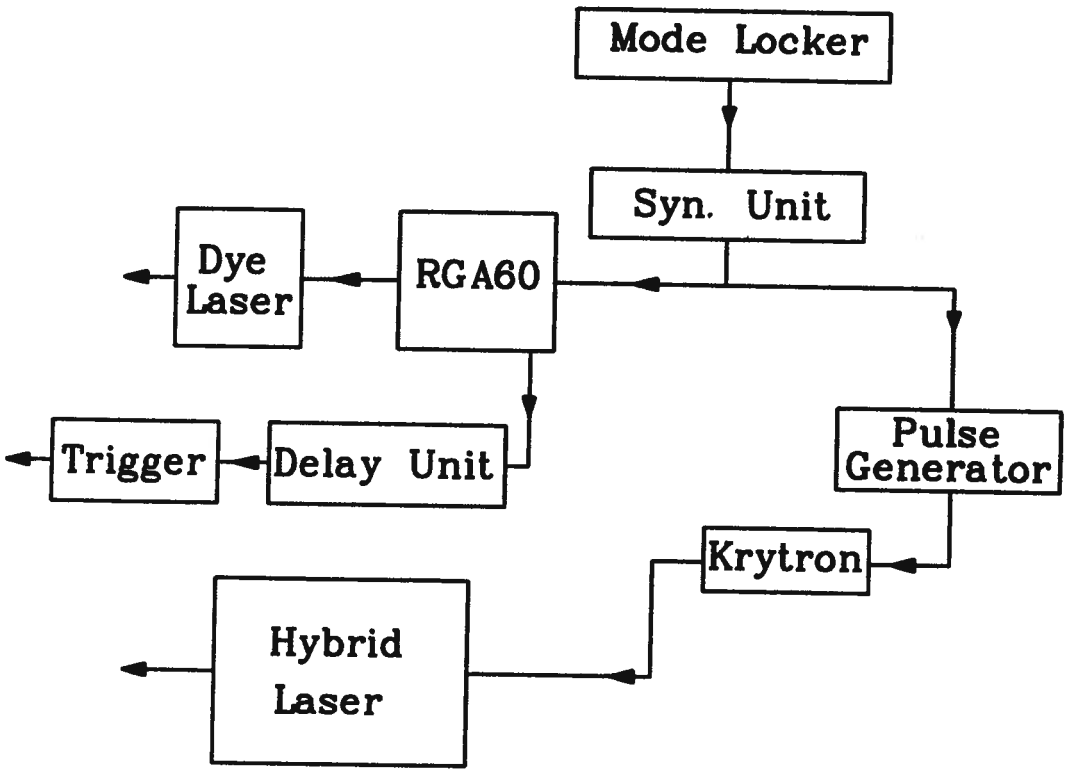

Figure 4.9: A layout of the synchronization between the hybrid CO_2 laser and the femtosecond laser pulse generating system.

arrangements. With this timing unit, the overall pulse jitter is ± 10 ns, which we believe originates from the krytron unit and the spark gap.

4.5 Infrared Pulse Detection and Timing System

4.5.1 The Cu:Ge Infrared Detector

The detection of ultrashort CO_2 laser pulses is quite difficult because conventional infrared detectors with time constants of $\sim$ 100 ps are too slow. Since the pulse width of the reflected infrared pulses is much less than the response time of an infrared detector, the output amplitude depends on the response time of the detector. In this case, the detector integrates the input optical pulse, thus acting as a very sensitive energy meter.

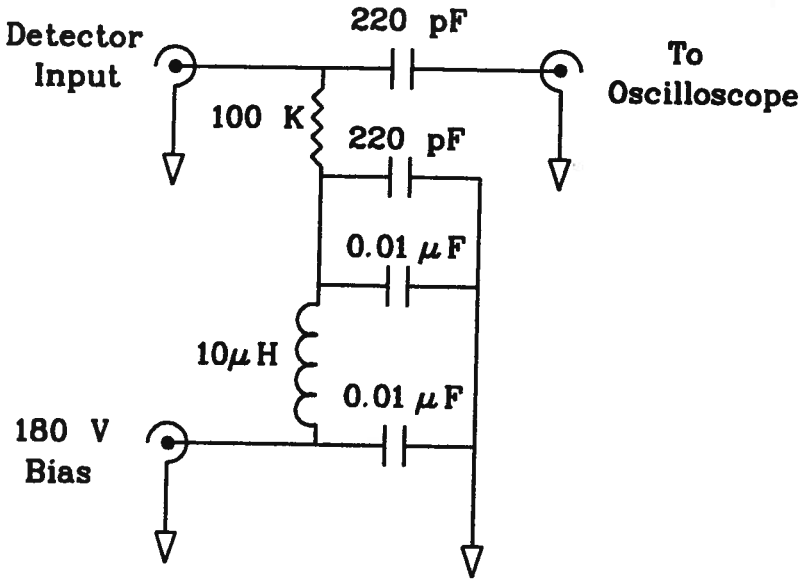

Figure 4.10: The Cu:Ge infrared detector bias/output circuit.

A Cu:Ge infrared detector (Santa Barbara Research Center) is utilized to detect the infrared reflected pulses. The detector has a spectral response over the range between 2 μm to 30 μm with a risetime of $\sim$ 0.5 ns. In preparation for the experimental measurements, the detector's dewar is pumped to $\sim 10^{-5}$ torr, then filled with liquid nitrogen and left to cool for about 1 hour. After that, the liquid nitrogen is disposed and the dewar is filled with liquid helium to cool it to 4.2 K°. When in use, the detector is biased at 160 V with the circuit arrangement displayed in figure 4.10. The detector can be operated for a period of six hours on a single liquid helium fill.

4.5.2 Electronic Amplifier

When conducting experiments with the CW CO_2 laser, at detector output signals of the order of 1 mV, the detector's signals cannot be measured by the oscilloscope, thus, the signals are electronically amplified in a GHz amplifier connected directly on top of the Cu:Ge infrared detector. The amplifier is impedance matched to the 50 Ω output

impedance of the infrared detector. The electronic amplifier was designed and built through the UBC Physics Department Electronics Shop. A complete electronic circuit is presented in appendix B. The amplifier gain is measured to be 34 dB with a noise level of –88 dB. The amplifier shows excellent range of linearity with no pulse distortion. The amplifier is shielded in an RF Faraday cage to minimize the RF noise from the lasers.

4.5.3 Experimental Data Collection System

The experimental data of the reflected infrared and the visible excitation pulses are displayed on a Tektronix 7104 oscilloscope with a 50 Ω plug-in (7A19) unit. The effective bandwidth of this oscilloscope is 1 GHz. Initially, we performed some of the experiments by measuring the reflected signals directly from the oscilloscope traces. Both infrared and visible signals are recorded simultaneously using a video camera for each laser shot. This technique proved to be inexpensive (compared to using Polaroid film) and allows real-time analyses of the data; however, it is very time consuming since all the analysis is done manually. Therefore, we have developed a computer controlled electronic data collection system to perform this task.

In the time resolved measurements, we are interested in the amplitude of the reflected pulses (or energy) as a function of the time delay. Thus, the maximum amplitude level of an integrated infrared pulse is proportional to the energy contained in the pulse itself. It is evident that the electronic system must have certain characteristics, such as: (1) the ability to perform the integration process on a time scale of $\sim$ 1 ns with a linear integration curve independent of the duration of the pulse; (2) it can be synchronized with the commercial femtosecond laser system; (3) it must be compatible with the Cu:Ge detector/amplifier arrangement; (4) it must have a low signal to noise ratio with a maximum input signal sensitivity of $\sim$ 20 mV in 50 Ω; (5) it should allow a real-time oscilloscope

observation if desired. Clearly, our experimental constraints cannot be met by inexpensive commercial sample-hold electronic systems, and a custom-made design had to be developed. A pulse integration module (PIM), which satisfies the above properties, was designed and built through the UBC Physics Department Electronics Shop. Complete electronic circuit designs are presented in appendix C.

The PIM channels are triggered from the "Sync-out" signal from the output of the Nd:YAG regenerative amplifier which arrives 30 ns earlier than the output of the 70 ps 0.532 μm optical pulse. The electronic data capture system consists of dual channel integration modules, one for the infrared pulse and the other for the excitation pulse. Each integration channel has an integration window of $\sim$ 5 ns in width; therefore, the signals are timed very accurately to within 250 ps using a built-in variable delay circuit, so that the pulses fall inside their respective integration window. The signal synchronization can be performed by monitoring the signal and the integration window, through the analog output of the device, on the oscilloscope while varying the delays. Both signals are captured and integrated simultaneously. The device was tested for proper bandwidth and linearity before its use in the experiments. Figure 4.11 shows the linearity from both channels using simulated 1 ns input pulses. The linearity of the device is $\sim \pm 8\%$, which is sufficient for our experimental purposes.

The integral values from the infrared pulse and its corresponding visible excitation pulse are digitized and stored directly on a personal computer for further analysis. The attractive features of this device make it an indispensable laboratory instrument for pulse-probe type experiments.

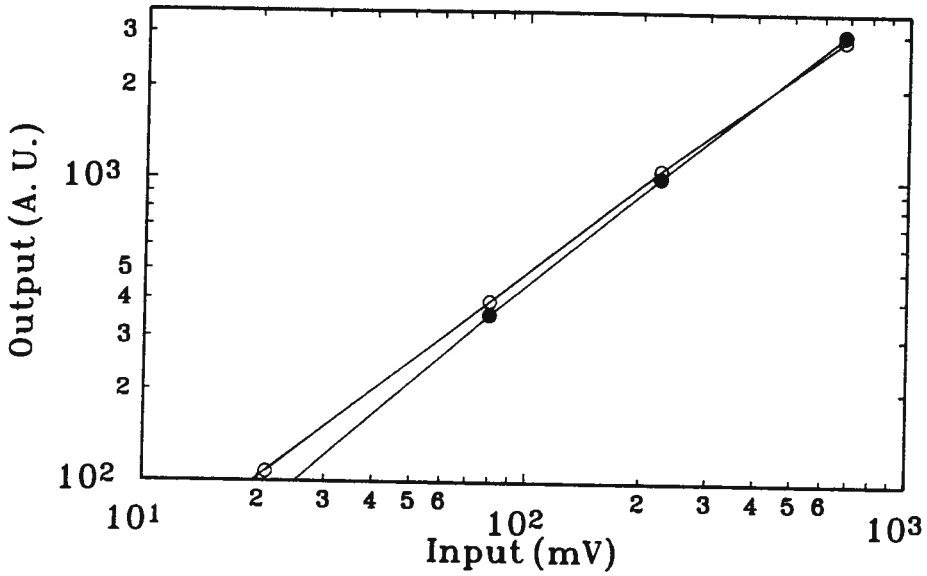

Figure 4.11: Integrated output from the dual channel pulse integration module as a function of the input pulse voltage amplitude. The solid circles denote channel 1 and the empty circles denote channel 2.

4.6 Hall Conductivity Measurements in Si

The Van der Pauw method [150, 151] is used to measure the conductivity, minority carrier concentration, and the type of the carriers in several Si wafers. The measurements are performed in a high magnetic field of 0.4 T produced by a 3.8 A power supply.

4.7 Autocorrelation Pulse Width Measurements

In this experiment, we are working with ultrashort excitation pulses; therefore, the characterization and the ability to control the duration of the control excitation pulses from the dye laser (amplifier) are extremely important. The duration of the excitation pulse determines the temporal response of the optical semiconductor switch. The pulse duration of the laser system is very sensitive to the daily alignment and the operating conditions of the Nd:YAG laser; therefore, pulse width measurements must be performed

before the start of any experiment. The manufacturer's specification on the dye laser pulse is $\leq$ 500 fs. However, since we replaced several components in the laser system: laser mode locker and laser cavity in the Nd:YAG laser, and the optical fiber in the pulse compressor stage, the optimum parameters, including the pulse width, of the laser system must be finely tuned.

When working with ultrafast optical pulses of a few picoseconds or less, there is no convenient direct method of observing the duration of the laser pulses with conventional photodetector/oscilloscope having an adequate bandwidth. The correlation techniques [152]–[160] using nonlinear optical processes in suitable crystals are the most popular and cost effective experimental methods to measure femtosecond pulse durations. We have constructed an autocorrelator based on a non-collinear beam Michelson type interferometer which permits the performance of background free pulse width autocorrelation measurements. The layout of the autocorrelator is illusrated in figure 4.12. The 82 MHz pulse train from the dye laser is equally split by a beam splitter; half of the pulse train is incident on M_4 and M_5. A linear time delay, τ, is repetitively produced in one arm of the Michelson interferometer. This time delay is achieved by using a pair of parallel mirrors (M_4 and M_5) mounted on a plate which is rotating at a constant frequency, f_r. When the shaft is rotated by an angle, θ_r, this beam traverses a different path and is reflected back by M_2 parallel to the its original direction. The second half is reflected by the retroreflector mirrors (M_6 and M_7) and is slightly displaced. The two pulses can be overlapped in time at the KDP second harmonic crystal (SH) by mechanically changing one of the optical path lengths by a small amount (a 400 fs pulse duration is only 130 μm long).

The parallel mirror assembly [152] leads to an increase (or decrease) of the optical path length for the optical pulse. Thus the transmitted pulse train is delayed (or advanced) about a reference position (zero delay). With a small angle approximation, the time

delay varies linearly with the angle rotation. The two pulses are focused by a 3 cm focal length plano-convex lens on a KDP, SH generating crystal. The maximum U.V. output is obtained when the two pulses are coincident in time, and the SH decreases as one pulse is delayed with respect to the other. This technique measures the second order autocorrelation function of an intensity pulse, $I_p(t)$, which is given by the following expression

$$G^2(\tau) = \frac{< I_p(t) I_p(t+\tau) >}{< I_p^2(t) >} \tag{4.6}$$

were $< >$ indicates the average over a sufficiently long interval of time. The true pulse shape is shown to be a double exponential and is related to the autocorrelation signal width by [160]

$$\triangle\tau = 2.421 \triangle\tau_p, \tag{4.7}$$

where $\triangle\tau$, and $\triangle\tau_p$ are the FWHM pulse widths of $G^2(\tau)$ and $I_p(t)$, respectively. The details of the design of the autocorrelator and the optical components are presented in Appendix D. The autocorrelator is found to have excellent stability and pulse reproducibility. Its characteristics are comparable with the commercially available autocorrelators. The autocorrelator can be modified so that it can be used to measure both the dye laser pulse train at 82 MHz and the amplified dye laser output pulses at 10 Hz.

The femtosecond dye laser system is optimized to produce the shortest pulses possible. Figure 4.13 shows a typical autocorrelation trace from the dye laser pulses before amplification. Assuming a double exponential pulse shape [160], the shortest pulse width obtained from our dye laser system is 370 fs at 616 nm. Detuning the dye laser cavity length by less than 1 μm results in various pulse durations. In the case of the dye resonator cavity being longer than the optimum length, the resulting pulse is wide. On the other hand, when the dye resonator cavity is tuned to be shorter than its optimum length, a double-pulse shape results. These pulses are shown in figure 4.13 (b,c). Clearly,

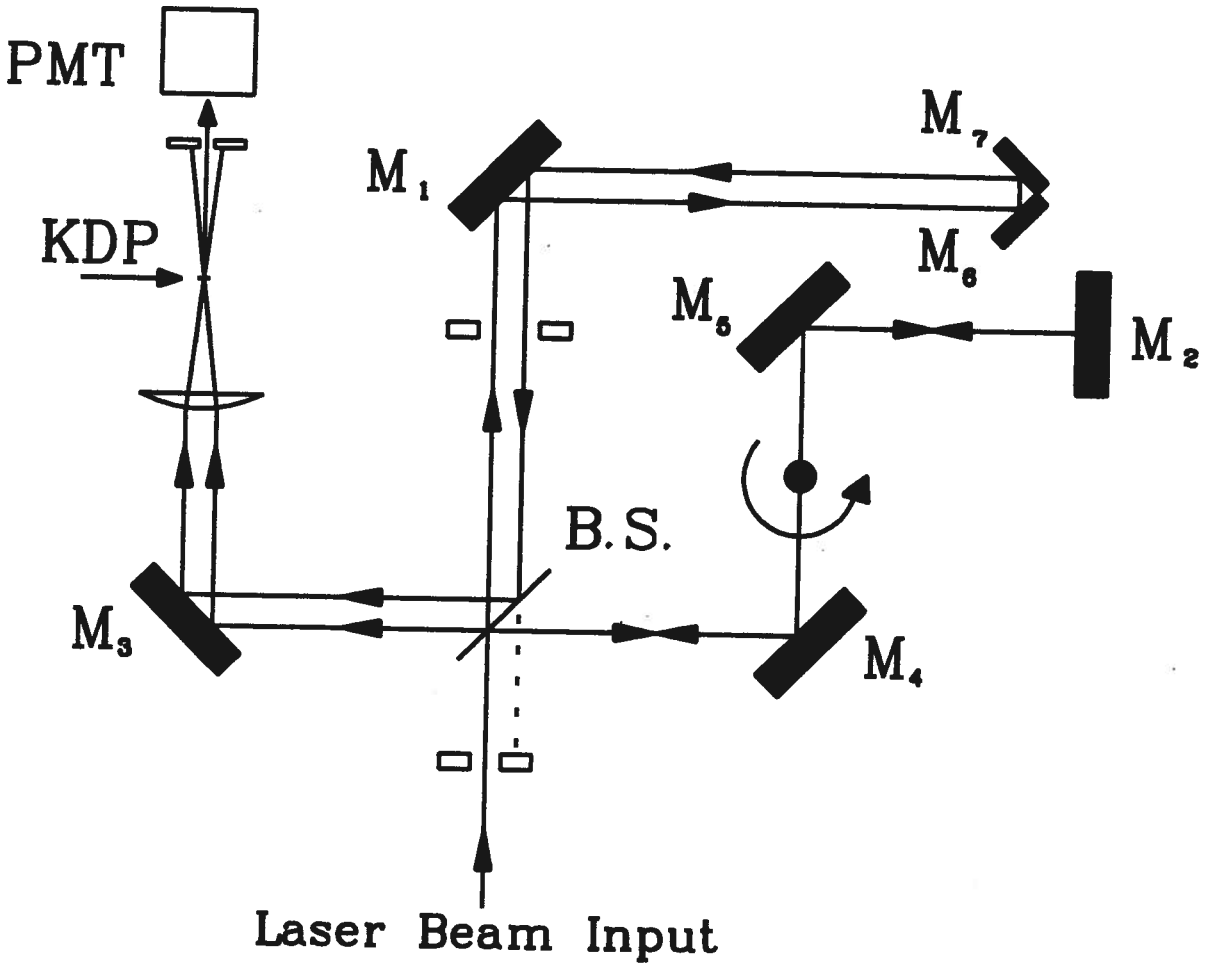

Figure 4.12: The autocorrelator. B.S.= beam splitter, PMT= photomultiplier, and KDP= second harmonic generation crystal (Potassium Dihydrogen Phosphate).

the pulse duration is very sensitive to the optical alignment and cavity detuning length of the dye laser; therefore, the duration of the dye pulse is always monitored during the experiments and before injecting the laser pulse into the dye amplifier.

The autocorrelation method described above is a scanning quasi-CW technique, which looks at signals that are repeating every 12 ns (82 MHz). What is observed on the oscilloscope is a sample average over thousands of pulses. However, the situation is more complicated when dealing with laser pulses with a low repetition rate such as the ones from the dye amplifier. One can interchange the role of the arms of the Michelson interferometer, so that the rotating arm of the interferometer is used as a reference arm and the reference arm is used as a scanning one. Measurement of the amplified pulse duration is done manually by fixing the rotating mirrors at a certain position and scanning the delay of the retroreflecing mirrors (M_7 and M_6). This interferometer arm is moved through the overlap region, thus obtaining a slow scan of the autocorrelation signal. The autocorrelation trace is recorded as a function of the relative time delay. We have performed several experiments to measure the duration of the amplified pulse as a function of the input dye laser pulse; figure 4.14 shows a measured amplified dye pulse duration of 490 fs (assuming double exponential pulse shape). Each point in the graph is averaged over 15 shots and the standard error is indicated. This pulse is obtained by injecting the dye amplifier with a 370 fs pulse for the dye laser system. The increase in the duration of the pulse width is a result of group velocity dispersion in the dye amplifier dye-cells and the optical components. With proper pulse compression techniques, it is possible to restore the pulse duration to its original width. Our results indicate that the limiting factor in the dye amplifier output pulse duration is the duration of the injected dye laser pulse. It is evident that by injecting the amplifier with a pulse similar to the one in figure 4.13 (b), this results in an amplified pulse of almost the same shape as shown in figure 4.14 (b), thus care must be taken during the experiment to avoid obtaining such

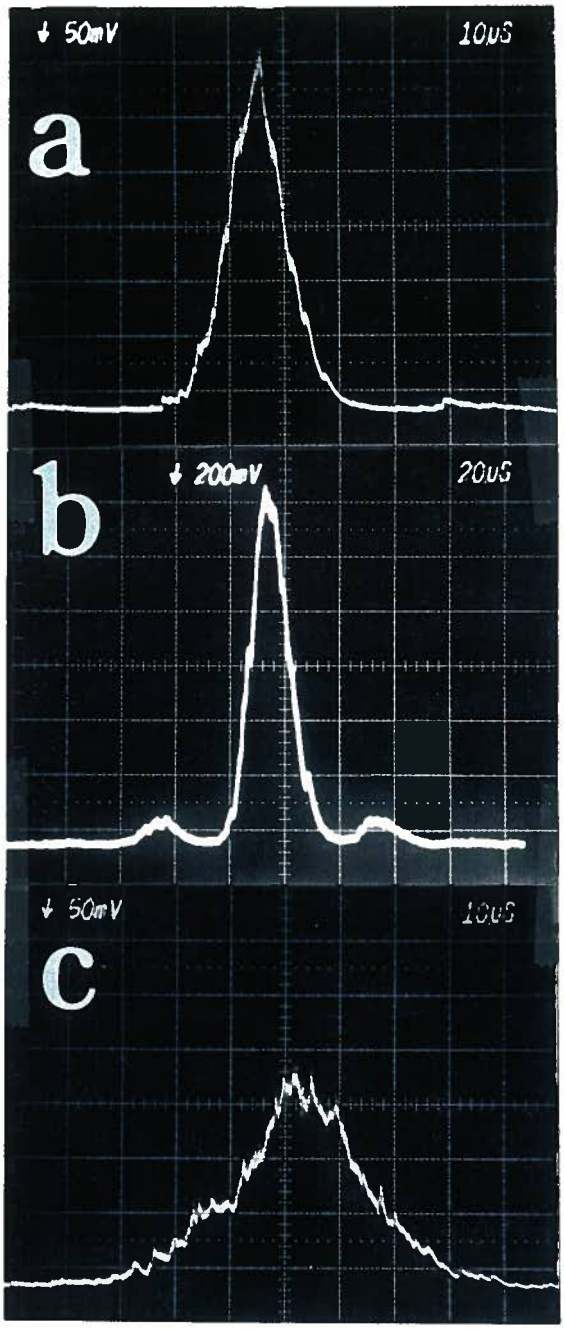

Figure 4.13: Typical autocorrelation traces from the dye laser system. (a) Cavity length is optimum resulting in a pulse width = 370 fs. (b) Cavity length is too short resulting in a pulse width = 500 fs; note the side peaks in the autocorrelation trace. (c) Cavity length is too long resulting in a pulse width = 830 fs. The time scale in (a) and (c) is 10 μs/div, whereas in (b) it is 20 μs/div.

pulse shapes.

4.8 Optical Semiconductor Switch Setup

The experimental layout for the optical switch is illustrated in figure 4.15. The single crystal semiconductor samples used in experiments are undoped GaAs (Crystal Specialties, Intl.) with a resistivity of $\sim 10^8\ \Omega$ cm. The GaAs samples are cleaved to 2×1.5 cm^2 from a 2.54 cm (diameter) wafer, as shown in figure 4.15. The sample thickness is 450 μm, polished on both surfaces, and it is mounted on a rotary-xy translation stage.

The infrared beam is focused by a 20 cm focal length KCl lens to an elliptical spot of an area 1.2 mm^2 on the GaAs wafer. The semiconductor wafer is set at Brewster's angle of 72° to obtain a high contrast ratio relative to background infrared reflection. This is necessary to detect small changes in the transient reflectivity. The accurate setting of Brewster's angle is achieved by rotating the GaAs crystal until a minimum reflection is obtained from the front surface. Due to the finite divergence of the infrared beam in the focal region and due to the thickness of the wafer, it is not possible to obtain zero reflection from both surfaces simultaneously. Therefore, the wafer is adjusted for zero reflection with respect to the wafer's front surface only. A high contrast signal to background ratio of 10^4:1 ratio is obtained during the experiment.

The visible excitation pulse is split into two identical pulses by a 50:50 beam splitter (as shown in figure 4.16). One pulse is directed towards the GaAs reflection switch, and the second pulse is passed through a variable delay line (which is used for pulse width measurements). The accuracy of the temporal delay is $\pm$40 fs. Sharply focusing the high energy visible pulse on the switch is undesirable. If the excitation pulse spot size is smaller than the CO_2 beam spot size, then this results in the reflection of only a small portion of the infrared beam. Thus, infrared pulses of low energy and high divergence

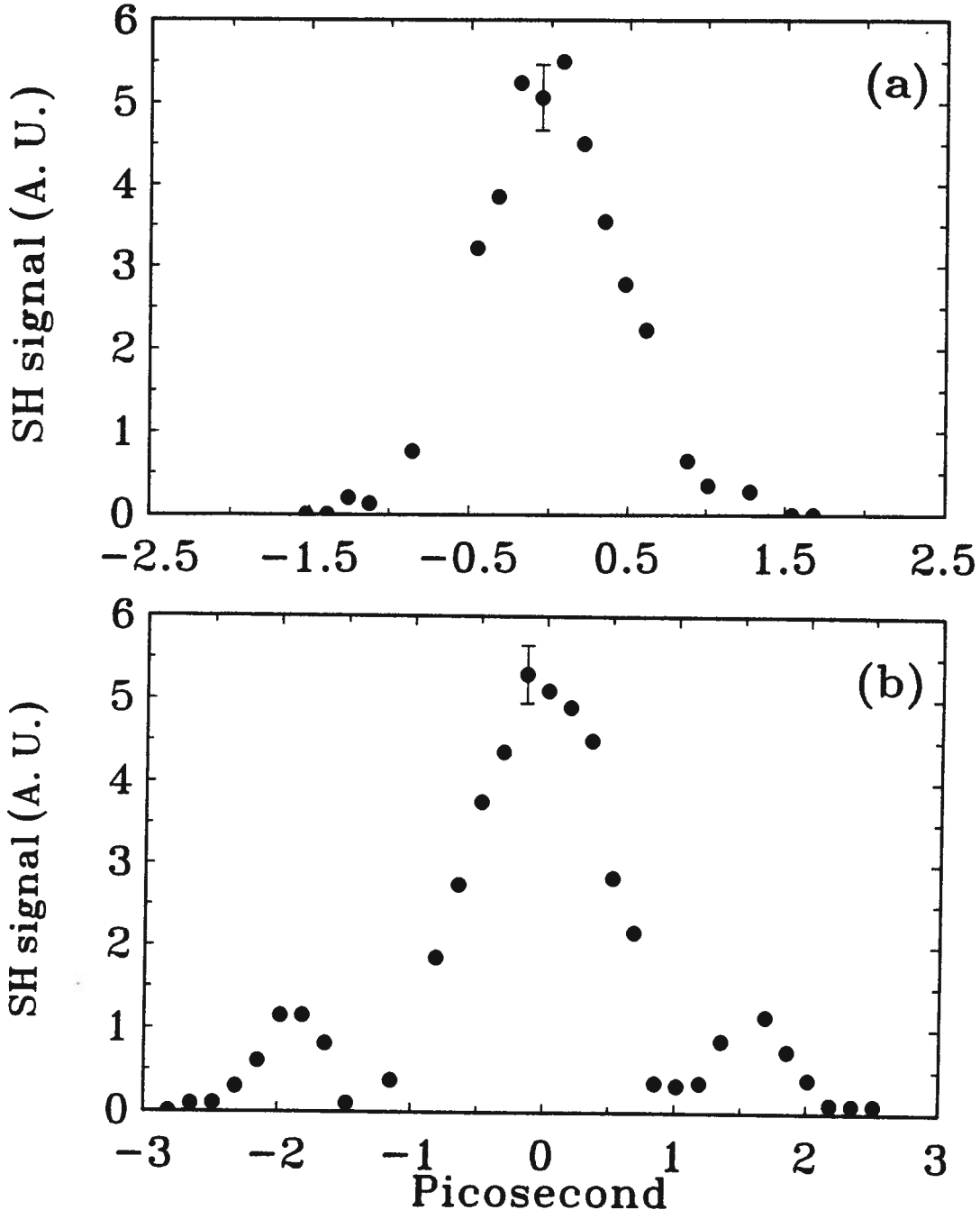

Figure 4.14: (a) Autocorrelation signal of an amplified, 1 mJ, 616 nm dye pulse showing a pulse duration of 490 fs. (b) Same conditions but with the injected pulse from figure 4.13(b).

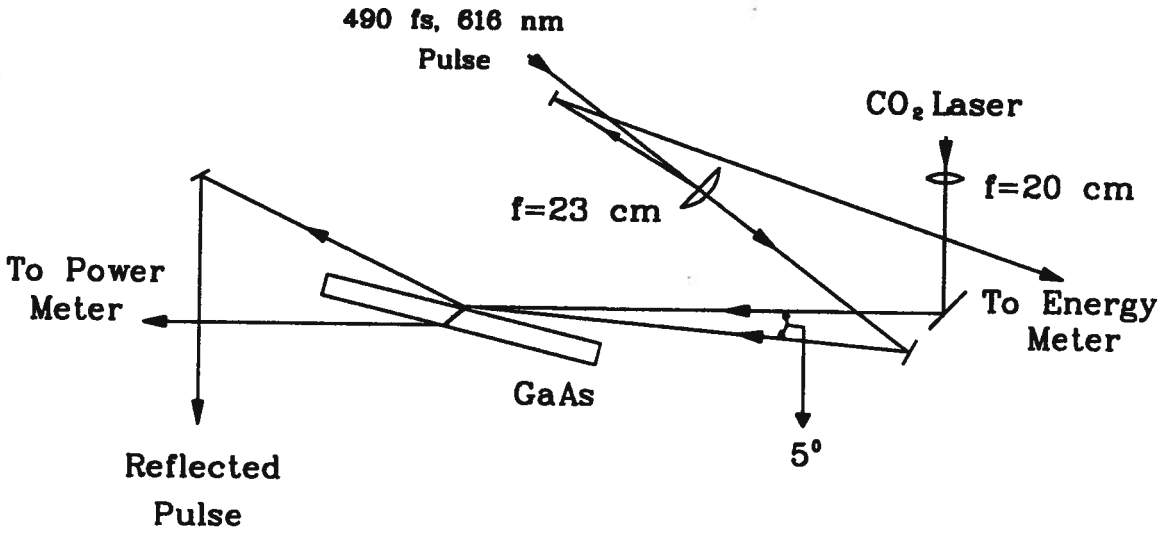

Figure 4.15: The experimental arrangement for a GaAs optical semiconductor switch.

are produced. In order to ensure good reflected beam quality, the visible excitation pulse is reduced to a spot size of ~ 3 mm^2 in area and is superimposed on the infrared laser spot. The angular spread between the infrared beam and the visible pulse is kept to a minimum angle of $\sim 5°$ so that the reflected infrared pulses do not suffer from wave front distortion as the control pulse wave front sweeps across the switch. Approximately 2% of the excitation pulse is picked up from the surface reflection from the focusing lens and is used to monitor the visible pulse excitation energy. The detection is performed with a fast photodiode (Hamamatsu-R1193U.03) having a risetime of ≤ 500 ps.

4.9 Time Integrated Infrared Reflectivity Setup

In order to reach low excitation levels, the intensity of the visible control pulse is gradually reduced by passing it through a sequence of variable stacks of calibrated neutral density filters (Kodak Wratten Gelatin). The linearity of the calibration is checked with a stable

HeNe laser, and the calibration factors are found to be about $\pm 5\%$ from their nominal values. A new calibration curve is deduced and used throughout our experimental work. In this experiment, the natural shot-to-shot fluctuations in the amplified visible laser pulse allow us to access a continuous range of excitation energies which provides an overlap range between the different neutral density filters. During the course of the experiments, great care is taken to ensure that placing the neutral density filters in front of the visible excitation pulse does not disturb the alignment of the infrared and the visible laser spots. The duration of the 370 fs dye oscillator laser pulse is measured after passing through the filters with no change in its duration.

4.10 10.6 μm Pulse Width Measurement Techniques

Measurement of the reflected infrared 10.6 μm laser pulse durations cannot be performed directly with photodiodes. The fastest photodiode operating at 10.6 μm has a risetime of $\sim$ 100 ps with a fall time of $\sim$ 1 ns. Clearly this is not sufficient to resolve the subpicosecond reflected pulses. We are interested in measuring the temporal shape of the reflected infrared pulses with an expected pulse duration of $\leq$ 50 ps; but since the peak power of the reflected pulse is low, it is impossible to use conventional second harmonic autocorrelation techniques or conventional measurements through frequency upconversion mixing with the control visible pulse. Moreover, the low repetition rate of the pulses creates an additional difficulty.

It is evident that the measurement of the pulse duration has to be performed by some indirect manner. Indirect methods using nonconventional correlation techniques can overcome the limitations imposed by the measuring system. In the following section we briefly review the principles underlying two independent schemes for measuring the reflected pulse durations: reflection-reflection correlation and cross-correlation. The

principle of these methods is to transform the temporal pulse duration information into spatial information which is clearly easier to analyse. These correlation techniques are capable of determining the infrared pulse duration with subpicosecond time resolution and can be applied to other ultrashort infrared laser pulses at different wavelengths. Since the duration of the visible excitation pulse is well-characterized (490 fs), in both correlation techniques, one uses the visible excitation optical pulse (control pulse) as a measuring scale to determine the infrared pulse duration.

4.10.1 Reflection-Reflection Correlation Procedure and Optical Setup

The reflection-reflection correlation infrared pulse measuring method is similar to the autocorrelation technique in the sense that the reflected infrared pulse is convoluted with an identical copy of itself as a function of time. In this type of experiment, we require the use of a second identical GaAs infrared reflection switch which is optically-triggered synchronously with the first GaAs reflection switch. Due to the nature of the reflection-reflection correlation technique, certain assumptions have to be made about the pulse shape. The reflection-reflection correlation measurements can produce ambiguous signals, and any sharp temporal features associated with the pulse are washed out through the correlation process. However, this type of experiment is necessary to obtain an estimate of the overall pulse width.

The measured reflection-reflection correlation signal, $A(\tau)$, is proportional to:

$$A(\tau) \propto \int_0^\infty I(t)I(t+\tau)dt \tag{4.8}$$

where, $I(t)$, is the infrared reflection pulse produced by the first switch, and $I(t+\tau)$ is the reflection from the second optical semiconductor switch at a delay time, τ. The second GaAs switch reflectivity is delayed by time τ relative to the first GaAs switch. The delay time, τ, must be long enough to encompass the infrared pulse width from the

first GaAs switch. The product signal is largest when the two peaks of the infrared pulse and the control pulses of the second switch overlap at the second switch (τ=0). The product signal is smallest when those two signals are separated by τ which is longer than the infrared pulse width. Concentrating initially on the expression for $A(\tau)$ in equation 4.8, it is clear that $I(t)$ cannot be recovered from equation 4.8 without some additional information. The shape of $A(\tau)$ is always symmetrical about τ=0, even if the initial pulse is asymmetrical.

The schematics of the whole experimental measuring system is in figure 4.16(a). Both reflection switches are taken from the same semiconductor wafer. Here, a second GaAs reflection switch is set at Brewster's angle with respect to the reflected infrared pulse from the first GaAs switch. Since reflection-reflection correlation type experiments are sensitive to the alignment of both switches and the background infrared reflection, the angle setting is accurately adjusted for the first GaAs switch, then the semiconductor is removed and a small mirror (gold-coated Si wafer of the same thickness as the GaAs wafer) is mounted in its place. The full CO_2 laser beam is reflected and is used to align the second semiconductor switch exactly at Brewster's angle. The experimental conditions on both GaAs switches are made to be almost identical.

The infrared pulse is focused on the second GaAs switch with a 15 cm focal length KCl lens, and its visible excitation pulse is delayed and focused to an approximately identical spot size to that of the first GaAs switch. However, the angle between the infrared pulse and the visible excitation pulse on the second GaAs switch is limited by our optical setup and is measured to be $\sim 8°$. A removable mirror is placed in the optical path of the collection system to provide a reference signal corresponding to the infrared reflection from the first GaAs reflection switch. With this optical arrangement, we are not able to entirely eliminate the back surface reflection from the first GaAs switch, and the reflection-reflection experiments are performed with the presence of a small background

infrared reflection. The stray visible pulse light reflection coming onto the detector is eliminated by placing a GaAs wafer at Brewster's angle at the entrance to the detector.

The exact time delay range is initially set by accurately measuring the optical paths that the infrared and the visible pulses take to within $\sim \pm 3$ mm. Then the delay line is scanned over this distance range, and at the same time the infrared reflection from the second switch is monitored on the oscilloscope until a maximum reflection is obtained (this defines the overlap of the reflection pulses from the two switches). The delay line is then moved forward and backward to measure the wings of the pulse by $\sim 30 - 60$ ps.

4.10.2 Cross-Correlation Procedure and Optical Setup

We are interested in measuring the exact temporal shapes of the reflected infrared pulses. Therefore, we present a simple method to perform this task: the time-resolved cross-correlation experiment is basically a method of convolving the infrared reflected pulse with an ultrafast transmission function.

The cross-correlation method does not directly provide the pulse width but the pulse differential with respect to time. Also, it is superior to autocorrelation schemes in preserving the details of the pulse shape and providing an indication of the background level. The technique relies on the e-h plasma generation in a semiconductor which serves as a fast temporal transmission gate. The semiconductor must have a large absorption depth for the visible radiation, a long recombination lifetime compared to the measured pulse width, and a small free-carrier absorption cross-section for the infrared wavelength. We have experimented with two semiconductors, germanium and silicon, as possible candidates for infrared transmission cut-off switches; however, since the plasma layer in Ge is approximately 180 nm thick, the 10.6 μm radiation is able to penetrate and leak through the plasma layer. Thus, the experiments performed with Ge are done above a background level and are not discussed in this work. On the other hand, Si provided an excellent

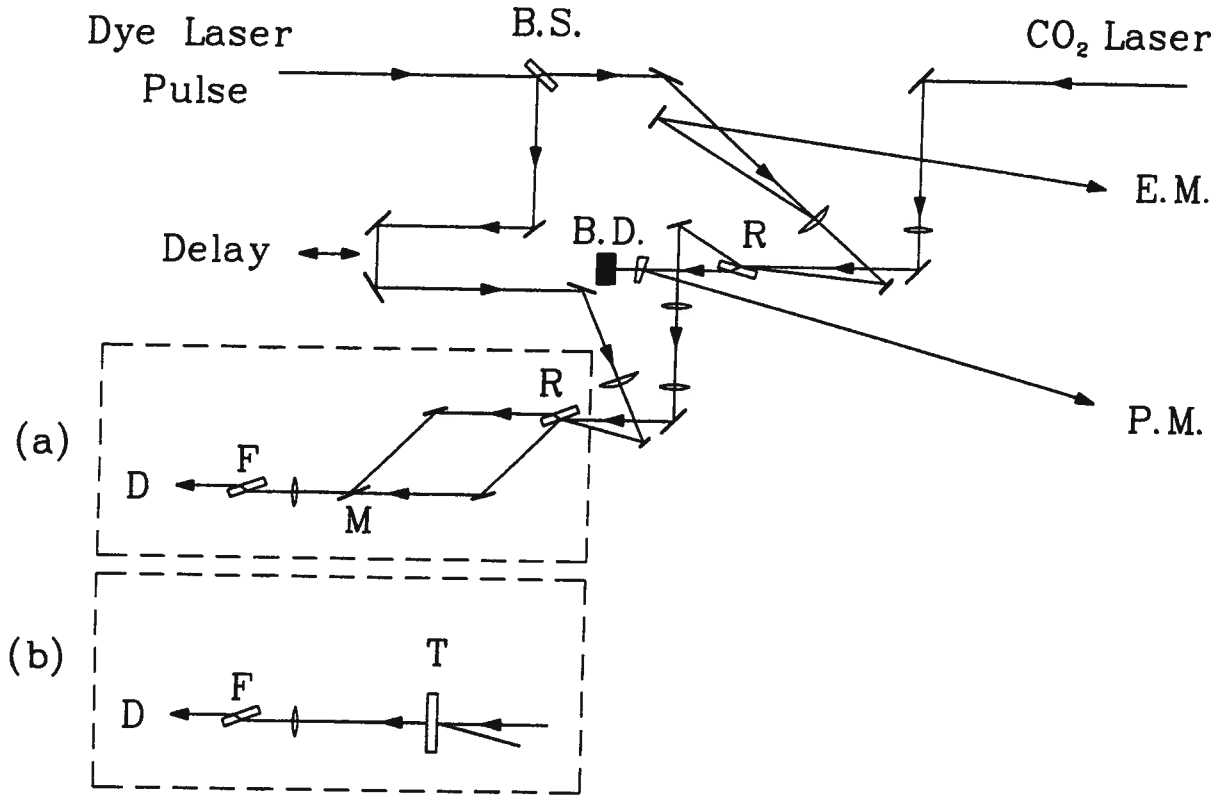

Figure 4.16: Typical experimental configurations used to measure the infrared pulse duration: (a) Reflection-reflection correlation experimental setup. (b) Cross-correlation experimental setup. B.S.= beam splitter, B.D.= beam dump, E.M.= energy meter, P.E.= power meter, R= reflection switch (GaAs), M= temporary mirror, F= filter (GaAs wafer), D= Cu:Ge infrared detector, and T= transmission switch (Si).

contrast ratio; therefore, it is used throughout this work. It will be shown in chapter 5 that silicon is an ideal semiconductor for this type of experiment.

The cross-correlation experiments are performed in the following manner: the probe visible pulse is directed towards a transmission cut-off switch to optically excite the semiconductor, and thus creates a plasma density greater than the critical density ($\sim 5\times10^{19}$ cm^{-3}) in the absorption skin depth of silicon. The thickness of the plasma layer is $\sim$ 3 μm. When the visible excitation pulse arrives at the Si transmission cut-off switch earlier than the infrared pulse, the infrared pulse is both reflected and absorbed by the free carriers. As the visible pulse is delayed, part of the infrared pulse from the reflection switch propagates through the Si switch. The part of the pulse which arrives after the critical plasma density is created suffers from large reflection and absorption. By scanning the relative delay between the infrared pulse and the visible probe pulse, the infrared pulse is temporally gated and integrated by the detector as a function of time, and a transmission step whose risetime is the cross-correlation between the infrared and the visible pulse is obtained. The time integral of the pulse is obtained as a function of the relative delay. The measured integrated pulse shape, I_{ir}, is calculated from the following expression:

$$I_{ir} \propto \int_0^\infty R(t)T(t+\tau)dt \tag{4.9}$$

where $R(t)$ is the reflectivity of the optical semiconductor reflection GaAs switch and $T(t+\tau)$ is the transmission of the cut-off Si switch at a time delay, τ.

The experimental optical arrangement of the cross-correlation experiment is illustrated in figure 4.16(b). The transmission cut-off switch is made of a 50 μm thick p-doped (1.56×10^{16} cm^{-3}) Si wafer (optically polished on both surfaces) cut to a size of 1×1 cm^2. The surface reflection of the Si sample is measured to be 35% at 10.6 μm, and resistivity of the sample is measured to be 1.41 Ω cm. The sample is mounted behind a

small hole of $\sim$ 0.5 mm diameter and is placed normal to the incoming infrared pulse. The excitation pulse (visible) is made to cover the pinhole; therefore, the cut-off switch is uniformly illuminated. Furthermore, with the introduction of the pinhole, the uncertainty involving the overlap of the pump and probe pulse is eliminated. The angle of illumination of the Si cut-off switch is kept to a minimum of $\sim 9°$ relative to the infrared pulse. This is limited only by the geometry of the optical setup.

In this type of experiment, one must eliminate the reflection from the rear of the semiconductor GaAs reflection switch. Therefore, the stray reflection is eliminated with the optical collection system, as shown in figure 4.17. With the aid of the HeNe laser beam we are able to trace the exact path of the reflected infrared pulse, and we measure the separation between the position of the reflected pulse and the reflection resulting from the rear surface to be $\sim$ 7 mm. An adjustable iris is placed between the two collimating lenses at a distance of $\sim$ 18 cm away from the focus to obstruct the stray reflection. With this simple arrangement we are able to obtain a signal to background ratio of $1{:}10^{-5}$. In some experiments an optically polished Ge flat is used as an infrared filter to ensure that no visible radiation leaks through to the infrared detector.

The correct time delay range is initially set by accurately measuring to within $\sim$ 3 mm, the optical paths between the infrared and the visible pulses. Then the delay line is scanned over this distance range, and at the same time the infrared signal transmission is monitored on the oscilloscope until the infrared transmission is completely cut-off (this defines the zero delay time). The delay line is then moved forward (for earlier arrival of the visible pulse relative to the infrared pulse) by $\sim$ 5–10 ps to provide a long zero-transmission base-line in order to resolve the initial risetime of the pulse.

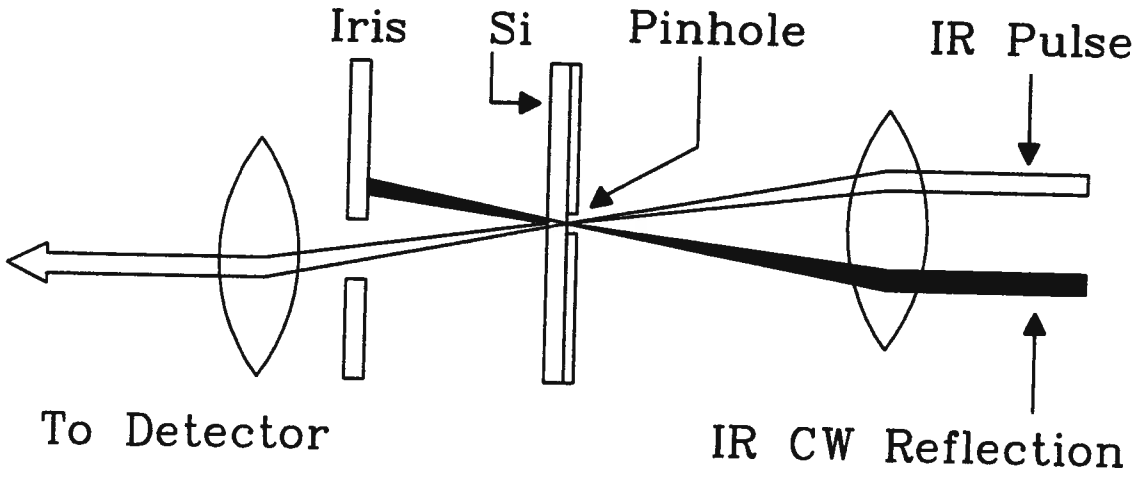

Figure 4.17: Optical arrangement used to eliminate the rear reflection resulting from the first GaAs reflection switch.

4.11 Infrared Pulse-Frequency Measurement Technique

Measurement of the frequency spectrum of the reflected infrared pulses should provide a complementary and independent method to both reflection-reflection correlation and cross-correlation techniques. However, there is a difficulty associated with the detection of the infrared spectrum, mainly the lack of a fast sensitive charged coupled device operating at 10.6 μm. Although pyroelectric arrays can serve this purpose, they lack the sensitivity and the temporal response at 10.6 μm. In fact, we have used unsuccessfully such a device to record the frequency spectrum. Thus we investigate the use of an image disector optical setup, combined with an infrared spectrometer, to measure the frequency spectrum of the infrared pulse on a single shot basis. The apparatus permits the measurement of the spectrum with a very high detectivity by using only a single infrared detector.

4.11.1 The Image Disector

The image disector has been used widely in our laboratory to measure the frequency spectrum from scattered light in laser-plasma interaction experiments. It is based on the principle that the individual frequencies making up the pulse spectrum are mapped onto time delayed signals (in contrast to correlation experiments where the temporal information is mapped into spatial distribution). To explain further, an ultrashort optical infrared pulse at 10.6 μm, with a duration less than the response time of the detector, has a frequency spectrum whose width in frequency is inversely proportional to the pulse duration. The spectrum of the infrared pulse is spatially dispersed by passing the pulse through a spectrometer, and if the frequency spatial dispersion is made wide enough, then by circulating the optical pulse through a special optical mirror arrangement (image disector), one can allow only successive parts of the frequency spectrum to exit the optical arrangement for each transient reflection the infrared pulse takes through the optical system. Consequently, one can use a single fast infrared detector to obtain a pulse train (channels) that maps out the full pulse frequency spectrum. Clearly, the temporal delay for the pulse inside the optical system must be longer than the response time of the infrared detector. By proper choice of spatial dispersion of the spectrum, one can obtain the desired frequency resolution per channel of the optical setup.

4.11.2 Optical Setup and Alignment of the Image Disector

The optical arrangement of the image disector and the optical collection system is illustrated in figure 4.18. The image disector itself consists of three concave gold-coated mirrors, M_1, M_2 and M_3, all of the same focal length of 50 cm. Both M_2 and M_3 are 5.08 cm in diameter and are separated form M_3 by a distance of 1 m. The M_1 mirror is square edged (7 cm$\times$7 cm) with the flat sides cut to a sharp edge of 10° to allow the part of the

infrared image spectrum to exit the multi-pass optical arrangement. Since the technique requires a few reflections on each pass, the optical qualities and the reflectivities of the mirrors, M_1, M_2, and M_3 must be high: $\lambda/10$ and $\sim$ 99%, respectively.

The reflected infrared pulse is collimated with two NaCl lenses (f.l.= 15 cm) to form a 1:1 telescope arrangement. The infrared pulse is directed toward the spectrometer where it is focused on a 380 μm entrance spectrometer slit with a NaCl (f.l.= 15 cm) lens. Upon exiting the spectrometer, the infrared pulse image spectrum is focused at a point directly over the front surface of M_1 of the image disector by a 45 cm focal length (7.62 cm diameter) concave mirror. With this focusing mirror, the image of the exit slit of the spectrometer is made to fully cover M_2. Mirror M_2 produces series of images of the spectrum progressing down and towards the right edge of M_1, while mirror M_3 produces images of the spectrum progressing down and to the left edge of M_1. On successive reflections, a small part of the spectrum is sliced off and allowed to exit the disector. This in turn represents the first channel of a spectrum. The rest of the spectrum image is reflected back again through the optical arrangement, successively displaced vertically from one another and to the right near the mirror's M_1 edge, and progressively sliced off (later in time) as the spectrum of the pulse is scanned by the spectrometer. By proper alignment of the mirrors, as much as 10 channels can be obtained. The resolution of the image disector depends on the spatial spacing between the channels. Figure 4.19 shows a typical ten channel output spectrum from the image disector system. The output channels of the image disector are collected with a 77 cm focal length mirror (7.62 cm in diameter), a 50 cm focal length NaCl lens (12.7 cm in diameter) and a 10 cm focal length NaCl lens to focus the channels on a single Cu:Ge infrared detector.

Several temporary mirrors are placed in the pulse path to bypass the image disector and the spectrometer. This proved to be very useful before the start of the experiment when the visible control pulse spot and the infrared beam spot are aligned. Once a

reflected pulse in detected by the Cu:Ge detector, these mirrors are removed and spectrum is measured.

4.11.3 Calibration of the Image Disector Optical System

In order to simplify the alignment procedure of the optical system, we placed a gold coated Si wafer, a Si wafer, and the GaAs optical switch on the same sample holder. The sample holder is mounted on a fine linear translation stage, so that each sample or the mirror can be placed at the focus of the CO_2 laser beam without disturbing the alignment of the optical system. Figure 4.20 illustrates the wafers' arrangements. The gold-coated mirror is used to reflect the CO_2 laser beam so that the laser beam can be used for the purpose of aligning both the spectrometer and the image disector.

The spectrometer used in this experiment requires a precise calibration against a known wavelength. Initially, a HeNe laser (λ=0.6328 μm) is used to calibrate all the 17 orders from the grating against the dial reading on the spectrometer; however, over this long calibration range, the dial reading is nonlinear with the wavelength reading. For a small dial range, the dial linearity is found to be excellent. Therefore, the spectrometer calibration is performed with the aid of CW CO_2 laser lines combined with the 0.6328 μm HeNe laser line (over a small wavelength range). To obtain different lines from the CO_2 laser, the Ge etalon output coupler temperature is adjusted so that the laser is made to lase at three different lines: 10.611 μm, 10.632 μm, and 10.591 μm. The lasing wavelength is checked with another calibrated infrared spectrometer (Optical Engineering). Two other calibration wavelengths of 10.125 μm and 10.758 μm are obtained from the 16^{th} and the 17^{th} orders of the HeNe laser line. Figure 4.21 shows a complete plot of the calibration of the dial reading as a function of a wavelength. A linear fit through the data points gives a calibration value of 10 Å per one dial reading.

Since each channel of the spectrum goes through a different number of reflections

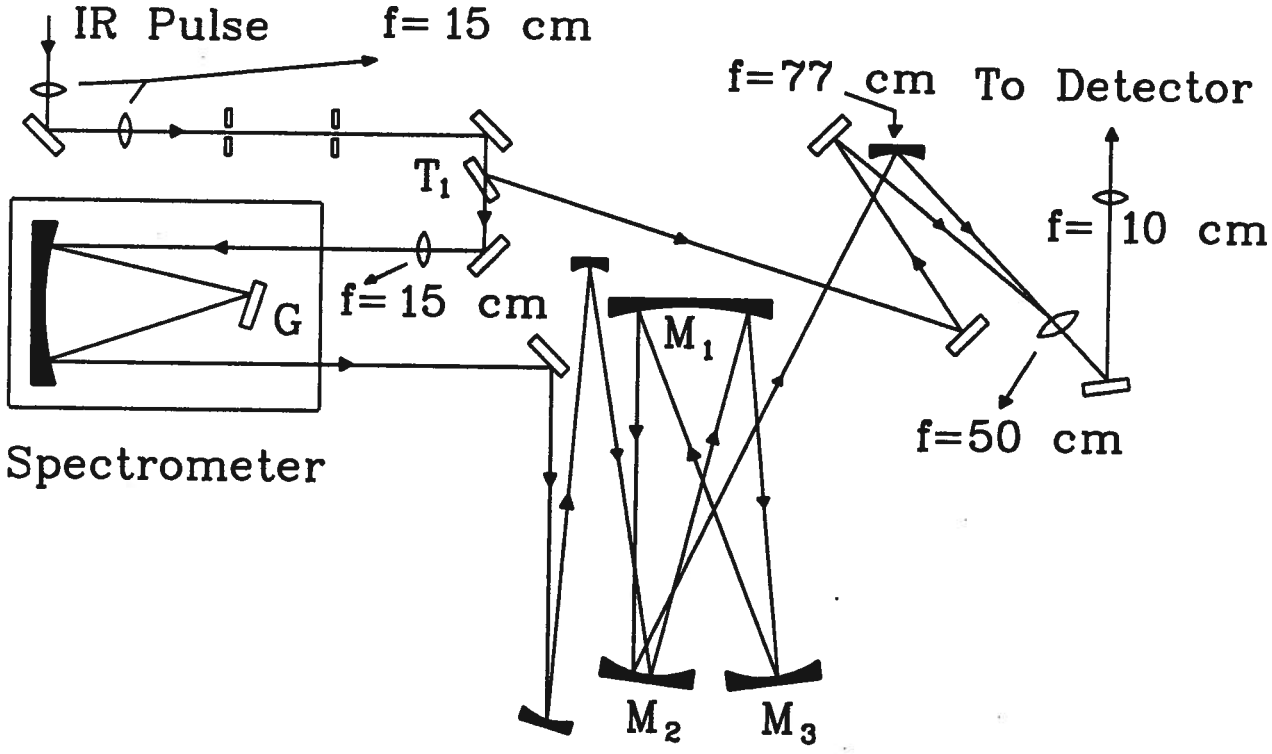

Figure 4.18: Experimental optical setup for the reflected pulses spectrum measurement. T_1= temporary mirror, and G= grating.

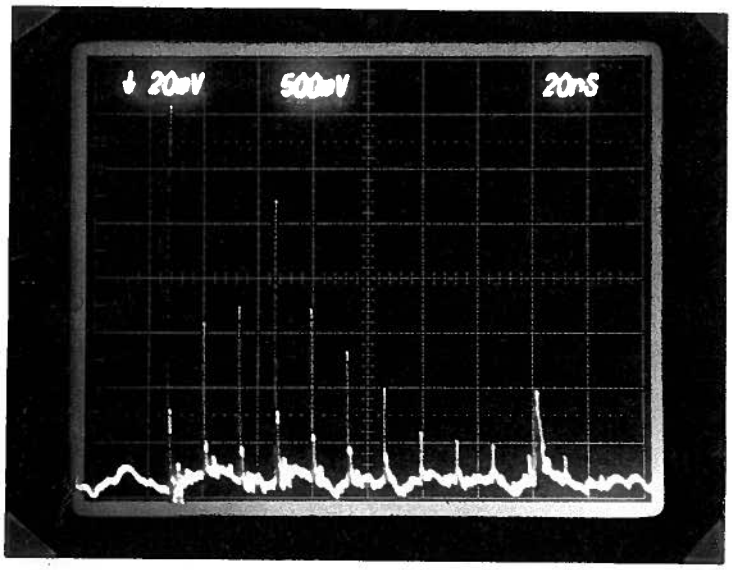

Figure 4.19: A typical oscilloscope trace of the output of the image disector showing ten channels.

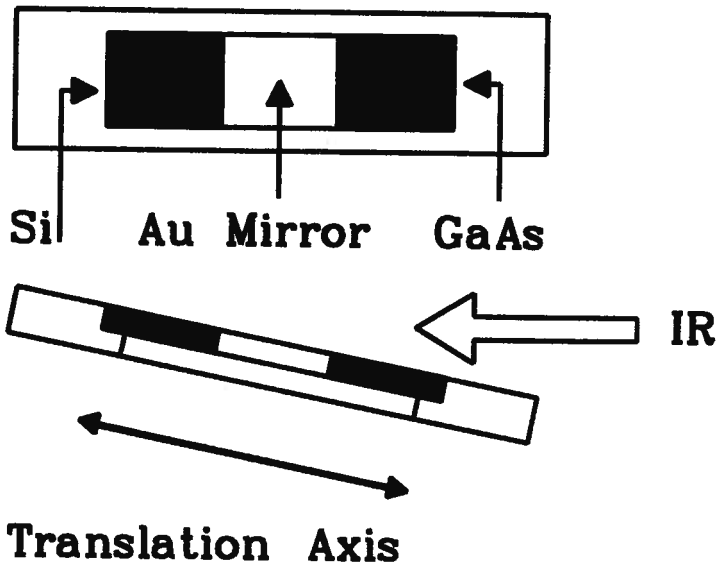

Figure 4.20: Samples arrangement

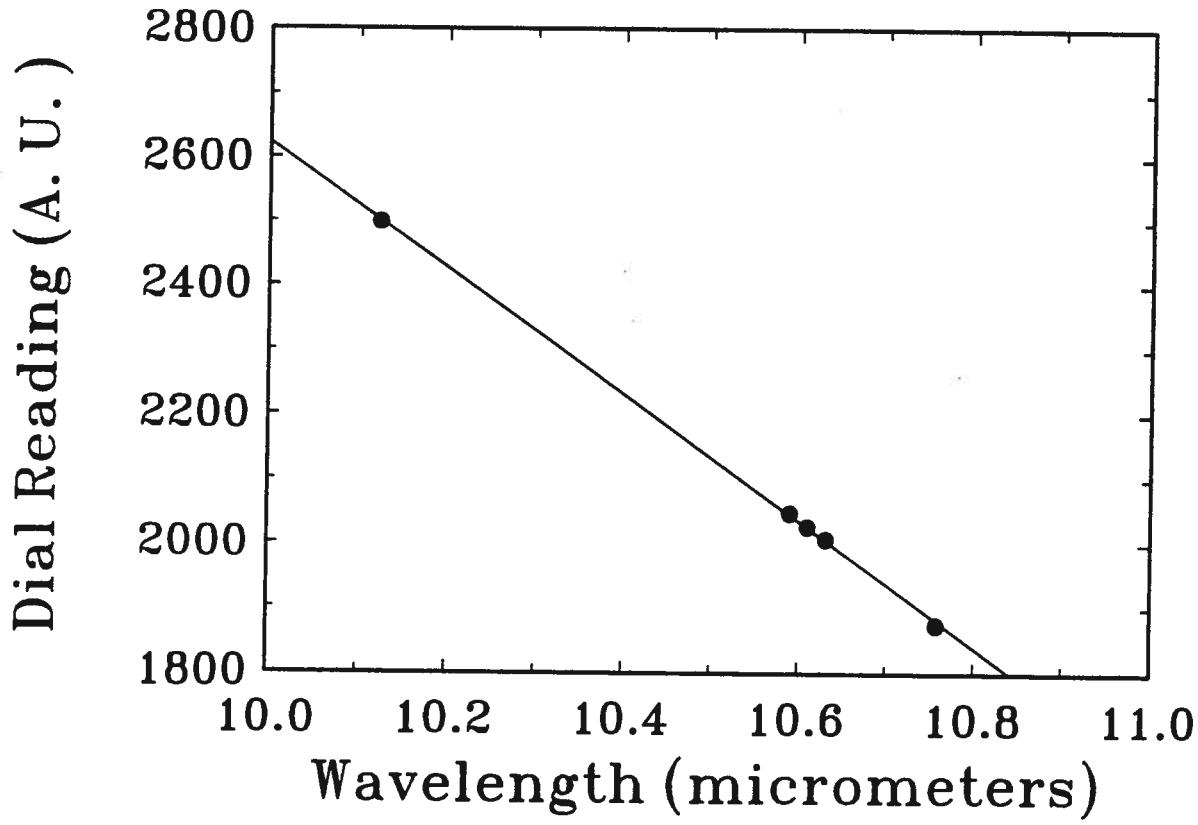

Figure 4.21: Calibration curve of the spectrometer reading against the CO_2 laser wavelength.

inside the image disector, it is expected that the reflectivity of the image disector optics varies for each one. A simple method to calibrate the reflectivity of each channel is to use a long 10.6 μm laser pulse. A Si wafer is used as an optical semiconductor switch (in place of GaAs) to generate $\sim$ 1 ns pulses at 10.6 μm. These pulses have a narrow spectrum (narrower than the ones generated from the GaAs) which can fit in one channel. Then the spectrometer output spectrum is scanned across a 160 μm exit slit so that the maximum of each channel is displayed on the oscilloscope. A total of six channels are obtained with relative normalized reflectivity, as shown in figure 4.22. The spectrum of the reflected infrared pulse from the GaAs optical switch is deconvoluted with the calibration curve in figure 4.22. The spacing between the channels is obtained directly from the dial reading. The alignment and the calibration of the image disector is adjusted before the start of each experiment.

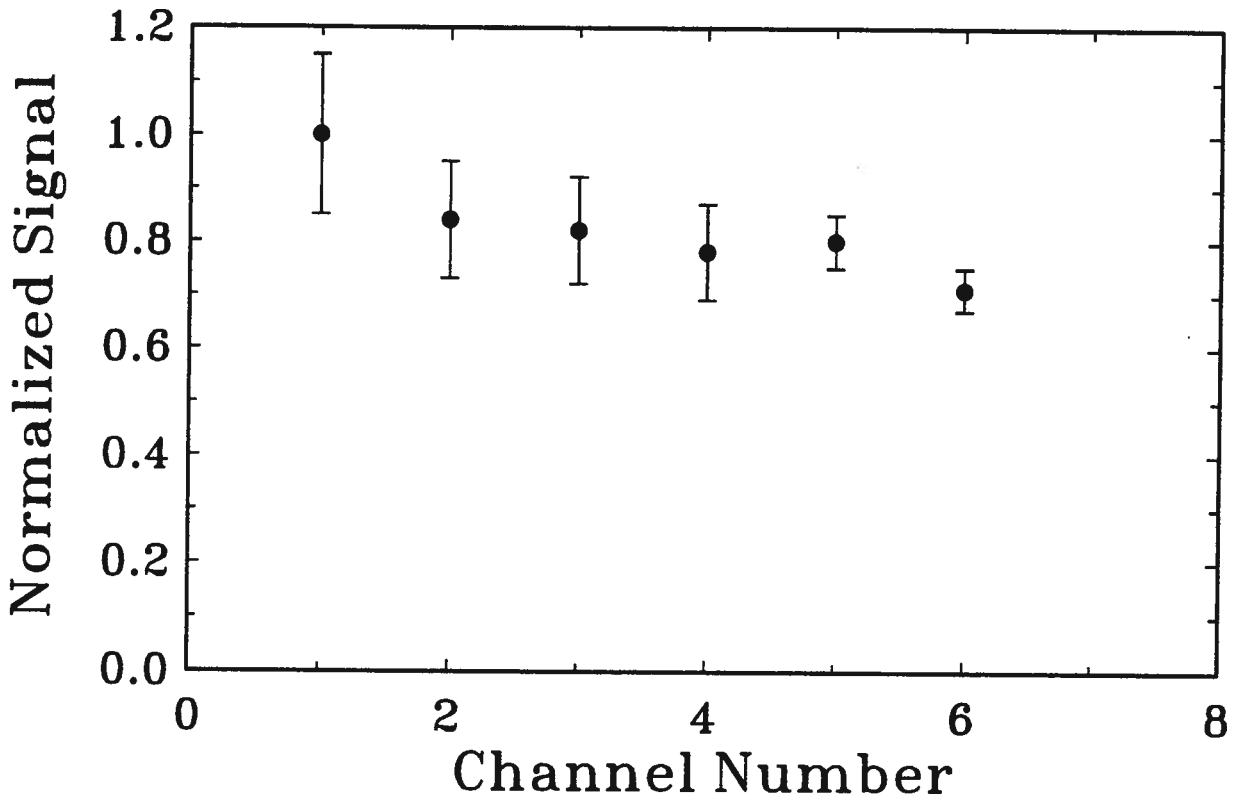

Figure 4.22: Image disector calibration curve. The error bars are the standard deviation of signals for 10 consecutive shots separated by 13.3 ns.

Chapter 5

Experimental Investigation of Infrared Reflection from GaAs

5.1 Introduction

This chapter describes the experimental results and methods used to generate and to measure ultrafast infrared optical pulses at 10.6 μm. The infrared reflection experiments are mainly performed on GaAs semiconductor plasmas. The major experimental work and results in this chapter have been presented in our current publications [161, 162]. In order to have a clear understanding of the optical semiconductor switching process(es), we have performed four types of experiments followed by theoretical modelling of the switching process. We start the chapter by examining in detail the optical and temporal response of a Si transmission cut-off switch by performing infrared transmission experiments. This type of experiment is undoubtly crucial in determining the temporal resolution of the time resolved measurements. Moreover, we present some theoretical considerations of the dielectric constant as a function of the optically generated free-carrier concentration and its spatial distribution and calculate the transmission of an infrared pulse through such a distribution as a function of the carrier density at the surface of the illuminated Si-wafer. The results of the experimental work and the analysis of the results based on model predictions are also presented. Next, we present the experimental work dealing with the variations of the infrared reflectivity with the photogenerated plasma density. This experiment is used to examine the proper e-h density operation region of the reflection switch. Details of time resolved experiments used to measure the durations

and temporal shapes of the 10.6 μm reflectivity pulses are determined by two independent methods: cross-correlation and reflection-reflection correlation measurements. The limits and advantages of the two methods are presented and the results are discussed in great detail. A modifed infrared reflection model is also presented to account for the observed time resolved experimental data. Finally, the experimental results of the infrared reflected pulses frequency spectrums are outlined at the end of this chapter.

5.2 The Si Transmission Cut-Off Optical Switch

Before proceeding with the time resolved cross-correlation measurements, one needs to characterize the speed of the optical switching elements. We have developed a novel method for measuring the infrared pulse durations and temporal shapes. This cross-correlation technique is reviewed in section 4.10.2. Clearly, its temporal sensitivity and resolution is determined by the choice of the active optical switching element. The choice of a proper semiconductor switching element is limited by the magnitudes of both free-carrier and intervalence band absorption, and the lifetime of the optically generated carriers. As we will show later in this section, the magnitude of the first two absorption processes determine the speed of the initial transmission cut-off of the switch from full transmission (T= 1) to zero level (T= 0), whereas the lifetime of the carriers determines the temporal persistance of the off-state of the optical transmission switch. It is evident that for an ideal situation one needs to minimize the initial infrared transmission temporal cut-off so that it is less than the optical excitation pulse by reducing the effects due to the free-carrier absorption process. On the other hand, the carrier lifetime (due to Auger and two-body recombinations) must be optimized to be longer than the measured infrared pulse. Ideally, the transmission switching element behaves as a temporal step function.

The knowledge of free-carrier absorption cross-sections is especially useful in understanding the behavior of other types of high power optical-optical semiconductor switches. Optical-optical reflection and transmission cut-off switches [55] have been used extensively for short pulse generation schemes. In such applications, one relies on both the degree of free-carrier absorption and the level of reflection of infrared radiation to operate the Si cut-off switch in the THz range. Rolland and Corkum [55] have used Si as a transmission cut-off switch where they managed to gate high-power 130 fs pulses at 10.6 μm. The authors calculated the transmission of the switch as a function of the optically generated carriers; however, they did not provide the necessary experimental work to optimize the switch, such as an investigation of the type of doping needed for faster operations.

In our current work, we were interested in using this switch to perform time-resolved cross-correlation measurements. In order to model the performance of the switch, detailed knowledge of the dielectric constant $\epsilon = \epsilon_r + \epsilon_i$, in particular its imaginary component, ϵ_i, arising from free carrier and possibly intervalence band absorption, is important. We, for example, are especially interested in the response time of a Si transmission switch for 10.6 μm radiation after irradiation with 0.49 ps, 616 nm laser pulse, in which case the magnitude of ϵ_i critically affects the switching speed [161]. The main question to be investigated is: can the switch transmission be turned off on a time scale less than the excitation visible pulse?

In general the absorption cross-section for such photoexcited free carrier Si-plasmas is inferred from measurements on both p- and n-doped samples in which the infrared wavelength and magnitude of the reflectivity minimum is determined as a function of carrier concentration [163]. However, it is not at all clear whether this inference is justified considering that both electrons and holes are photogenerated with significant energies above the band minima leading to highly elevated carrier and lattice temperatures. It would

therefore be desirable to conduct measurements of the relevant parameters directly on photoexcited free carriers. Here, we present the results on infrared pulse transmission experiments which permit such measurements. The results show that at 10.6 μm, in contrast to intervalence band absorption, free-carrier absorption dominates the absorption process [163]. From these experiments, the momentum relaxation times can be determined. Also, the experiments reveal the interesting fact that these relaxation times are shorter by a factor of 0.4 if the carriers are generated in n-type as compared to p-type Si.

5.2.1 Theoretical Considerations

The model treatment of the physical processes involved is very simple. Here, several assumptions are introduced to simplify the physical situation. We begin by treating the optically generated plasma in Si as being an inhomogeneous plasma which is subjected to 10.6 μm radiation. It is appropriate to treat the situation as a one dimensional problem. This is justified because the diameter of the excitation area on the Si surface is much larger than the absorption skin depth of the visible radiation. Moreover, the spatial profile of the plasma in the transverse direction is assumed to be uniform. The model treats the absorption of the 10.6 μm radiation to be proportional to the free-carrier concentration; this situation is similar to free-carrier absorption in highly doped semiconductors [164]. Since interband transitions are not allowed at this wavelength, the response of the medium to the applied electromagnetic field can be characterized by the Drude theory for the frequency-dependent dielectric function. The Drude model of free carriers has been very successful in describing the optical properties of semiconductors after quantum corrections for intervalence band absorption have been made [164]. Combining the effects of electrons and holes [163] and transferring averages over the carrier energy distributions to that over the carrier relaxation times [165], we write the real and imaginary parts of

the dielectric constant as:

$$\epsilon_r = \epsilon_b \left(1 - \frac{4\pi n e^2}{\epsilon_b m^* \omega^2} \frac{\omega^2 < \tau_o >^2}{1 + \omega^2 < \tau_o >^2}\right) \tag{5.1}$$

and

$$\epsilon_i = \epsilon_b \left(\frac{4\pi n e^2}{\epsilon_b m^* \omega^2} \frac{\omega < \tau_o >}{1 + \omega^2 < \tau_o >^2} + \frac{\lambda}{\sqrt{\epsilon_b}\pi} \sigma_{vb} n\right). \tag{5.2}$$

Here ϵ_b= 11.8 is the background dielectric constant for the bulk Si and σ_{vb} is the intervalence band absorption cross-section. For carrier densities less than 10^{20} cm^{-3}, the carriers effective masses may be taken to have their low-density values [166] (m^{*-1} = m_e^{*-1}+m_h^{*-1}, with m_e^*= $0.26m_o$ and $m_h^* = 0.38m_o$) [163], $< \tau_o >$ is the mean momentum relaxation time for the optical process, and σ_{vb} the intervalence (heavy to light hole) band absorption cross-section. The electrons and holes are assumed to have the same relaxation time which is taken to be independent of the energy of the carriers. Also the dependence of the dielectric function on the lattice temperature is ignored in this model. We now define a critical density n_c:

$$n_c = \frac{\epsilon_b m^* \omega^2}{4\pi e^2} \frac{(1 + \omega^2 < \tau_o >^2)}{\omega^2 < \tau_o >^2} \tag{5.3}$$

and write for the complex dielectric constant:

$$\epsilon = \epsilon_b \left(1 - \frac{n}{n_c}(1 - i\alpha)\right). \tag{5.4}$$

Here α combines the effect of both free-carrier and intervalence band absorption: α = $\alpha_{fc} + \alpha_{vb}$ with $\alpha_{fc} = 1/(\omega < \tau_o >)$, where α_{fc} and α_{vb} are the first and second terms of equation 5.2, respectively. The only free parameter in this model is the free-carrier absorption cross-section which is due to a combination of both electrons and holes and is considered to be constant over the range of the plasma e-h density used in this experiment.

In the experiments to be described later the free carriers are produced by absorption of photons in a 490 fs, 616 nm laser pulse; the generation rate is taken to be a delta

function in time as compared to the experimental time scale. This pulse generates a density distribution in a direction perpendicular to the illuminated Si-wafer surface at z= 0 of the form:

$$n(z) = n_o e^{-\gamma z}. \tag{5.5}$$

The absorption depth, γ^{-1}, at an excitation wavelength of 616 nm is measured to be 3 μm [167]. Due to this large depth, ambipolar diffusion has very little effect on the density profile over time scales of interest in the present experiment (<50 ps) and we neglect it in our calculations [168]–[170]. At these time scales both Auger and two-body recombination can also be neglected. Auger coefficients of Si are measured to be 9.9×10^{-32} cm^{6}s^{-1} for p-type, 2.8×10^{-31} cm^{6}s^{-1} for n-type, and 4×10^{-31} cm^{6}s^{-1} for highly excited Si [171]. Therefore, by using a maximum plasma density of 7×10^{19} cm^{-3}, we can obtain recombination times of 2×10^{-9} s for p-type, 7.3×10^{-10} s for n-type, and 5.1×10^{-10} s for the highly excited Si, respectively. All three are several orders of magnitudes larger than the experimental time scale. Two-body recombination time is measured by us during the experiment and is found to be of the order of 2×10^{-8} s. Figure 5.1 shows the transmission cut-off for a CW laser beam at 10.6 μm just after excitation with the 0.49 ps pulse. The photograph shows a sharp initial drop in the transmission followed by a transmission-recovery tail lasting for 35 ns.

We now proceed to calculate the transmission of a normally incident pulse of below bandgap photon energy (wavelength λ) through the photoexcited Si-wafer. We normalize the density as $\nu = n/n_c$ and write $\epsilon(\nu) = \epsilon_b[1 - \nu(1 - i\alpha)]$. The amplitude reflectivity and transmission from a discontinuity in the dielectric function from ϵ_1 to ϵ_2 are given by:

$$r = \frac{\sqrt{\epsilon_1} - \sqrt{\epsilon_2}}{\sqrt{\epsilon_1} + \sqrt{\epsilon_2}} \tag{5.6}$$

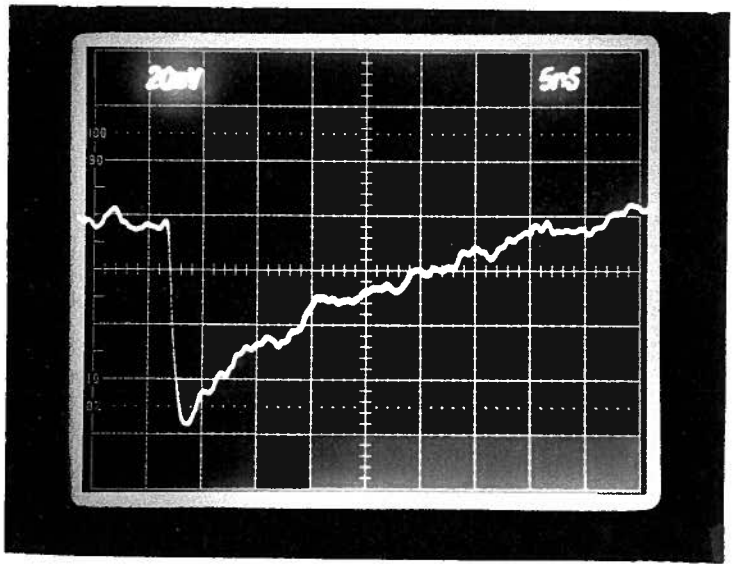

Figure 5.1: Transmission signal temporal recovery of the P-type Si transmission cut-off switch.

and

$$t = 1 - r. \tag{5.7}$$

At the Si wafer surface we then have:

$$r_o = \frac{1 - \sqrt{\epsilon(\nu_o)}}{1 + \sqrt{\epsilon(\nu_o)}} \tag{5.8}$$

and

$$t_o = 1 - r_o \tag{5.9}$$

where $\nu_o = n_o/n_c$. The plasma layer is modeled by a finely layered medium where the electric field is constant in each region. We consider a small density step of $\Delta\nu$ at a density ν_q inside the wafer with a reflectivity of:

$$r_q = \frac{\sqrt{\epsilon(\nu_q)} - \sqrt{\epsilon(\nu_q - \Delta\nu)}}{\sqrt{\epsilon(\nu_q)} + \sqrt{\epsilon(\nu_q - \Delta\nu)}}. \tag{5.10}$$

We now approximate the exponential density profile $\nu_o e^{-\gamma z}$ by one consisting of a large number m of density steps $\Delta\nu = \nu_o/m$. Propagating from one step to the next the wave

suffers a phase change of:

$$\triangle\beta_q = \frac{2\pi}{\lambda}\gamma^{-1}\frac{\triangle\nu}{\nu_q}\sqrt{\epsilon(\nu_q)}. \tag{5.11}$$

The transmission of light not reflected from the e-h plasma is then:

$$t_1 = t_\circ \prod_{q=0}^{m-1}(1 - r_q)e^{i\triangle\beta_q}. \tag{5.12}$$

If m is chosen to be large enough (in our case $m \geq 50$), then the magnitude of the r_q is much smaller than one. With this choice of large m, one can ignore the higher order terms in equation 5.12, and equation 5.12 can be approximated as:

$$t_1 = t_\circ(1 - \rho_1)e^{i\beta} \tag{5.13}$$

with

$$\rho_1 = \sum_{q=0}^{m-1} r_q \tag{5.14}$$

and

$$\beta = \sum_{q=0}^{m-1} \triangle\beta_q. \tag{5.15}$$

Light reflected from the density profile (reflectivity ρ_2) is reflected from the wafer surface at a potentially large reflectivity $-r_\circ$ and propagates again through the carrier distribution:

$$\rho_2 = \sum_{q=0}^{m-1} r_q exp\left(2i\sum_{j=0}^{q}\triangle\beta_j\right). \tag{5.16}$$

For this part of the incident radiation the transmission coefficient is:

$$t_2 = -r_\circ t_\circ \rho_2(1 - \rho_1)e^{i\beta}. \tag{5.17}$$

Subsequent reflections from the profile can be neglected if $\alpha > 0.02$. The total transmission coefficient is then $t = t_1 + t_2$. Thus the intensity transmission coefficient T can be calculated:

$$T = \sqrt{\epsilon_b} \mid t_o(1-\rho_1)(1-r_o\rho_2)e^{i\beta} \mid^2 . \tag{5.18}$$

The described calculation can be simply performed using common math-software on a PC. The transmission T is calculated as a function of surface free-carrier density ν_o for various values of α. For comparison with experiments it is convenient to normalize the transmission to that for ν_o= 0 (bulk) and display the results as a function of log (ν_o). Figure 5.2 shows resulting curves for the calculated values of α = 0.1, 0.2, 0.3, and 0.5. The transmission curves are normalized to the transmission coefficient at zero photoexcitation, T_o.

5.2.2 Transmission Cut-off Results at 10.6 μm.

The infrared transmission results are measured with the optical setup described in Chapter 4 for the cross-correlation setup. The details of the experimental procedure and sample preparations are also outlined in section 4.10.2.

In the first part of each experimental series for a given Si sample, we recorded the transmitted infrared energy as a function of visible laser light energy, while the pump pulse blocked off the Si-wafer. These proved to be necessary in order to obtain accurate measurements of the photoexcited plasma densities. The results, shown in figure 5.3 for two Si samples indicate the variation of the infrared pulse energy as a function of control pulse energy incident on the GaAs reflection switch. The straight lines through the data points are linear regression curves and serve as reference values for the analysis of each experiment. Figure 5.3 shows that a certain control minimum pulse energy, I_i, is necessary to generate a measurable infrared signal. Above this intercept the energy of the infrared signal increases linearly with the control pulse energy over the range used in the present experiments. As it will be discussed later in section 5.3.1, the intercept energy

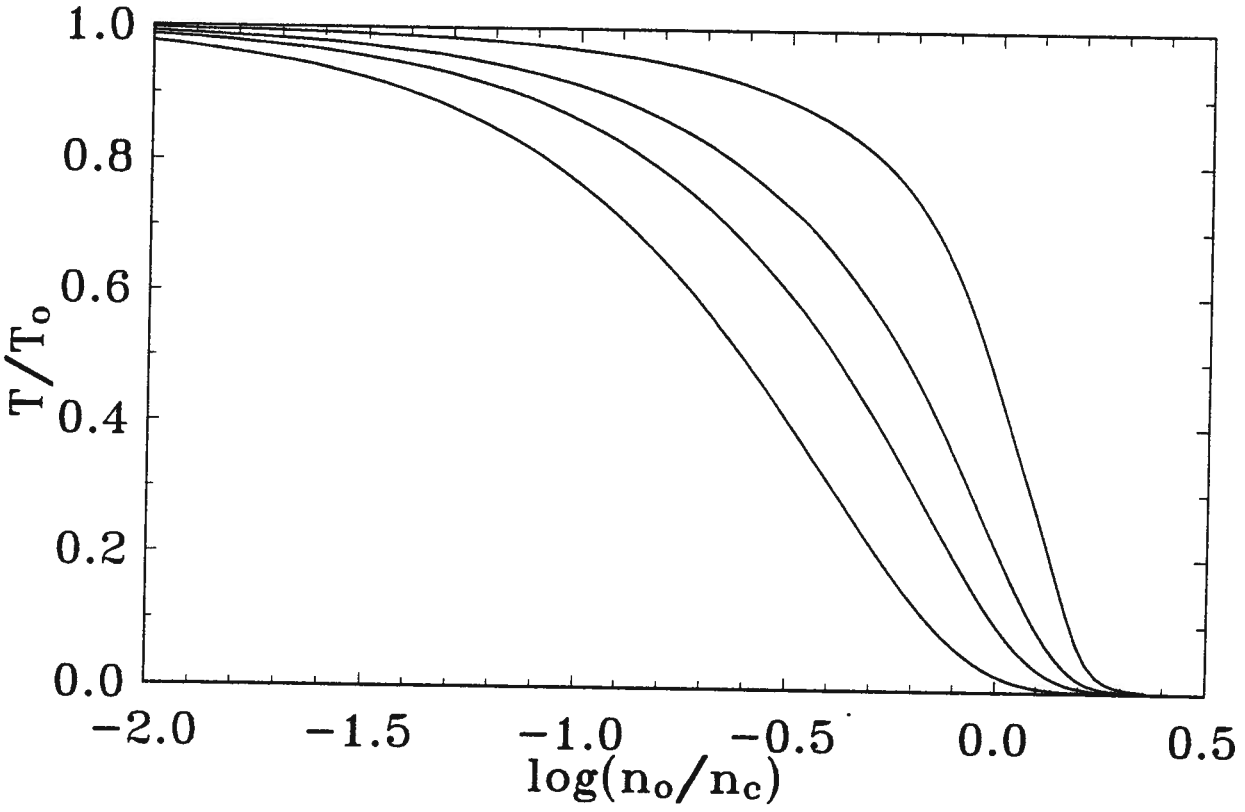

Figure 5.2: Calculated relative transmission for 10.6 μm radiation through a photoexcited Si wafer as a function of normalized free-carrier surface density n_o/n_c for four values of of α [α= 0.1 (uppermost), 0.2, 0.3, and 0.5 (lowest)].

corresponds to that necessary to generate the critical free-carrier density of 10^{19} cm^{-3} at the surface of the GaAs switch, as can be expected from theoretical considerations [84]. Since this energy, I_i, is the same for each experimental series and is independent of the optical condition of the investigated Si wafer, its determination can serve to calibrate the individual experiments with respect to one another. In the second part of each experimental series, the transmitted infrared pulse energy is recorded at pump pulse energies varying over several orders of magnitude. The pump intensity, I_p, in arbitrary units is calculated by multiplying the monitored visible laser energy with the transmission coefficient of the neutral density filter stack placed in the pump beam.

The relative transmission T/T_o is determined by dividing the monitored infrared energy by the reference value at the same visible laser energy as measured in part one of the series. The resulting data are averaged over at least 15 points with a standard deviation of the order of 10% in pump intensity bins of $I_p \pm$ 5%. In order to compare the results with the theory of the previous section the average values of T/T_o are plotted as a function of $\log(I_p)$. The photoexcited free-carrier density at the surface of the Si wafer is proportional to I_p, and $\log(I_p)$ equals $\log(\nu_o)$ plus a constant. Therefore curves of the form shown in Figure 5.2 can be fitted to the data and the best fitting value of α can be determined. Figures 5.4, to 5.7 show the results for the four investigated Si samples. The fitted theoretical curves determine α to $\pm$ 25%. For the basically intrinsic (p-type) sample of figure 5.4 and the p-type sample of figure 5.5 curves with $\alpha = 0.2$ provide the best fit, while for both n-doped samples (figures 5.6 and 5.7) a value of $\alpha = 0.5$ is determined. Using the calibration procedure of equating the intercept energy I_i of the reference curves described in the previous paragraph, we can also compare the pump energies I_{pc} required to generate the critical free-carrier surface density [$\log(\nu_o) = 0$]. By performing this cross calibration, we find that I_{pc} for the samples with $\alpha = 0.5$ is (1.7$\pm$0.5) times larger than that for samples with $\alpha = 0.2$. This indicates a relationship

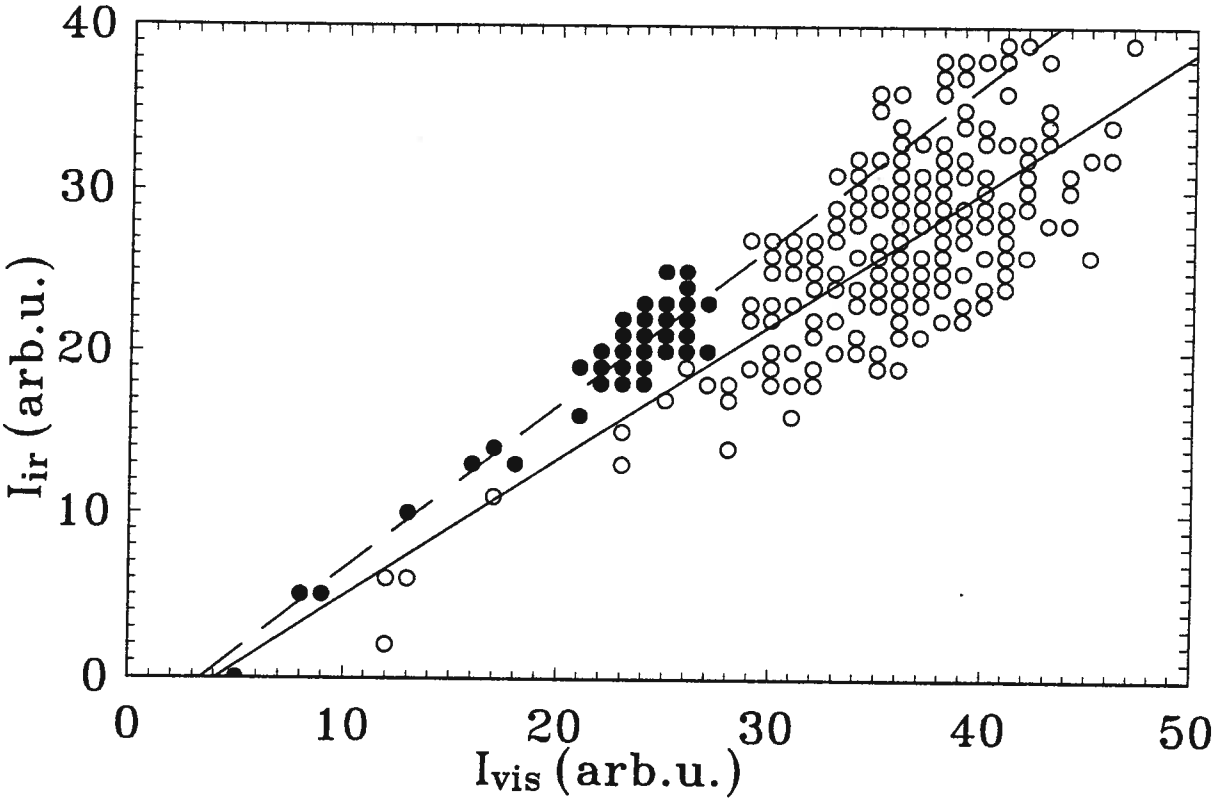

Figure 5.3: Infrared pulse intensity I_{ir} detected for two different Si wafers at zero photoexcitation as a function of visible laser pulse intensity incident on GaAs reflection switch. The solid line is a linear regression fitted to the data points (empty circles) up to $I_{vis} \leq 34$, and the dashed line is a linear regression through the solid circles.

between the critical densities of the form:

$$n_c(n-type) = (1.7 \pm 0.5) \times n_c(p-type). \tag{5.19}$$

5.2.3 Discussion of the Transmission Results

Comparison of the experimental points and the theoretical curves in figures 5.4 to 5.7 indicates that for a given value of α the model developed in section 5.2.1 provides a good description of the transmission of an infrared light pulse through crystalline Si in which free carriers have been generated by absorption of above band gap radiation.

Thus the imaginary part of the dielectric constant can be accurately determined by the technique described in the previous section. As pointed out in section 5.2.1, α is potentially composed of two components: one (α_{fc}) arising from free-carrier absorption and the other (α_{vb}) from intervalence band absorption. At the laser probe wavelength of 10.6 μm, the contribution of intervalence band absorption to the dielectric function is insignificant compared to free-carrier absorption contribution [163, 164], and the intervalence band absorption term can be ignored.

Changing α_{vb} does not alter n_c. On the other hand n_c is related to α_{fc}. According to the considerations of section 5.2.1 this relationship (see equation 5.3) is of the form:

$$n_c = \frac{\epsilon_b m^* \omega^2}{4\pi e^2}(\alpha_{fc}^2 + 1). \tag{5.20}$$

The experimental results show the critical plasma density depends on the magnitude of the free-carrier absorption term (or the carrier type). Thus if the absorption is predominantly determined by free-carrier absorption, one can calculate the absorption cross section for each α:

$$\sigma = \frac{\pi\sqrt{\epsilon_b}}{\lambda n_c}\alpha. \tag{5.21}$$

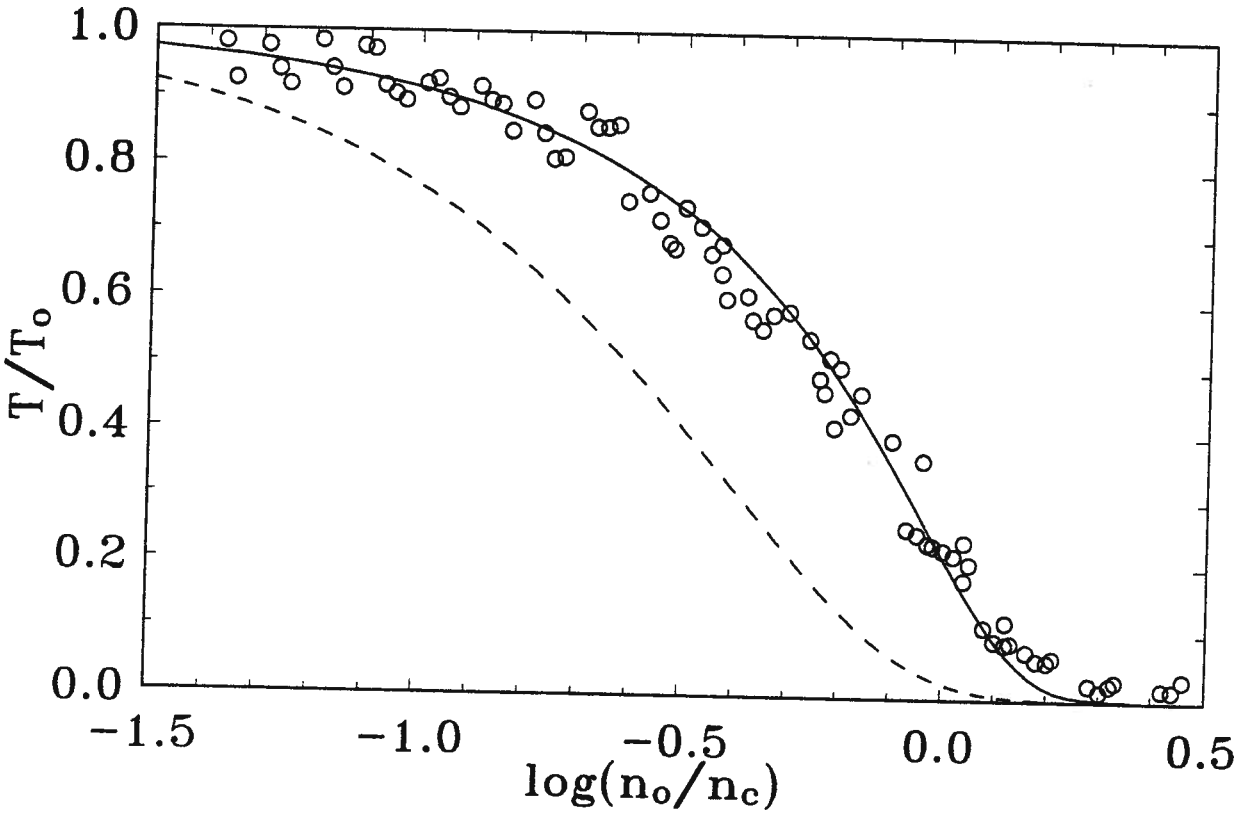

Figure 5.4: Relative transmission coefficient for an infrared laser pulse through basically intrinsic Si (p-type concentration of 1.6×10^{14} cm^{-3}) as a function of free-carrier surface density generated by photoexcitation. The full curve is the best fitting theoretical prediction to the data points at $\alpha = 0.2$. The theoretical curve for $\alpha = 0.5$ is also shown (dashed).

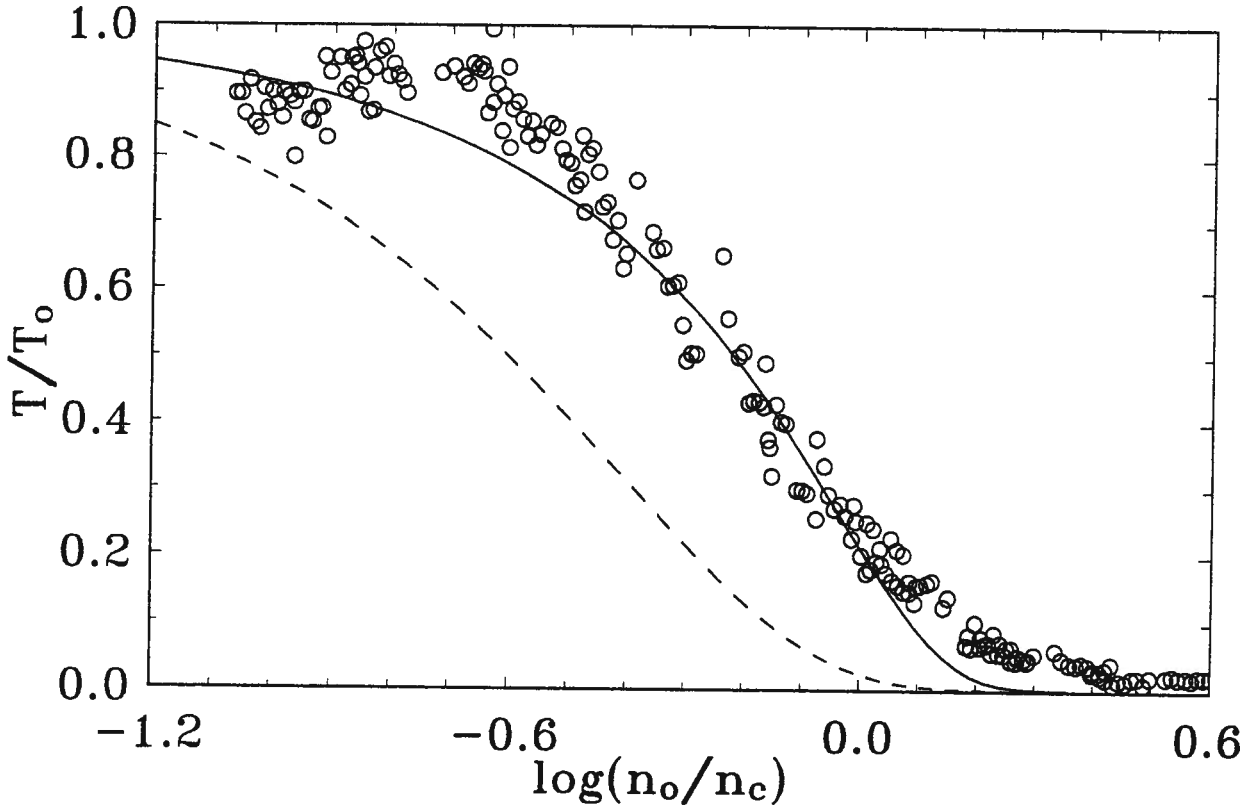

Figure 5.5: Relative transmission coefficient for an infrared laser pulse through basically intrinsic Si (p-type concentration of 2.6×10^{14} cm^{-3}) as a function of free-carrier surface density generated by photoexcitation. The full curve is the best fitting theoretical prediction to the data points at $\alpha = 0.2$. The theoretical curve for $\alpha = 0.5$ is also shown (dashed).

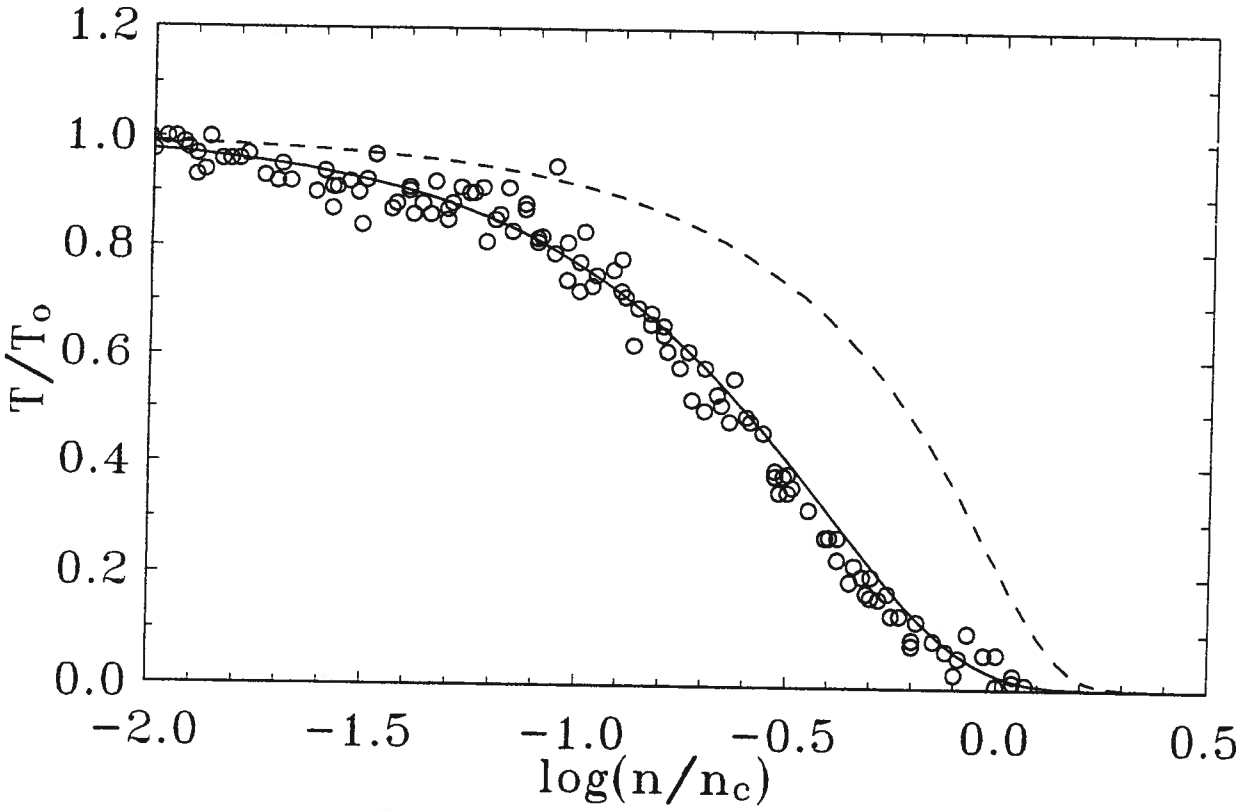

Figure 5.6: Relative transmission coefficient as in figure 5.4 for n-type Si concentration of 4.9×10^{15} cm^{-3}). The full curve is the best fitting theoretical prediction to the data points at $\alpha = 0.5$. The theoretical curve for $\alpha = 0.2$ is also shown (dashed).

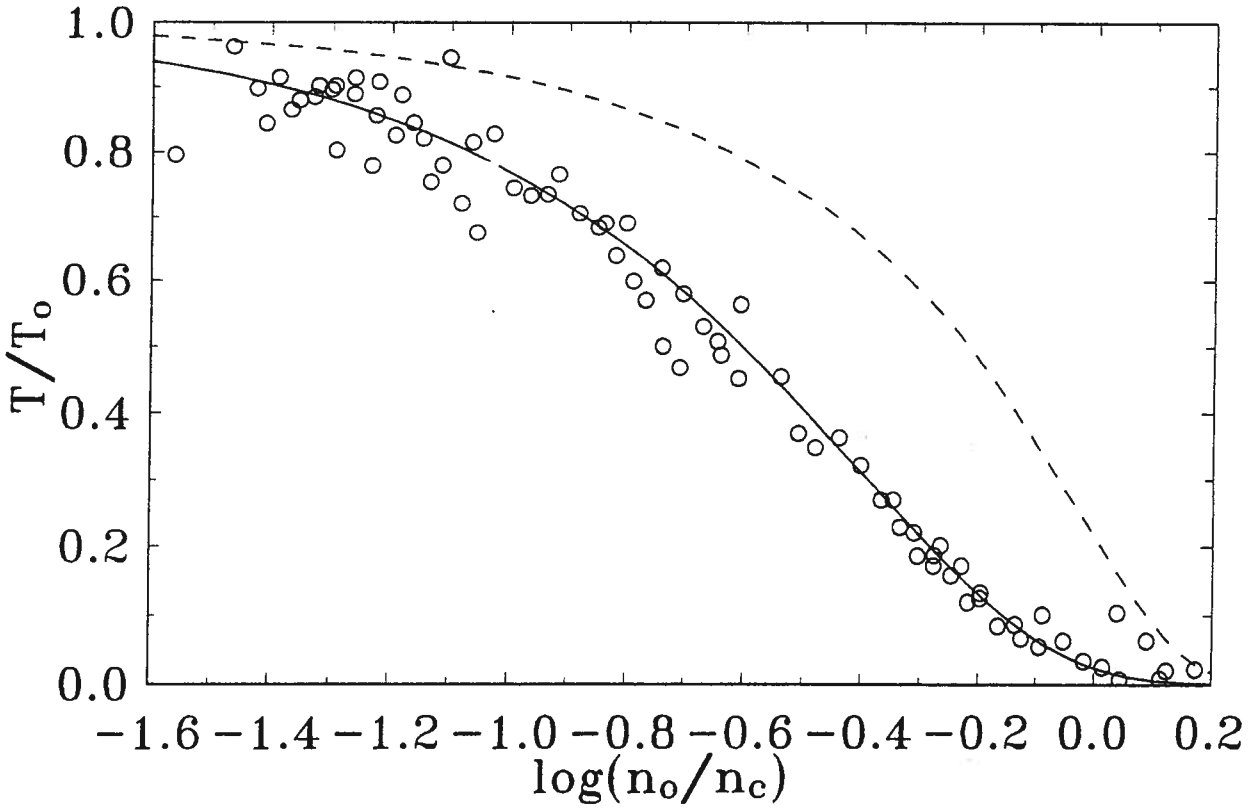

Figure 5.7: Relative transmission coefficient as in figure 5.4 for n-type Si concentration of 6×10^{15} cm^{-3}). The full curve is the best fitting theoretical prediction to the data points at $\alpha = 0.5$. The theoretical curve for $\alpha = 0.2$ is also shown (dashed).

For the p-type samples we obtain $\sigma_p = 1.1\times 10^{-16}$ cm^2 and for the n-type ones $\sigma_n = 2.3\times10^{-16}$ cm^2. These cross sections are the result of phonon scattering of both hot electrons in the conduction band and hot holes in the valence band, in contrast to cross sections determined from absorption measurements of doped samples without photoexcited free carriers. For p-doped Si, in which case the absorption arises due to hole relaxation in the valence band, a value of $\sigma_h = 1.3\times10^{-16}$ cm^2 has been reported [172] whilst for the case of absorption due to electron relaxation in the conduction band in n-doped Si, a value of $\sigma_e = 3.2\times10^{-16}$ cm^2 has been measured [163]. The difference between σ_h and σ_e is understandable due to the different types of carriers involved in the absorption process. However, in our experiments the carriers are photogenerated by the pump pulse, hence the number of the photoexcited electrons and holes are equal and one should measure a combined free-carrier absorption cross-section due to the holes and electrons. The dopant concentrations are very small compared to the photoexcited carrier concentration and therefore should have an insignificant contribution to the absorption process. However, we have found that the absorption process depends on the type of dopant. Presently, it is not clear to us what the effects of the dopants are on the absorption mechanism. The measurement of α also permits an estimate of the average momentum relaxation time $< \tau_o >$. Taking the frequency for CO_2 laser radiation in $\alpha = 1/(\omega < \tau_o >)$, we find $< \tau_o >_p$= 26.5 fs for p-type and $< \tau_o >_n$= 10.6 fs for n-type samples. It is evident from these results that p-type silicon has higher $< \tau_o >$ than n-type. This is in contrast to the experimental results presented in reference [163] for doped silicon. Considering the very low doping concentrations as compared to the critical density ($\sim 1.8\times10^{19}$ cm^{-3}) of the investigated samples, again this significant difference of $< \tau_o >$ between p- and n-doped Si is rather interesting.

To sum up, we have measured the free-carrier absorption of 10.6 μm radiation in Si of various dopings in which free carriers have been generated by absorption of photons with

above band gap energy. By fitting experimental measurements to theoretical predictions for the absorption of an infrared pulse propagating through a photoexcited e-h plasma, the absorption cross-sections and the momentum relaxation times are calculated. We find that in contrast to p-doped material, n-doping has a significant effect on the absorption process, increasing the momentum relaxation rate and thus the absorption cross-section and the critical density.

We would like to point out that because the free-carrier absorption cross-section is lower in p-type Si than in n-type Si, it is desirable to use p- rather than n-type Si for high-contrast optical semiconductor switching. That is, because the slope of the transmission curve turn-off for p-type Si as a function of the incident energy fluence (or the plasma density) is much steeper than that of n-type Si, then for a given finite excitation pulse duration, a full switch transmission turn-off can occur at much lower plasma density. Such a condition can be satisfied during the risetime of the 490 fs excitation pulse. In order to gain an insight on the speed of the transmission cut-off switch, we have to consider how the photoinjected plasma density evolves over time. The time evolution of the initially generated e-h plasma corresponds to the expression:

$$n(t) = n_o \left(1 - exp(-[t/\tau_p]^2)\right) \tag{5.22}$$

where n_o is the initially generated plasma density, and τ_p is the optical excitation pulse width. In the following calculations n_o is set to the experimental value of $6n_c$. Here, we assume that the critical density is reached at the peak of the excitation pulse. From equations 5.18 and 5.22, we can calculate the transmission cut-off time of the Si switch. The results of the calculations for p-type Si are presented in figure 5.8. It is clear from the figure that the termination of the transmission occurs in a time of approximately $0.49\tau_p$. In our experiment this corresponds to 240 fs which is fast enough to be used to perform time-resolved cross-correlation experiments on the reflected pulses from a GaAs

switch.

5.3 Ultrafast 10.6 μm Reflectivity Pulses from a GaAs Switch

In this section we report on the results of ultrafast pulse generation from GaAs semiconductor plasma. In Chapter 3, we outlined the basic underlying theory. We have shown that, in accordance with a simple diffusion model which describes the temporal behaviour of the switching process, it should be possible to produce picosecond or shorter pulses at 10.6 μm. The pulse width was predicted to be a strong function of the excitation energy fluence.

Of interest are the variation of the reflected pulse energy with the amount of the excitation energy fluence and the variations of the pulse width with the level of the excitation.

5.3.1 Time-Integrated Infrared Reflectivity

We have performed a series of experiments to investigate the behaviour of the time-integrated infrared intensity as a function of the visible pulse excitation energy fluence incident on the GaAs switch. This allows us to determine the visible irradiation level required to induce a measurable infrared reflection change in the GaAs switch. This type of experiment is also essential to perform because the time-integrated reflectivity should provide an initial check on the validity of the infrared reflectivity model proposed in Chapter 3. That is, time-resolved measurements are usually difficult to interpret. However, by integrating the infrared reflectivity pulses calculated for various initial e-h plasma densities, one should be able to fit the calculations to the experimental data.

The basic experimental setup and procedures are outlined in section 4.9. Because of the sensitivity of the model to the photoinjected carrier density, to carry out this study

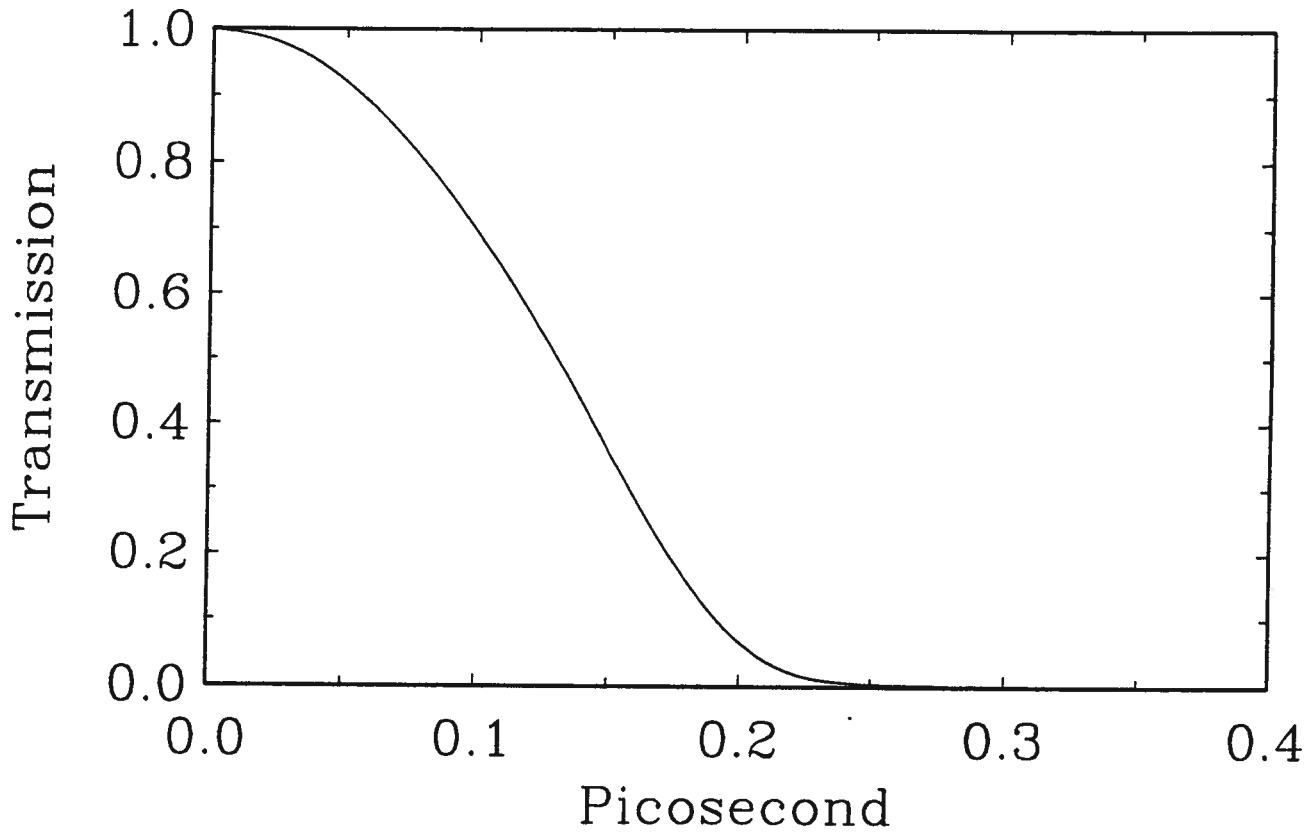

Figure 5.8: Calculated transmission of p-type Si as a function of time.

we must first determine the initial e-h photoexcited carrier density. Figure 5.9 shows a photograph of the observed time-integrated reflectivity pulse measured simultaneously with its corresponding visible excitation pulse. The integrated temporal profiles of these pulses correspond to the time-integrated reflectivity and the excitation energy.

A typical result of the experimental data is presented in figure 5.10. The figure shows the data point for each single shot, and the scatter of the data points is indicative of the experimental uncertainty. The horizontal scale of the figure is calibrated (from the excitation energy recorded directly by the detector) in terms of the plasma density. We should point out that this conversion is meaningful only for a well-characterized laser beam profile.

One way to estimate the carrier density is by knowing that the maximum possible excitation energy is 0.2 mJ, which is deposited into a 0.5 mm$\times$3 mm spot on the wafer at an incidence angle of 80°. This allows the calculation the maximum energy fluence. By using the Fresnel reflectivity equation for S-polarized light, the above angle of incidence, a refractive index of 3.4 and an absorption coefficient of γ= 4.5$\times 10^4$ cm^{-1} at λ= 616 nm, it can be shown that 20% of this fluence is absorbed by the wafer and thus generates free carriers. The product of this absorbed fluence, F_{ph}, γ, and the assumed quantum efficiency of unity gives the maximum possible free-carrier density, n_{om}, at the wafer surface, which would result in the absence of any recombination or diffusion mechanisms acting during the time scale of the generating pulse. This value is calculated to be $n_{om} \approx 2\times 10^{20}$ cm^{-3}. This method for obtaining the plasma density can provide a good estimate only for high excitation levels ($\sim 2n_c$). A better estimate of the plasma density around the critical density and over a wider density range can be obtained from a simple experimental procedure. By plotting the measured time-integrated reflectivity signal as a function of 'low' visible excitation energy, we obtain a linear relationship. The least square fitted line through these points intercepts the excitation energy horizontal axis

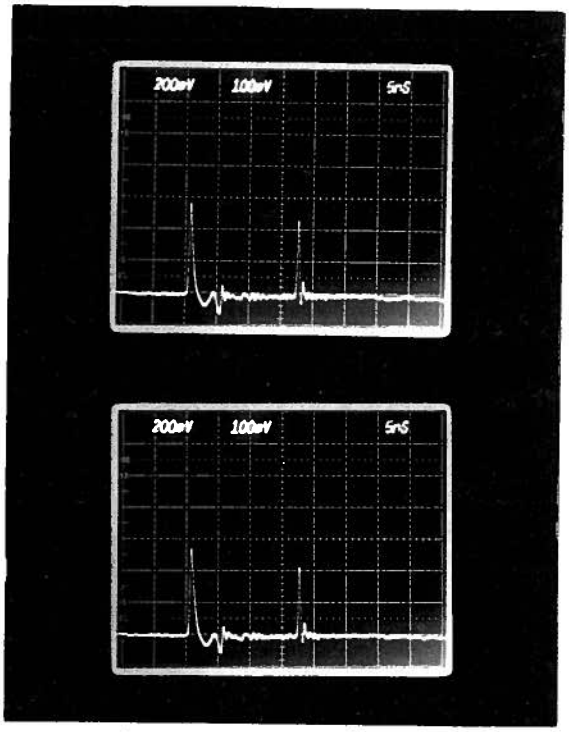

Figure 5.9: Typical ultrafast reflected infrared pulses (left) and their corresponding excitation visible pulses (right). The bottom photograph is presented to illustrate the reproducibility of the experimental signals.

at n_c. We have used the latter method throughout our experimental analysis to obtain more accurate values for the carrier density.

We normalized the maximum excitation energy to the n_c value and plotted in figure 5.10 the reflected infrared energy as a function of γF_{ph} in terms of the critical density n_c. The data in figure 5.10 show that over the density range of $1.5 \leq \gamma F_{ph}/n_c \leq 5$ the reflected infrared energy increases linearly with the excitation energy. For excitation energies with $\gamma F_{ph}/n_c > 6$ the reflected infrared energy starts to saturate and remains effectively constant for $\gamma F_{ph}/n_c > 8$. Integration of the calculated reflectivity pulses from the model presented in Chapter 3 shows that the experimental data do not agree with the model predictions. Our calculations show that an increase of an initial plasma density from $n/n_c = 1$ to $n/n_c = 6$ results in an integrated reflectivity pulse ~ 180 times larger than the one calculated at the critical density. This is just a representation of the width of the reflectivity pulse. However, the experimental results (see figure 5.10) indicate that the integrated reflectivity is only ~ 13 times its value at the critical density. Moreover, the observed saturation of the time-integrated signal cannot be obtained with such model. Contrary to our observations, the calculated time-integrated signal increases strongly with initial plasma density. Obviously, the saturation of the signal is a clear indication that the reflectivity pulse widths remain almost unchanged when the GaAs switch is operated in the region $\gamma F_{ph}/n_c > 6$. The temporal behaviour of the reflectivity pulses cannot be explained by diffusion model; a mechanism which is more significant at high plasma densities must be included in the calculations to account for these observations.

5.3.2 Reflection-Reflection Correlation Measurements

Here, we report the first experimental results on time-resolved ultrafast reflection from optically induced transient plasmas. As mentioned previously in the discussion of the reflection-reflection correlation technique (section 4.10.1), this type of experiment is not

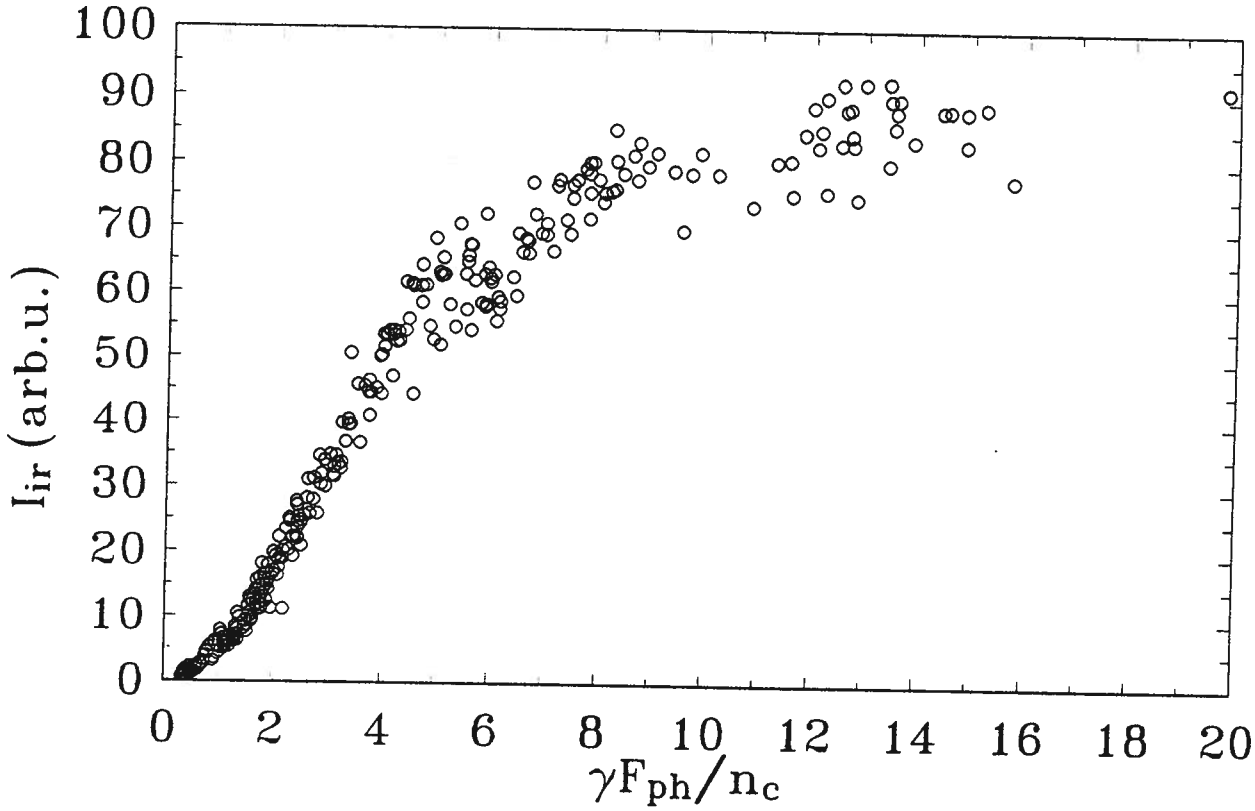

Figure 5.10: Experimental results of the normalized time integrated reflectivity as a function the normalized free-carrier density.

sensitive to the infrared pulse shape; however, one should be able to obtain an overall pulse duration, which may help to explain the observed time-integrated reflection saturation at high excitation fluences. That is, if the infrared reflected pulse duration does not change with the level of photoinjected carriers, then this can be easily detected from the measurements of the full widths at half maximum of the durations of the reflection-reflection correlation signals.

Several experiments are performed at various levels of optical exciation. Typical results from the reflection-reflection correlation measurements are presented in figures 5.11, 5.12, and 5.13 for $\gamma F_{ph}/n_c$= 3, 5, and 7, respectively. Here, the correlation signal is normalized to a reference reflection obtained when the excitation pulse on the second switch is blocked-off and the transmission through it is detected. The data points are averaged over at least 10 shots, and the error bars are an indication of the standard error of the experiment.

The time delay t= 0 in the figures corresponds to the peak overlap between the reflected infrared pulse from the first GaAs switch and the peak of the visible excitation pulse at the second GaAs switch. The measured correlation signal represents the width of the dominant temporal features in the infrared pulse. The reason for the asymmetry of the reflection-reflection measurements is attributed to an experimental error in the delay line scan. For long time scans greater than 20 ps, the critical alignment of the infrared and the visible spots changes slightly. The asymmetry gives us information about the uncertainty of the measurements. This uncertainty is estimated to be $\pm$ 3 ps.

Even though the graphs correspond to different excitation energy fluences, all of the figures show the effective correlation width to be $\sim$ 17 ps at half of the full width half maximum. The experiments indicate that the infrared pulse width seems to be independent of the plasma density above $3n_c$. Evidently, this effect supports the results obtained from the time-integrated reflectivity experiments. The reflectivity pulse widths

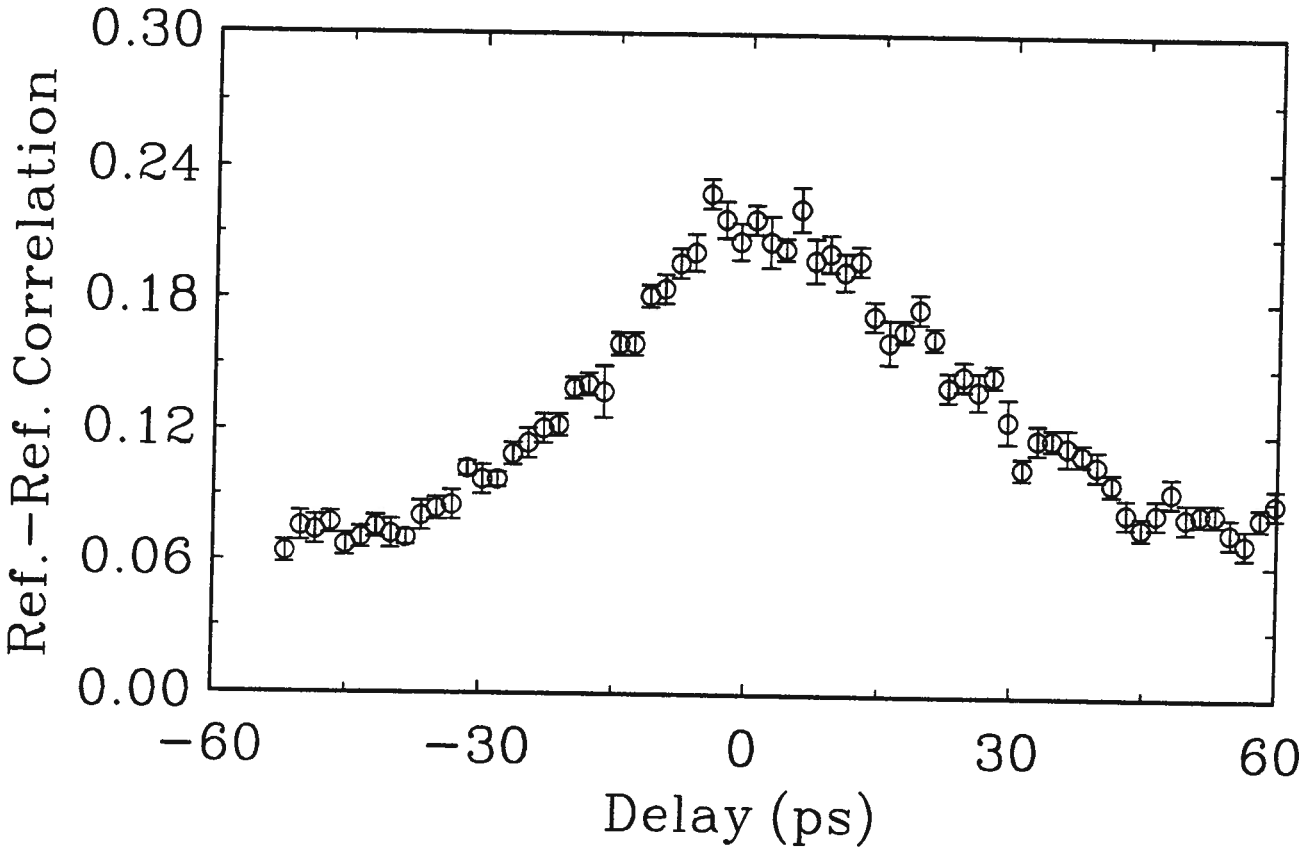

Figure 5.11: Reflection-reflection correlation signal for an excitation fluence corresponding to $\gamma F_{ph}/n_c = 3$.

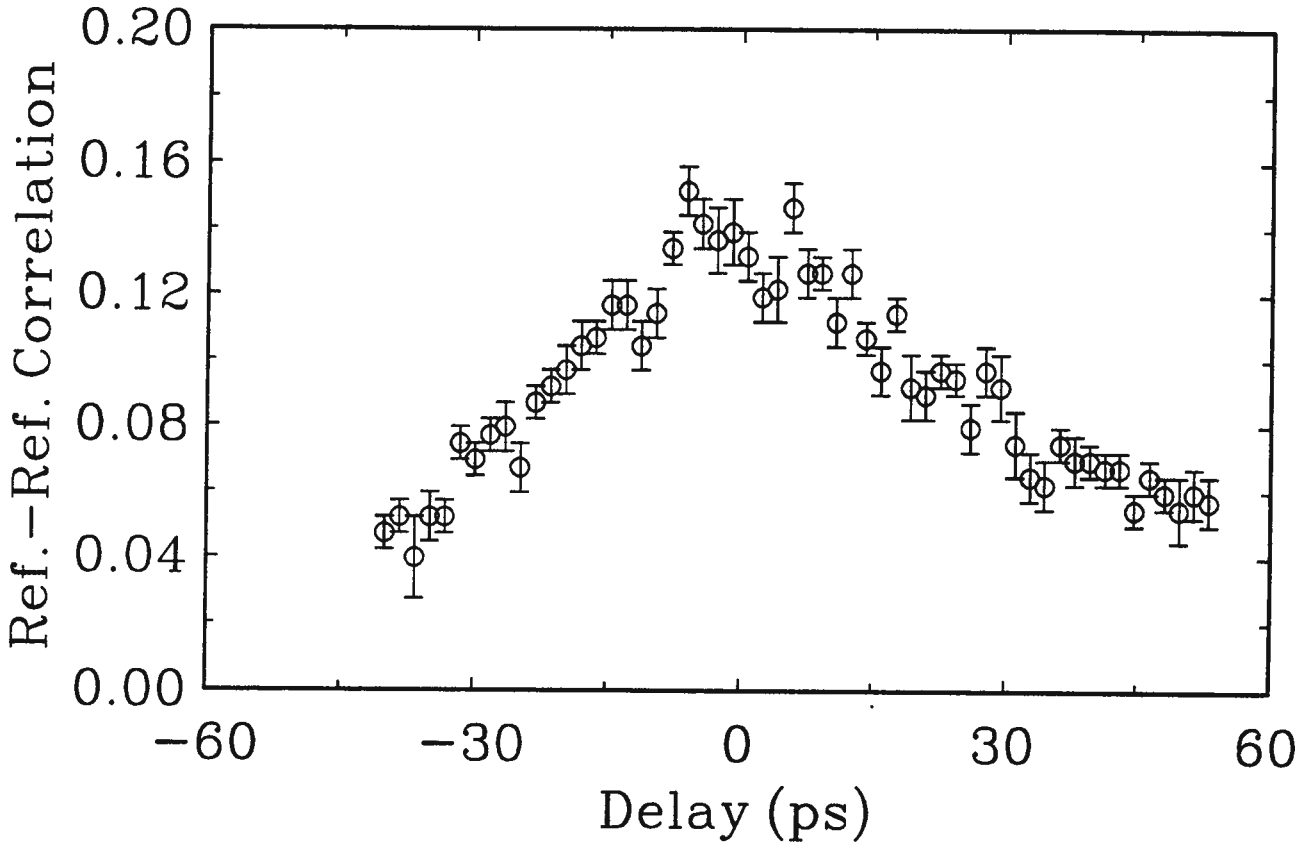

Figure 5.12: Reflection-reflection correlation signal for an excitation fluence corresponding to $\gamma F_{ph}/n_c = 5$.

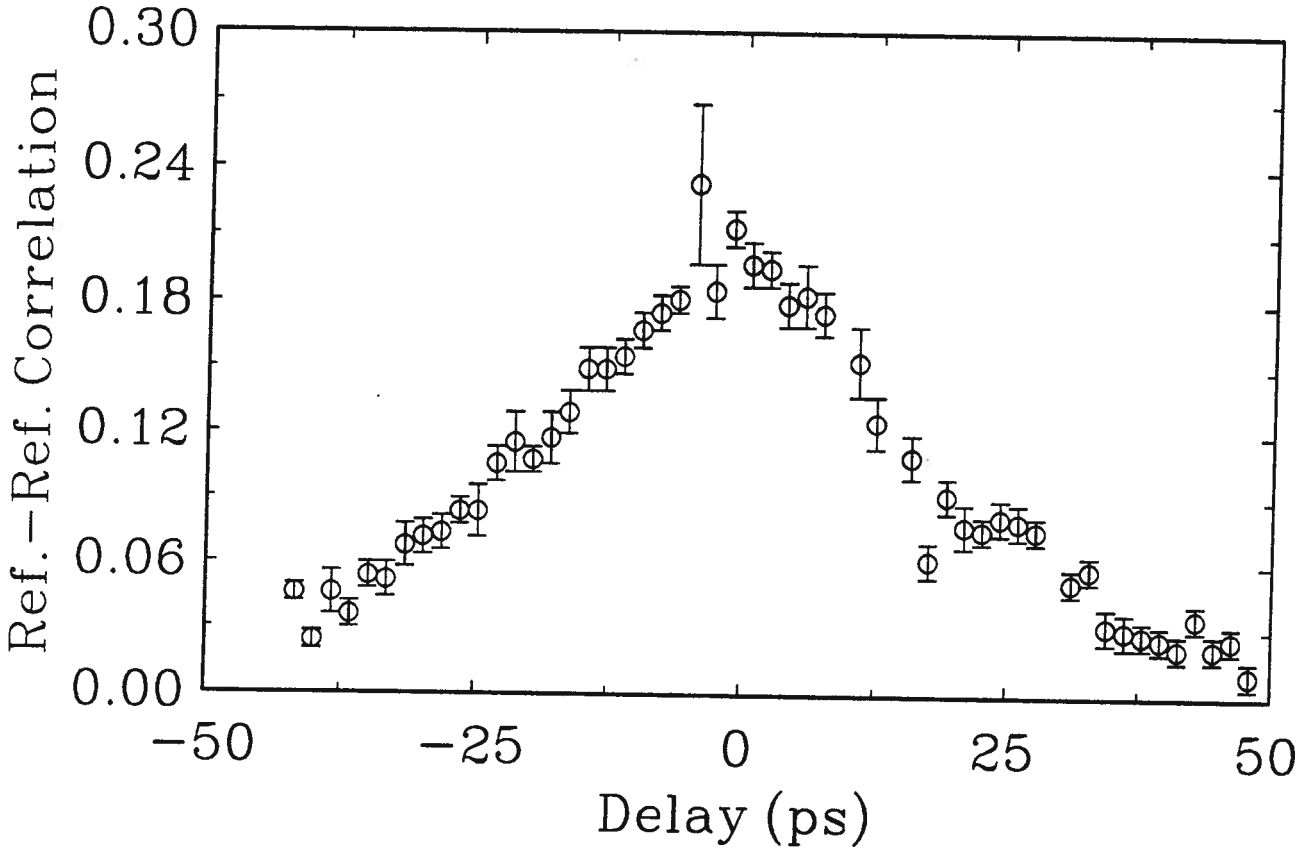

Figure 5.13: Reflection-reflection correlation signal for an excitation fluence corresponding to $\gamma F_{ph}/n_c = 7$.

do not scale with the calculated pulse widths as indicated by the diffusion model.

Unfortunately, with our limited infrared laser power and detection sensitivity, experiments at $\gamma F_{ph}/n_c < 2$ are not possible, since the level of the reflected signal to the background noise is high enough to wash out the reflection-reflection correlation signal. With our reflection-reflection correlation technique it is not easy to arrive at an exact pulse shape by these measurements alone. Of importance to our analysis is the time that the plasma density takes to reach the critical density. This will be discussed in the next section.

5.3.3 Cross-Correlation Measurements

In order to understand the nature of the disagreement between the diffusion based infrared reflectivity model and the experimental results, one needs to know the exact shape of the reflected infrared pulses, so that the time evolution of the plasma density can be inferred from the temporal shapes of the reflectivity signals. It has been shown before [84, 85] that the infrared reflectivity of a photoexcited GaAs wafer shows some significant variation with surface free-carrier density n_o. It has a minimum when n_o/n_c equals $(\epsilon - 1)/\epsilon$: ϵ is the dielectric constant of the bulk GaAs. At $n_o = n_c$ the reflectivity has a sharp maximum. Just above n_c it has a minimum and from then on increases monotonically with n_o. The magnitude of the features at $n_o/n_c = (\epsilon - 1)/\epsilon$ and 1 depend on the magnitude of the free-carrier absorption. It is therefore expected that the reflected infrared pulse will show some significant temporal variation as n_o decays from its maximum initial value. As shown in section 4.10.2, these measurements display $I_{ir}= \int_0^t R(t')dt'$ and its slope therefore determines the magnitude of the reflectivity.

We performed several time-resolved cross correlation measurements over a wide range of pump intensities which we relate to $\gamma F_{ph}/n_c$ of figure 5.10. Throughout the experimental work, we selected a fixed excitation energy range and we studied the reflected infrared

energy as a function of the time delay between the infrared and the optical excitation pulses. Since the detection sensitivity depends on details of the optical alignment and is likely to change from day to day, the experiments were performed in the following way. Before realignment and laser retuning became necessary, it was possible to conduct two experimental sequences. By placing two different sets of neutral density filters into the pump beam, the two experimental sequences covered two different ranges of $\gamma F_{ph}/n_c$ of which the first one was chosen to fall into the linear part of figure 5.10. At the start, at the end, and at various times during each experimental sequence, the control beam operating the Si cut-off switch was blocked-off and the measured infrared energy was displayed as a function of the monitored energy to derive reference signals. A least square fitted line was placed through the reference data points of the first sequence. Setting the line intercept of the pump energy axis equal to $\gamma F_{ph}/n_c = 1$ normalizes the pump energy. We have found that it is necessary to perform the 'reference' experiment at the beginning and at the end of the temporal scan.

At each optical delay line setting, which determines the cut-off time, the average of at least 30 infrared energy signals measured for the same pump energy was determined and normalized to the reference infrared signal for the equivalent $\gamma F_{ph}/n_c$. Due to the importance of this type of experiment, we have performed over 40 experiments covering a wide range of experimental conditions. The basic features of the experimental setup are discussed and outlined in section 4.10.2. The optical and data collection systems are constantly improved throughout this work. Figures 5.14 and 5.15 show the results from two experimental days for four values of $\gamma F_{ph}/n_c$ (0.7 and 2 in figure 5.14, 3 and 15 in figure 5.15) which are representative of all experiments performed. They display the normalized infrared energy I_{norm}, as function of cut-off delay time. Obviously towards the end of the reflected infrared pulse I_{norm} has to approach the value of 1. The detected infrared signals for figure 5.14 are quite small and as a result the standard error per

point is of the order of 20%. The best fitting curves through the points have a constant slope indicating basically a constant reflectivity after photoexcitation over the period examined in the experiments. After 50-ps, I_{norm} is still less than 0.2 which indicates that the reflected infrared pulses have a duration of several 100 ps. For the experiments of figure 5.15 the situation is quite different. The standard error per point during the first 40-ps is $\leq$ 4% increasing to 7% at times later than 60 ps. At the end of the examined period of 100 ps, the slope, and thus the reflectivity, has decreased to zero within the measurable accuracy. Fitting curves through each of the two sets of data points and measuring their slope as a function of time results in normalized infrared reflectivity pulses of the form shown in figure 5.16. The most prominent features of these pulses are the unresolved large transient maximum of <0.8 ps duration at the time of the pump pulse and the minimum observed 28 ps later which we identify as the reflectivity minimum at $n_o/n_c = (\epsilon - 1)/\epsilon$.

Also remarkable is that the normalized infrared pulses for the two energy fluences differing by a factor of five, up to t= 34 ps, are basically identical. However, since the reference signals at $\gamma F_{ph}/n_c = 15$ are three times larger than those at $\gamma F_{ph}/n_c = 3$ the actual reflected intensity for both pulses differs by a factor of three.

5.3.4 Discussion of the Time-Resolved Results

To describe the experimental results, we will consider two processes (diffusion and recombination) which determine the time evolution of the plasma density. Our previous calculations show that the effects of surface recombination on the time evolution of the plasma density is unimportant [84, 85] and hence is ignored in the following calculations. Carrier diffusion is known to increase with carrier temperature and decrease with lattice temperature; moreover, the diffusion coefficient is also shown to have a strong dependence on the carrier density above a certain value where carrier degeneracy is reached

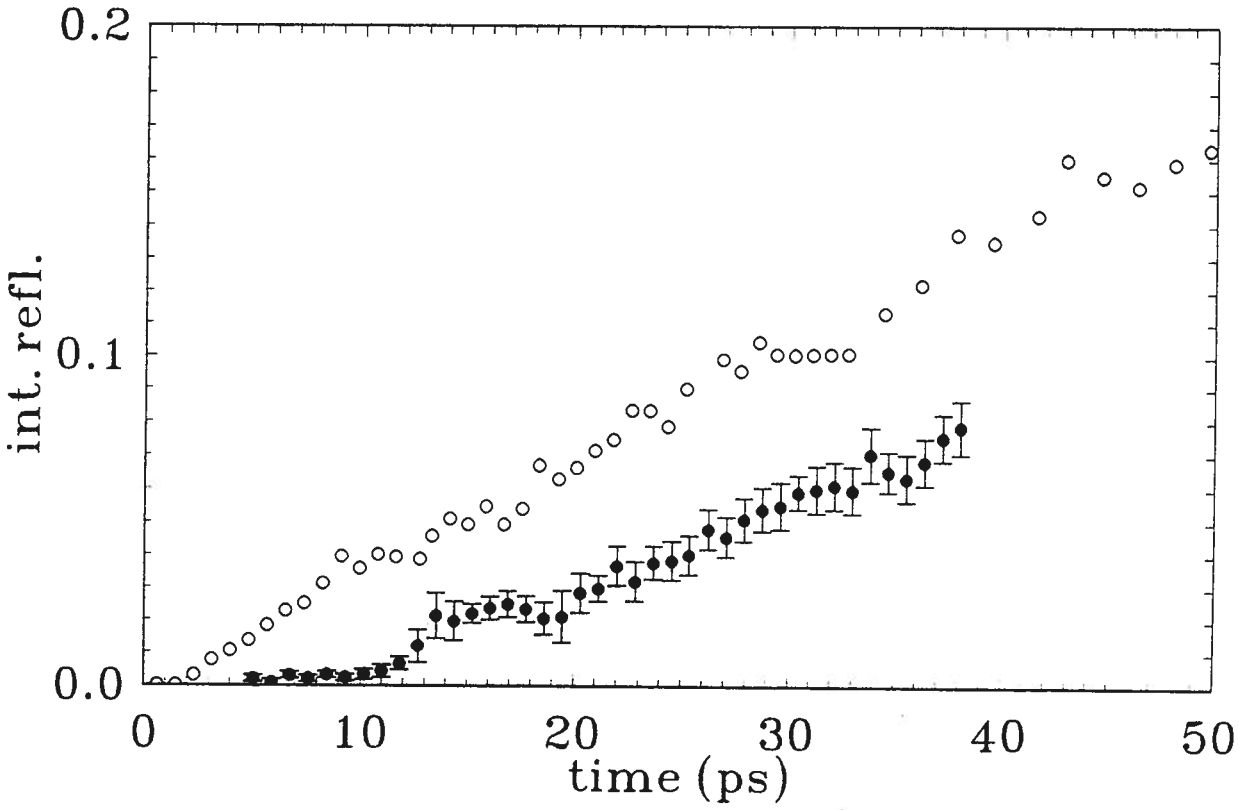

Figure 5.14: Cross-correlation signal as a function of time for $\gamma F_{ph}/n_c$= 0.7 (solid), 2.0 (empty).

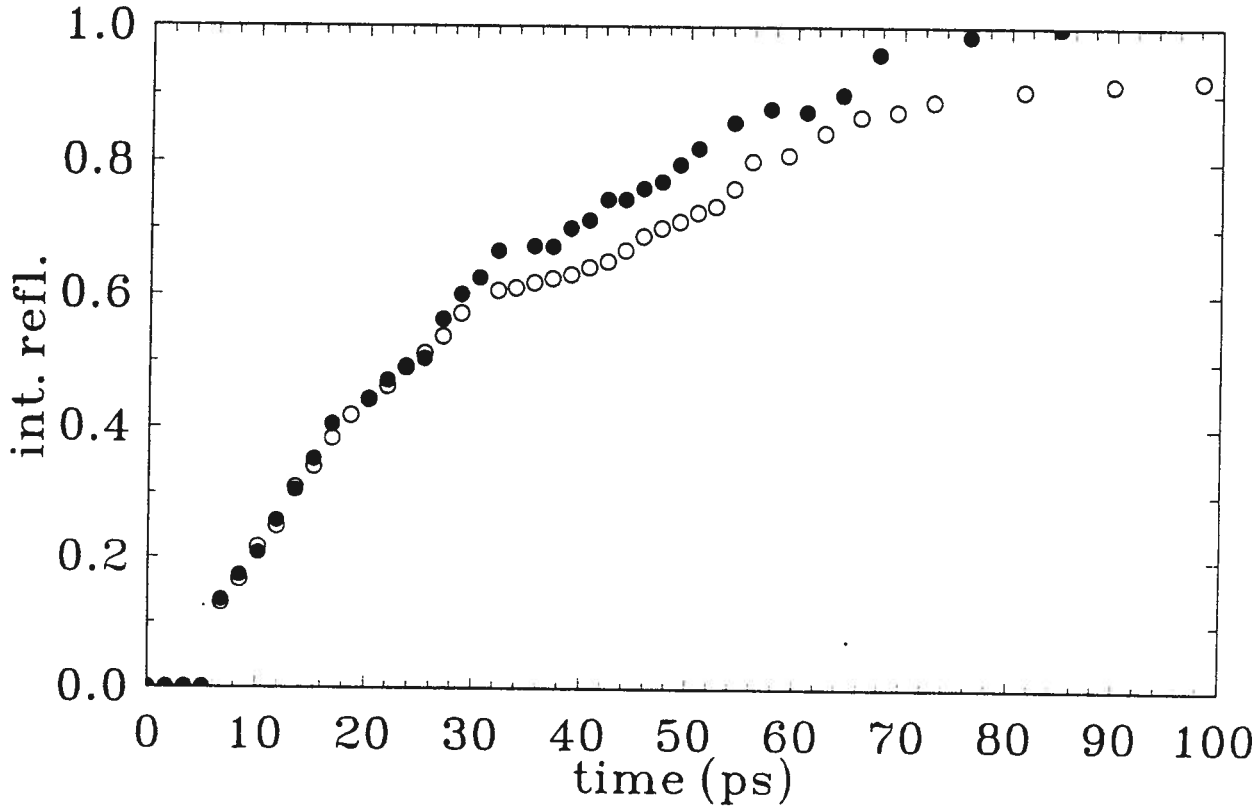

Figure 5.15: Cross-correlation signal as a function of time for $\gamma F_{ph}/n_c$= 3.0 (empty), 15.0 (solid).

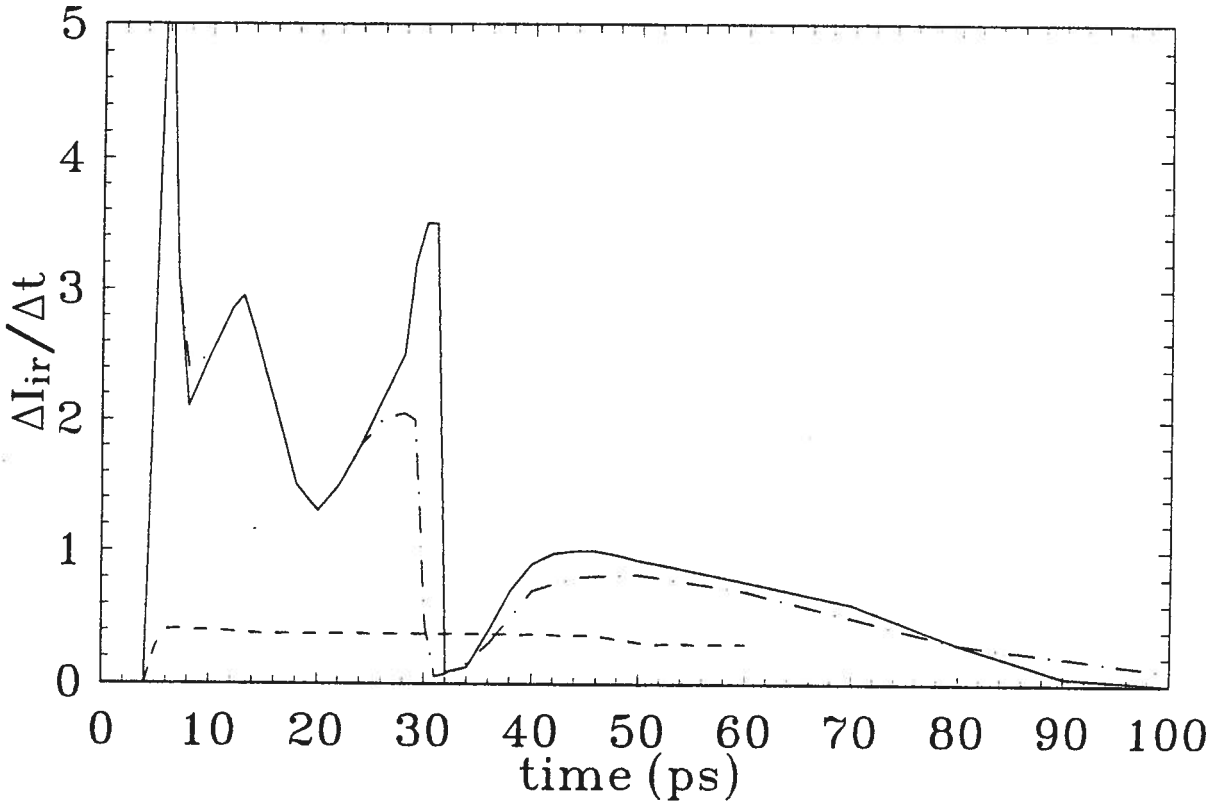

Figure 5.16: Reflectivity pulses as a function of time for $\gamma F_{ph}/n_c$= 3 (solid), 15 (dash-dot), and 2 (dash).

[173]. The experimental results show that once the initial carrier density surpasses $5n_c$, the integrated reflectivity saturates with increasing excitation fluence. This cannot be explained by diffusion of the free carriers alone. In fact, using various models for calculating the diffusion coefficient [173] in the reflectivity calculations show that the effect of the diffusion coefficient on the decay of the surface density from n_{0m} to n_c is negligible. The time that it takes the reflectivity to reach a minimum determines the time needed for the density of the photoexcited carriers to reach the critical density. This time is measured to be $\sim$ 28 ps; by then the photoexcited carriers have cooled to the lattice temperature and thus temperature effects on the diffusion coefficient are insignificant. Our calculations show that diffusion is important for carrier densities below the critical density. Hence, the simplest approach of treating the diffusion coefficient as temperature and density independent is adequate in the following analysis.

One would expect that the decay of the free-carrier surface density, n_o, during the first hundreds of picoseconds after photoexcitation, is dominated by diffusion, while the recombination processes catch up in nanosecond time scales. In order to study the evolution of $n_o(t)$ due to diffusion one has to solve the diffusion equation. However, such a solution shows [84, 85] that the free-carrier density as a function of distance from the surface, z, quickly resembles that of a gaussian distribution. Since a gaussian profile is a solution to the diffusion equation, we can assume for the present that the density, $n(z,t)$ is given by,

$$n(z,t) = n_o(t)exp\{-(\gamma(t)z)^2\} \tag{5.23}$$

with $n_o(t)/\gamma(t)$= constant. From equation 5.23 and the diffusion equation (3.54), we obtain a differential equation describing the time evolution of plasma density:

$$\frac{\partial\gamma}{\partial t} = -2D\gamma^3. \tag{5.24}$$

Then taking $n_o(0)=\gamma F_{ph}$ and setting $\gamma(t=0)=\gamma$, we find for n_o(t),

$$n_o(t) = \frac{\gamma F_{ph}}{\sqrt{1+4\gamma^2 Dt}}. \tag{5.25}$$

The time, t_c, it takes for $n_o(t)$ to decrease to the critical density can then be calculated. For the given values of γ and D this is:

$$t_c = 6.17\{(\gamma F_{ph}/n_c)^2 - 1\}\text{ps}. \tag{5.26}$$

The main contribution to the total reflected energy, I_{ir}, pulses of figure 5.10 for $\gamma F_{ph}/n_c > 3$ is generated during this time. One can estimate for these pulses,

$$\int_0^\infty R(t)dt \approx < R > t_c. \tag{5.27}$$

The average reflectivity $< R >$ increases also, but not rapidly with $\gamma F_{ph}/n_c$. At the very least, one would expect in the presence of diffusion only, that the pulse, I_{ir}, of figure 5.10 like t_c, increases with the square of the fluence. Figure 5.10 shows that this is not the case, instead I_{ir} initially increases linearly with γF_{ph} and then quickly saturates. Figure 5.16 indicates that t_c also saturates at $\sim$ 25 ps. In the case of carrier diffusion, one would have expected for $\gamma F_{ph}/n_c = 15$ a time t_c of the order of one nanosecond.

In order to show that normal Auger recombination at the given rate cannot explain the observed saturation, we examined a hypothetical situation in which only this process determines the decrease of $n_o(t)$. The time t_c is given by the solution to equation 3.48:

$$t_c = 14\{1 - (n_c/\gamma F_{ph})^2\}\text{ns}. \tag{5.28}$$

In order for this time (due to Auger recombination) to be comparable to t_c, due to diffusion only, it requires $\gamma F_{ph}/n_c \sim 48$. Therefore, if only diffusion and normal Auger recombination determine $n_o(t)$, the I_{ir} of figure 5.10 should increase with $(\gamma F_{ph}/n_c)^2$ over the range shown and would only be expected to saturate at twice the maximum value

attained in this experiment. Also t_c should only saturate at ns-time scales. Clearly, an additional, much more rapid recombination process governs the dynamics of high density photoexcited free carriers. This mechanism should be responsible for the saturation of the time-integrated reflectivity signal and for the observed t_c being density independent. That is, a recombination process whose recombination rate depends on the photoexcited plasma density should be considered in the analysis.

We can model our experimental results if we assume a decay process of the same form as Auger recombination at a rate of $\Gamma = 1.9\times10^{-28}$ cm^6/s. This could, for example, be a two-body recombination process for which the decay rate is nearly a linear function of free-carrier density.

5.3.5 Modeling of Free-Carrier Density and Reflectivity

In order to model the free-carrier density development one needs to know the excitation pulse shape. For mathematical convenience, we assume that this pulse has the form:

$$P(t) = 2\gamma F_{ph}\frac{t}{\tau_p^2}exp\{-(t/\tau_p)^2\}. \tag{5.29}$$

For τ_p= 0.49 ps this pulse has the same width as our laser pulse. In term of normalized densities $\nu = (n/n_c)$ and $f = (\gamma F_{ph}/n_c)$, we write the time evolution of the normalized plasma density as:

$$\frac{\partial\nu}{\partial t} = 2f\frac{t}{\tau_p^2}exp\{-\gamma z - (t/\tau_p)^2\} + D\frac{\partial^2\nu}{\partial z^2} - \kappa\nu^3. \tag{5.30}$$

Here $\kappa = \Gamma n_c^2$, and for Γ we take the rate from the previous section. The first term on the right hand side results from the e-h generation rate, the second term arises from the diffusion of the carriers, and the last term describes the recombination process. In order to perform numerical integrations we simplify the diffusion term. If the distribution has a gaussian shape of the form $\nu = \nu_o exp\{-[z/d(t)]^2\}$, where ν_o is the surface density, then

the diffusion term simplifies to:

$$D\frac{\partial^2\nu}{\partial z^2} = \frac{2D}{d^2(t)}\{2[z/d(t)]^2 - 1\}\nu(t,z) \tag{5.31}$$

with

$$d(t) = \frac{2N(t)}{\sqrt{\pi}\nu_o(t)}. \tag{5.32}$$

Here $N(t)(= \int_0^\infty \nu(z)dz)$ is the total normalized number of free carriers. We approximate the diffusion term by this form and now can numerically integrate the differential equation at each position z with the initial condition $\nu(0,z)= 0$. After each time step we integrate over the profile to determine $d(t)$. In performing the calculations one has to take into account that the density varies most rapidly near the surface and at early times. We chose a dimensionless length coordinate $x = exp(-\gamma z)$ and divided the interval $0 \leq x \leq 1$ into 100 equal steps. The time intervals progressed with step number p as $\Delta t_p/\tau_p = 10^{-4}p^3$.

Figure 5.17(a) shows the resulting density profiles at various times for $\gamma F_{ph}/n_c = 10$, and figure 5.17(b) indicates the temporal variation of the surface density for the same case. Profiles for all values of $\gamma F_{ph}/n_c \geq 3$ are quite similar and reach $\nu_o = 1$ at the same time. The only difference exists in an increase of the sharp initial surface density feature and an increase of the width of the density profile as the photon flux is increased.

Next we proceed to calculate the reflectivity for infrared radiation incident with Brewster's angle if $\nu_o = 0$. We use the Drude model for the dielectric constant $\{\epsilon(\nu) = \epsilon_b[1 - \nu(1 - i\alpha)]\}$ and introduce

$$\psi = \sqrt{\epsilon_b}\{1 - \nu_o(t)[1 - i\alpha(t)]\} \tag{5.33}$$

and

$$\chi = \sqrt{\epsilon_b\{1 - \nu_o(t)[1 - i\alpha(t)]\} - \nu_o(t)[1 - i\alpha(t)]}. \tag{5.34}$$

Then the amplitude reflectivity from the surface is given by [84, 85]:

$$r_o(t) = \frac{\psi - \chi}{\psi + \chi}. \tag{5.35}$$

Here we assumed that the imaginary part of the dielectric function, $\alpha(t)$, is a function of time. It arises from the free-carrier absorption and is a function of free-carrier temperature. In order to include the contribution to the reflectivity arising from the density profile inside the wafer, we make the use of density steps introduced previously. Similar to the previous approximation made for calculating the transmission cut-off, the plasma layer is treated as a multilayered structure of variable density. Each layer is considered to have a homogeneous density profile. Taking the density at step number m as ν_m we introduce:

$$a_m = 1 - \nu_m(t)[1 - i\alpha(t)] \tag{5.36}$$

and

$$b_m(t) = \sqrt{\epsilon_b\{1 - \nu_m(t)[1 - i\alpha(t)]\} - \nu_m(t)[1 - i\alpha(t)]}. \tag{5.37}$$

In terms of these functions the reflectivity of the density step from $m-1$ to m is given by:

$$r_m = \frac{a_m(t)b_{m-1}(t) - a_{m-1}(t)b_m(t)}{a_m(t)b_{m-1}(t) + a_{m-1}(t)b_m(t)}. \tag{5.38}$$

The transmission through the density step in the incident direction is $(1 - r_m)$ and it is $(1 + r_m)$ for propagation in the opposite direction.

In order to find the contribution from the whole profile we also have to consider the phase change, β_m due to the propagation through the different optical paths of individual layers. Writing for a length Δz_m of a plasma layer m:

$$\beta_m = k_o \Delta z_m \sqrt{\frac{\epsilon_b}{\epsilon_b + 1}} b_{m-1}(t) \tag{5.39}$$

one finds for a density profile reflectivity:

$$\rho(t) = \sum_m exp(2i \sum_{l=1}^{m} \beta_l) \prod_{l=1}^{m} [1 - r_{l-1}^2(t)] r_l(t). \tag{5.40}$$

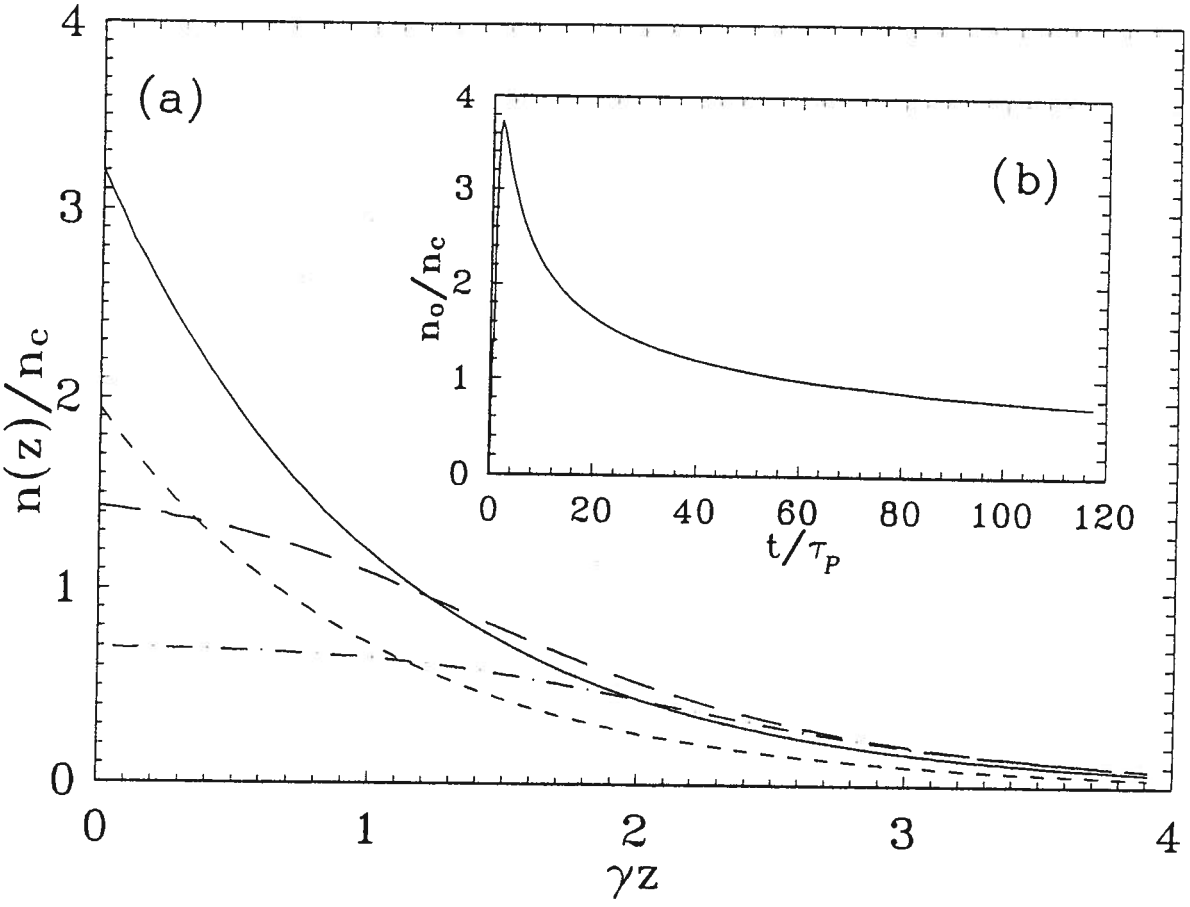

Figure 5.17: (a) Normalized density as a function of the longitudinal position and for times t/τ_p= 0.5 (short dash), 1.0 (solid), 27.00 (long dash) and 125.00 (dot-dash). The initial normalized plasma density $\gamma F_{ph}/n_c$= 10. (b) The insert indicates the normalized surface plasma density as a function of normalized time.

The total reflectivity from the plasma layer is due to the individual reflectivities from each homogeneous layer and is given by:

$$r(t) = \frac{r_o + \rho(t)}{1 + r_o(t)\rho(t)}. \tag{5.41}$$

Before we can calculate the intensity reflectivity $\mid r(t) \mid^2$ we have to assume a function for the absorption term, $\alpha(t)$. Based on the experimental results for initial carrier densities $> n_c$, we always measure a distinct reflectivity minimum which approaches zero after a time of the order of 28 ps. For this minimum reflectivity to exist, we require the imaginary part of the dielectric function to be much smaller than 1 (i.e. small free-carrier and intervalence band absorption). We can describe phenomenologically the time evolution of the free-carrier and intervalence band absorptions by a single absorption coefficient $\alpha(t)$. The coefficient can be written as:

$$\alpha(t) = 0.001 + f\{1 - exp[-(t/8\tau_p)^2]\}exp[-(t/10\tau_p)]. \tag{5.42}$$

The carrier absorption coefficient and thus the imaginary component of the dielectric constant is a function of the free-carrier temperature. The magnitude of the absorption is enhanced at higher carrier temperature. In this case, one has to consider the rate of cooling of the hot carrier distribution at a high initial carrier density which in turn should reflect the rate of decay of free-carrier absorption. The cooling rate is taken to be $\sim (10\tau_p)^{-1}$, which is slightly larger than the value of $\sim$ 1 ps from the measurements presented in reference [174]. Moreover, we also have to assume that it takes a finite time after photoexcitation for the free-carrier absorption to reach a maximum value, which is proportional to the absorbed photon flux. The constant term in the expression in equation 5.42 arises from the absorption at room temperature. Figure 5.18 shows the reflectivity pulses for f= 10 and 2 respectively. Also shown are, for f= 10, the integrated reflectivity simulating the reflectivity cross-correlation and the reflectivity-reflectivity correlation

measurements. Comparison with the experimental results of figures 5.13, 5.15, 5.16 to figure 5.18, and figure 5.10 to 5.19 , indicates that the model provides a good representation of the experimental situation. Note that the time scale in figure 5.19 is normalized to the excitation pulse width τ_p. It also shows that the situations in which the maximum free-carrier density is below critical ($f < 2.5$) one obtains very long, nearly constant, low-intensity, reflected infrared pulses. In figure 5.19 the total integrated reflectivity is shown as a function of $f = \gamma F_{ph}/n_c$. The calculations are performed by integrating the reflectivity curves for various initial plasma densities. The final integration time is taken to be 200 ps. Comparison with figure 5.10 again indicates the good agreement between the model and the experiment.

Clearly, by invoking an additional two-body recombination mechanism whose recombination rate is taken to be a function of the carrier density, we are able to obtain a good agreement between the experimental results and the proposed model calculations. So far we have no explanation as to the exact nature of the recombination mechanism.

We believe that this phenomenological model is essentially correct; however, more experimental and theoretical study is required to completely determine the exact nature of the recombination process.

5.4 Frequency Spectrum Measurements

Measurements of the frequency bandwidths, Δf_p of the reflected infrared pulses can provide complementary information on the duration of the pulses, $\Delta\tau_p$. We have performed this type of experiment for the following reason: since the infrared reflection occurs from a time-dependent plasma layer, one expects the infrared pulse to have a frequency chirp.

The overall pulse duration can be obtained by only one single shot measurement. However, the exact pulse width-bandwidth product for an arbitrary pulse shape depends

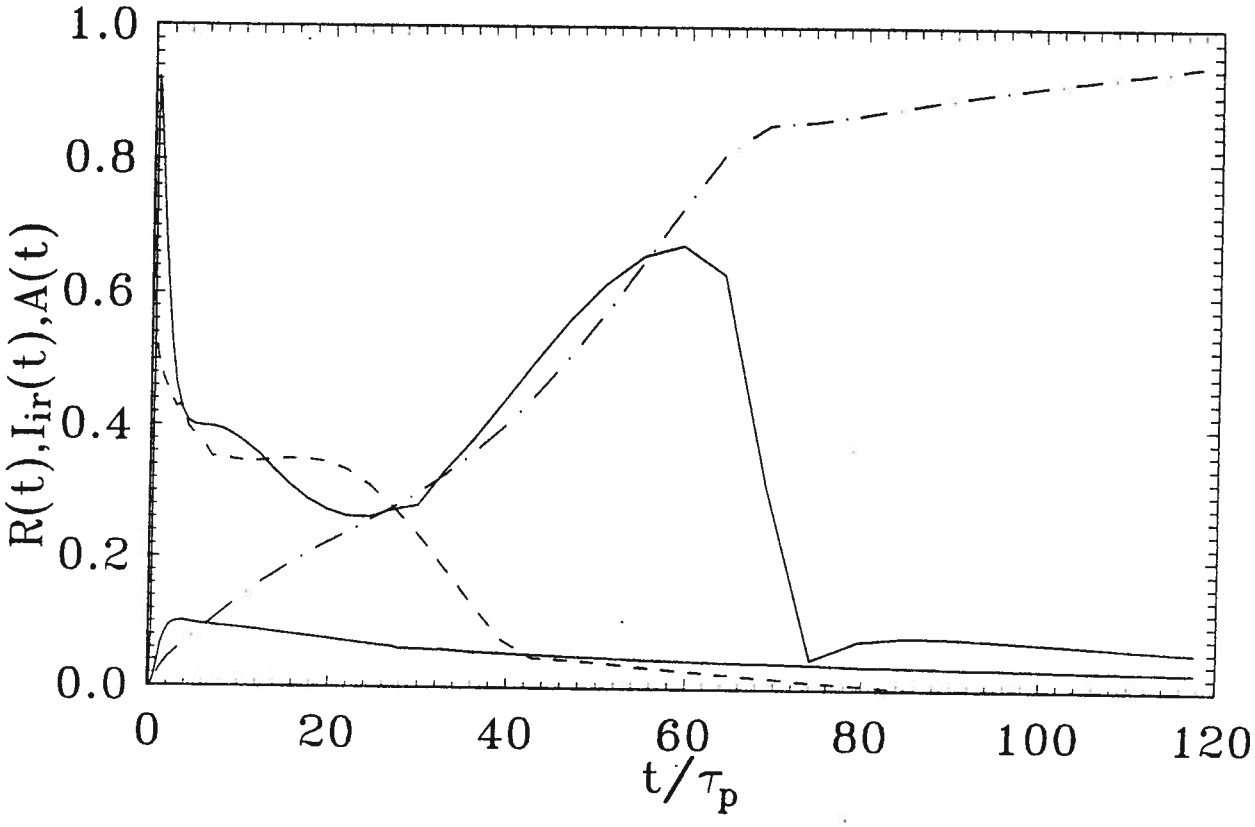

Figure 5.18: Model calculations as a function of normalized time of: the normalized infrared pulses for $\gamma F_{ph}/n_c$= 10 (upper solid line) and 2 (lower solid line), normalized cross-correlation signal for $\gamma F_{ph}/n_c$= 10 (dash-dot), and normalized reflection-reflection correlation signal for $\gamma F_{ph}/n_c$= 10 (dash).

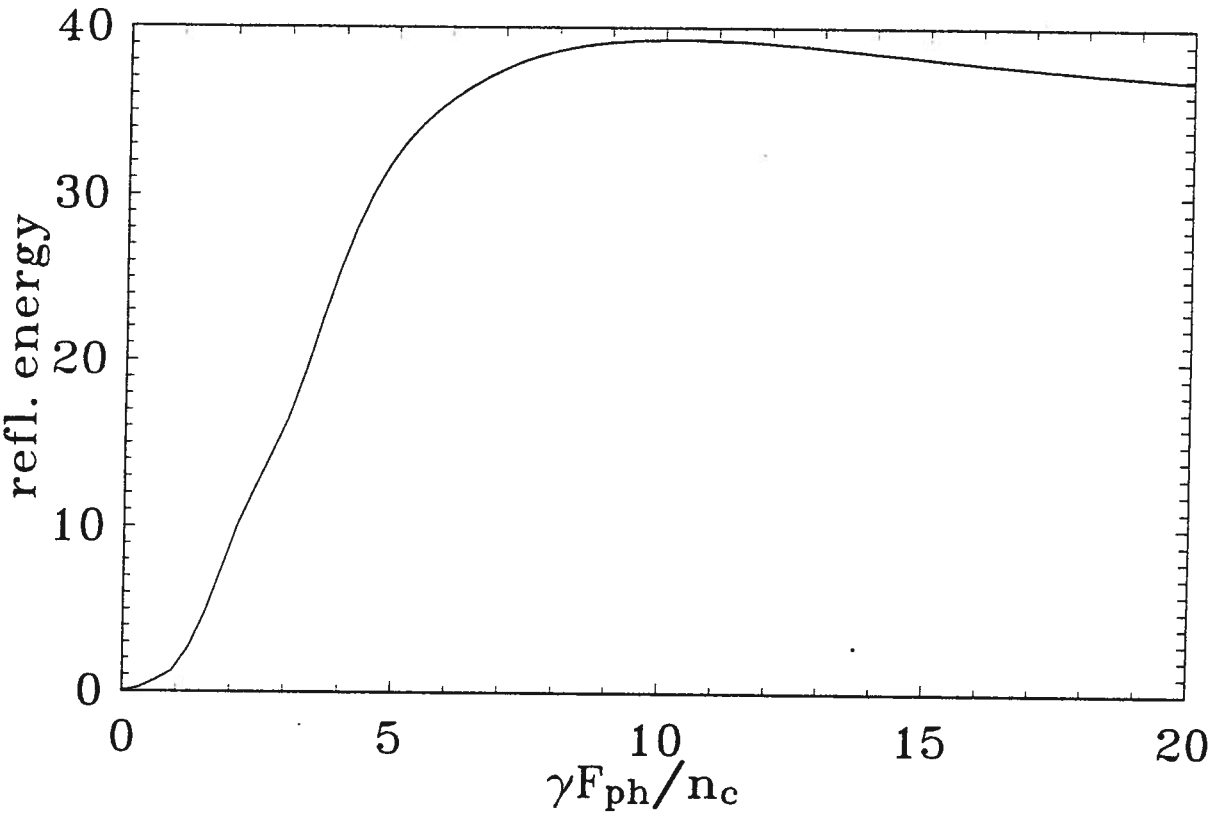

Figure 5.19: Model calculations for time integrated reflectivity (reflected pulse energy) as a function of the normalized carrier density. The vertical axis scale units are arbitrary.

on several factors: the exact shape of the pulse (gaussian, square, exponential, etc.), how Δf_p and $\Delta \tau_p$ are defined (rms, FWHM, $1/e$, etc.), and the amount of chirp or other amplitude or phase substructure within the pulse. From the previous time-resolved cross-correlation measurements, we find that the reflected infrared pulse shapes show very complicated structures. The main question in these cases is how to define the pulse widths. Our approach to this problem is to analyze the pulse widths measured by the reflection-reflection correlation experiments. This correlation experimental results shows that the overall shapes of the reflected pulses can be approximated by gaussian pulses with a pulse width-bandwidth product $\Delta \tau_p \Delta f_p \sim 0.44$.

The experimental setup and the procedures for the frequency spectrum measurements are outlined in section 4.11. We have performed several experiments to measure the frequency spectrum. Due to the low sensitivity of the optical system, we are not able to measure the frequency spectrum for different values of excitation energy fluences. Thus, the experiments are only performed for high excitation levels ($\gamma F_{ph}/n_c > 6$). Figure 5.20 shows a typical wavelength shift spectrum for an optical pulse with an initial excitation fluence $\gamma F_{ph}/n_c = 7$. Each data point in the figure is averaged over 10 points and the standard error of the measurements is shown as error bars. The figure shows asymmetry where the spectrum shifts more towards the longer wavelength. From the FWHM (87 Å) of the wavelegth spectrum curve, we can calculate a pulse width of $\sim$ 18 ps. This calculated pulse width is in very good agreement with the direct measurements of the correlation profile of figure 5.13.

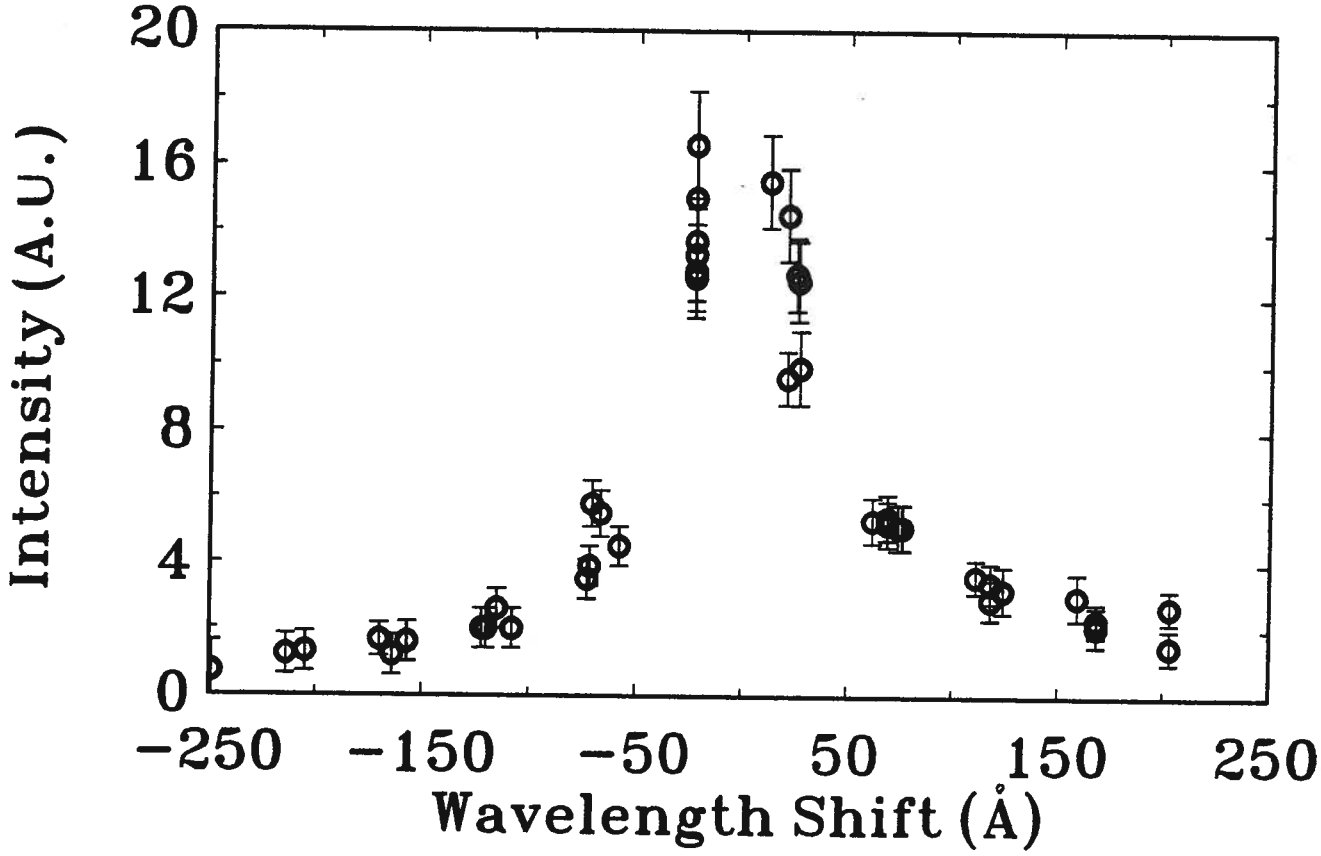

Figure 5.20: Wavelength shift of a reflected infrared pulse with an initial excitation fluence of $\gamma F_{ph}/n_c = 7$.

Chapter 6

Ultrafast Semiconductors for 10.6 μm Optical Switching

6.1 Introduction

This chapter deals with the experimental study of semiconductor materials having ultrashort recombination carrier lifetimes for possible application to optical infrared semiconductor switching. The major body of the experimental work is presented in our current publications [175]–[177]. Details of experimental measurements from three types of semiconductors: low-temperature grown GaAs, radiation damaged GaAs, and $In_{0.85}Ga_{0.15}As$/GaAs relaxed superlattice structures are presented as possible candidates for ultrashort pulse generation. Molecular beam epitaxy growth procedures for some structures and sample preparations are also discussed. Where appropriate, the time-resolved cross-correlation results for the carrier lifetimes are compared with the photoconductivity measurement values reported in the literature.

6.2 The Need for Semiconductors with Ultrashort Carrier Lifetimes

In chapter 5 we discussed the experimental infrared 10.6 μm reflection from intrinsic GaAs. Evidently, the pulses generated from such a reflection switch are too long for our practical use. Most of the generated pulses have long reflectivity tails which last for several picoseconds, and in order to get rid of this long reflection, alternative materials and techniques must be used to produce ultrashort reflectivity pulses. Since we are interested in the generation of a laser pulse with a duration of $\leq$ 1 ps using only one switching

element, we have investigated other modified GaAs based semiconductor switches to serve this purpose. In principle, the GaAs semiconductor is altered to have its carrier lifetime, τ_r, shorter than the radiative lifetime and the diffusion time. The nonradiative recombination centre density and capture cross section must be large enough such that the temporal evolution of the plasma is solely determined by the carrier recombination and the plasma density can be reduced below the critical density in a time scale $\sim \tau_r$. Now, if the semiconductor materials with ultrashort recombination lifetimes (of the order of a picosecond) are used in place of the GaAs switch, then it is possible, due to ultrafast carrier nonradiative recombination, to generate ultrashort infrared pulses limited only by the lifetimes of the semiconductor materials. When the semiconductor carrier lifetime is longer than the excitation optical laser pulse, then the generation rate of the e-h plasma can be considered to be instantaneous. That is, in time resolved cross-correlation experiments this shows as a fast risetime of the cross-correlation signal [175]–[177]. The decay rate of the electron hole plasma should follow the simple relation,

$$n(t) = n_o e^{-t/\tau_r}, \tag{6.1}$$

which in turn determines the decay rate of the reflectivity pulses. Therefore, in principle, this method is more attractive than just using intrinsic GaAs since the reflected infrared pulse duration does not depend on the amount of the excitation energy fluence. Moreover, the choice of the infrared pulse duration can be easily adjusted to the required value by proper selection of the carrier lifetime [176]. Finally, it should be pointed out that using time-resolved infrared reflectivity measurements provides an alternative method for measuring τ_r for semiconductor materials [175]–[177].

6.3 Ultrafast Recombination Semiconductors

In this section we give a brief and largely qualitative account of the techniques used to reduce semiconductor carrier lifetimes. Comprehensive reviews on the subject can be found in references [178]–[182]. Our main task is to search for optimal semiconductor materials with a minimum free-carrier absorption and a minimum carrier lifetime to guarantee that a high reflectivity and an ultrashort decay time are exhibited simultaneously. Different experimental approaches and techniques have been used to enhance the speed of response of semiconductor materials. Most of the work is directed towards the design and the fabrication of ultrawide bandwidth optoelectronic devices [178]–[180].

The techniques rely on the introduction of sufficient deep level states in the crystalline semiconductor material. Deep levels in semiconductors are basically energy levels close to the middle of the energy band gap. These levels can be created by impurities or by crystal defects (vacancies and interstitials)and dislocations. Photoexcited carriers can be captured at these sites and possibly recombine with their opposite kind. The recombination process can be either a single recombination event or a multi-level recombination event. In the latter, the photoexcited carriers are captured for a short time and then released to be captured by another deep level and so on. Depending on the nature of the recombination level, both types of carriers (electrons and holes) can be captured with capture cross-sections σ_{c-e} and and σ_{c-h}, for electrons and holes, respectively.

At high dopant concentrations, carrier recombination occurs through lattice defects generated by the dopant. This causes an increase in the density of the recombination centres. Free carriers excited in the conduction and valence bands of these materials are rapidly trapped at deep defect levels. The carrier lifetime of GaAs can be reduced from a few nanoseconds to $\sim$ 70 ps by the introduction of Cr [183]–[185], whereas by doping the GaAs with Er (5×10^{19} cm^{-3}) the carrier lifetime is reduced to $\sim$ 1 ps [186]. Experimental

observations have shown that for a doping range of 10^{16}–10^{19} cm^{-3} the carrier lifetime decreases with increasing dopant concentration [186]. Doping InP with Fe reduces the carrier lifetime to 100-1000 ps depending on the impurity concentration [187]–[190].

Even though these semiconductors have short lifetimes, the lifetimes for Cr:GaAs and Fe:GaAs are not fast enough to provide significant improvement in our optical semiconductor infrared switching system. For Er:GaAs, due to heavy Er doping, there is significant background reflection that reduces the contrast ratio of the reflected pulse relative to the background reflection.

Picosecond and subpicosecond carrier lifetimes can also be achieved in usual polycrystalline and amorphous semiconductors where the naturally occurring large defects at the grain boundaries act as effective carrier trapping and recombination centres. For polycrystalline materials, for example, Si, Ge, and CdTe carrier lifetimes are measured to be 2–50 ps [191], 50 ps [192] and 4 ps [193], respectively, and for amorphous materials carrier lifetimes are measured to be 5-20 ps for a:Si [194]. These semiconductors have ultrashort recombination times and clearly can be used as optical infrared semiconductor switches; however, the main problem associated with such semiconductors is that the carrier reflectivity is dramatically reduced due to increased elastic scattering. That is, the increase in the carrier scattering results in low infrared reflection efficiencies due to increased free-carrier absorption in the semiconductors. Consequently, a compromise between the reflection efficiency and the speed of the switch must be reached. For these reasons, no attempt has been made to study the infrared reflection from these materials.

The details of the theory dealing with recombination through a single level recombination centre is discussed by Schockley, Read and Hall (SRH) [195, 196]. The carrier lifetime can be related to the trap density, N_t through the following simple relation

$$\tau_r = \frac{1}{N_t \sigma_{c-e,h} < v_{th} >} \tag{6.2}$$

where $< v_{th} >$ is the mean thermal velocity of the carrier. In this case, the trap density and therefore the free-carrier lifetime are inversely related. In light of the above equation, it is clear that one needs to increase the defect and dislocation density in the semiconductors.

Next, we examine three types of semiconductors with ultrashort recombination carrier lifetimes. We investigate low-temperature grown GaAs (LT-GaAs), radiation damaged GaAs (RD-GaAs), and InGaAs/GaAs relaxed superlattice.

6.4 Using Low-Temperature Grown GaAs for Ultrafast Pulse Generation

A novel and interesting approach to shorten carrier lifetime is the use of low-temperature Molecular Beam Epitaxy (MBE) grown GaAs (LT-GaAs). This semiconductor exhibits a unique set of properties such as high carrier mobility ($\sim 10^3$ cm^2/V s), ultrashort carrier lifetime (0.4-60 ps depending on the growth temperature), high resistivity ($\sim 10^7$ Ω cm) and high quantum efficiency. The combination of the above properties attracted wide interest in low-temperature grown semiconductors for the development of wide bandwidth optoelectronic devices such as photoconductors and photoconductive switches [197]–[216]. Here, by using a GaAs layer grown by molecular beam epitaxy (MBE) at a low substrate temperature (LT-GaAs) as an optical semiconductor switch, we demonstrated the generation of ultrashort infrared pulses at 10.6 μm [175].

Two important parameters which determine the optical and electrical characteristics of epitaxial growth of GaAs layers on GaAs substrates are: the substrate temperature which must be maintained at $\sim$ 600°C, and the As/Ga beam-equivalent-pressure ratio. Lowering the substrate temperature to $\sim$ 200°– 300°C causes a highly nonstoichiometric growth where excess arsenic (of approximately $\sim$ 1%) is incorporated into the GaAs epitaxial layer [200, 203, 205, 208, 214, 215]. Post growth annealing of the substrate

causes the excess arsenic precipitates to form nanometer-size arsenic clusters [197] and the resistivity increases by several orders of magnitude from $\sim$ 10 Ω cm to $\sim$ 10^7 Ω cm [203, 214, 215]. It is these arsenic clusters that are of great interest since they deplete any photoexcited free carriers from the surrounding GaAs material. Ultrafast carrier recombination is attributed to the efficient recombination centres due to excess As clusters. Unannealed samples are found to have a variety of defects such as: neutral and ionized arsenic antisites ($[As_{Ga}]^0 \sim 10^{20}$ cm^{-3}, $[As_{Ga}]^+ \sim 5\times 10^{18}$ cm^{-3}) which may act as deep donors, arsenic interstatials (As_i) Ga vacancies ($V_{Ga} \sim 10^{18}$ cm^{-3}) and Ga antisites ($Ga_{As} \sim 5\times 10^{18}$ cm^{-3}). These last two defects may act as acceptors [198]–[201],[204, 217]. After annealing the defect concentration is reduced about an order of magnitude with no effect on the carrier lifetime. Either both types of carriers are trapped at midgap defect bands and then recombine; or the midgap donor or acceptor deep levels capture carriers which then recombine. Several authors reported on the growth/anneal temperature dependence of the carrier lifetime [203],[205]–[207],[214] and have shown that the degree of excess As is greater for lower substrate temperatures.

6.4.1 MBE Growth of LT-GaAs Layers

In this section the LT-GaAs growth procedure is outlined. The properties of LT-GaAs critically depend on the growth and the annealing conditions during the epitaxial growth, any small fluctuations in any of the growth parameters can significantly alter the carrier lifetime of the sample.

The incorporation of high density recombination centres is achieved using a nonconventional MBE growth technique. High densities of excess As are incorporated into a GaAs active layer using a low substrate growth temperature with a moderate As_2 over pressure.

The LT-GaAs samples are grown by S. R. Johnson in the U.B.C. Physics Department.

The LT-GaAs epi-layer is grown on a semi-insulating GaAs substrate using a vacuum generator V80H MBE system. The substrate and the holder are treated in a U.V. generated ozone atmosphere (for 4 min) to remove any residual organics from the surface of the wafer. After the ozone treatment, the holder and the GaAs wafer are placed into the MBE growth chamber where the oxide is thermally desorbed under an As_2 flux. The oxide is desorbed by ramping the substrate temperature at a rate of 5°C/min from 500°C to about 10°C above the oxide desorption temperature of $\sim$ 600°C. This process roughens the surface of the substrate. The increase in the surface roughness and hence the oxide desorption are monitored using laser light scattering [218]. The substrate is smoothed by growing a 2 μm thick (1 μm/hr) GaAs buffer layer at a temperature of 600°C. Next, a 100 nm thick GaAs temperature-transition layer is grown on the buffer layer. During the growth of this layer, the temperature of the substrate is lowered from 600°C to 320°C in 6 min. Following this, a 200 nm thick layer of LT-GaAs is grown at 320°C with a As_2 to Ga flux ratio of 3:1. After the growth of the LT-GaAs layer, the sample is heated inside the growth chamber by raising the substrate temperature from 320° C to 550° C (in 3 min) and annealed for 6 min at 550°C under an As_2 flux. All layers are grown nominally undoped. From the reported value in the literature, under these growth conditions, the arsenic precipitate density is estimated to be approximately 3×10^{17} cm^{-3} with an average cluster size of $\sim$ 2–5 nm [197, 219]. It has been shown that LT-GaAs maintains its crystalline structure [197, 199]; therefore, no attempt is made to characterize the degree of crystallinity of the layer. The surface morphology of the LT-GaAs shows a smooth surface with no diffuse reflection at 10.6 μm. We should point out that during the growth process the substrate temperature is measured using diffuse reflectance spectroscopy (DRS) [220]. This optical temperature measurement technique has ±1°C sensitivity. Figure 6.1 shows a schematic diagram of the LT-GaAs structure and a scanning electron micrograph of the LT-GaAs layer.

6.4.2 Subpicosecond 10.6 μm Pulse Generation from LT-GaAs as a Reflection Switch

We used a cross-correlation method outlined in section 4.10.2. to measure the temporal IR pulse shape. Figure 6.2(a) displays a typical integrated infrared pulse energy as a function of the relative delay. The experiment is performed at a fixed excitation energy fluence which corresponds to a plasma density of $\sim 5\times10^{19}$ cm^{-3}. The time origin in the figure represents the relative arrival time of the visible pulse prior to the arrival of the infrared pulse to signify the zero base line of the transmission. By differentiating the transmission step curve in figure 6.2(a), we can obtain the pulse width. The measured characteristic feature of the curve shows an initial rapid increase in transmission. The rise time of the transmission cross-correlation is a clear indication that the pulse width is about 1 ± 0.2 ps [175] with a long decaying tail. This kind of decay is expected since the visible pulse is mainly absorbed in the LT-GaAs 200 nm thick layer; hence, most of the e-h plasma is generated there. We attribute the short pulse to the fast recombination times in the material, whereas the long tail is due to the GaAs buffer and the substrate layers. Once the carriers are generated in the LT-GaAs layer they will recombine in about 0.5 ps, and the carriers which are generated in the buffer layer will persist for a longer time. Thus the infrared reflectivity decay time depends on the diffusion of the carriers through the buffer layer. The reflectivity tail can be reduced by making the LT-GaAs layer much larger than the absorption skin depth of the optical pulse. The energy of the IR pulse is estimated to be $\sim$ 10 pJ limited primarily by the source CO_2 laser power.

The cross-correlation measurements can be compared with calculations based on a simple model in which the free carriers are generated in the LT-GaAs film by the absorption of a 0.49 ps FWHM semi-gaussian visible pulse. The majority of the generated carriers recombine exponentially with a lifetime of 0.5 ps while ten percent are allowed to

diffuse into the buffer layer with a diffusion coefficient of 20 cm^2/s. The cross-correlation signal and its differential are evaluated based on a technique described in section 4.10.2. The good agreement with the experiment indicates a free-carrier lifetime of 0.5 ps which agrees with the reported carrier lifetime based on the presence of a high density of As precipitates in this material. That is, if one considers equation 6.2 with the following parameters [203]: $N_t = 3\times10^{17}$ cm^{-3}, $\sigma_c = 2.83\times10^{-13}$ cm^2, and $< v_{th} > = 2.5\times10^7$ cm/s (300 K), we calculate a carrier lifetime of $\sim$ 0.5 ps. Our measured carrier lifetime is the same as the one measured by other techniques [203].

We examined the reflected infrared energy for different levels of visible laser excitation. Figure 6.3 illustrates the variation of the reflected infrared pulse energy as a function of the plasma density (or energy fluence) generated in a 2 μm thick LT-GaAs switch. In contrast to the GaAs measurements (figure 5.10), the experimental results show a linear relation and no indication of saturation at high excitation levels. The linear behaviour for LT-GaAs is consistent with what is expected if one assumes that the existence of the recombination centres in the sample, and that the width of the reflected pulses do not vary with the amount of the excitation energy fluence.

In practice, the switching element is shown to be very reliable and simple to operate. Our experimental results show that LT-GaAs, grown under the conditions specified above, is ideally suited for optical semiconductor switching of 10.6 μm radiation.

6.5 Using Radiation Damaged GaAs for Ultrafast Pulse Generation

We have explored another potential semiconductor material for ultrashort infrared pulse generation. Radiation damaged semiconductors are known to have ultrashort carrier

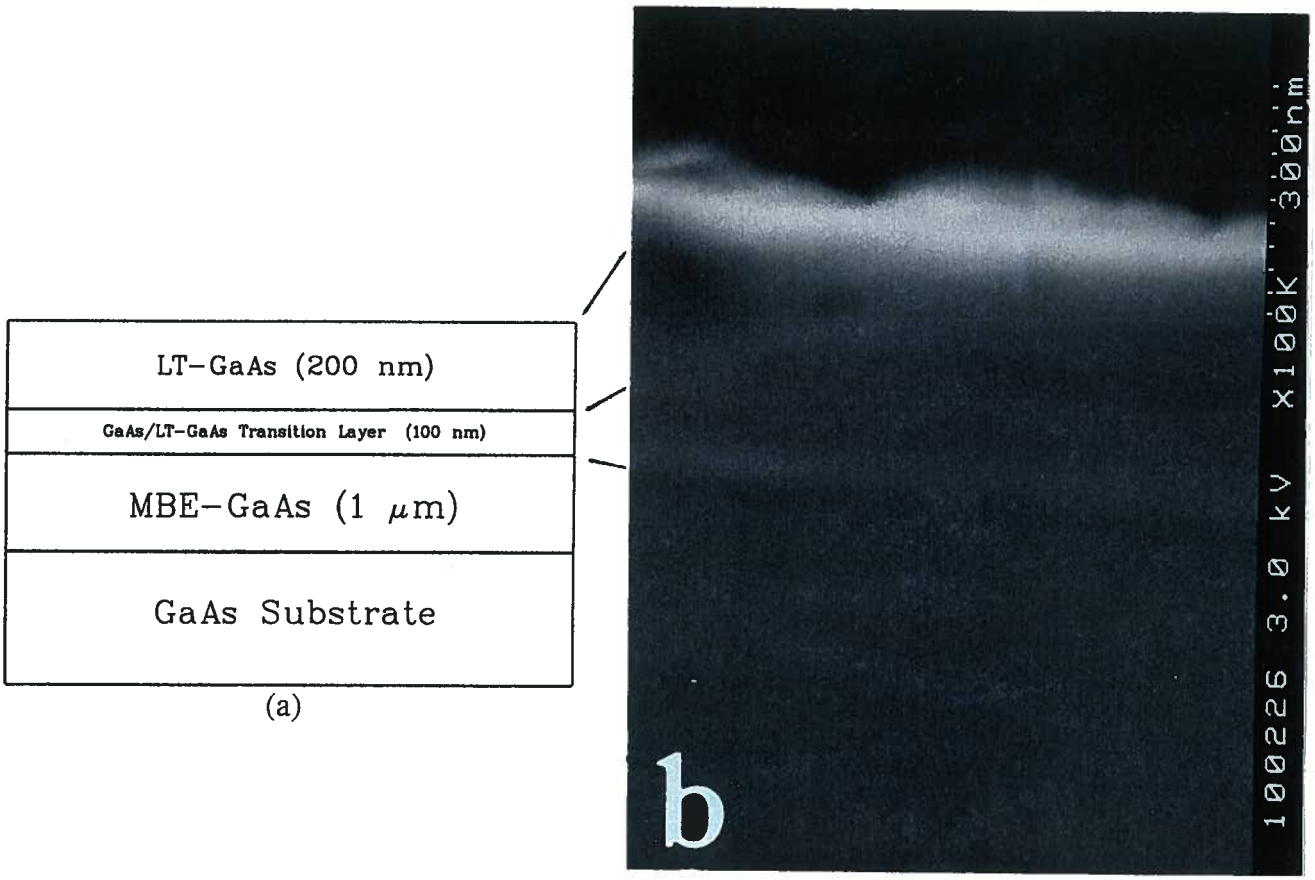

Figure 6.1: (a) Schematic diagram representing the LT-GaAs growth layer. (b) Scanning electron micrograph of the LT-GaAs layer.

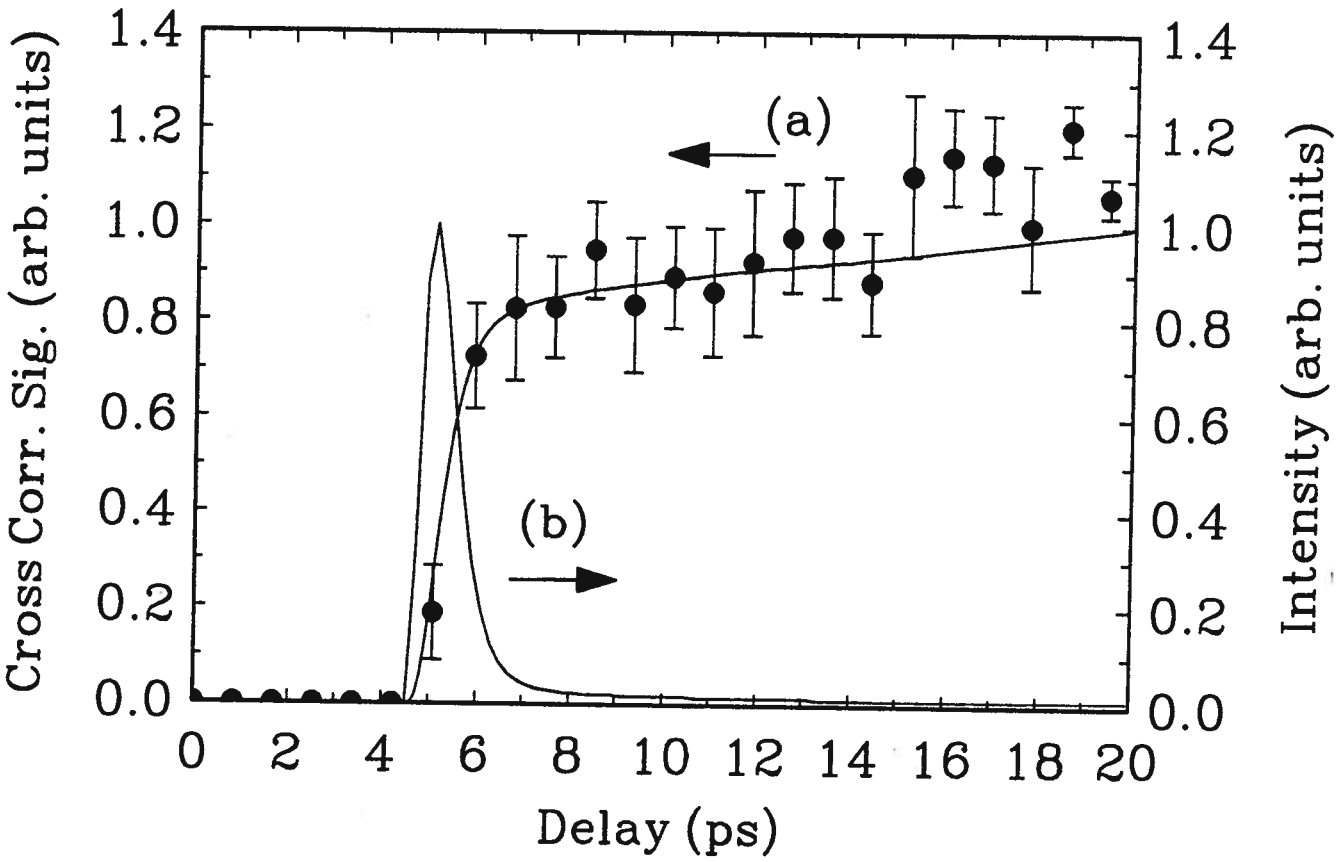

Figure 6.2: (a) A cross-correlation transmission signal between the IR pulse and the visible pulse creating the transmission temporal gate. The solid line is the model calculations. (b) The infrared pulse as obtained from differentiating the cross-correlation curve.

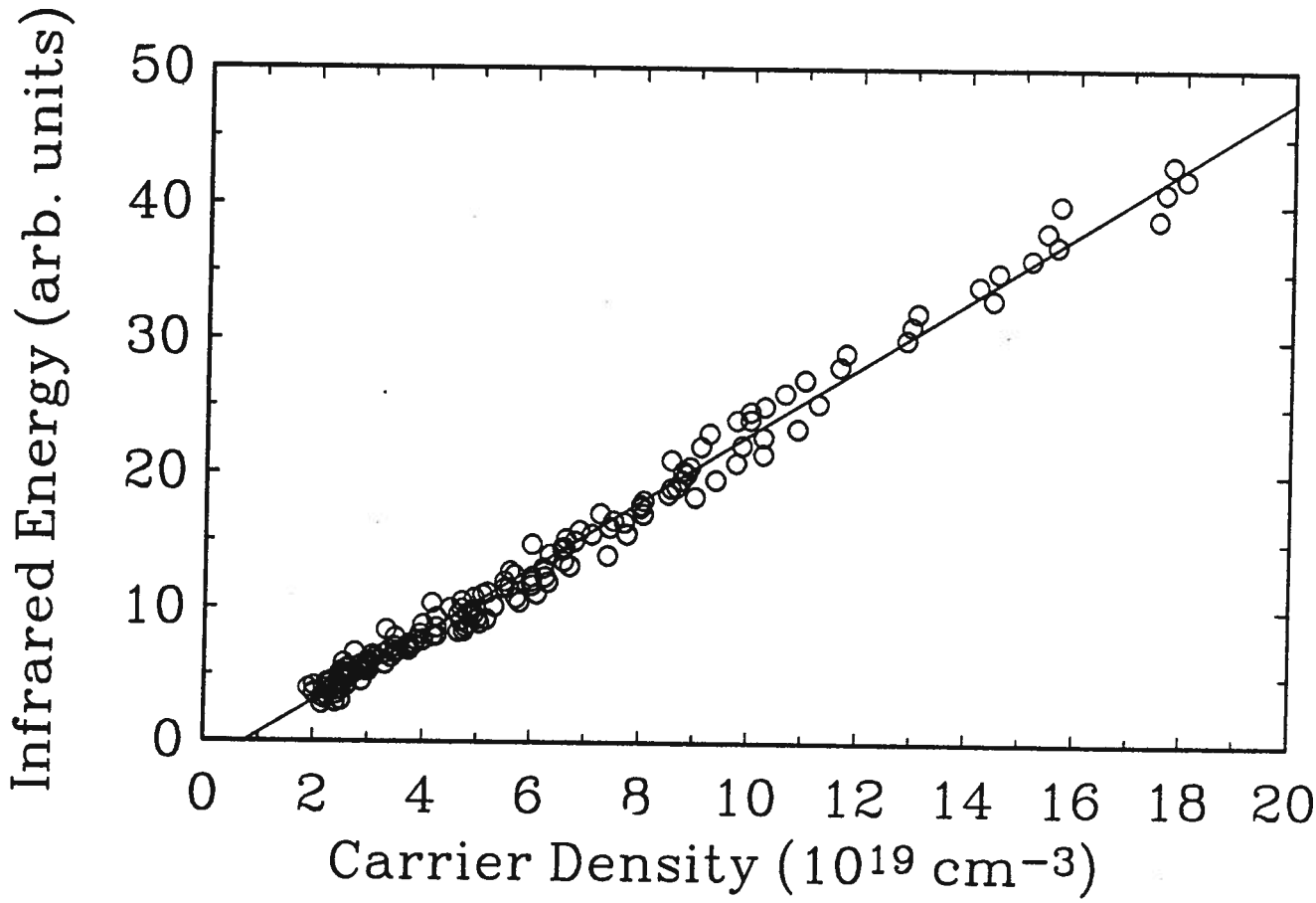

Figure 6.3: Variations of the reflected IR pulse energy as a function of the e-h plasma density. The LT-GaAs layer thickness is ~ 2 μm.

lifetimes ranging from ~ 100 fs to ~ 10 ps [221]–[230]. Our purpose in using ion bombardment is to take advantage of the resulting damage as a means of introducing a predetermined defect density into the crystalline semiconductor [231]–[235]. The reduction of the free-carrier lifetime is a direct result of the defects introduced by the irradiating ion beam. The carrier lifetime of the radiation damaged semiconductor depends on several factors such as: the energy of the radiation beam, type of semiconductor, type of impurities, and the material temperature. When a GaAs substrate is irradiated with high energy particles two processes occur: the atoms in the host lattice are displaced into interstitial sites producing a vacancy pulse interstitial (what is known as Frenkel pairs V_{Ga}-Ga_i and V_{As}-As_i). Both V_{Ga} and V_{As} are effective electron and hole traps, respectively [233, 234], and the interstitial sites Ga_i and As_i behave as donors [182]. In addition, nanometer-size defect clusters are also formed due to impurities implant. These defects and vacancies act as ultrafast efficient traps and recombination centres. Radiation damaging GaAs with a proton beam produces various trap levels with energies 0.11, 0.31, and 0.71 eV for electrons and energies of 0.06, 0.44, and 0.57 eV for holes with capture cross sections of ~ 1.3×10^{-13} cm^2 for electrons and ~ 2.3×10^{-13} cm^2 for holes [235]. Earlier work on radiation damaged GaAs (RD-GaAs) [224, 225] has shown that the carrier lifetime is reduced to 500 fs by irradiating the semiconductor with a 180 keV proton beam at a dose of 1.37×10^{15} cm^{-2}. The irradiated GaAs shows no sign of loss of crystalline structure [224, 225]; however, above that dosage, the observed carrier lifetime is found to reach a lower limit of 500 fs.

6.5.1 RD-GaAs Samples' Preparations and Characterizations

The infrared reflection switches are made from a 450 μm thick semi-insulating (~10^8 Ω cm) GaAs (100) wafer. The wafer is optically polished on both surfaces and is cleaved into three pieces each irradiated with a different H^+ ion dose. The ion damaging is

performed at Dr. N. Jaeger's Ion Implant Laboratory in the U.B.C. Electrical Engineering Department. The samples are bombarded with a 180 keV H^+ ion beam to produce effective doses of 1×10^{12}, 1×10^{14}, and 1×10^{16} cm^{-2}. During the implantation process, the samples are mounted on an aluminum block in order to reduce sample damage due to ion beam heating. The ion beam current density is 1.5×10^{-4} A/cm^2 incident at an angle of 7° to the surface normal and is scanned uniformly over the samples. For these samples the thickness of the damaged layers is larger than the penetration depth of the dye laser excitation pulse (~ 0.2 μm), thus the carriers are generated only in the radiation damaged layer and diffusion of the carriers outside the damaged layer is of no effect.

Heavy ion bombardment of the GaAs wafer may result in a permanent change in the crystalline structure of the semiconductor. Early work showed that bombardment with a high H^+ ion dose $> 1.37\times10^{15}$ cm^{-2} on crystalline GaAs transforms it into an amorphous material [224, 225]. In order to characterize accurately the structure of the ion damaged layer, several ellipsometric measurements were performed on the highly radiation damaged samples and compared to the measured dielectric function of undamaged GaAs. The ellipsometric measurements were performed by Dr. R. Parsons' group in the U.B.C. Physics Department. Figure 6.4 shows the resultant dielectric function for the radiation damaged GaAs with an ion dose of 1×10^{16} cm^{-2}. It is clear that there is no significant change in the form of the dielectric function except the disappearance of the peaks around 3 eV. This and the overall small deviations of the dielectric function are attributed to the surface roughness. The result suggests that the RD-GaAs samples maintain their crystalline structures even at an ion dose level of 1×10^{16} cm^{-2}.

6.5.2 Subpicosecond 10.6 μm Pulse Generation from RD-GaAs as a Reflection Switch

The experimental arrangement and the procedure used to generate and to measure the pulse widths are similar to the ones presented in section 4.10.2 except for the replacements of the LT-GaAs switch with RD-GaAs switches.

We have used a cross-correlation method again to time resolve the reflected infrared laser pulse shapes. In performing the experiments, all the switches are irradiated with enough excitation energy fluence to produce electron-hole plasma density of $\sim 2\times10^{19}$ cm^{-3}. Figure 6.5 shows some of the typically measured cross-correlation signals from the three RD-GaAs switches. Each data point in the plots is averaged over at least 60 single shots and the error bar is an indication of the standard error in the measurements. These curves represent the temporal integral of the reflected infrared pulses. The differentials of these curves with respect to time provides an accurate representation of the temporal shape of the reflected infrared pulses. The risetimes of these pulses is governed by the risetime of the excitation pulse (490 fs). The measured pulse width is found to be a strong function of the ion dosage on the switch. At an H^+ ion dose of 1×10^{12} cm^{-2} the reflected infrared pulse is measured to be 15±1.5 ps. By increasing the irradiation ion level to 1×10^{14} cm^{-2} the reflected infrared pulse width is reduced to 2.4±0.3 ps. An additional increase in the dosage level to 1×10^{16} cm^{-2} further reduces the reflected infrared pulse to 600±200 fs. By taking our detectivity for these pulses, we estimate the reflected energy of the infrared pulses to be $\sim$ 5 pJ. This corresponds to a peak reflectivity of 50%. The results for the 1×10^{16} cm^{-2} RD-GaAs switch reflection pulse width is comparable with the visible excitation pulse width of 490 fs. Therefore, under our experimental conditions, the reflected infrared pulse width is mainly determined by the lifetime of the semiconductor switch and the width of the visible excitation pulse. In

light of the above experimental results, to produce and measure pulse widths of shorter duration the visible excitation pulse must be compressed.

In order to explain the observed ultrafast carrier recombination times, we can approximate the carrier lifetime by equation 6.2. If one assumes that N_t is directly proportional to the H^+ ion dose and that the reflectivity pulse width represents the carrier lifetime, then a log–log plot of the ion dose as a function of infrared reflected pulse width should result in a linear curve with a slope of –1. Figure 6.6 represents a plot of the measured reflected infrared pulse width as a function of the H^+ ion dose. The curve shows the predicted linear relationship between the reflected infrared laser pulse and the ion dose. However, the calculated experimental slope is –0.4 which differs from the predicted slope of –1. One possible explanation is that the density of the recombination centres is not directly proportional to the ion dose. This is similar to what has been observed in erbium-doped GaAs [186]. The other possibility is that the defect density is lower than the density of the optically generated carriers which may result in the saturation of the traps and the recombination centres due to excess free carriers.

From figure 6.6 we can calculate the relationship between the ion dose, Q, and the reflected infrared pulse width, τ_p, in picoseconds to be:

$$\tau_p = 10^6 Q^{-0.4} \tag{6.3}$$

With the above relation, one can simply tailor the infrared pulse width to the required duration by simply adjusting the amount of damage on the switch. In fact, by adjusting the dosage across the surface of the wafer, a multi-speed switch can be easily constructed on a single wafer.

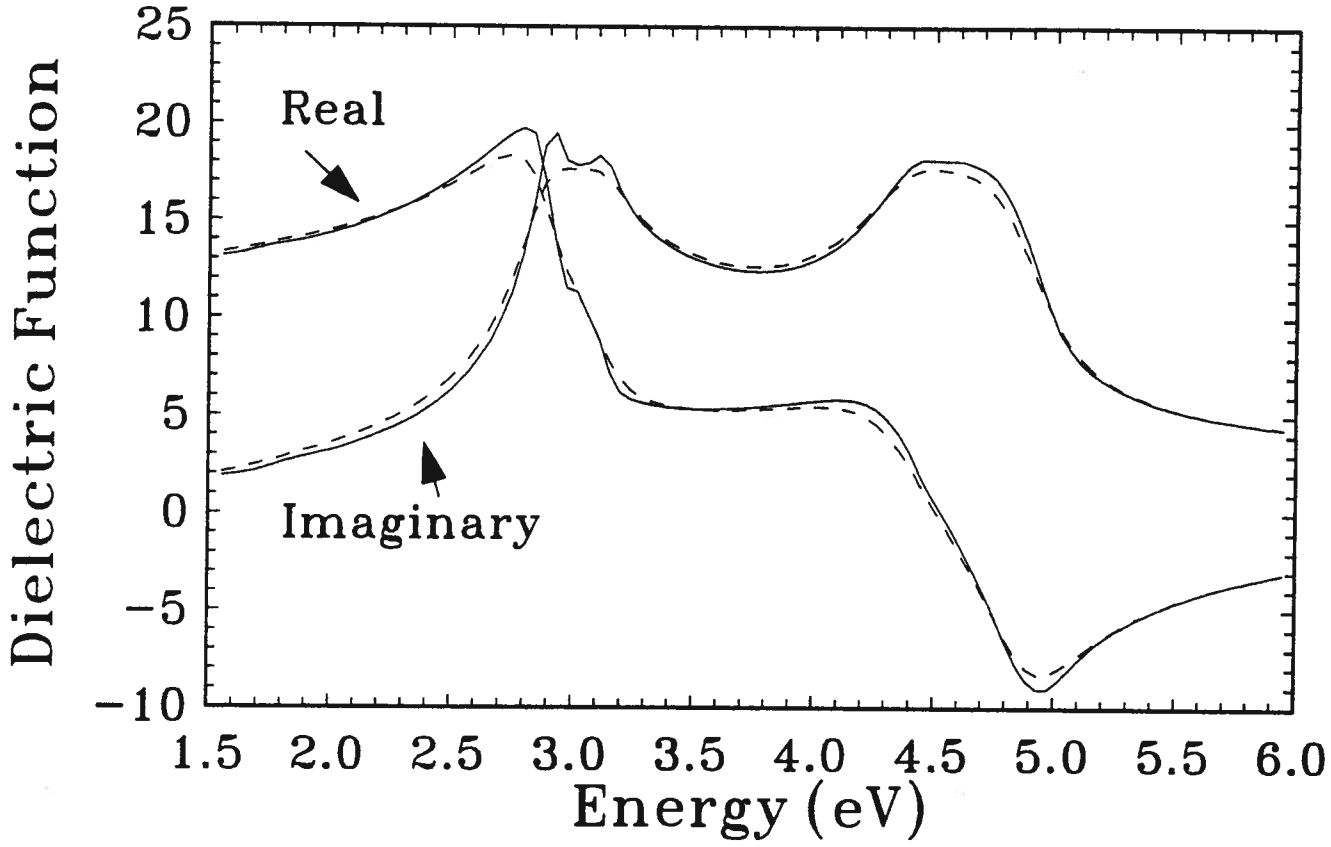

Figure 6.4: Real and Imaginary parts of the dielectric function of undamaged GaAs sample (solid) and the ion damaged (dashed). For the damaged GaAs, the ion dose level is 1×10^{16} cm^{-2}.

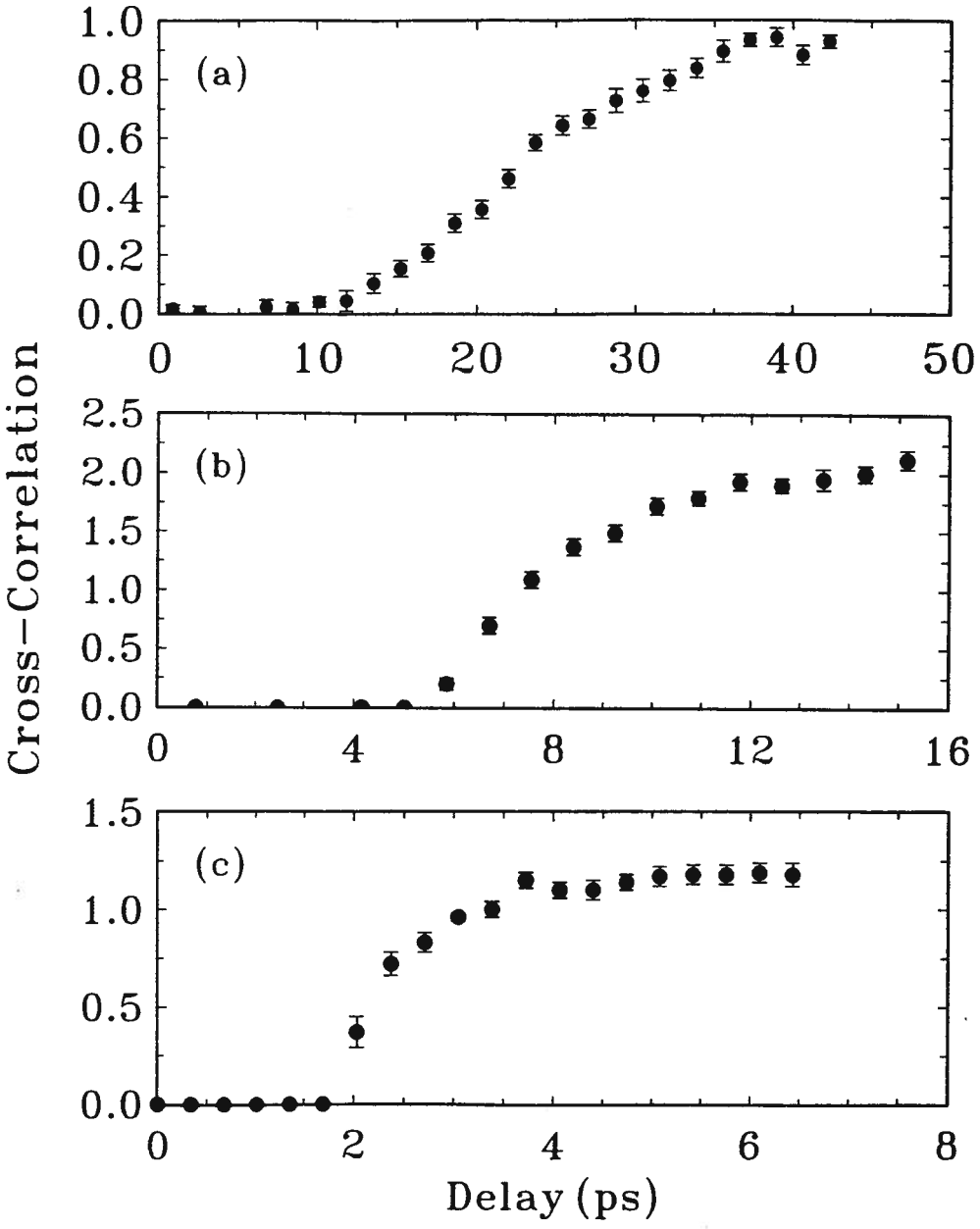

Figure 6.5: Cross-correlation measurements for the reflected infrared laser pulses for an ion damage dose of (a) 1×10^{12}cm^{-2}, (b) 1×10^{14} cm^{-2} and (c) 1×10^{16} cm^{-2}. Note that in all plots, the cross-correlation signal is plotted in arbitrary units which differ for each diagram.

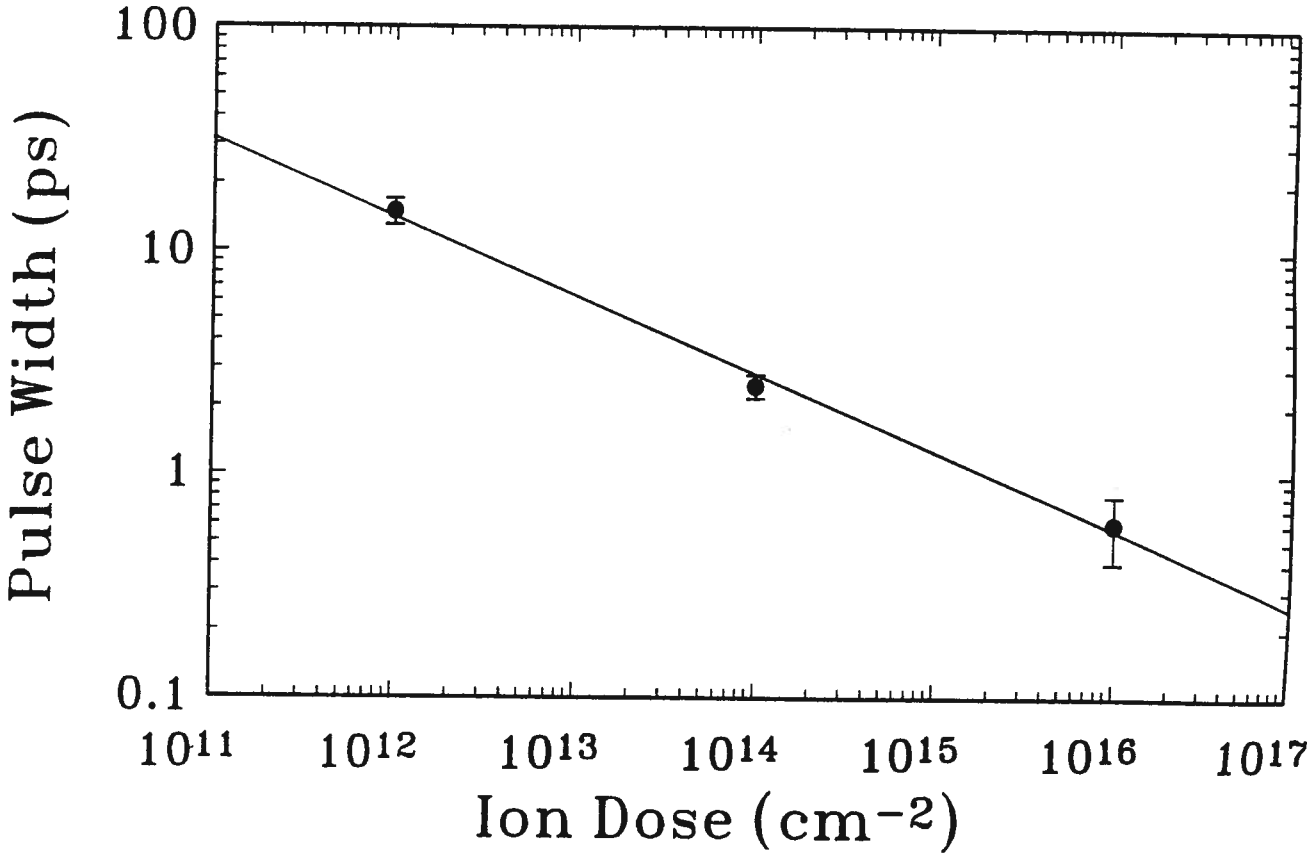

Figure 6.6: Measured 10.6 μm infrared laser pulse widths as a function of the H^+ ion dose in GaAs.

6.6 Using $In_{0.85}Ga_{0.15}As$/GaAs GaAs for Ultrafast Pulse Generation

In this section, we investigate a novel and alternative semiconductor structure for application to infrared semiconductor switching. The growth of lattice mismatched semiconductor layers by MBE above the critical layer thickness results in the formation of defects and dislocations. Clearly, in the fabrication of electronic devices, it is undesirable to introduce dislocations where the ultimate performance, efficiency, and lifetime of the devices are mainly limited by the dislocations introduced during epitaxial growth [236]–[239]. However, increasing the recombination centre density during the epitaxial growth enhances the speed of the material. Dislocations at the interfaces between lattice mismatched semiconductors such as InGaAs and GaAs, can serve as ultrafast non-radiative recombination centres. The growth sequence of $In_xGa_{1-x}As$/GaAs can be divided into the following stages: (a) initial growth where $In_xGa_{1-x}As$ is grown under coherent strain where only a finite amount of lattice mismatch is accommodated by strain; (b) intermediate growth when the $In_xGa_{1-x}As$ layer thickness reaches the critical layer thickness (which depends on the strained alloy indium concentration) and dislocations are generated at the interface; and (c) the final growth phase when the thickness of the InGaAs layer is increased far beyond the thickness of the critical layer, a relaxation of the structure takes place and as a result some of the lattice mismatch is accommodated by misfit dislocations. Continual growth above this point results in an island-type growth structure [239, 240].

6.6.1 MBE Growth of $In_{0.85}Ga_{0.15}As$/GaAs Relaxed Superlattice

The samples are grown by S. R. Johnson in the U.B.C. Physics Department. The layers are grown on a semi-insulating (100) GaAs substrate using the Vacuum Generators V80H molecular beam epitaxy (MBE) machine. The substrate preparation procedure is similar

to the one discussed previously in section 6.4.1. The layer thicknesses of the superlattice are as follows: the first three layers consist of 210 Å of GaAs on 84 Å of $In_{0.85}Ga_{0.15}As$, the next three layers consist of 210 Å of GaAs on 126 Å of $In_{0.85}Ga_{0.15}As$, and the last four layers consist of 210 Å of GaAs on 84 Å of $In_{0.85}Ga_{0.15}As$. These layers are grown at a substrate temperature of 500 °C. The substrate is annealed at 630 °C for 3 min. A schematic diagram of the structure is presented in figure 6.7

The lattice mismatch between the $In_{0.85}Ga_{0.15}As$ layer and the GaAs layer is 6%. The layers of the InGaAs/GaAs superlattice are relaxed as they are much thicker than the critical layer thickness which is only a few monolayers ($\sim$ 20 Å) [239, 241]. The surface roughness of the grown structure is greater than the surface roughness of the lattice matched buffer layer. However, this roughness is not large enough to cause diffuse reflection at 10.6 μm. The sample showed a smooth and featureless surface when observed with a scanning electron microscope.

In order to enhance the effects of non-radiative recombination at the defects, several steps are taken to ensure maximum recombination efficiency: alternating layers of InGaAs and GaAs are chosen so that the total number of interface boundaries and, hence, the total number of the dislocations is maximized. The total thickness of the relaxed superlattice is chosen to be about the same as the absorption skin depth of the visible excitation pulse, such that the majority of the carriers are optically generated throughout the superlattice structure. At this high In concentration, the layer grows as islands [239, 240, 242, 243].

6.6.2 Ultrafast 10.6 μm Pulse Generation from $In_{0.85}Ga_{0.15}As$/GaAs as a Reflection Switch

We have used a cross-correlation technique to measure the carrier lifetime in the superlattice structure. The details of the experimental set up and the measurement procedure are similar to previous ones except for the replacement of the LT-GaAs or RD-GaAs

with the $In_{0.85}Ga_{0.15}As/GaAs$ relaxed superlattice structure. The ultrafast change of the 10.6 μm reflection is monitored as a function of time delay between the visible excitation pulse used to turn on the Si switch and the infrared pulse. The excitation energy fluence throughout the experiment is kept constant and is estimated to be 0.4 mJ/cm^2. With knowledge of the pulse energy, spot size, and the absorption skin depth, we can estimate the maximum generated electron-hole (e-h) plasma density per pulse to be 5×10^{19} cm^{-3}.

The cross-correlation reflectivity curve represents the temporal behaviour of the optically generated plasma inside the relaxed superlattice structure. The risetime is governed by the generation rate of the e-h plasma created by the 490 fs excitation laser pulse. Initially, the optically induced plasma remains confined to the absorption skin depth layer of 220 nm. As time evolves, the defects/dislocations at the interfaces and throughout the rest of the relaxed superlattice will act as ultrafast non-radiative recombination centres for the plasma as it diffuses throughout the layers. Figure 6.8 illustrates a typical cross-correlation curve, where the reflectivity is plotted versus the time delay following the plasma excitation for the initial 10-ps following excitation. The cross-correlation curve resembles the integral of a double exponential reflectivity function. When the differential of the reflectivity cross-correlation curve is plotted on a logarithmic scale, as shown in figure 6.9, it is clear that there are linear regions representing two intrinsic recombination times. The initial ultrafast decay is measured to be 2.6 $\pm$ 0.3 ps, and the slow decay is 10.0 $\pm$ 0.3 ps. The 2.6 ps exponential decay time represents the effective recombination lifetime of the carriers at the dislocations and defects. The origin of the long 10 ps decay tail may be due to space charge regions near dislocations which produce potential barriers and wells for non-equilibrium holes and electrons. These barriers/wells occur in regions around dislocations, where strain is maximized. Once the plasma is created, all the electrons/holes occupy different states high/low in the conduction/valence bands.

While most of the carriers recombine rapidly at recombination centres, a significant number with low energy get trapped by the barriers/wells and therefore have a much longer recombination time. These trapped carriers recombine through Auger recombination. As a result, one expects a long infrared reflectivity tail indicating the presence of these carriers. The structure's carrier lifetime is comparable to that of RD-GaAs (with a dose of $\sim 2\times10^{12}$ cm^{-2}) and LT-GaAs semiconductors (grown at 300 °C). It should be noted that this structure can be utilized as an ultrafast optical-optical infrared reflectivity switch [177]. Here, we managed to generate ultrashort 10.6 μm laser pulses of $\sim$ 10 ps duration.

After this experiment was completed and the results were submitted for publication [177], two papers appeared in the literature which discuss carrier lifetime in similar structures [237, 244]. Pelouch and Schlie [244] measured a rapid absorption recovery signal of the order of $\sim$ 10 ps in a $In_{0.65}Ga_{0.35}As/GaAs$ structure. They attribute the ultrafast absorption recovery to recombination at misfit dislocations. On the other hand, the results of the recently published work by Hugi et al. [237] showed two lifetime scales for similar structures mainly 3 ps for electrons and 10 ps for holes. They attribute the 3 ps lifetime to trapping at substitutional oxygen on arsenic site O_{As} (with corresponding density and capture cross-section of 8×10^{16} cm^{-3} and 1.9×10^{-13} cm^2, respectively) and the 10 ps lifetime due to large densities of misfits and threading dislocations due to lattice mismatch.

6.7 Conclusion of the Chapter

In conclusion, we have demonstrated the feasibility of generating ultrashort pulses at 10.6 μm using LT-GaAs, RD-GaAs, and $In_{0.85}Ga_{0.15}As/GaAs$ relaxed superlattice as single switching elements. The pulse duration ranges from 600 fs to 15 ps depending on the active switching elements. Furthermore, with the optimization of the growth parameters

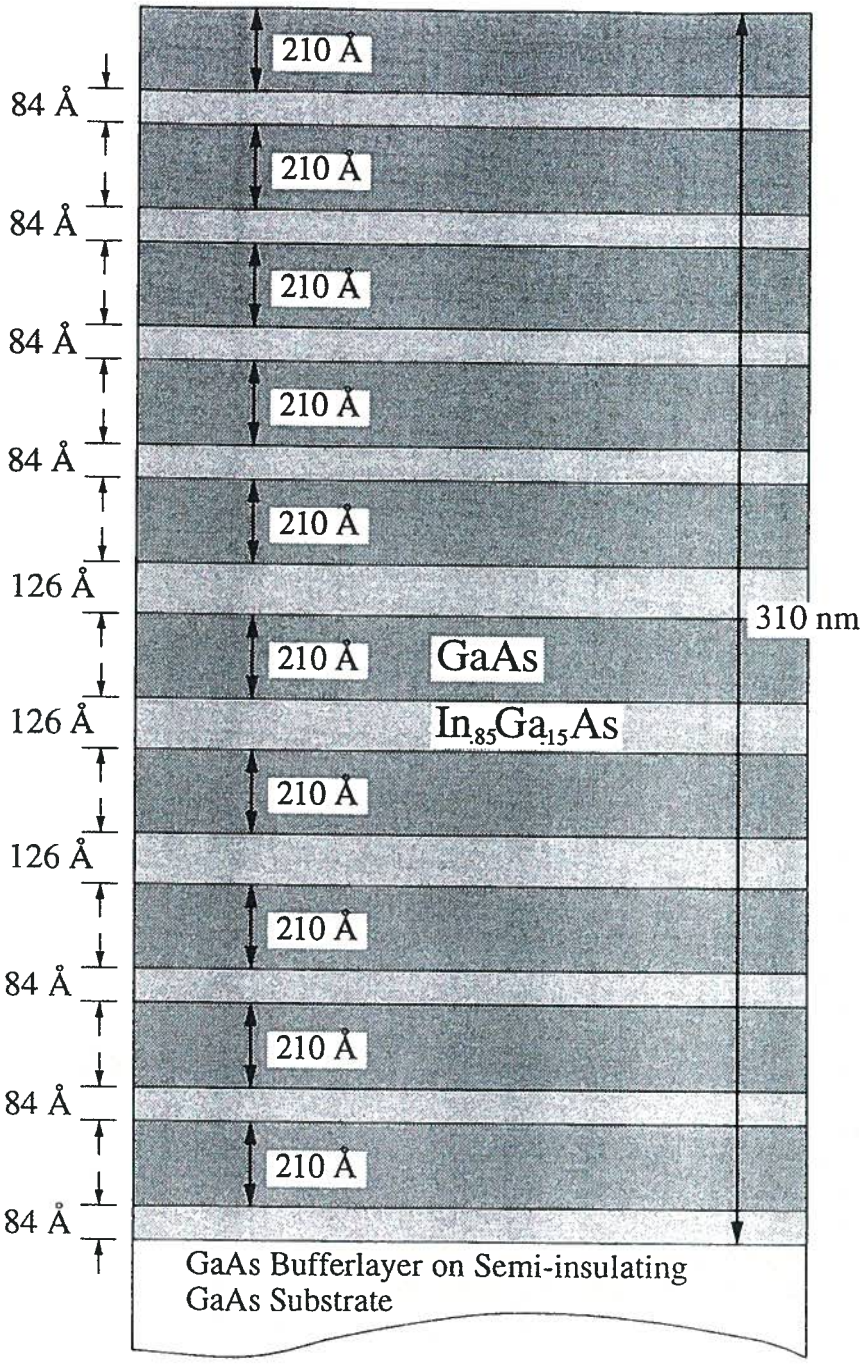

Figure 6.7: A Schematic diagram of the $In_{0.85}Ga_{0.15}As/GaAs$ relaxed superlattice.

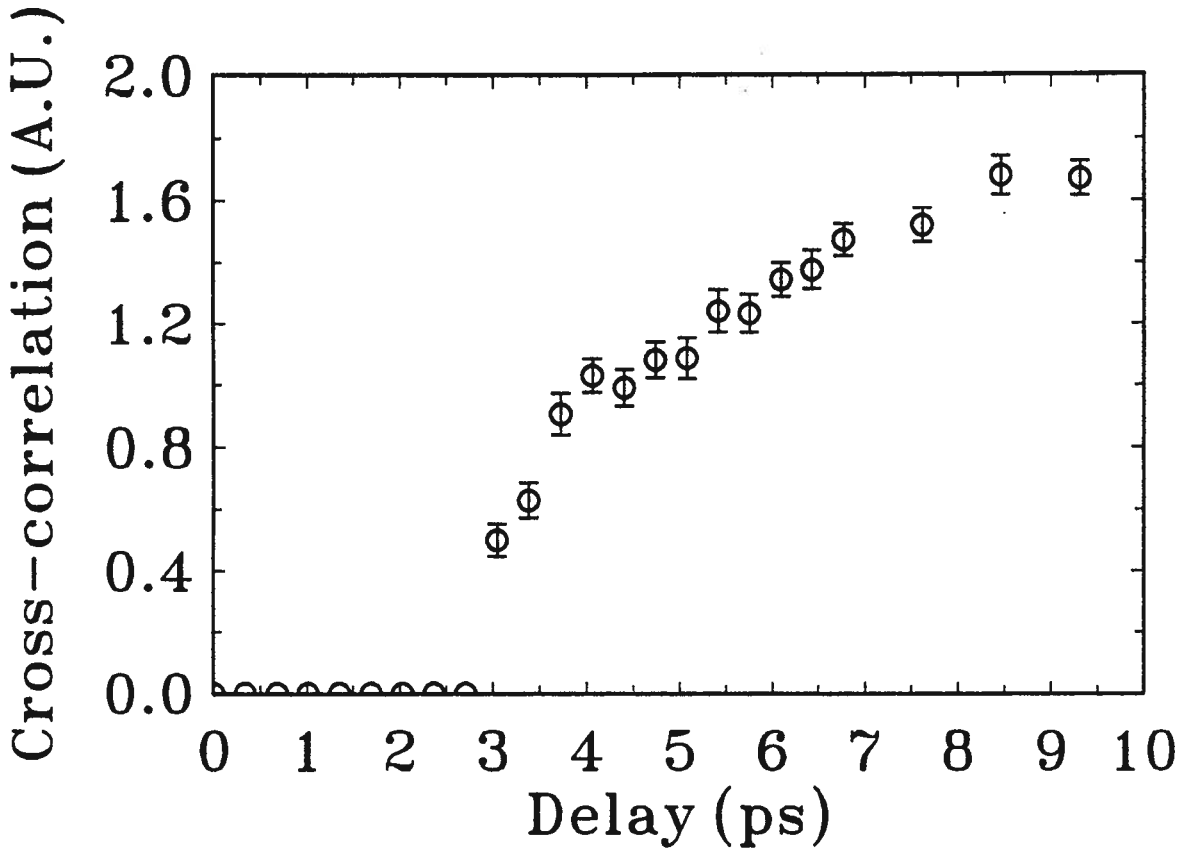

Figure 6.8: Cross-correlation infrared reflectivity signal as a function of time delay.

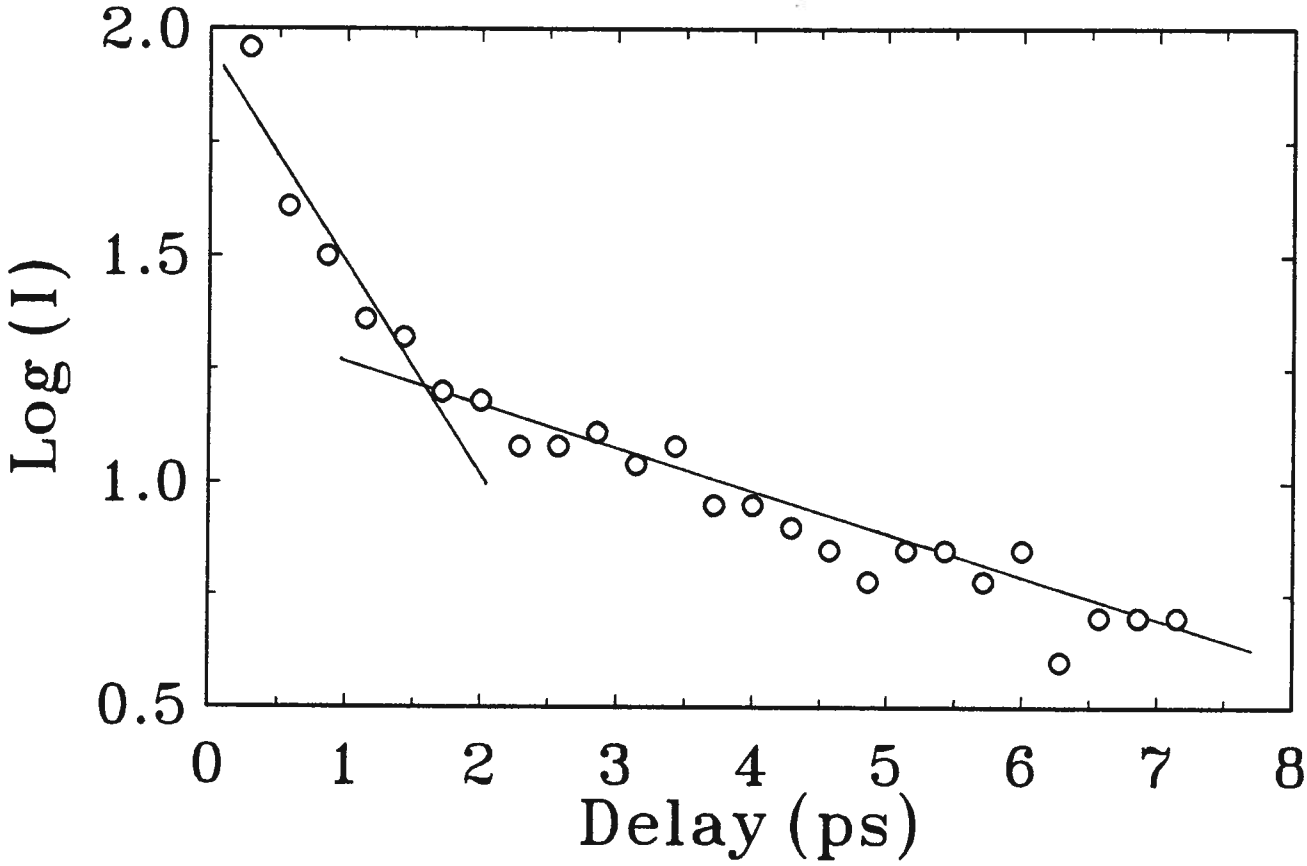

Figure 6.9: Differential of the cross-correlation, I, curve as a function of time.

of LT-GaAS, and the use of RD-InP pulses as short as 100 fs at 10.6 μm can be easily produced. Obviously this requires reducing the pumping pulse width to $\leq$ 100 fs.

The sensitivity of this technique to low-density photogenerated plasmas (compared to using the visible beam as an optical probe) and the deep penetration depth of the probe laser beam make it ideal for studying carrier dynamics of buried interfaces where electrically injected carriers are generated deep within the structure. This is clearly demonstrated in the measurement of the non-equilibrium carrier lifetime in $In_{0.85}Ga_{0.15}As/GaAs$ relaxed superlattice [177].

It should be emphasized that the experiment described above provides an example of the utilization of this switch at 10.6 μm; however, the frequency of the reflected pulse is determined by the infrared laser radiation source. By replacing the CO_2 laser with another infrared laser ($\lambda \geq 1$ μm), it is possible to generate ultrashort pulses at these wavelengths. It is interesting to note that the generation of optical pulses in the far-infrared range, with a pulse duration of less than one optical cycle, can be achieved with this method.

Finally, we should point out that in conducting the previous experiments, the carriers are initially injected with excess energy high in the conduction band. The contribution of intraband carrier relaxation and intervalley scattering may play a role in determining the duration of the reflectivity pulses. Clearly, it is preferable to photoexcite the carriers with photon energy just above the band gap such that the effects of these processes are minimized.

Chapter 7

Conclusions and Suggestions for Further Work

7.1 Introduction

This chapter summarizes the major experimental results of this dissertation, followed by some useful suggestions for future experimental work on ultrashort pulse generation and semiconductor probing.

7.2 Summary and Conclusions

In this thesis, we first described the principles and the theory behind optical semiconductor switching and the possibility of generating subpicosecond infrared pulses at 10.6 μm. A numerical simulation of the switching process was presented to aid in the understanding of the infrared single-switching process. The original model, which is based on the carrier diffusion from the surface of the switch into the bulk, shows the feasibility of producing picosecond and femtosecond laser pulses. The pulse duration is found to depend on the initial injected carrier density.

The measurement techniques used during the course of the experiments are time - integrated infrared reflectivity measurements, time-integrated infrared transmission measurements, time-resolved reflection-reflection correlation measurements, and time - resolved cross-correlation measurements. The information obtained from these experiments is used to determine the speed and the optimum operation of the optical semiconductor

switches. Even though the initial original-model calculations provide a reasonable description of some of the observed infrared reflectivity experimental results, the model does not fully describe the observed time-resolved reflectivity pulses from GaAs. This is confirmed by performing detailed experimental investigations of the basic characteristics and the temporal evolution of the photogenerated plasma in a GaAs infrared reflection switch. The information obtained from the original model and an enormous number of experiments on GaAs are used to develop a better model that accounts for the overall temporal and integrated behaviour of the infrared reflectivity pulses. By introducing an additional two-body recombination mechanism, whose rate is a function of the carrier density, we are able to obtain good agreement between the proposed model calculations and the experimental results. Experimentally, at carrier densities $\sim 10n_c$, the two-body recombination time is found to be 0.5 ps. It is clear that this ultrashort recombination time cannot be explained in terms of Auger or density independent two-body recombination processes. A possible recombination mechanism might be a nonradiative plasmon-assisted recombination with a recombination rate $\Gamma = 1.9\times10^{-28}$ cm^6/s. This recombination mechanism is more efficient at high plasma density. As the plasma density and plasma frequency increase, the electrons at the bottom of the conduction band recombine with the holes high in the valence band. The recombination mechanism results in the emission of plasmons. To our knowledge, there is no experimental observation of plasmon-assisted recombination in GaAs, and one cannot conclude that from performing reflectivity measurements alone. Clearly, other experiments are required to verify this recombination mechanism.

In addition to the transient 10.6 μm reflectivity from the GaAs switch, the absorption of infrared radiation in Si of various doping is investigated after free carriers are generated by absorption of a subpicosecond laser pulse of above band gap photon energy. A theoretical model is presented which predicts the transmission coefficient for an infrared

laser pulse through a photogenerated e-h plasma in Si of various surface free-carrier densities. By fitting the experimental data to the theoretical predictions, the imaginary component of the dielectric function is accurately determined. From the results, the free-carrier absorption cross-sections at 10.6 μm and the relaxation times are calculated. The momentum relaxation time in n-doped Si is measured to be 10.6 fs, whereas for p-doped and intrinsic Si it is found to be 26.5 fs. These measurements are used to determine the speed of the infrared transmission cut-off switch. Application of the transmission cut-off switch to the time-resolved cross-correlation method showed that it is possible to measure the duration and the shape of infrared pulses with a resolution limited only by the duration of the excitation laser pulse.

Clearly, for ultrashort pulse generation, the type of semiconductor material used for the switching process is crucial. The duration of the 10.6 μm laser pulses generated from a single GaAs optical semiconductor switch are $\sim$ 20–30 ps long. These pulses are two orders of magnitude longer than what we expected to produce. We have found that to operate a single switch with a subpicosecond speed, the optically induced carrier lifetime must be reduced. Thus, several techniques were explored during the course of the experimental work to reduce the carrier lifetime. Ultrafast recombination centres are introduced during the semiconductor material growth procedure, by irradiation of the semiconductor material with an ion beam, and by the creation of defects in lattice mismatched semiconductors.

By using a 200 nm low-temperature molecular beam epitaxy grown GaAs layer grown at a low temperature of 320 °C on a GaAs substrate, we demonstrated the generation of 1 picosecond infrared pulses at 10.6 μm. The presence of many As precipitates in this material act as fast recombination centres, giving the optically generated carrier a lifetime of 0.5 ps. Furthermore, ultrafast infrared pulses at 10.6 μm as short as 600 fs are produced by using radiation damaged GaAs with a 180 KeV H^+ dose of 1×10^{16} cm^{-2}

as an optical-optical switch. It was found that the generated infrared reflectivity pulse widths are proportional to the H^+ dose to the power –0.4. This allowed precise control over the generated pulse duration. We believe pulses as short as 100 fs can be relatively easily achieved by the use of radiation damaged InP as an optical semiconductor switch.

We have also investigated the recombination lifetime of nonequilibrium carriers in a highly excited $In_{0.85}Ga_{0.15}As/GaAs$ relaxed superlattice structure by studying the time-resolved infrared reflectivity at 10.6 μm. Lattice mismatch between $In_{0.85}Ga_{0.15}As$ and GaAs layers gives rise to misfit dislocations which act as ultrafast recombination centres which result in a dramatic decrease of the carrier lifetime. We demonstrated that this carrier lifetime is 2.6 ps. Laser pulses as short as 10 ps were produced using this structure.

This thesis demonstrates the feasibility of generating femtosecond laser pulses using only a single optical semiconductor switch. The lasers, the electronic equipment, and the optical diagnostic systems built as part of this thesis work are still in use and many more interesting experiments are planned using this ultrashort pulse laser system. Currently, a unique high-energy $\sim$ 1 J, 500 fs CO_2 laser system, based on this work, is being developed. The low power optically switched 10.6 μm laser pulses will be amplified in a 15 atmosphere CO_2 laser amplifier module for the purpose of studying laser-plasma interactions.

7.3 Suggestions for Further Work

During the course of the experimental work, several alternative techniques concerned with the generation of ultrashort laser pulses were frequently discussed in our laboratory. Here, we present an experimental proposal for producing such pulses and an alternate method for probing semiconductors.

7.3.1 Ultrashort 10.6 μm Laser Pulse Generation by Beam Deflection

Here, we propose a simple technique for producing an ultrashort laser pulse in a wide range of wavelengths. The proposed technique is based on ultrafast beam deflection using the transient optical Kerr effect in highly nonlinear materials [245]–[252] . The principle of ultrafast all-optical laser beam (pulse) deflection is discussed by several authors for application to all-optical modulation [248], all-optical subpicosecond streak camera [250], ultrafast pulse duration measurement [249], and femtosecond laser pulse generation [250, 251]. The analysis presented in this section is similar to those of references [248]–[252].

The optical arrangement of the ultrafast optical Kerr deflector is illustrated in figure 7.1, and it consists of the following components: a CW CO_2 laser, an intense ultrashort pump pulse of a duration of $\leq$ 500 fs, a nonlinear material such as CS_2, a small entrance slit, a focusing lens, and a small pinhole. The basic operation of the ultrashort pulse generation scheme is simple: the nonlinear optical material is placed behind a small entrance slit of width d_o, then the CO_2 laser beam is directed perpendicular onto the aperture and is focused by a small focal length lens on the edge of a pin hole of width W. The intense $\sim$ 1 mJ, 616 nm, 490 fs laser pulse is directed on the entrance slit at an angle α with respect to the CO_2 beam, so that it excites a prism-shaped volume in the CS_2 cell, as shown in figure 7.1. The CO_2 laser beam passes through an optically induced temporal prism which is created by the intense pump beam due to the optical Kerr effect. The nonlinear refractive index, n_{nl}, is time dependent and it is equal to $n_2 I_{vis}(t)$, where n_2 is the nonlinear refractive index coefficient, and $I_{vis}(t)$ is the visible pump pulse intensity. As the 10.6 μm beam propagates through the medium of length L, the temporal Kerr prism causes spatial phase modulation that results in the infrared beam deflection. Clearly, the deflection angle, $\theta_d(t)$, is a function of time; therefore, for ultrafast deflection operation, it is appropriate to use materials with an ultrafast

nonlinear response. If the infrared deflected beam is made to scan a small pinhole placed at a distance S away from the nonlinear medium, the transit time of the deflected beam through the opening, W, can be of the order of a picosecond or less. Thus, an ultrashort pulse is produced by ultrafast transmission through the pinhole.

As an illustrative example, we present some simple approximate calculations to determine the minimum pulse width that can be produced at 10.6 μm. The numerical values that are used in the calculations are based on the lasers, material, and components which are available in our laboratory. More comprehensive calculations should be performed to properly characterize the speed of the device in detail.

In the far field approximation where $S \gg L$ and d_o, the time, τ_D, needed for the deflected infrared beam to scan a small pinhole is related to the deflection angle θ_d by

$$\tau_D = \frac{W}{S}\left(\frac{d\theta_d}{dt}\right)^{-1}. \tag{7.1}$$

With the aid of figure 7.1 and by using Snell's law for light refraction, we obtain the expression

$$(n_o + n_{nl})L = n_o[Lcos\theta_d + d_o sin\theta_d] \tag{7.2}$$

where n_o is the linear refractive index. By using a small deflection angle approximation, $sin\theta_d \approx \theta_d$ and $cos\theta_d \approx 1$, the expression reduces to

$$\theta(t)_d = \frac{n_{nl}(t)L}{d_o} \tag{7.3}$$

An important parameter that must be considered is the diffraction of the deflected beam. The diffraction angle determines the number of the resolvable spots (resolution of the deflector), N_s, and thus the minimum aperture width of the pinhole. For a gaussian beam, the far field diffraction angle, θ_f, is given by

$$\theta_f = \frac{\lambda}{\pi w_o}, \tag{7.4}$$

where w_o is the beam waist. Using equations 7.3 and 7.4, the number of resolvable spots is

$$N_s = \frac{\theta_d}{\theta_f} = \frac{\pi w_o n_{nl} L}{d_o \lambda} \tag{7.5}$$

The minimum aperture size is limited by the diffraction spot of the infrared beam. For minimum separation of two observable spots, the minimum pin hole width is given by

$$W = \frac{\lambda S}{\pi w_o} \tag{7.6}$$

The rate of change of the deflection angle with time is proportional to the rate of change in the nonlinear refractive index, n_{nl}. Therefore it is highly desirable to use a nonlinear material with an ultrafast response time, T_r. For an ultrafast excitation pulse, the expression $d\theta_d/dt$ can be approximated by its instantaneous response to the pulse:

$$\frac{d\theta_d}{dt} = \frac{dn_{nl}}{dt}\frac{L}{d_o} \approx \frac{n_{nl} L}{T_r d_o}. \tag{7.7}$$

By combining equations 7.1, 7.6 and 7.7, one obtains an expression for the minimum pulse width that can be obtained from such a deflector

$$\tau_{D,min} = \frac{\lambda d_o T_r}{\pi w_o n_{nl} L} \tag{7.8}$$

It is possible to produce intense pulses with our ultrashort laser system (1 mJ in 490 fs pulse) of the order of 50 GW/cm^2. Using this intensity and n_2= 1.5×10^{-11} (esu) for CS_2, we obtain a value for n_{nl}=6.3×10^{-3}. By substituting some realistic numerical values: T_r= 2 ps [251], $d_o \approx w_o$, L = 23 mm (i.e. α= 85°), and λ= 10.6 μm, we calculate a minimum pulse width of 46 fs with N_s= 43. This pulse is approximately 1.5 optical cycles of the CO_2 laser radiation. The potential for this technique to generate even shorter pulses is possible by simply using a faster nonlinear medium.

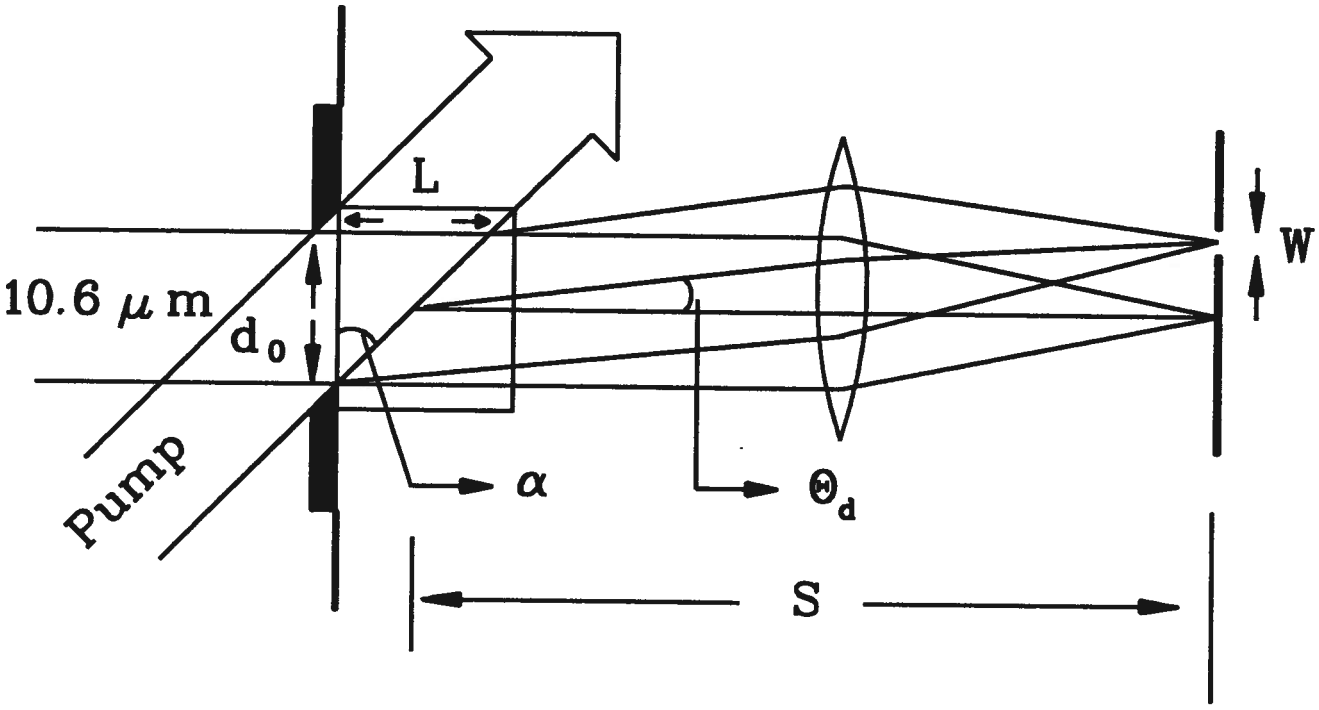

Figure 7.1: Schematics of the all-optical beam deflector used for ultrashort pulse generation.

7.3.2 Back Surface Infrared Reflectivity Measurements

An interesting experiment that can be performed is a measurement of the backside infrared reflection from GaAs as illustrated in figure 7.2. The experimental arrangement is the same as that used for front surface probing of GaAs, except that the optical excitation pulse is made incident on the GaAs from the backside and the infrared probe is incident on the front surface. As a result, the e-h plasma density gradient is created in the opposite direction from the usual infrared switch operation. The 10.6 μm radiation interacts with an e-h plasma which is exponentially increasing with depth. Clearly, the reflection properties (efficiency, pulse shape, and duration) of the backside illuminated switch are different from the standard operation. Unlike time-resolved front side probing, where the infrared beam is reflected off a thin overdense plasma layer, for backside reflection the probing infrared radiation propagates through a thicker plasma layer with its critical density layer propagating into the bulk. Thus, one expects to observe a stronger phase modulation across the reflected pulse. We performed with success a pilot experiment to see whether we could observe this effect. However, no further attempt was made to time-resolve the duration of the reflected pulses. The detector-limited pulse shapes are found to be very sensitive to the angle of the excitation beam relative to the sample. It is not clear why this is the case. Unfortunately, due to time constraints, no further work was done to characterize the observations. A follow-up experiment of interest would be to perform accurate frequency shift measurements on both front and back surface reflections and the variations of the pulse width with the excitation angle. This experiment also shows that it is possible to probe with high sensitivity the dynamics of electrically or optically injected e-h plasma buried inside semiconductor devices.

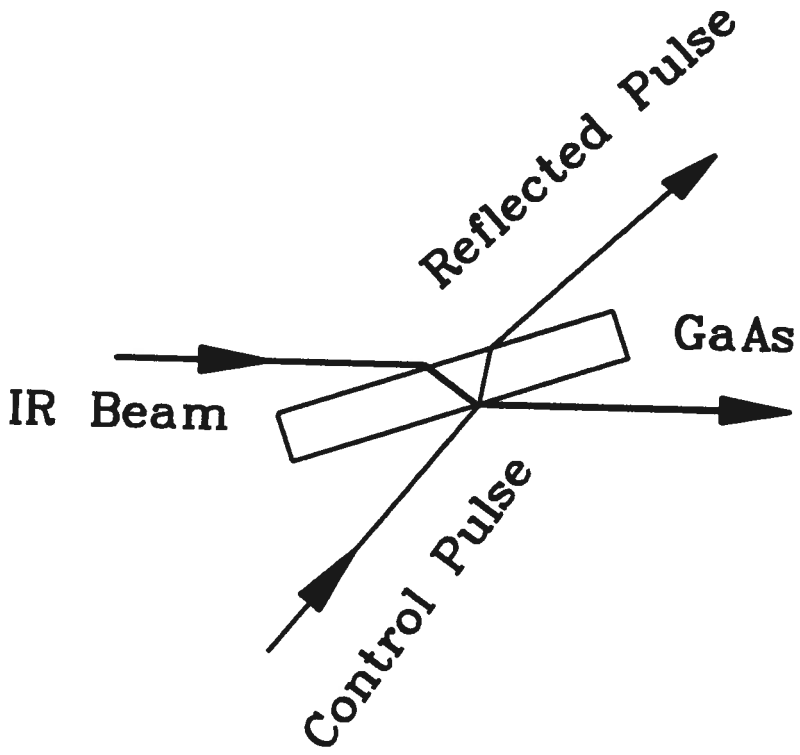

Figure 7.2: Schematics of the backside infrared reflection experiment.

Bibliography

[1] R. K. Brimacombe and J. Reid, IEEE J. Quantum Electron., **19**, 1668 (1983).

[2] A. J. Alcock, R. Fedosejevs, and A. C. Walker, IEEE J. Quantum Electron., **11**, 767 (1975).

[3] N. G. Basov, A. V. Danilychev, O. M. Kerimov, and A. S. Podsosonnyi, Sov. Phys. JETP Lett., **17**, 102 (1973).

[4] N. G. Basov, E. M. Belenov, V. A. Danilychev, O. M. Kerimov, I. B. Kovsh, A. S. Podsosonnyi, and A. F. Suchkov, Sov. Phys. JETP, **37**, 58 (1973).

[5] H. Houtman and J. Meyer, J. Appl. Phys., **61**, 843 (1987).

[6] P. B. Corkum, IEEE J. Quantum Electron., **21**, 216 (1985).

[7] R. Fortin, F. Rheault, J. Gilbert, M. Blanchard, and J. L. Lachambre, Can. J. Phys., **51**, 414 (1973).

[8] P. E. Dyer, and D. J. James, Appl. Phys. Lett., **26**, 331 (1974).

[9] A. F. Gibson, M. F. Kimmitt, and B. Norris, Appl. Phys. Lett., **24**, 306 (1974).

[10] B. J. Feldmann and J. F. Figueira, Appl. Phys. Lett., **25**, 301 (1974).

[11] A. J. Alcock and A. C. Walker, Appl. Phys. lett., **25**, 299 (1974).

[12] F. A. Van Goor, Opt. Commun., **57**, 254 (1986).

[13] A. C. Walker and A. J. Alcock, Opt. Commun., **12**, 430 (1974).

[14] A. E. Siegman, *Lasers,* University Science Books, Mill Valley, CA, p. 966 (1986).

[15] W. J. Witteman, *The CO_2 Laser*, Springer Series in Optical Sciences, Springer Verlag, Berlin, 1987.

[16] H. Houtman and J. Meyer, Opt. Lett., **12**, 87 (1987).

[17] O. R. Wood, R. L. Abrams, T. J. Bridges, Appl. Phys. Lett., **17**, 376 (1970).

[18] R. L. Abrams and O. R. Wood, Appl. Phys. Lett., **19**, 518 (1971).

[19] K. Stenersen, S. Landrø, P. I. Jensen, and S. Lovold, IEEE J. Quantum Electron., **27**, 1869 (1991).

[20] E. Yablonovitch and J. Goldhar, Appl. Phys. Lett., **25**, 580 (1974).

[21] M. Sheik-Bahaei, and H. S. Kwok, Appl. Opt., **25**, 3333 (1986).

[22] M. Sheik-Bahaei, and H. S. Kwok, Appl. Opt., **24**, 666 (1985).

[23] H. S. Kwok and E. Yablonovitch, Appl. Phys. Lett., **30**, 158 (1977).

[24] H. S. Kwok, Infrared Phys., **25**, 53 (1985).

[25] D. P. Scherrer and F. K. Kneubühl, Infrared Phys., **33**, 67 (1992).

[26] D. P. Scherrer, A. W. Kälin, R. Kesselring, and F. K. Kneubühl, Opt. Commun., **87**, 249 (1992).

[27] A. W. Kälin, R. Kesselring, C. Hongru, and F. K. Kneubühl, Infrared Phys., **33**, 73 (1992).

[28] R. Kesselring, A. W. Kälin, H. J. Schötzau, and F. K. Kneubühl, IEEE J. Quantum Electron., **29**, 997 (1993).

[29] R. Kesselring, A. W. Kälin, and F. K. Kneubühl, *Digest 15^{th} Intern. Conf. on Infrared and Millimeter Waves.* SPIE, Orlando, Fl., Vol. 1514, p. 475 (1990).

[30] J. Knittel, D. P. Scherrer, and F. K. Kneubüh, Infrared Phys. Technol., **35**, 67 (1995).

[31] Proceedings of the XIVth International FEL Conference, Kobe, 1992. Nucl. Instrum. Methods Phys. Res., Sect. **A 311** (1993).

[32] F. Glotin, R. Chaput, D. A. Jaroskynski, R. Prazeres, and J. M. Ortega, Phys. Rev. Lett., **71**, 2587 (1993).

[33] B. N. Murdin, C. Merveille, A. K. Kar, C. R. Pidgeon, D. A. Jaroskynski, J. M. Ortega, R. Prazeres, Opt. Quantum Electron., **25**, 171 (1993).

[34] R. Chaput, F. Glotin, G. Humbert, B. Kergosien, J. Lesrel, J. M. Ortega, L. Serin, J. C. Bourdon, M. Bernard, H. Coulle, M. Dehamme, T. Garvey, M. Mencik, B. Mouton, J. Rodier, P. Roudier, and M. Taurigna, Nucl. Instrum. Methods Phys. Res., **A 331**, 267 (1993).

[35] R. Prazeres, J. M. Berset, F. Glotin, D. A. Jaroskynski, and J. M. Ortega, Nucl. Instrum. Methods Phys. Res., **A 331**, 15 (1993).

[36] D. A. Jaroskynski, J. M. Ortega, R. Prazeres, F. Glotin, B. N. Murdin, C. Merveille, M. F. Kimmitt, A. K. Kar, and C. R. Pidgeon, Nucl. Instrum. Methods Phys. Res., **A 331**, 640 (1993).

[37] P. Hamm, C. Lauterwasser, and W. Zinth, Opt. Lett., **18**, 1943 (1993).

[38] F. Seifert, V. Petrov, and M. Woerner, Opt. Lett., **23**, 2009 (1994).

[39] P. C. Becker, M. R. X. de Barros, T. M. Jedju, R. S. Miranda, L. C. West, J. Dunkel, C. W. Roberts, J. W. Stayt, Jr, and V. Swaminathan, R. P. Trebino, and I. A. Walmsley, eds., SPIE Proceedings, Vol. 2116, p. 16, 1994.

[40] T. Dahinten, U. Plödereder, A. Seilmeier, K. L. Vodopyanov, K. R. Allakhverdiev, and Z. A. Ibragimov, IEEE J. Quantum Electron., **29**, 2245 (1993).

[41] T. Elsaesser, H. Lobentanzer, and A. Seilmeier, Opt. Commun., **52**, 355 (1985).

[42] P. C. Becker, D. Gershoni, A. Prosser, in *Ultrafast Phenomena VII,* Springer Verlag, Berlin, p. 81, 1990.

[43] A. J. Alcock, P. B. Corkum, and D. J. James, Appl. Phys. Lett., **27**, 680 (1975).

[44] S. A. Jamison, A. V. Nurmikko, and H. J. Gerritsen, Lett., **29**, 640 (1976).

[45] S. A. Jamison, and A. V. Nurmikko, Appl. Phys. lett., **33**, 598 (1978).

[46] P. B. Corkum, A. J. Alcock, D. F. Rollin, and H. D. Morrison, Appl. Phys. Lett., **32**, 27 (1978).

[47] A. J. Alcock, and P. B. Corkum, Can., J. Phys., **57**, 1280 (1979).

[48] A. J. Alcock, and P. B. Corkum, Phil. Trans. R. Soc. Lond. **A 298**, 365 (1980).

[49] A. V. Nurmikko, and B. D. Schwartz, Soc. Japan, **49**, Suppl. A, 511 (1980).

[50] A. V. Nurmikko, and B. D. Schwartz, **21**, 229 (1982).

[51] P. B. Corkum, Opt. Lett., **8**, 514 (1983).

[52] H. Salzmann, T. Vogel, and G. Dodel, Opt. Commun., **47**, 340 (1983).

[53] P. B. Corkum and D. Keith, J. Opt. Soc. Am. B, **2**, 1873 (1985).

[54] P. B. Corkum, IEEE J. Quantum Electron., **21**, 216 (1985).

[55] C. Rolland and P. B. Corkum, J. Opt. Soc. Am. B, **3**, 1625 (1986).

[56] W. M. Dennis, J. Opt. Soc. Am. B, **6**, 1045 (1989).

[57] R. E. M. de Bekker, L. M. Claessen, and P. Wyder, J. Appl. Phys., **68**, 3729 (1990).

[58] T. Vogel, G. Dodel, E. Holzhauer, H. Salzmann, and A. Theurer, Appl. Opt., **31**, 329 (1992).

[59] J. Burghoorn, W. Roest, J. Bij, T. O. Klaassen, and W. T. Meas. Sci. Technol., **4**, 1415 (1993).

[60] I. Pogorelsky, I. Ben-Zvi, W. D. Kimura, N. A. Kurnit, and Infrared Phys. Technol., **36**, 341 (1995).

[61] *Semiconductors Probed by Ultrafast Spectroscopy*, R. R. Alfano, ed., Vol. I, II, Academic Press, Inc., Orlando, 1984.

[62] J. Shah, *Hot Carriers in Semiconductor Nanostructures: Physics and Applications,* Academic Press, Inc., Boston 1992.

[63] *Ultrashort Processes in Condensed Matter,* W. E. Born, ed., Plenum Press, New York, 1992.

[64] *Ultrafast Phenomena IV,* D. H. Auston and K. B. Eisenthal, Springer Verlag, Berlin, 1984.

[65] *Ultrafast Phenomena V,* G. R. Fleming and A. E. Siegman, Springer Verlag, Berlin, 1986.

[66] *Ultrafast Phenomena VI,* T. Yajima, K. Yoshihara, C. B. Harris, and S. Shionoya, Springer Verlag, Berlin, 1988.

[67] *Ultrafast Phenomena VII,* C. B. Harris, E. P. Ippen, G. A. Mourou, and A. H. Zewail, Springer Verlag, Berlin, 1990.

[68] *Ultrafast Phenomena VIII,* J. L. Martin et al., eds., Springer Verlag, Berlin, 1993.

[69] *Ultrafast Lasers Probe Phenomena in Bulk and Microstructure Semiconductors,* R. R. Alfano, ed., SPIE Proceedings, Vol. 793, 1987.

[70] *Ultrafast Lasers Probe Phenomena in Bulk and Microstructure Semiconductors II,* R. R. Alfano, ed., SPIE Proceedings, Vol. 942, 1988.

[71] *Hot Carriers in Semiconductors,* Proceedings of the Fifth International Conference, J. Shah and G. J. Iafrate, ed., Solid State Electron., **31**, (1988).

[72] *Hot Carriers in Semiconductors,* Proceedings of the Sixth International Conference, D. K. Ferry and L. K. Akers, ed., Solid State Electron., **32**, (1989).

[73] *Ultrafast Lasers Probe Phenomena in Semiconductors and Superconductors,* R. R. Alfano, ed., SPIE Proceedings, Vol. 1677, 1992.

[74] *Ultrafast Phenomena in Semiconductors,* D. K. Ferry and H. M. van Driel, ed., SPIE Proceedings, Vol. 2142, 1994.

[75] H. Ehrenreich, *Optical Properties of Solids,* J.Tauc, ed., Academic Press, New York, 1966.

[76] R. Loudon, *The Quantum Theory of Light*, Clarendon, Oxford, 1973.

[77] Y. F. Chen, C. M. Kwei, C. J. Tung, Phys. Rev. B, **48**, 4373 (1993).

[78] D. H. Auston, S. McAfee, C. V. Shank, E. P. Ippen, and O. Teschke, Solid Stat Electron., **21**, 147 (1978).

[79] E. N. Glezer, Y. Siegal, L. Huang, and E. Mazur, Phys. Rev. B, **51**, 6959 (1995).

[80] J. R. Dixon, in *Optical Properties of Solids*, S. Nudelman and S. S. Mitra, eds., Plenum Press, New York, 1969.

[81] Y. Siegal, E. N. Glezer, and E. Mazur, Phys. Rev., B, **49**, 16403 (1994).

[82] Y. Siegal, E. N. Glezer, L. Huang, and E. Mazur, Reference [74], p 158.

[83] M. A. Cavicchia and R. R. Alfano, SPIE proceedings, Vol. 2142, p 128. 1994.

[84] J. Meyer and A. Y. Elezzabi, Appl. Phys. Lett., **58**, 1940 (1991).

[85] A. Y. Elezzabi and J. Meyer, IEEE J. Quantum Electron., **28**, 1830 (1992).

[86] V. L. Ginzburg, *The Propagation of Electromagnetic Waves in Plasma.* New York, Pergamon Press Ltd., 1970.

[87] W. C. Chew, *Waves and Fields in Inhomogeneous Media.* New York, Van Nostrand Reinhold, 1990.

[88] J. R. Wait, *Electromagnetic Waves in Stratified Media.* Oxford, Pergamon Press, 1970.

[89] W. L. Kruer, *The Physics of Laser Plasma Interactions.* Addison-Wesley Publishing Company, 1988.

[90] H. M. Milchberg and R. R. Freeman, J. Opt. Am. B., **6**, 1351 (1989).

[91] I. F. Vakhnenko and V. L. Strizhevskii, Sov. Phys. Semiconductors, **3**, 1562 (1970).

[92] V. K. Subashiev and A. A. Kukharskii, Phys. Stat. Sol., **23**, 447 (1967).

[93] G. Cicconi, J. Plasma Phys., **47**, 1 (1992).

[94] M. I Gallant and H. M. van Driel, Phys. Rev. B., **26**, 2133 (1982).

[95] N. G. Denisov, Sov. Phys. JETP, **4**, 544 (1957).

[96] K. Försterling and H. O. Wüster, J. Atm. Terr. Phys., **2**, 22 (1951).

[97] S. Sharma, R. K. Khardekar, and H. C. Pant, Physica Scripta, **T30**, 95 (1990).

[98] J. L. Coutaz, "*Nonlinear Optics in Solids.*" Proceedings of the International Summer School, Aalborg, Denmark, July 31-August 4 1989. Springer Verlag, Berlin, p 44.

[99] Y. R. Shen, *The Principles of Nonlinear Optics.* New York, John Wiley, 1984.

[100] H. M. Milchberg and R. R. Freeman, Phys. Fluids B, **2**, 1395 (1990).

[101] D. G. Mclean, M. G. Roe, A. I. D'Souza, and P. E. Wigen, Appl.Phys. Lett., **48**, 992 (1986).

[102] H. Melchior, *Laser Handbook.* Vol. 1, Edited by E. J. Arecchi and E. O. Schulz-Dubois, North Holland Publishing Company, Amsterdam, The Netherlands, 1972.

[103] I. P. Kaminow and E. Turner, *Linear Electrooptical Materials,* in *Handbook of Lasers.* Chemical Rubber Co., Cleveland, OH, 1971.

[104] B. Carnahan, H. A. Luther, and J. O. Wilkes, *Applied Numerical Methods.* New York, John Wiley and Sons, Inc., 1969.

[105] R. L. Burden, J. D. Faires, and A. C. Reynold, *Numerical Analysis.* Boston, Massachusetts, Prindle, Weber and Schmidt, 1981.

[106] R. E. Moore, *Interval Analysis.* Englewood, N.J., Prentice-Hall, Inc., 1966.

[107] D. R. Corson and P. Lorrain, *Introduction to Electromagnetic Fields and Waves.* San Francisco, W. H. Freeman and Company, 1962.

[108] M. Born and E. Wolf, *Principles of Optics,* 3rd ed., Oxford, Pergamon Press, 1965.

[109] J. R. Wait, *Wave Propagation Theory.* New York, Pergamon Press, New York, 1981.

[110] A. Vasicek, *Optics of Thin Films.* Amsterdam, North Holland Publishing Company, 1960.

[111] J. Macdonald, *Metal Dielectric Multilayers.* Adam Hilger Ltd., 1971.

[112] J. I. Pankon, *Optical Processes in Semiconductors.* Englewood, N.J., Prentice-Hall, 1971.

[113] Z. Vardeny and J. Tauc, Phys. Rev. Lett., **46**, 1223 (1981).

[114] M. S. Tyagi and R. Van Overstraeten, Solid Stat Electron., **26**, 577 (1983).

[115] P. T. Landsberg, *Recombination in Semiconductors.* Cambridge, Cambridge University Press, 1991.

[116] J. W. Orton and P. Blood, *The Electrical Characterization of Semiconductors: Measurement of Minority Carrier Properties.* London, Academic Press, 1990.

[117] P. T. Landsberg, Phys. Stat. Sol., **41**, 457 (1970).

[118] J. L. Moll, *Physics of Semiconductors.* Chapter 6, McGraw-Hill, New York, 1964.

[119] W. Van Roosbroeck and W. Schockley, Phys. Rev., **94**, 1958 (1954).

[120] L. R. Weisberg, J, Appl. Phys., **39**, 6096 (1968).

[121] W. Rosenthal, Solid State Commun., **13**, 1215 (1973).

[122] D. C. Marvin, S. M. Beck, J. E. Wessel, and J. G. Rollins, IEEE J. Quantum Electron., **25**, 1064 (1989).

[123] J. S. Blakemore, *Semiconductor Statistics.* New York, Pergamon Press, 1962.

[124] Jeff F. Young and H. M. van Driel, Phys. Rev. B., **26**, 2147 (1982).

[125] R. Brunetti and C. Jacoboni, in *Semiconductors Probed by Ultrafast Laser Spectroscopy,* R. R. Alfano, Ed., pp 367-412, Academic Press Inc., Orlando, Fl., 1984.

[126] D. H. Auston and C. V. Shank, Phys. Rev. Lett., **32**, 1120 (1974).

[127] M. Wautelet and J. A. Van Vechten, Phys. Rev. B, **23**, 5551 (1981).

[128] H. M. van Driel, J. S. preston, and M. I. Gallant, Appl. Phys. Lett., **40**, 385 (1982).

[129] M. Wautelet and L. D. Laude, in *Semiconductors Probed by Ultrafast Laser Spectroscopy,* R. R. Alfano, Ed., pp 353-366, Academic Press Inc., Orlando, Fl., 1984.

[130] A. L. Smirl, S. C. Moss, and J. R. Lindle, Phys. Rev. B, **25**, 2645 (1982).

[131] A. Olsson, D. J. Erskine, Z. Y. Xu, A. Schremer, and C. L. Tang, Appl. Phys. Lett., **41**, 659 (1982).

[132] C. A. Hoffman, K. Jarasiunas, and H. J. Gerritsen, Appl. Phys. Lett., **33**, 536 (1978).

[133] M. A. Yurek, C. D. Striffler, and C. H. Lee, in *Infrared and Millimeter Waves.* K. J. Burton, Ed. Orlando, FL, Academic Press, Vol. 14, part V, pp. 249-290, 1985.

[134] H. Houtman, A. Cheuck, A. Y. Elezzabi, J. E. Ford, M. Laberge, W. Liese, J. Meyer, G. C. Stuart, and Y. Zhu, Rev. Sci. Instrum., **64**, 839 (1993).

[135] H. Houtman and J. Meyer, Rev. Sci. Instrum., **54**, 1629 (1983).

[136] J. E. Ford, J. Meyer, and H. Houtman, Appl. Phys. Lett., **48**, 1639 (1986).

[137] H. Houtman, *Transmission Line and LC Inversion Circuits*, Plasma Physics, UBC Laboratory Report No. 112, 1984.

[138] H. Houtman and J. Meyer, J. Appl. Phys., **61**, 843 (1987).

[139] H. Houtman and J. Meyer, Opt. Lett., **12**, 87 (1987).

[140] J. Meyer and A. Y. Elezzabi, J. Appl. Phys., **68**, 3938 (1990).

[141] H. Houtman and C. J. Walsh, *High Power CO_2 Lasers at UBC,* Plasma Physics, UBC Laboratory Report No. 79, 1980.

[142] B. Norris and A. L. S. Smith, J. Phys. E, **10**, 551 (1977).

[143] B. Norris and A. L. S. Smith, Appl. Phys. Lett., **34**, 385 (1979).

[144] H. Houtman, *Measurement of Current Transients Using Helical-Line Rogowski Coils of Arbitrary Shape,* Plasma Physics, UBC Laboratory Report No. 121, 1989.

[145] I. A. D. Lewis and F. H. Wells, *Millimicrosecond Pulse Techniques,* Pergamon, London, 1959.

[146] F. B. A. Frügel, *High Speed Pulse Technology,* Vols. I (1965), II (1965), III (1976), and IV (1980), Academic Press, New York.

[147] T. W. Carman and P. E. Dyer, J. Appl. Phys., **49**, 3742 (1978).

[148] T. W. Carman and P. E. Dyer, Appl. Phys., **17**, 27 (1978).

[149] G. C. Stuart, H. Houtman, and J. Meyer, Rev. Sci. Instrum., **58**, 261 (1987).

[150] L. J. Van der Pauw, Philips Res. Repts., **13**, N1, 1 (1958).

[151] V. N. Dobrovolsky and V. G. Litovchenko, *Surface Electronic Transport Phenomena in Semiconductors,* Clarendon Press, Oxford,1991

[152] Z. A. Yasa and N. M. Amer, Opt. Commun., **36**, 406, (1981).

[153] A. Brun, P. Georges, G. Le Saux, and F. Salin, J. Phys. D: Appl. Phys., **24**, 1225 (1991).

[154] K. L. Sala, G. A. Kenney-Wallace, and G. E. Hall, IEEE J. Quantum Electron., **16**, 990 (1980).

[155] H. Harde and H. Burggraf, Opt. Commun., **38**, 221 (1981).

[156] E. Bourkoff and A. Dienes, IEEE J. Quantum Electron, **16**, 425 (1980).

[157] J. M. Diels, J. J. Fontaine, I. C. McMichael, and F. Simoni, Appl. Opt., **24**, 1270 (1985).

[158] D. C. Edelstein, R. B. Romney, and M. Scheuermann, Rev. Sci. Instrum., **62**, 579 (1991).

[159] K. N. Choi, Meas. Sci. Technol., **4**, 850 (1993).

[160] R. S. Chin, Masters thesis, University of British Columbia, 1991.

[161] J. Meyer, A. Y. Elezzabi, and M. K. Y. Hughes, IEEE J. Quantum Electron., **31**, 729 (1995).

[162] J. Meyer, A. Y. Elezzabi, and M. K. Y. Hughes, IEEE J. Quantum Electron., **31**, 1292 (1995).

[163] L.M. Lambert, Phys. Stat. Sol. (a), **11**, 461 (1972).

[164] W.G. Spitzer and H.Y. Fan, Phys. Rev., **106**, 883 (1957).

[165] P.A. Schumann and R.P. Phillips, Solid State Electron., **10**, 943 (1967).

[166] H. M. van Driel, Appl. Phys. Lett., **44**, 617 (1984).

[167] C.V. Shank, R. Yen, and C. Hirlimann, Phys. Rev. Lett., **50**, 454 (1983).

[168] N. J. Halas and J. Bokor, Phys. Rev. Lett., **62**, 1679 (1989).

[169] N. J. Halas and J. Bokor, IEEE J. Quantum Electron., **25**, 2550 (1989).

[170] J. P. Long, H. R. Sadeghi, J. C. Rife, and M. N. Kabler, Phys. Rev. Lett., **64**, 1158 (1990).

[171] J. Dwiezor and W. Schmid, Appl.Phys.Lett., **31**, 346 (1977).

[172] A.F. Gibson, C.A. Rosito, C.A. Raffo, and M.F. Kimmit, Appl. Phys. Lett., **21**, 356 (1972).

[173] Jeff F. Young and H. M. Van Driel, Phys. Rev. B., **26**, 2147 (1982).

[174] H. Kurz, W. Kuett, K. Seibert amd M. Strahnen, Solid-State Electronics, **31**, 447 (1988).

[175] A. Y. Elezzabi, J. Meyer, M. K. Y. Hughes, and S. R. Johnson, Opt. Lett., **19**, 898 (1994).

[176] A. Y. Elezzabi, J. Meyer, and M. K. Y. Hughes, Appl. Phys. Lett., **56**, 402 (1995).

[177] A. Y. Elezzabi, M. K. Y. Hughes, J. Meyer, and S. R. Johnson, Opt. Lett., **20**, 587 (1995).

[178] J. Khul, in *Ultrashort Processes in Condensed Matter,* W. E. Born, ed., NATO ASI Series, Plenum Press, New York, pp. 143-194, 1992.

[179] D. H.Auston, in *Ultrashort Laser Pulses and Applications,* W. Kaiser, ed., Vol. 60, Springer-Verlag, Berlin, pp. 183-233, 1988.

[180] P. P. Vasil'ev, Sov. J. Quantum Electron, **20**, 209 (1990).

[181] P. R. Wilshaw, T. S. Fell, and G. R. Booker, in *Point and Extented Defects in Semiconductors,* G. Benedek, A. Cavallini, and W. Schröter, eds., NATO ASI Series, Plenum Press, New York, pp. 243-257, 1988.

[182] R. C. Newman, in *Imperfections in III/V Materials,*, Semiconductors and Semimetals, E. R. Weber. ed., Vol. 38, Academic Press, Inc., 1993.

[183] C. H. Lee, Appl. Phys. lett., **30**, 84 (1977).

[184] G. A. Mourou and K. E. Meyer, Appl. Phys. Lett., **45**, 492 (1984).

[185] C. H. Lee, A. Antonetti, and G. A. Mourou, Opt. Commun., **21**, 158 (1977).

[186] S. Gupta, S. Sethi, and P. K. Bhattacharya, Appl. Phys. lett., **62**, 1128 (1993).

[187] F. J. Leonberger, P. F. Moulton, Appl. Phys. Lett., **35**, 712 (1979).

[188] R. B. Hammond, N. G. Paulter, A. E. Iverson, R. C. Smith, *Tech. Dig. 1981 Int. Electr. Dev. Mtg.,* 157 (1981).

[189] P. M. Downey and B. Schwartz, Proc. SPIE Int. Soc. Opt. Eng., **439**, 30 (1983).

[190] J. R. Karin P. M. Donney, and R. J. Martin, IEEE J. Quantum Electron., **22**, 677 (1986).

[191] D. R. Bowman, R. B. Hammond, R. W. Dutton, IEEE Electr. Device. Lett., **6**, 502 (1985).

[192] A. P. DeFonzo, Appl. Phys. Lett., **39**, 480 (1983).

[193] A. M. Johnson, D. W. Kisker, W. M. Simpson, R. D. Feldman, in *Picosecond Electronics and Optoelectronics,* ed. by G. A. Mourou, D. M. Bloom, C. H. Lee, Vol. 21, Speringer-Verlag, Berlin, p 188, 1985.

[194] A. M. Johnson, in *Semiconductors Probed by Ultrafast Laser Spectroscopy,* R. R. Alfano, Ed., Vol. 2, Academic Press, New York, 1984, p 13.

[195] W. Schockley and T. W. Read Jr., Phys. Rev., **87**, 835 (1952).

[196] R. N. Hall, Phys. Rev.,**87**, 837 (1952).

[197] M. R. Melloch, N. Otsuka, J. M. Woodall, A. C. Warren, and J. L. Freeout, Appl. Phys. Lett., **57**, 1531 (1990).

[198] D. J. Keeble, M. T. Umlor, P. Asoka-Kumar, K. G. Lynn, and P. W. Cooke, Appl. Phys. Lett., **63**, 87 (1993).

[199] P. W. Yu, D. N. Talwar, and C. E. Stutz, Appl. Phys. Lett., **62**, 2606 (1993).

[200] H. Shen, F. C. Rong, R. Lux, J. Pamulapati, M. Taysing-Lara, Appl. Phys. Lett., **61**, 1585 (1992).

[201] N. Hozhabri, S. C. Sharma, R. N. Pathak, and K. Alvai J. Electronic Materials, **23**, 519 (1994).

[202] R. Takahashi, Y. Kawamura, T. Kagawa, and H. Iwamura, Appl. Phys. Lett., **65**, 1790 (1994).

[203] S. Gupta, J. F. Whitaker, and G. A. Mourou, IEEE J. Quantum Electron., **28**, 2464 (1992).

[204] Y. Kostoulas, T. Gong, B. C. Tousley, G. W. Wicks, P. Cooke, and P. M. Fauchet, in *Ultrafast Phenomena in Semiconductors*, D. K. Ferry and H. M. van Driel, Eds. SPIE Proceedings, **2142**, p 100, 1994.

[205] E. S. Harmon, M. R. Melloch, J. M. Woodall, D. D. Nolte, N. Otsuka, and C. L. Chang., Appl. Phys. Lett., **63**, 2248 (1993).

[206] M. Y. Frankel, B. Tadayon, and T. F. Carruthers., Appl. Phys. Lett., **62**, 255 (1993).

[207] J. D. Morse, R. P. Mariella Jr., J. W. Adkisson, G. D. Anderson, J. S. Harris, R. W. Dutton, Appl. Phys. Lett., **62**, 1382 (1993).

[208] X. Q. Zhou, H. M. van Driel, W. W. Rühle, Z. Gogolak, and K. Ploog., Appl. Phys. Lett., **61**, 3020 (1992).

[209] T. Takamori, Y. K. Sin, K. Watanabe, and Kamijoh, Appl. Phys. Lett., **61**, 2266 (1992).

[210] S. Y. Chou and M. Y. Liu, IEEE J. Quantum Electron., **28**, 2358 (1992).

[211] S. Y. Chou, Y. Liu, W. Khalil, T. Y. Hsiang, and S. Alexandrou, Appl. Phys. Lett., **61**, 819 (1992).

[212] S. Gupta, P. K. Bhattacharya, J. pamulapati, and G. Mourou, Appl. Phys. Lett., **57**, 1543 (1990).

[213] M. Klingenstein, J. Kuhl, R. Nötzel, K. Ploog, J. Rosenzweig, Appl. Phys. Lett., **60**, 627 (1992).

[214] S. Gupta, M. Y. Frankel, J. A. Valdmanis, J. F. Whitaker, G. A. Mourou, F. W. Smith, and A. R. Calawa, Appl. Phys. Lett., **59**, 3276 (1991).

[215] F. W. Smith, H. Q. Le, V. Diadiuk, M. A. Hollis, A. R. Calawa, S. Gupta, M. Frankel, D. R. Dykaar, G. A. Mourou, and T. Y. Hsiang, Appl. Phys. Lett., **54**, 890 (1989).

[216] L. F. Lester, K. C. Hwang, P. Ho, J. Mazurowski, J. M. Billingall, J. Sutliff, S. Gupta, J. Whitaker, and S. L. Williamson, IEEE Photon. Tech. Lett., **5**, 551 (1993).

[217] M. Kaminska, E. R. Weber, K. M. Yu, R. Leon, T. George, F. W. Smith, and A. R. Calawa, in *Semi-Insulating III-V Materials,* A. G. Milnes, C. J. Miner, eds., Adam Hilger, Bristol, p. 111, 1990.

[218] C. Lovie, S. R. Johnson, J. A. Mackenzie, T. Tiedje, T. van van Buuren, J. Vac. Sci. Technol. **A 10**, 930 (1992).

[219] A. C. Warren, J. M. Woodall, P. D. Kirchner, X. Yin, F. Pollak, M. R. Melloch, Phys. Rev. **B 46**, 4617 (1992).

[220] S. R. Johnson, C. Lavoie, T. Tiedje, J. Mackenzie, J. Vac. Sci. Technol, **B 11**, 1007 (1993).

[221] K. F. Lamprecht, S. Juen, L. Palmetshofer, and R. A. Höpfel, Appl. Phys. Lett., **59**, 926 (1991).

[222] M. B. Ketchen, D. Drischkowsky, T. C. Chen, C-C. Chi, N. Duling, III, N. J. Halas, J-M. Halbout, J. A. Kash, and G. P. Li, Appl. Phys. Lett., **48**, 752 (1986).

[223] M. B. Johnson, T. C. McGill, and N. G. Paulter, Appl. Phys. Lett., **54**, 2424 (1989).

[224] M. Lambsdorff, J. Kuhl, J. Rosenzweig, A. Axmann, and Jo. Schneider, Appl. Phys. Lett., **58**, 1881 (1991).

[225] K. F. Lamprecht, S. Juen, L. Palmetshofer and R. A. Höpfel, Proceedings SPIE *Ultrafast Lasers Probe Phenomena in Semiconductors* **1677**, 24-25 March 1992, Somerset New Jersey, pp 9-14.

[226] K. F. Lamprecht, S. Juen, L. Palmetshofer and R. A. Höpfel, Appl. Phys. Lett., **59**, 926 (1991).

[227] R. A. Höpfel and N. Sawaki, Appl. Phys. Lett., **55**, 460 (1989).

[228] D. H. Auston and P. R. Smith, Appl. Phys. Lett., **41**, 599 (1982).

[229] F. E. Doany, D. Grischkowsky, and C. C. Chi, Appl. Phys. Lett., **50**, 460 (1987).

[230] P. R. Smith, D. H. Auston, A. M. Johnson, and W. M. Augustyniak, Appl. Phys. Lett., **38**, 47 (1981).

[231] V. S. Vavilov, and N. A. Ukhin, *Radiation Effects in Semiconductors and Semiconductor Devices,* Plenum Press, New York, 1977.

[232] P. D. Townsend, P. J. Chandler, and Zhang, *Optical Effects of Ion Implantation,,* Cambridge University Press, Cambridge, 1994.

[233] J. A. van Vechten, *Handbook on Semiconductors,* T. S. Moss, and S. P. Keller, Eds., Vol. 3, North-Holland, pp. 1-111, 1980.

[234] D. Pons and J. Bourgoin, Phys. Rev. Lett., **47**, 1293 (1981).

[235] S. S. Li, W. L. Wang, P. W. Lai, and R. T. Owen, J. Electr. Mat., **9**, 335 (1980).

[236] L. P. Ramberg, P. M. Enquist, Y. K. Chen, E. F. Najjar, L. F. Eastman, E. A. Fitzgerald, and K. L. Kavanagh, J. Appl. Phys., **61**, 1234 (1987).

[237] J. Hugi, Y. Haddab, R. Sachot, and M. Ilegems, J. Appl. Phys., **77**, 1785 (1995).

[238] D. L. Rogers, J. M. Woodall, G. D. Pettit, and D. McInturff, IEEE Electron Device Lett., **9**, 515 (1988).

[239] W. J. Schaff, P. J. Tasker, M. C. Foisy, and L. F. Eastman, in *Strained-Layer Superlattices: Materials Science and Technology,* Semiconductors and Semimetals, T. P. Pearsall, Ed., Vol. 33, Academic Press, Inc., pp. 73-138, 1991.

[240] K. H. Chang, P. R. Berger, R. Gibala, P. K. Bhattacharya, J. Singh, J. F. Mansfield, and R. Clarke, in *Dislocations and Interfaces in Semiconductors,* K. Rajan, J. Narayan, and D. G. Ast, Eds., The Metallurgical Society, Inc., p 157, 1988.

[241] J. W. Matthews and A. E. Blackeslee, J. Cryst. Growth, **27**, 118 (1974).

[242] K. Rajan, R. Devine, W. T. Moore, and P. Maigne, J. Appl. Phys., **62**, 1713 (1987).

[243] P. O. Vaccaro, M. Takahashi, K. Fujita, and T. Watanabe, J. Appl. Phys., **76**, 8037 (1994).

[244] W. S. Pelouch and L. A. Schlie, Appl. Phys. Lett., **65**, 2323 (1994).

[245] H. S. Albrecht, P. Heist, J. Kleinschmidt, D. Van Lap, and T. Schröder, Meas. Sci. Technol., **4**, 492 (1993).

[246] H. S. Albrecht, P. Heist, J. Kleinschmidt, D. Van Lap, and T. Schröder, Appl. Opt., **32**, 6659 (1993).

[247] H. S. Albrecht, P. Heist, J. Kleinschmidt, D. Van Lap, and T. Schröder, Appl. Phys. B, **55**, 362 (1992).

[248] Y. Li, D. Y. Chen, L. Yang, and R. R. Alfano, Opt, Lett., **16**, 438 (1991).

[249] P. Heist and J. Kleinschmidt, Opt. Lett., **19**, 961 (1994).

[250] J. Soto-Manriquez, Opt. Commun., **52**, 221 (1984).

[251] I. Golub, Opt. Commun., **94**, 143 (1992).

[252] H. S. Albrecht, P. Heist, J. Kleinschmidt, and D. Van Lap, Appl. Phys. B, **57**, 193 (1993).

[253] N. P. Ernsting and M. Kaschke, Rev. Sci. Instrum., **62**, 600 (1991).

Appendix A

Design Circuits of the Synchronization Unit

This appendix outlines the electronic circuit diagrams of the synchronization unit used to synchronize the hybrid CO_2 laser with the femtosecond laser pulse system.

Diagram A.1:

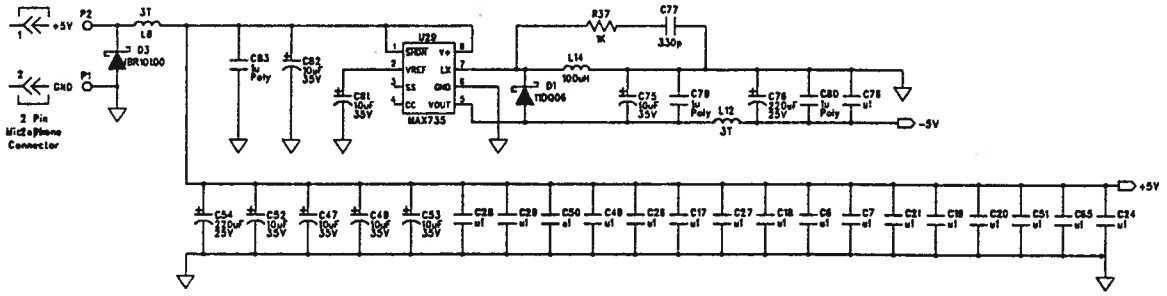

UBC PHYSICS - ELECTRONICS LAB	
DATE: 84/5/5	SHEET: 6 of 8
TITLE: POWER SUPPLY	

Diagram A.2:

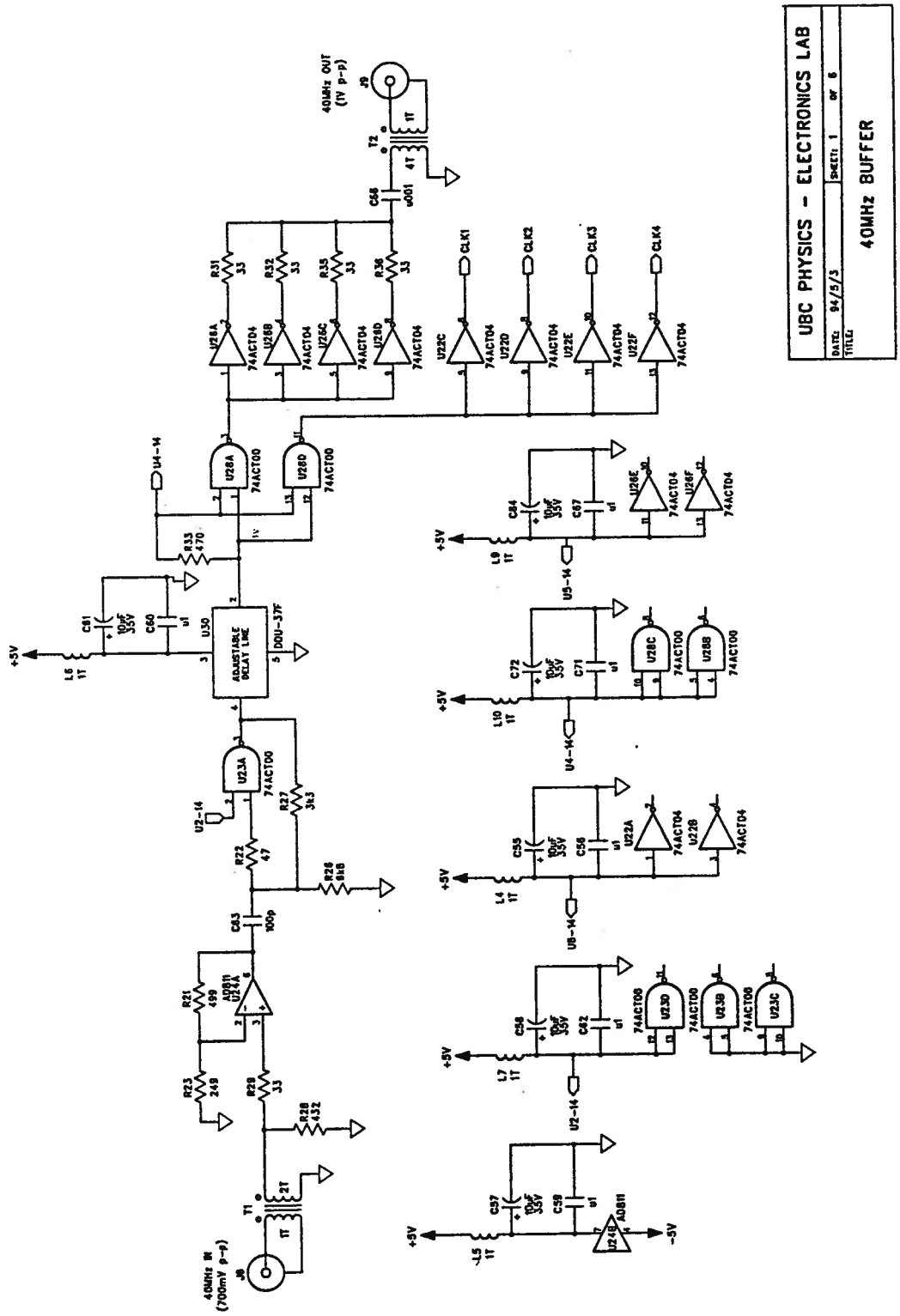
UBC PHYSICS - ELECTRONICS LAB
DATE: 94/5/3
SHEET: 1 OF 6
TITLE: 40MHz BUFFER
40MHz OUT (1V p-p)
40MHz IN (700mV p-p)
ADJUSTABLE DELAY LINE
DDU-37F
74ACT00
74ACT04
AD811
+5V
-5V
CLK1
CLK2
CLK3
CLK4

Diagram A.3:

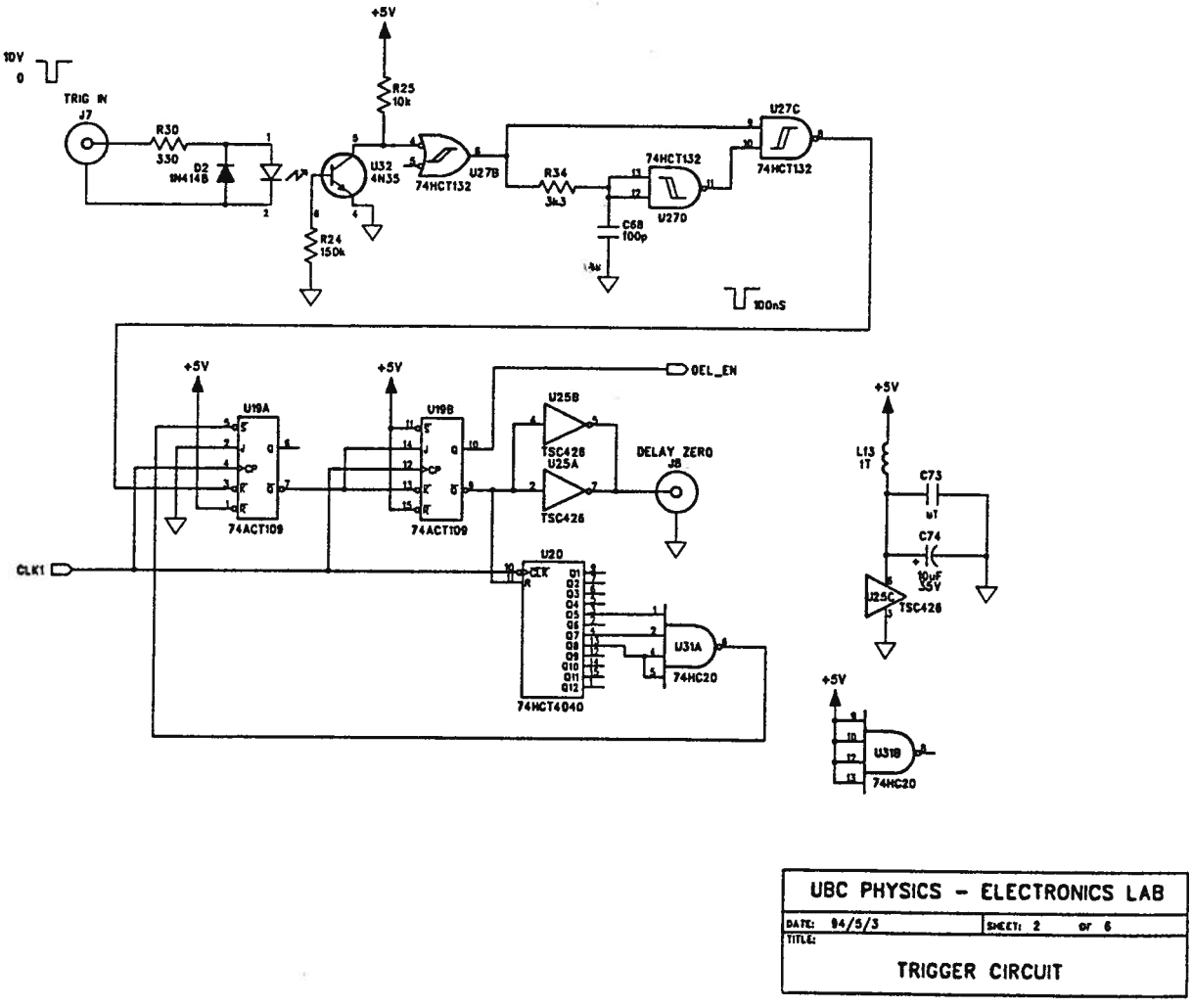

UBC PHYSICS - ELECTRONICS LAB	
DATE: 94/5/3	SHEET: 2 OF 6
TITLE: TRIGGER CIRCUIT	

Diagram A.4:

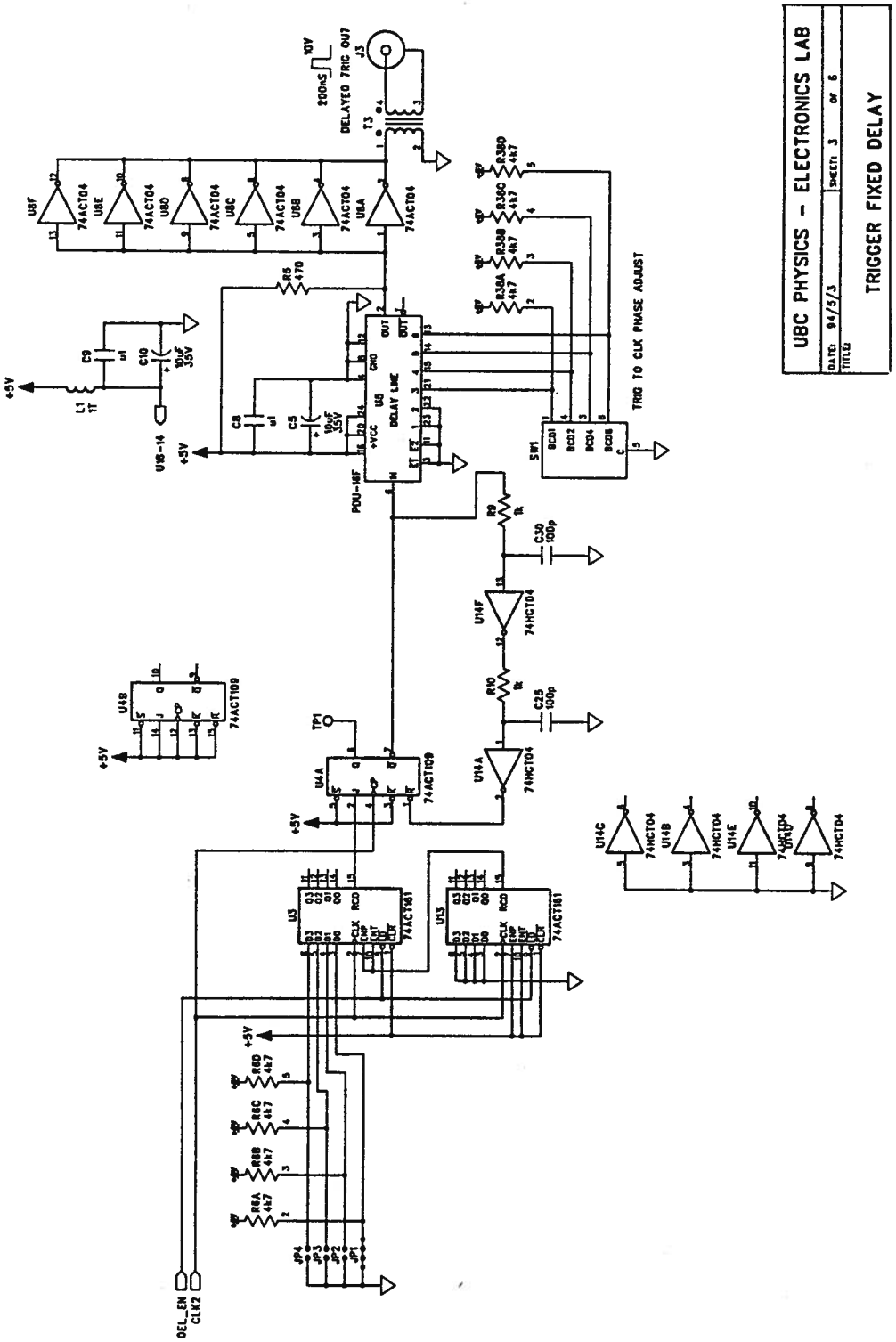
UBC PHYSICS - ELECTRONICS LAB
DATE: 94/5/3
SHEET: 3 OF 6
TITLE: TRIGGER FIXED DELAY
DELAYED TRIG OUT
TRIG TO CLK PHASE ADJUST
DEL_EN
CLK2

Diagram A.5:

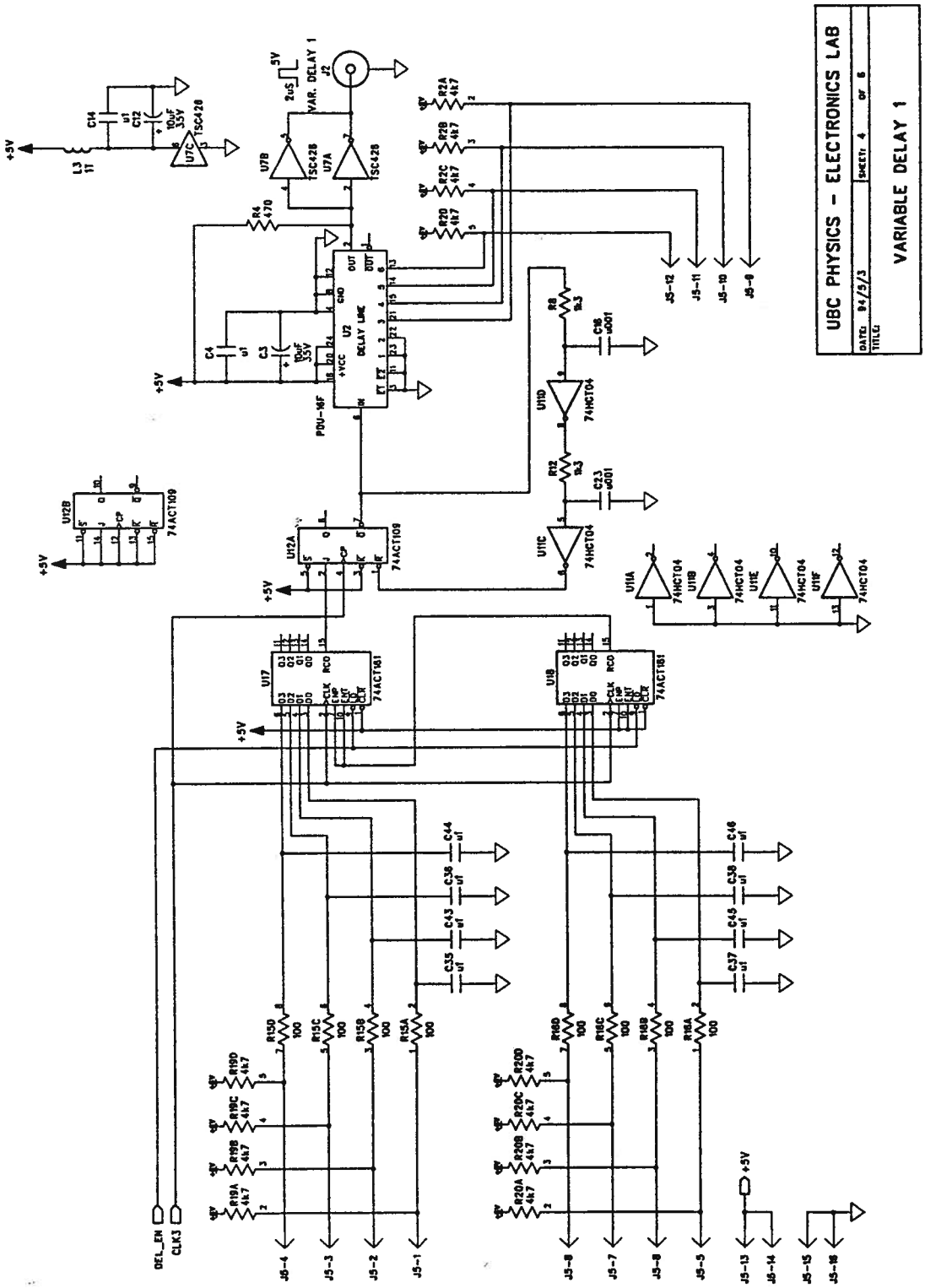
UBC PHYSICS - ELECTRONICS LAB
VARIABLE DELAY 1
DEL_EN
CLK3
74ACT109
74ACT161
74HCT04
TSC428
DELAY LINE

Diagram A.6:

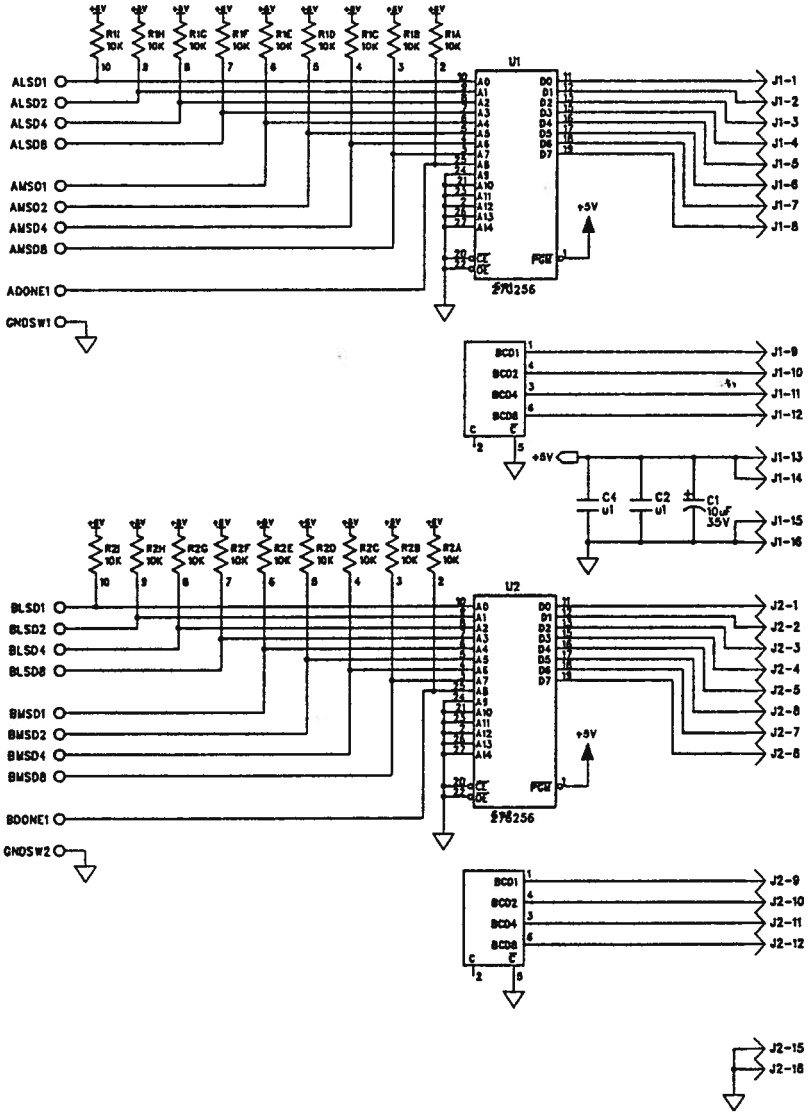

UBC PHYSICS – ELECTRONICS LAB		
DATE: 94/5/12	SHEET: 1	OF 1
TITLE: DELAY LINE Thumbwheel Switch Decoders		

Diagram A.7:

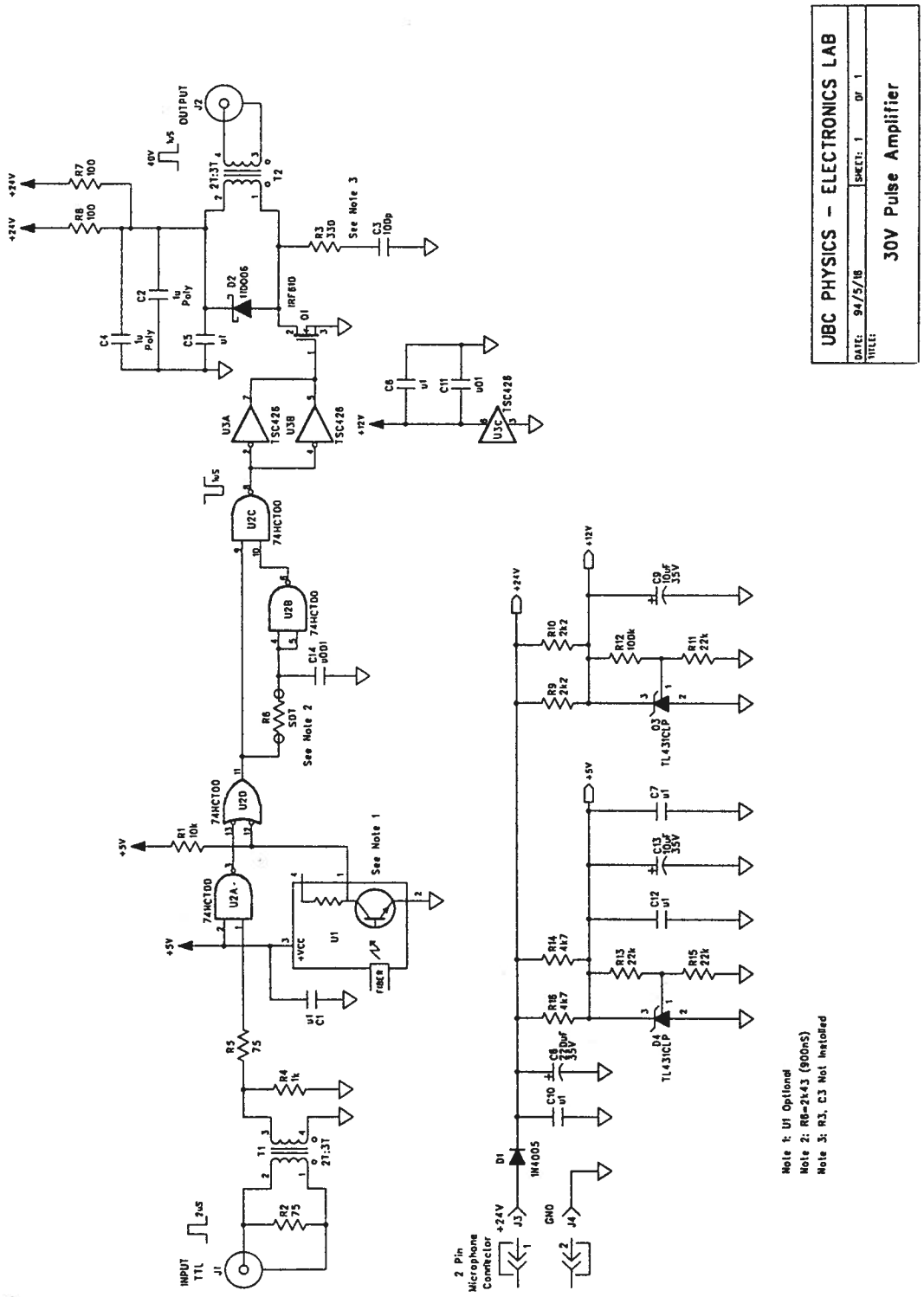
UBC PHYSICS - ELECTRONICS LAB
DATE: 94/5/18
SHEET: 1 OF 1
TITLE:
30V Pulse Amplifier
Note 1: U1 Optional
Note 2: R6=2k43 (900nS)
Note 3: R3, C3 Not Installed

Appendix B

The Fast Photodetector Amplifier Circuit and Performance

In this appendix we present a complete electronic circuit design of a fast photodetector amplifier which was discussed in Chapter 4. The amplifier electronic circuit is shown in figure B.1. The amplifier's output as a function of pulse frequency is presented in figure B.2.

In order to check the pulse width distortion and measure the gain of the amplifier, a 1 ns (337 nm) pulse from a nitrogen laser is attenuated to the signal level of that from Cu:Ge. The signal is detected with a fast detector (Hamamatsu-R1193U.03) and displayed on the 1 GHz bandwidth oscilloscope. The amplifier does not cause any pulse distortion, as shown in figure B.3. The measured gain at 1 GHz is 34 dB.

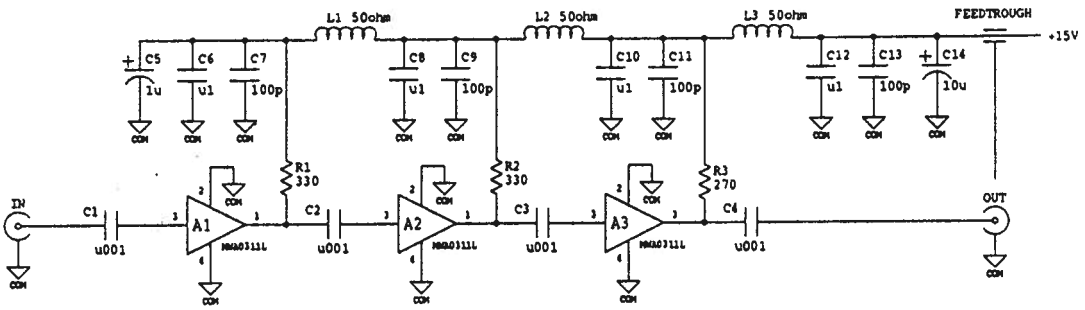

Figure B.1: The amplifier circuit.

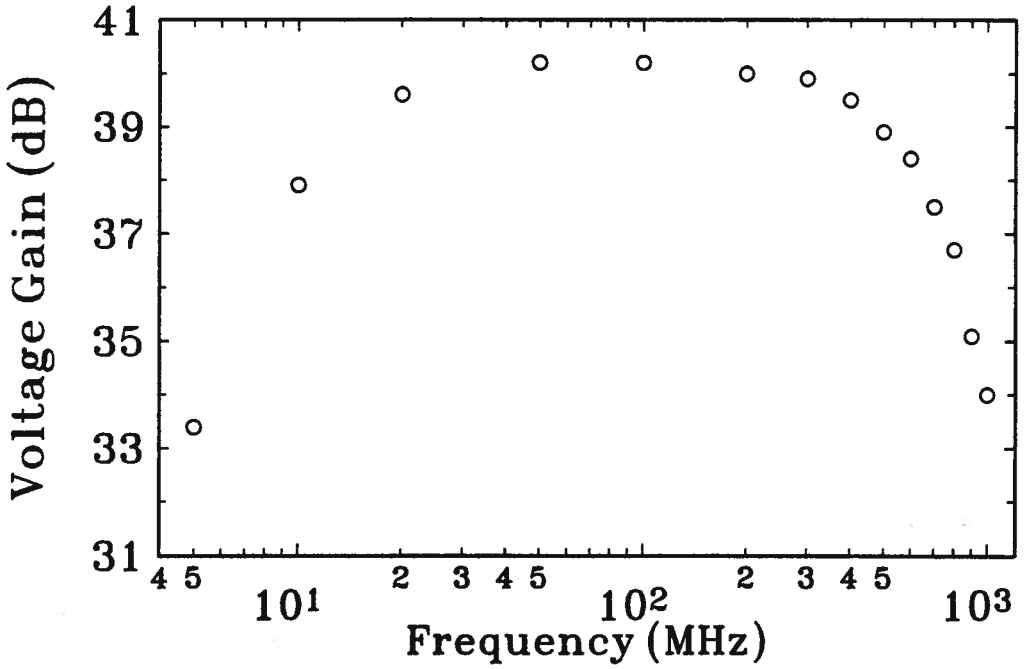

Figure B.2: Photodetector amplifier gain as a function of the input frequency.

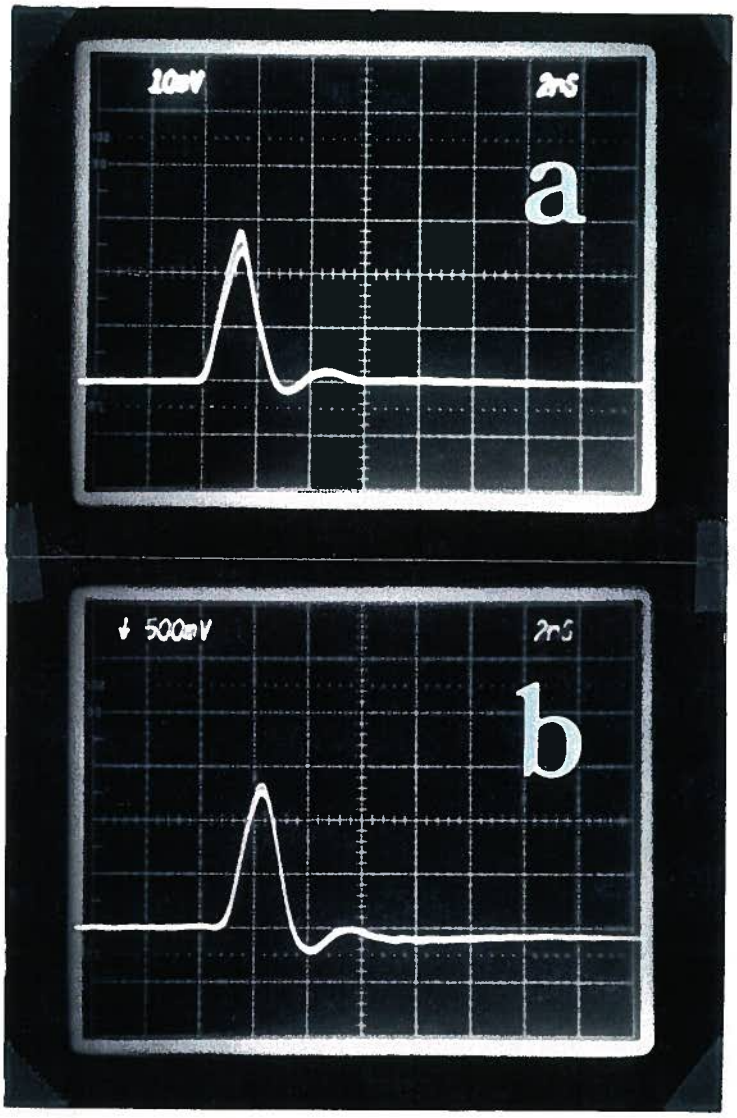

Figure B.3: (a) Input signal to the amplifier. (b) Amplified output signal from the amplifier.

Appendix C

Circuit Design of the Pulse Integration Module

In this appendix, we present the circuit diagrams for the pulse integration module (PIM) which was discussed in Chapter 4.

Diagram C.1:

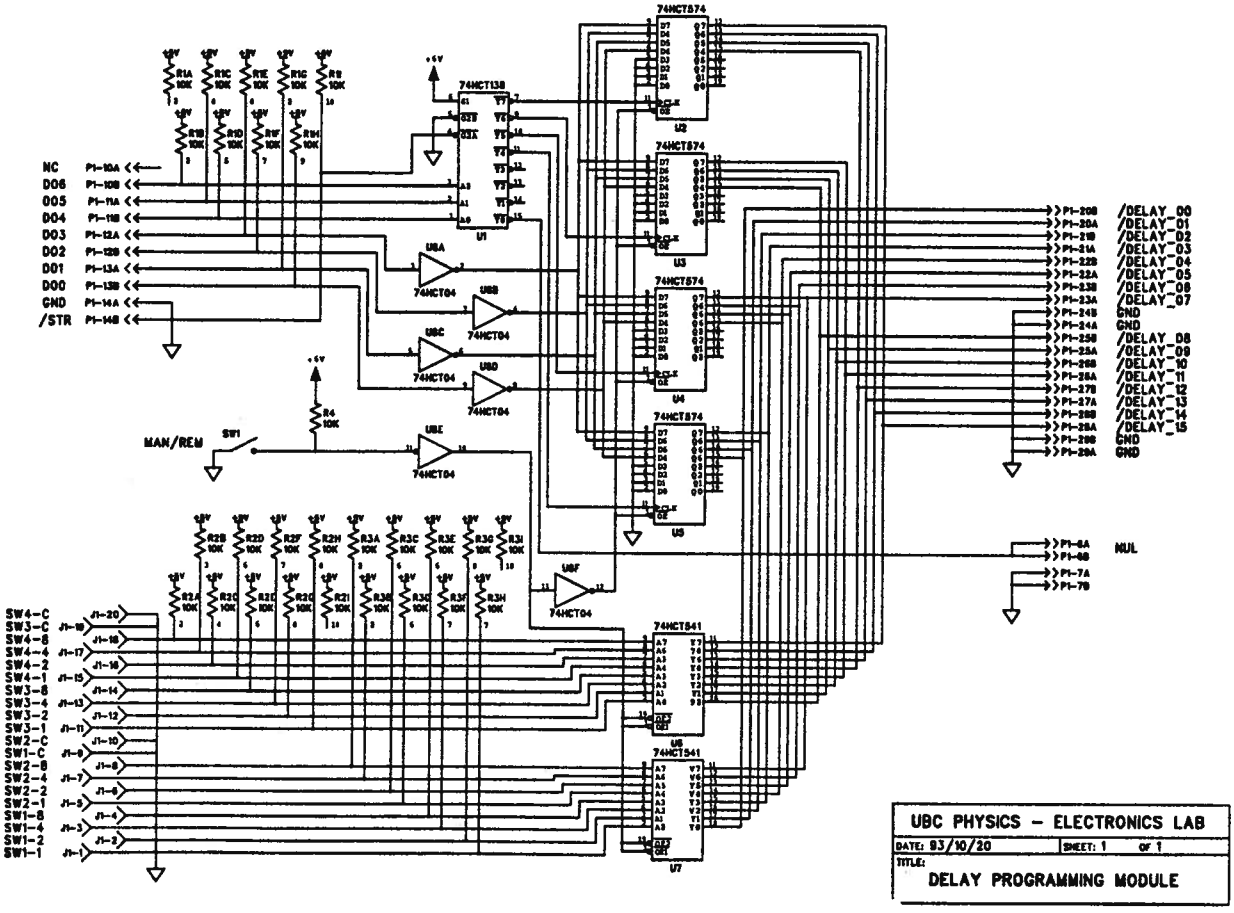

Diagram C.2:

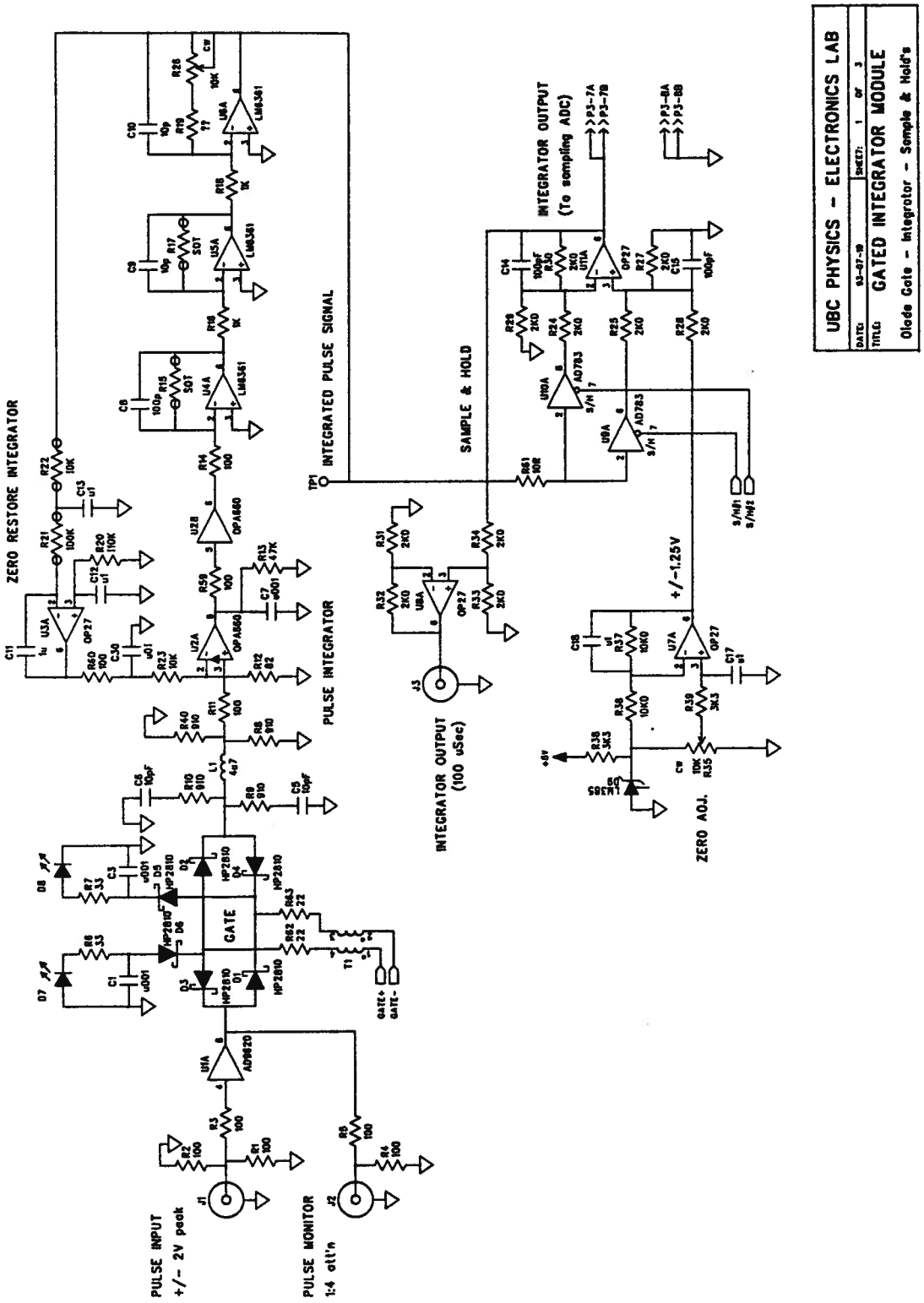
UBC PHYSICS - ELECTRONICS LAB
DATE: 93-07-19
SHEET: 1 OF 3
TITLE: GATED INTEGRATOR MODULE
Diode Gate - Integrator - Sample & Hold's
ZERO RESTORE INTEGRATOR
INTEGRATED PULSE SIGNAL
SAMPLE & HOLD
INTEGRATOR OUTPUT
(To sampling ADC)
PULSE INTEGRATOR
INTEGRATOR OUTPUT
(100 uSec)
+/-1.25V
ZERO ADJ.
GATE
PULSE INPUT
+/- 2V peak
PULSE MONITOR
1:4 attn

Diagram C.3:

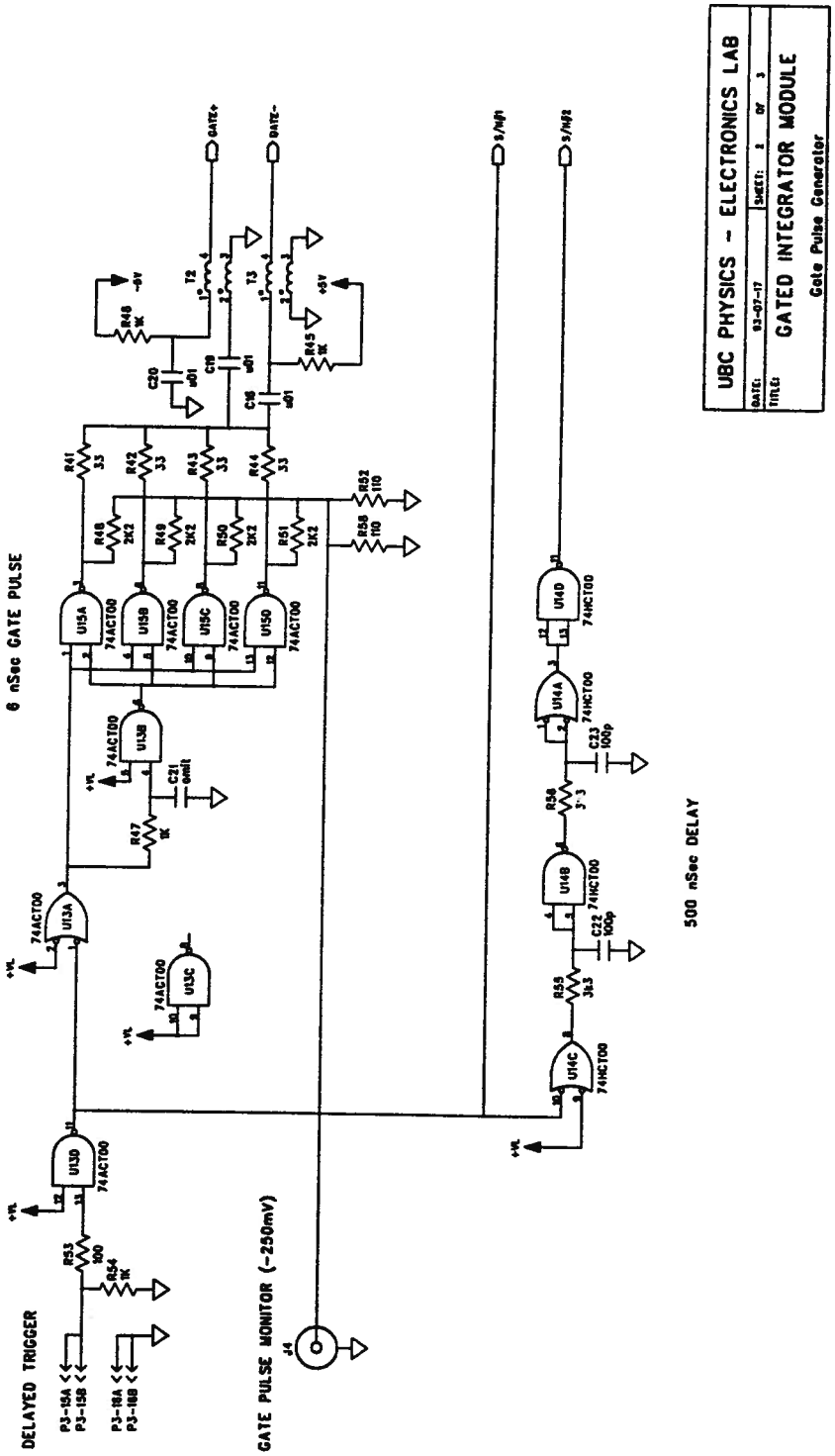
UBC PHYSICS - ELECTRONICS LAB
GATED INTEGRATOR MODULE
Gate Pulse Generator
6 nSec GATE PULSE
500 nSec DELAY
DELAYED TRIGGER
GATE PULSE MONITOR (-250mV)
GATE+
GATE-
S/H1
S/H2
74ACT00
74HCT00

Diagram C.4:

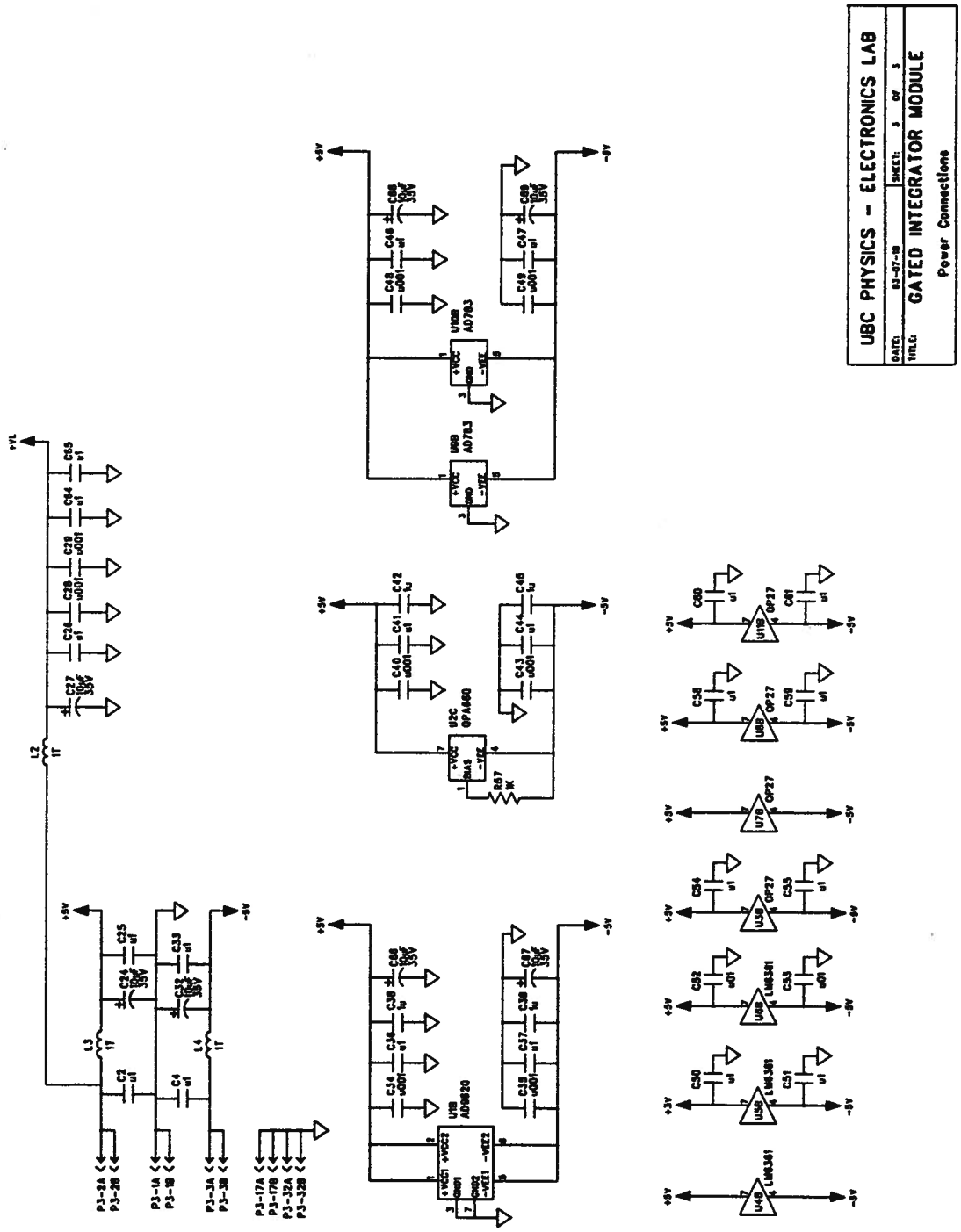
UBC PHYSICS - ELECTRONICS LAB
GATED INTEGRATOR MODULE
Power Connections

Diagram C.5:

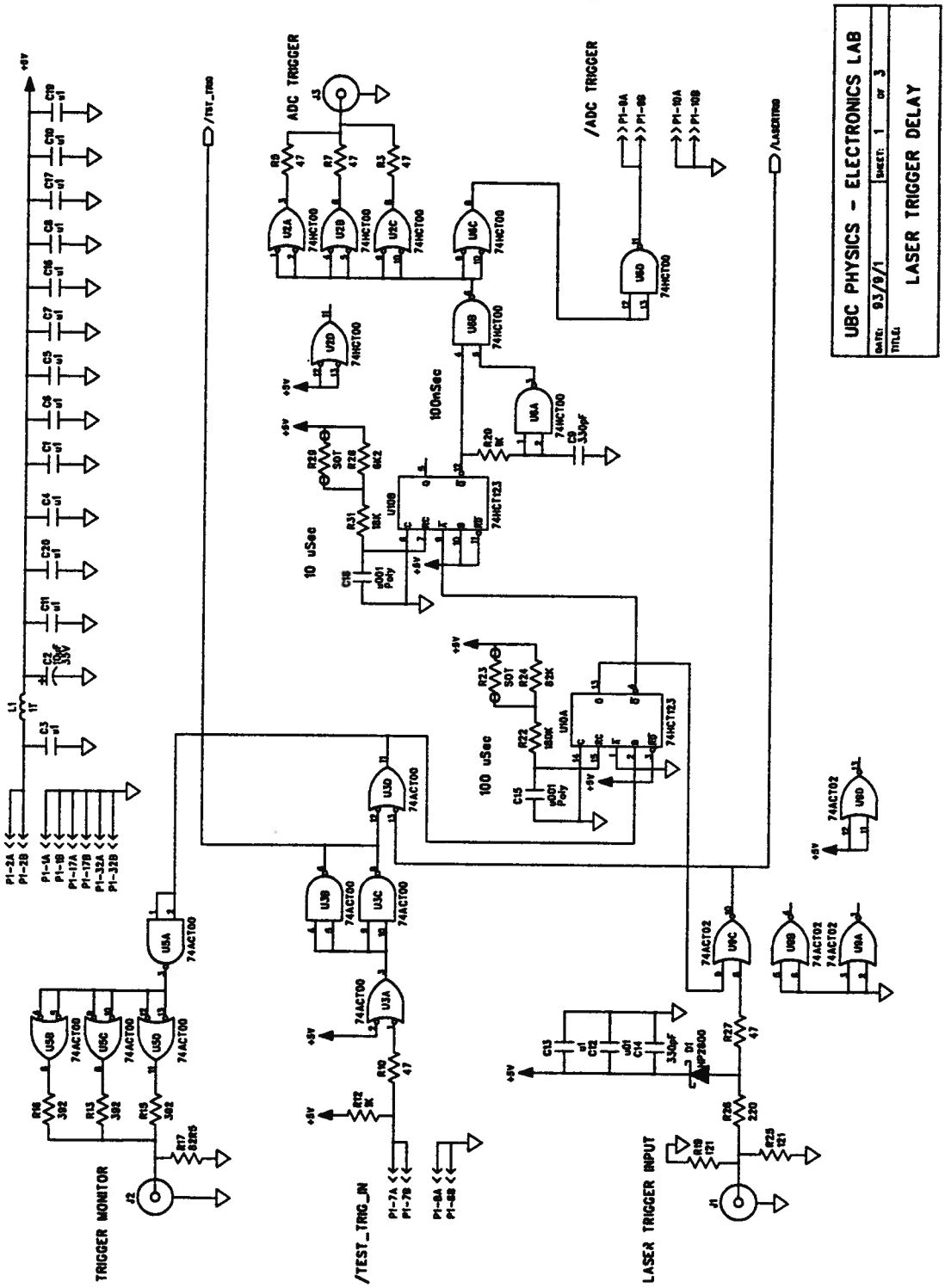
UBC PHYSICS - ELECTRONICS LAB
LASER TRIGGER DELAY
ADC TRIGGER
/ADC TRIGGER
/TEST_TRG
/LASERTRG
100nSec
10 uSec
100 uSec
TRIGGER MONITOR
/TEST_TRG_IN
LASER TRIGGER INPUT
74HCT00
74HCT123
74ACT00
74ACT02

Diagram C.6:

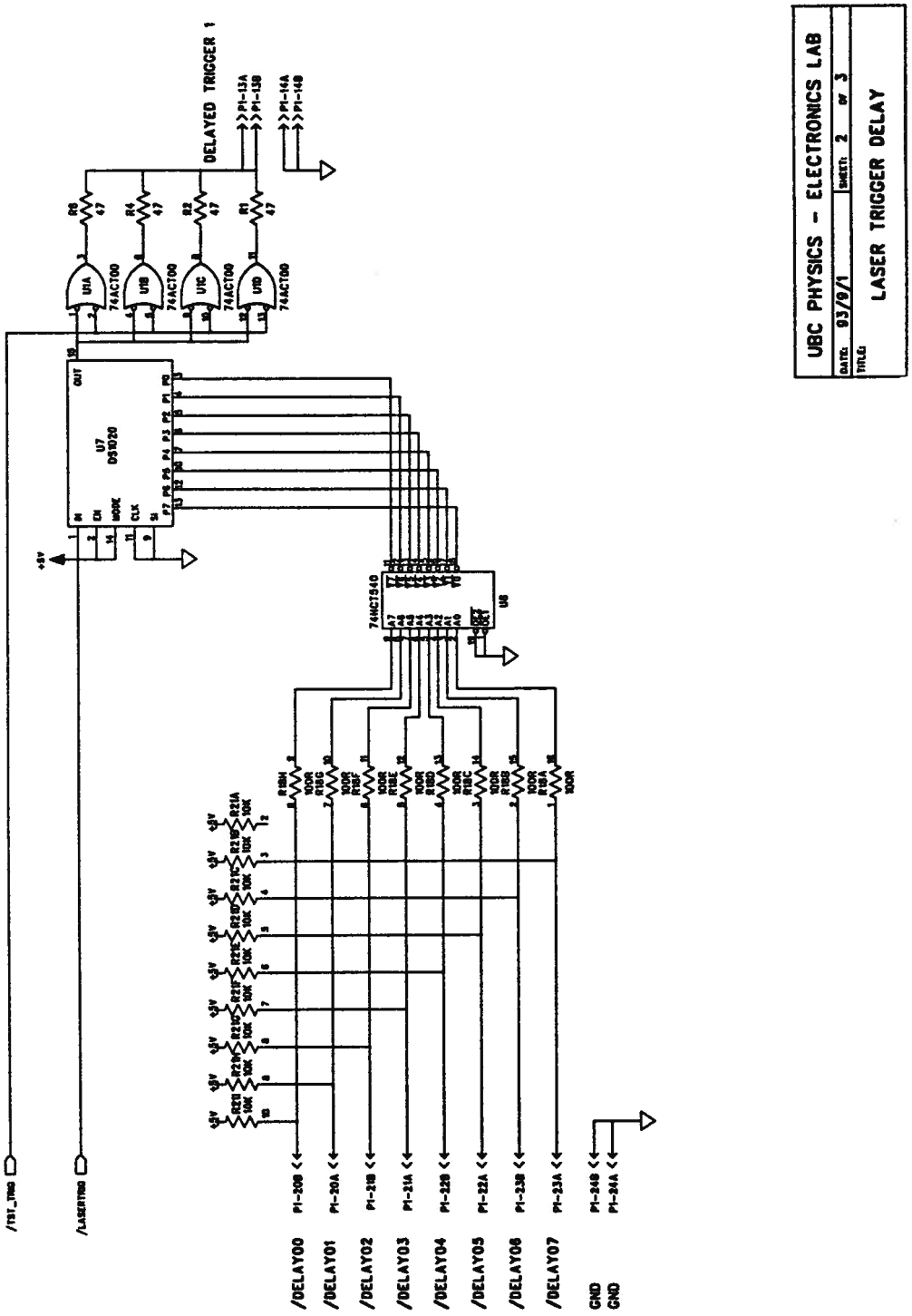
UBC PHYSICS - ELECTRONICS LAB
DATE: 93/9/1
SHEET: 2 OF 3
TITLE: LASER TRIGGER DELAY
DELAYED TRIGGER 1
74ACT00
74HCT540
/DELAY00
/DELAY01
/DELAY02
/DELAY03
/DELAY04
/DELAY05
/DELAY06
/DELAY07
GND
GND

Diagram C.7:

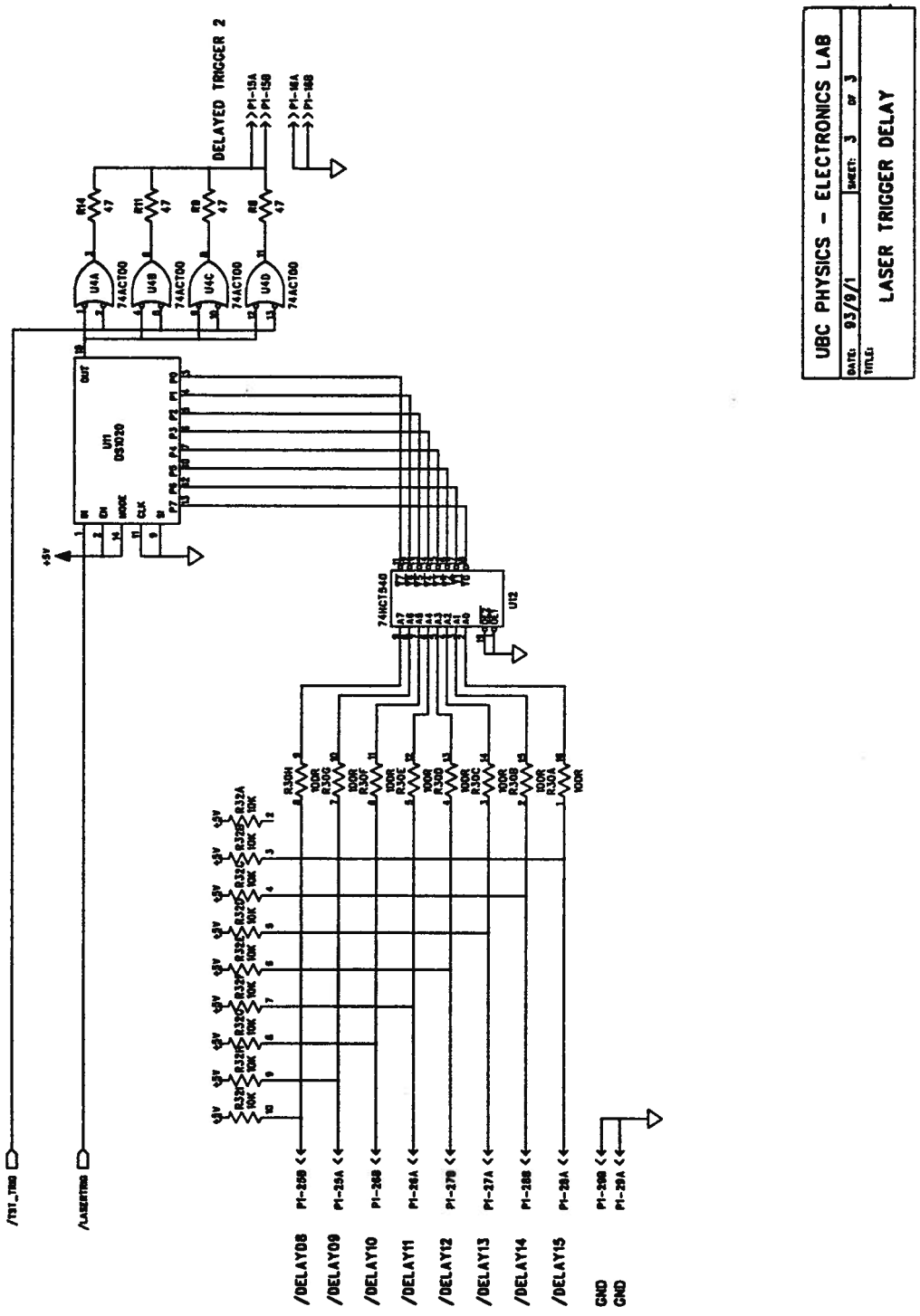
UBC PHYSICS - ELECTRONICS LAB
DATE: 93/9/1
SHEET: 3 OF 3
TITLE: LASER TRIGGER DELAY
DELAYED TRIGGER 2
74ACT00
74HCT540
/DELAY08
/DELAY09
/DELAY10
/DELAY11
/DELAY12
/DELAY13
/DELAY14
/DELAY15
GND
GND

Diagram C.8:

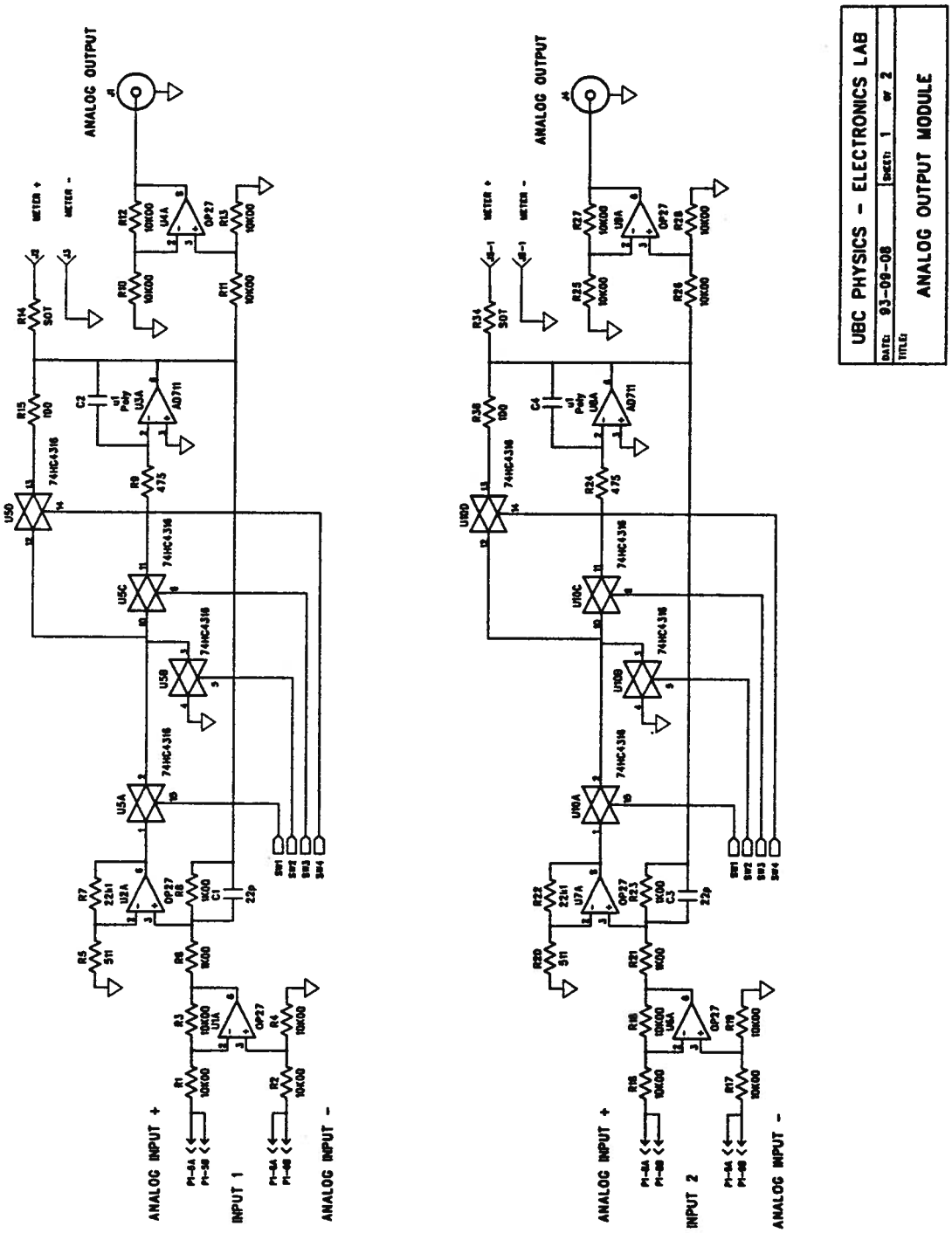
UBC PHYSICS - ELECTRONICS LAB
DATE: 93-09-08
SHEET: 1 OF 2
TITLE: ANALOG OUTPUT MODULE
ANALOG OUTPUT
METER +
METER -
ANALOG INPUT +
ANALOG INPUT -
INPUT 1
INPUT 2
74HC4316
AD711
OP27

Diagram C.9:

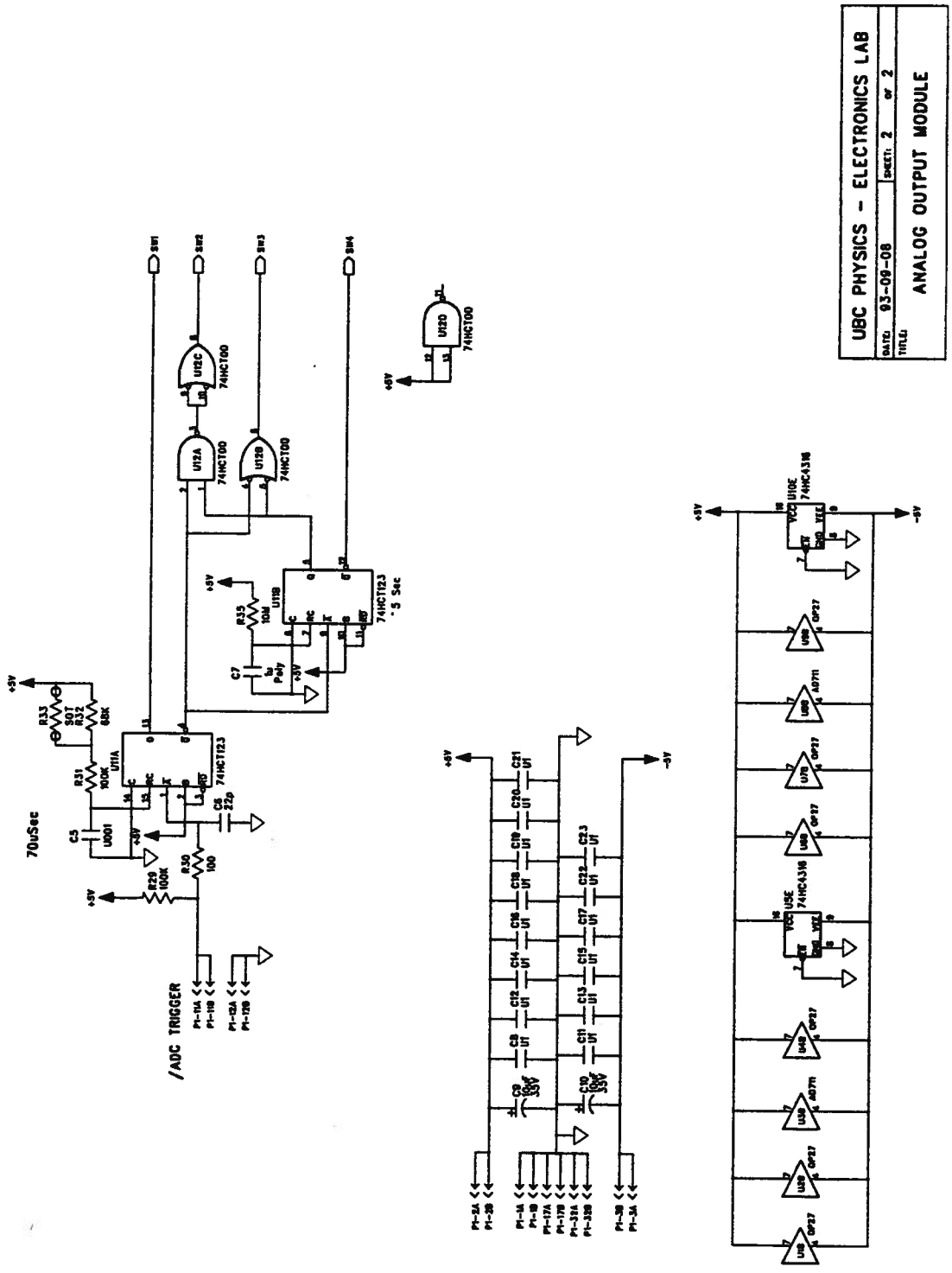
UBC PHYSICS - ELECTRONICS LAB
DATE: 93-09-08
SHEET: 2 OF 2
TITLE: ANALOG OUTPUT MODULE
/ADC TRIGGER
70uSec
74HCT123
74HCT00
74HC4538
74HC100

Diagram C.10:

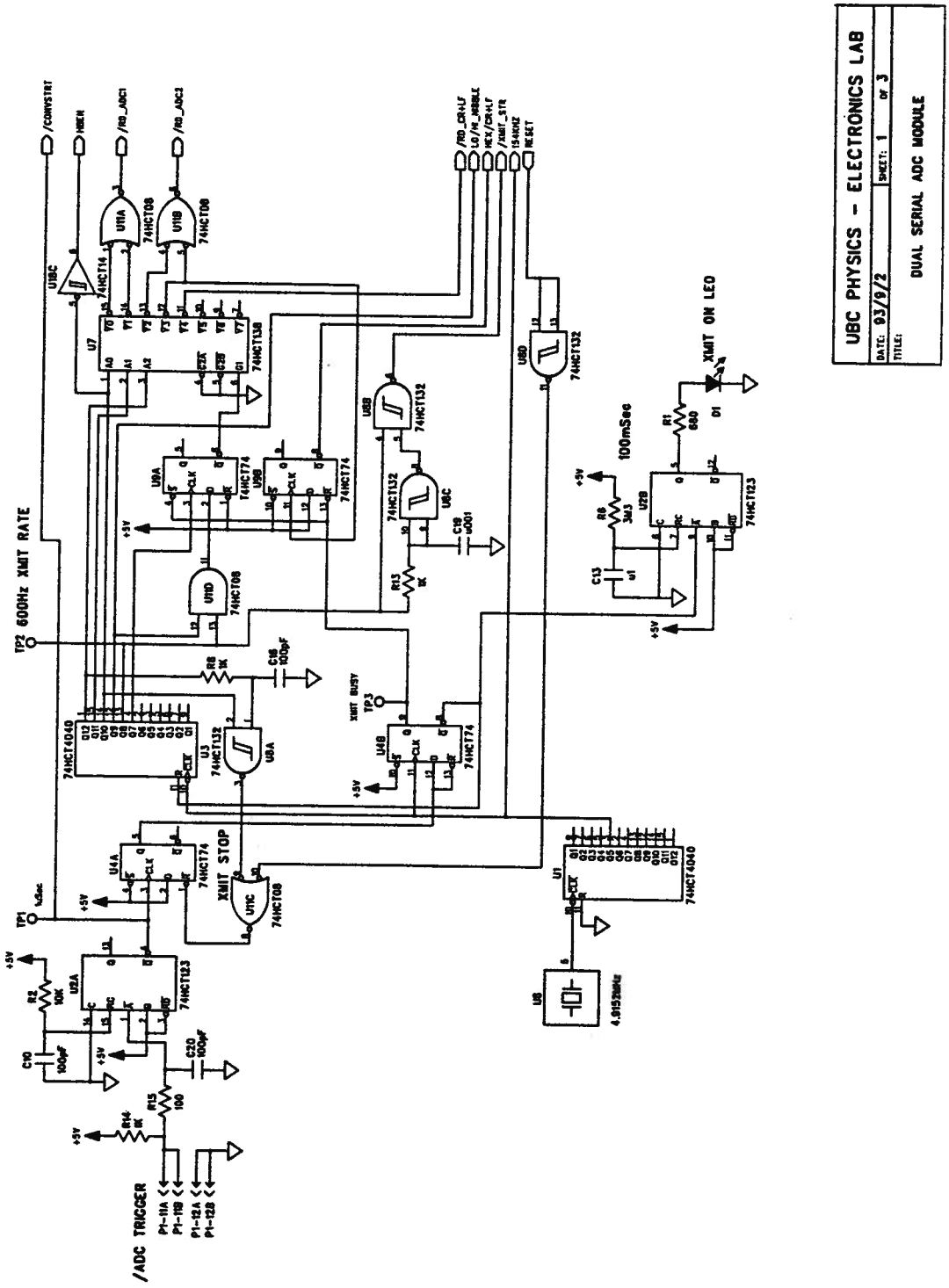
UBC PHYSICS - ELECTRONICS LAB
DATE: 93/9/2
SHEET: 1 OF 3
TITLE: DUAL SERIAL ADC MODULE
/CONVSTRT
HBEN
/RD_ADC1
/RD_ADC3
/RD_CRAM
LB/HB_MSBLE
HEX/CRAM
/XMIT_STR
154KHZ
RESET
XMIT ON LED
100mSec
TP2 600Hz XMIT RATE
XMIT BUSY
TP3
XMIT STOP
TP1
/ADC TRIGGER
P1-11A
P1-11B
P1-12A
P1-12B
74HCT14
74HCT08
74HCT138
74HCT174
74HCT132
74HCT4040
74HCT123
+5V

Diagram C.11:

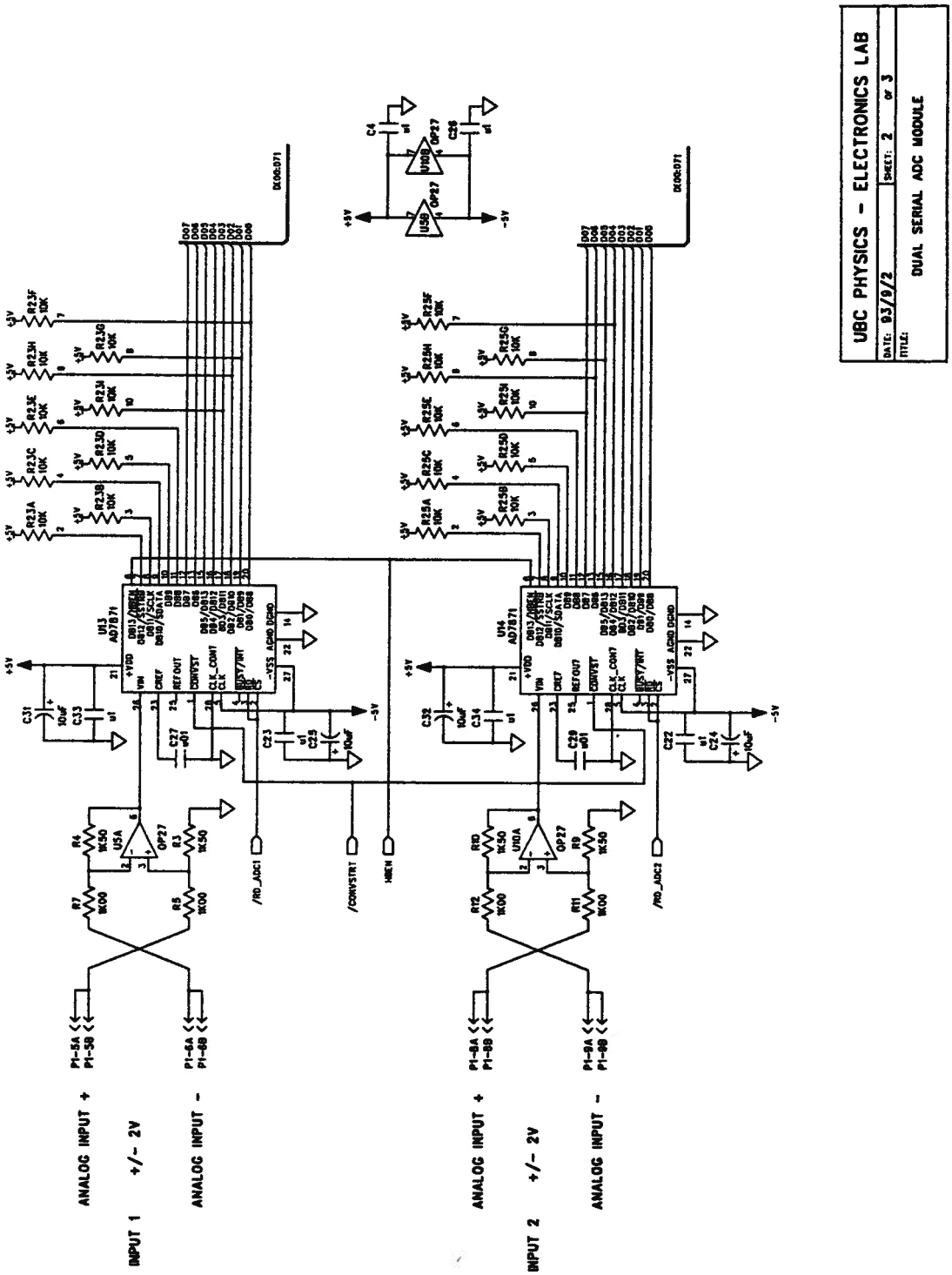
UBC PHYSICS - ELECTRONICS LAB
DATE: 93/9/2
SHEET: 2 OF 3
TITLE:
DUAL SERIAL ADC MODULE
ANALOG INPUT +
+/- 2V
ANALOG INPUT -
INPUT 1
ANALOG INPUT +
+/- 2V
ANALOG INPUT -
INPUT 2
/RD_ADC1
/CONVSTRT
HOLD
/RD_ADC2

Diagram C.12:

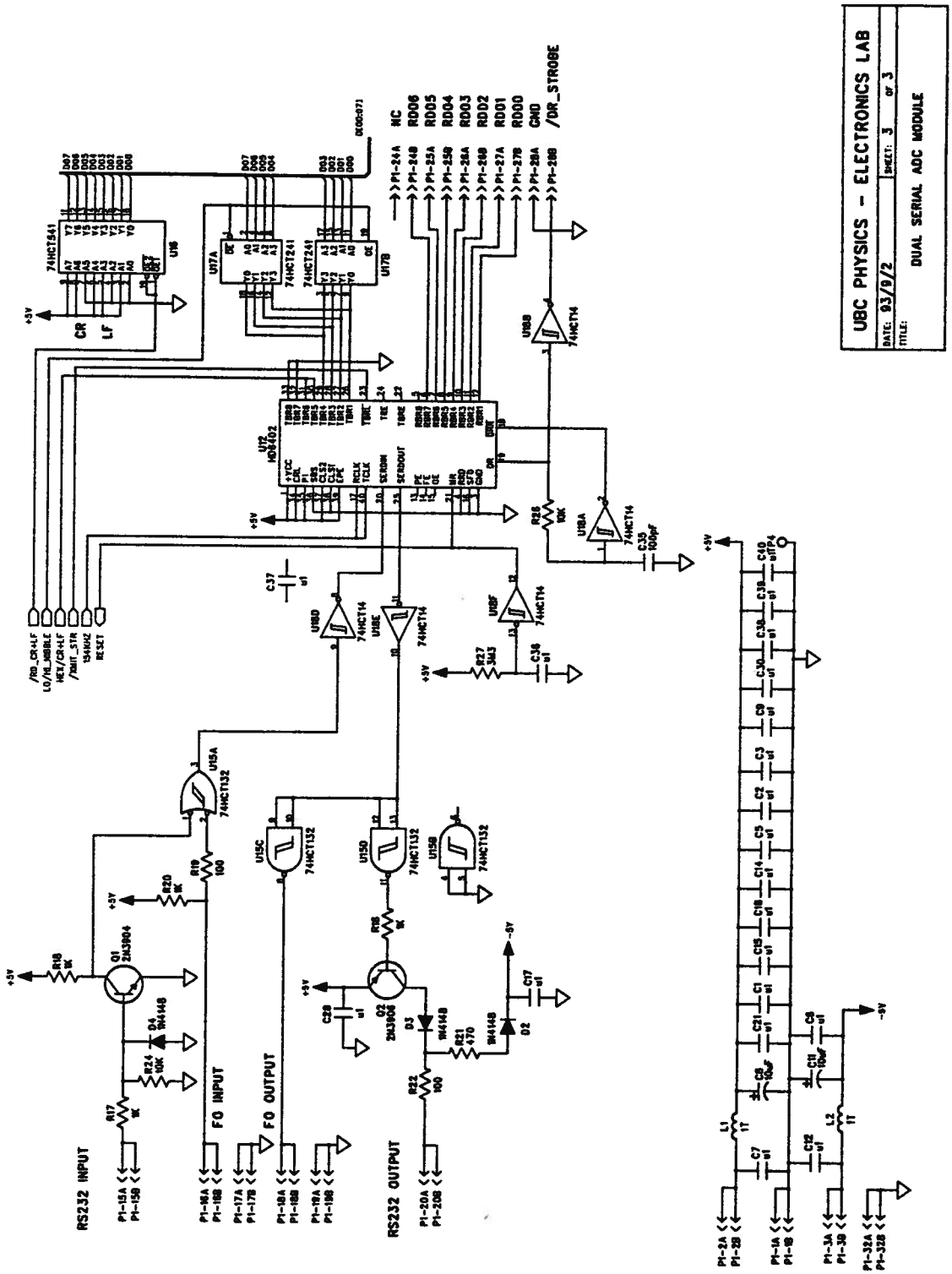
UBC PHYSICS - ELECTRONICS LAB
DUAL SERIAL ADC MODULE
RS232 INPUT
FO INPUT
FO OUTPUT
RS232 OUTPUT

Appendix D

The Autocorrelator Design and Optical Components

The main component in the design of the autocorrelator is the second harmonic generation crystal (SHG). The nonlinear crystal used in the current setup is a 0.5 mm thick Potassium Dihydrogen Phosphate (KDP) crystal with a 10 mm aperture. The angular adjustment of the crystal is very crucial in obtaining a SH signal; therefore, the crystal is mounted on a fine-rotational-tilt stage which provides excellent control over the crystal alignment. The crystal is oriented to obtain a maximum SH signal which emerges from the crystal along the bisector of the two converging input light beams.

In order to produce a SH signal from the 616 nm laser pulses, the two pulses must be simultaneously present at the crystal with a phase matching angle of 59.26° from the optical axis. The crystal is cut at an angle of 58.6° which is slightly less than the phase matching angle. The small angle difference of 0.7° eliminates the back reflection into the laser cavity.

The thickness of the crystal limits the temporal resolution of the autocorrelator. This can limit the minimum pulse that can be measured with this device. The crystal length determines the bandwidth of the SHG signal, and it should be shorter than the coherence length of the frequency components of the light pulse in order to avoid dispersion. For a given KDP crystal length, $\triangle L_{cry}$, one can calculate the bandwidth resolution, $\triangle \nu_{cry}$, of the autocorrelator from the following relation [253]

$$\triangle \nu_{cry} \triangle L_{cry} = 0.3122(nm - cm) \tag{D.1}$$

From our experimental parameters, the temporal resolution of the autocorrelator

is calculated to be 90 fs times the pulse shape factor. For a double exponential pulse shape the autocorrelator resolution, due to the crystal thickness only, is $\sim$ 40 fs. The overall resolution is $\sim$ 60 fs. This temporal resolution is adequate for our experimental purposes.

The KDP crystal is transparent to both fundamental (616 nm) and SH (308 nm) signals; therefore, for proper SH detection, the fundamental signal must be filtered out. In the autocorrelator design, a piece of $3\times5\times5$ cm^3 Corning (G 57-54-1) U.V. glass filter is used. The filter is inserted directly in front of the photomultiplier housing.

Since the SH signal is in the U.V. range, for the detection of such signal one requires a photomultiplier which is sensitive to this wavelength. In the autocorrelator design, we used a Hamamatsu photomultiplier with a U.V. input window and a risetime of $\sim$ 2.5 ns. The photomultiplier is biased to a voltage of 600 V. Due to the operating sensitivity of the photomultiplier, it is placed in a light-tight cylindrical housing with the SH signal entering through a 3 mm diameter pinhole.

A low pass filter/amplifier is used to filter out the high frequency components in the autocorrelation trace and to amplify the autocorrelation signal. The circuit design for the filter/amplifier is presented in figure D.1. The output signal from the electronic amplifier/filter arrangement is used to drive the vertical axis of a high impedence oscilloscope, where the signal amplitude corresponds to points on the autocorrelation trace. All the mirrors used in the autocorrelator are front surface aluminum coated silica: M_1–M_5 are 2.5 cm in diameter and 6.5 mm in thickness. The retroreflector mirrors M_6 and M_7 have a dimension of $12.5\times$ 12.5×6 mm^3. The 50:50 beam splitter used in the autocorrelator is 6.35 cm in diameter. The focussing lens is a plano convex type with a focal length of 3 cm and a diameter of 12 mm. This lens is mounted on a homemade fine-translation stage to adjust the focus on the SH crystal. The rotation of the mirrors is done with a torque motor

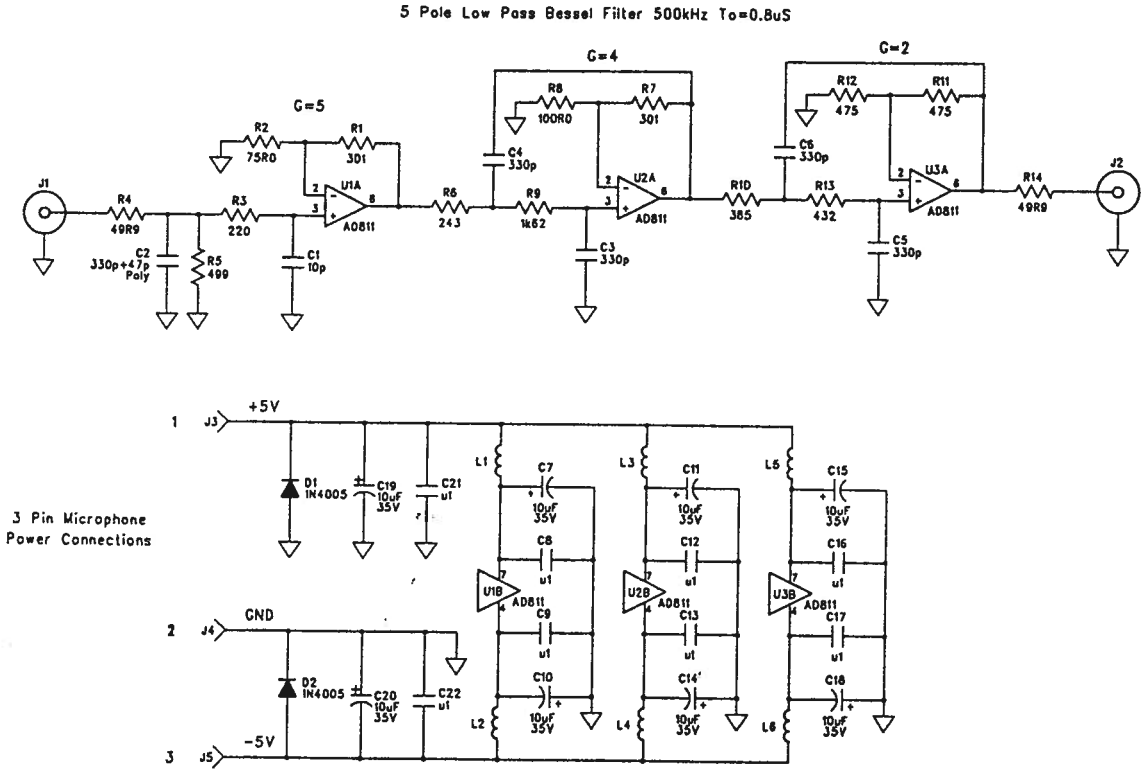

Figure D.1: Low pass filter and amplifier circuit used for the autocorrelation pulse measurements.

which rotates at a constant reliable frequency of 25 Hz. This motor provided an almost vibrational-free scanning mechanism. The control box of the autocorrelator has the functions of: relative delay scan adjustment between the trigger pulse and the autocorrelation scan, and signal gain adjustment. Triggering of the oscilloscope from the autocorrelator is performed using an optical interrupter placed under the rotating mirrors. The delay of the trigger signal can be adjusted between 0.5 to 10 ms relative to the beginning of the scan.

D.1 Calibration of the Autocorrelator

It is clear that one is required to calibrate the time scale on the oscilloscope screen from the relative scanning time to the real time. The calibration of the horizontal scale is done manually. Here, one uses the optical pulse itself to calibrate the time scale. If the two arms of the interferometer are equal, both laser pulses overlap only at one point in time. When the retroreflector is scanned while the rotating arm is spinning, the dye pulses overlap at different points in time, resulting in the SH signal peak being shifted as a function of the retroreflector scan. One can use this to obtain a calibration factor for the autocorrelator from the following relation

$$T_{scale} = 2\frac{X_d}{0.3S_d}t(ps/ms) \tag{D.2}$$

where X_d is the distance in mm travelled by the retroreflector arm, S_d is the peak shift in ms of the SH signal, and t is the time scale. The factor of 2 accounts for the actual distance travelled by the pulse. Experimentally, the calibration factor is measured to be 81.33 ps/ms. Theoretical calculation of the calibration factor from reference [134] gives

$$T_{scale} = \frac{4\pi f_r D_r}{c} \tag{D.3}$$

where c is the speed of light, D_r (= 7.62 cm) is the distance between the two rotating mirrors, and f_r (= 25 Hz) is the rotational frequency, giving a calibration

factor of 79.79 ps/ms which is in good agreement with the above measured value.